Measurement of the High Energy Neutrino Interaction Cross Section Using Neutrino-Induced Electromagnetic and Hadronic Showers Observed in Five Years of IceCube Data

A Dissertation Presented

by

Yiqian Xu

to

The Graduate School

in Partial Fulfillment of the Requirements

for the Degree of

Doctor of Philosophy

in

Physics

Stony Brook University

May 2019

Stony Brook University

The Graduate School

Yiqian Xu

We, the dissertation committee for the above candidate for the Doctor of Philosophy degree, hereby recommend acceptance of this dissertation.

Joanna Kiryluk - Dissertation Advisor
Associate Professor, Department of Physics and Astronomy

George F. Sterman - Chair of Defense
Professor, Department of Physics and Astronomy

Xu Du
Associate Professor, Department of Physics and Astronomy

Emlyn W. Hughes
Professor, Department of Physics
Columbia University

This dissertation is accepted by the Graduate School.

Richard Gerrig
Interim Dean of the Graduate School

Abstract of the Thesis

Measurement of the High Energy Neutrino-Nucleon Cross Section Using Neutrino-Induced Electromagnetic and Hadronic Showers Observed in Five Years of IceCube Data

by

Yiqian Xu

Doctor of Philosophy

in

Physics

Stony Brook University

2019

The neutrino-nucleon interaction cross section at the TeV to EeV energy range has been calculated within the Standard Model using the parton distribution functions. Due to the limited energy from ground-based accelerators, the cross section in this energy range cannot be measured directly. The astrophysical neutrinos detected in the IceCube detector are a perfect candidate to perform this kind of measurement. IceCube is a 1 cubic kilometer size neutrino detector located at the South Pole. It is capable of detecting all-sky neutrinos of all flavors from GeV to EeV energies. After the detector completion, the IceCube collaboration discovered and measured the flux of extraterrestrial neutrinos in the TeV - PeV energy range, along with the flux of neutrinos from the known atmospheric origin.

This dissertation presents a novel analysis method and the result of the neutrino interaction total cross section measurement as a function of neutrino energy in the 6.3 TeV - 10 PeV energy range with neutrino-induced electromagnetic and hadronic showers (cascades) observed in five years of IceCube data. The final sample consists of 654 cascade events mainly induced by astrophysical electron and tau neutrinos with energies from 6.3 TeV to 10 PeV and all-sky directions. The events are assigned in four energy bins and two zenith bins ("down-going" from the southern hemisphere and "up-going" from the

northern hemisphere). When assuming an all-sky isotropic astrophysical neutrino flux, the ratio of the down-going to the up-going events (which are absorbed by the Earth at high energies) is sensitive to the magnitude of the interaction cross section but insensitive to the large astrophysical neutrino flux uncertainties. The measured cross section is the combination of the Standard Model neutrino-nucleon deep inelastic scattering cross section and the Glashow Resonance cross section of electron antineutrino scattering off atomic electrons, which depends on the neutrino generation process type (pp or $p\gamma$) at the astrophysical source.

The resulting cross section is consistent with the Standard Model expectation and with the previous IceCube results. With the next generation of IceCube (Gen2 upgrade), the measurement will potentially have the sensitivity to detect the Beyond Standard Model effects for neutrino energies above EeV if they exist.

Acknowledgements

I would like to express my sincere gratitude to my dissertation defense committee:

Prof. Joanna Kiryluk

Prof. George Sterman

Prof. Xu Du

Prof. Emlyn W. Hughes

, especially my advisor Prof. Joanna Kiryluk who has taught me so much during my years in Stony Brook. Not only she provided me with insightful advice in doing physics research, but also she has taught me interpersonal skills that I will benefit from for life.

I would also like to thank Dr. Hans Niederhausen who has been a great colleague and a dear friend. His broad knowledge about statistics and IceCube software has been a truly useful resource for my research. I'm also grateful that he was patient enough to explain them to me.

My grateful thanks are also extended to Dr. Xiyuan Chi and Schecki who have provided me with a tremendous amount of emotional support which was much needed during my graduate school.

My friends Dr. Gongjun Choi, Ms. Wenqing Fan, Dr. Hualong Gervais, Dr. Spencer Horton, Dr. Bertus Jordaan, Dr. Ludwig Krinner, Mr. Tyler Kutz, Mr. Yusong Liu, Dr. Aleksas Mazaliauskas, Mr. Scott Mills, Dr. Jean Paul Nery, Ms. Shinhae Sohn, Ms. Juliana Stachurska, and Dr. Mingliang Zhou have made my time at Stony Brook very special. For which I'm very grateful.

Last but not least, I would like to express my gratitude to my family. They may not understand my decisions, but they have always been most supportive.

This material is based upon work supported by the National Science Foundation under Grant No. 1130728.

Contents

Abstract iii

Acknowledgements v

List of Figures ix

List of Tables xiv

1 Neutrinos and Interactions 1
- 1.1 Neutrino Properties . . . 2
  - 1.1.1 The Standard Model . . . 2
  - 1.1.2 Neutrino Oscillation . . . 3
- 1.2 Neutrino Sources . . . 4
  - 1.2.1 Cosmic Rays . . . 4
  - 1.2.2 Atmospheric Neutrinos . . . 9
  - 1.2.3 Astrophysical Neutrinos . . . 12
- 1.3 Neutrino Interactions . . . 18
  - 1.3.1 Deep Inelastic Scattering . . . 18
  - 1.3.2 Glashow Resonance . . . 22

2 The IceCube Detector 27
- 2.1 Neutrino Detection . . . 27
- 2.2 IceCube Instrumentation . . . 29
- 2.3 Data Acquisition and Processing . . . 33
- 2.4 Event Signature and Reconstruction . . . 36
- 2.5 Monte Carlo Simulation . . . 39

3 Event Selection 41
- 3.1 Cascade Level2 . . . 42
  - 3.1.1 Cascade Level2 Filter Passing Rate . . . 42
  - 3.1.2 Experimental Data Good Runs . . . 43
- 3.2 Cascade Level3 . . . 45
- 3.3 Level 4 . . . 46
  - 3.3.1 Variable Definition . . . 46
  - 3.3.2 Level 4A: Polygon Cut . . . 49

3.3.3 Level 4B: Monopod Z Cut . . . 51
3.3.4 Level 4C: Qtot_HLC Cut . . . 52
3.3.5 Level 4D: TimeSplitPosition Cut . . . 54
3.3.6 Level 4E: Delay Time Cut . . . 56
3.3.7 Level 4F: MaxDomChargeOM Cut . . . 58
3.3.8 Level 4G (Final Level): Starting Track Charge Cut . . . 59
3.4 Signal Efficiency, Background Rejection and Effective Area . . . 61
3.4.1 Signal Efficiency and Background Rejection . . . 63
3.4.2 Effective Area . . . 64
3.5 Cross Year Comparison . . . 65
3.6 Merging with the Low Energy Event Selection . . . 65
3.7 Unblinded Sample . . . 68
3.7.1 Dust Layer Events . . . 69
3.7.2 Dust Layer Events Energy Reconstruction using Gradient Boosted Decision Trees . . . 74
3.7.3 Final Level Contained Cascade Five Years Data Sample Statistic . 83

4 Analysis Method 87
4.1 An Overview of the Analysis Method . . . 87
4.2 Ratio Versus Cross Section . . . 90
4.3 Ratio Versus Neutrino Energy . . . 91
4.3.1 Detector Acceptance Effect Correction Factor . . . 91
4.3.2 Ratio Versus Neutrino Energy for Asimov Data . . . 93
4.4 Cross Section Versus Neutrino Energy . . . 93
4.4.1 Cross Section vs. Neutrino Energy for Asimov Data . . . 93
4.4.2 Neutrino to Antineutrino Ratio . . . 94
4.5 Tau Regeneration . . . 96
4.6 Validation Study with ν_τs . . . 99

5 Unfolding 102
5.1 Iterative Unfolding . . . 103
5.1.1 Iterative Unfolding Method . . . 103
5.1.2 Iteration Optimization . . . 105
5.2 Uncertainty Estimation . . . 108
5.2.1 Markov Chain Monte Carlo . . . 108
5.2.2 Truth Coverage Test . . . 110

6 Systematic Uncertainties 117
6.1 The Ice Property of the South Pole Ice . . . 117
6.1.1 Hole Ice Scattering . . . 117
6.1.2 The Absorption Length Uncertainty in the South Pole Ice (Bulk Ice) 122
6.1.3 The Scattering Length Uncertainty in the South Pole Ice (Bulk Ice) 124
6.2 The Detector Response - the Relative DOM Efficiency . . . 127
6.3 The Earth Atmosphere . . . 129
6.3.1 The Conventional Atmospheric Neutrino Flux . . . 129

6.3.2 The Self-Veto Effect for Atmospheric Neutrinos 132
6.4 The Astrophysical Neutrino Flux 135

7 Results **137**
7.1 Analysis Procedure Summary 137
7.2 Unfolding Result 138
7.2.1 Unfolded Distribution 138
7.2.2 Statistical Uncertainty Calculation 138
7.3 Cross Section Measurement Result 139
7.3.1 Statistical Uncertainty 139
7.3.2 Systematic Uncertainty 141
7.4 Discussion of the Cross Section Measurement Result 145
7.4.1 Physical Interpretation of the Measured Cross Section 145
7.4.2 Comparison with Neutrino-Nucleon DIS Cross Section Calculations 147
7.4.3 P-Value 149
7.4.3.1 The P-Value of the Standard Model DIS Cross Section . 149
7.4.3.2 The P-Value of the Glashow Resonance Cross Section . . 151

8 Summary and Outlook **154**

Bibliography **156**

List of Figures

1.1 The Flux of the Individual Primary Nuclei in the Cosmic Rays 5
1.2 The Flux of the Combination of All Primary Nuclei in Cosmic Rays . . 7
1.3 An Illustration of the Creation of the Secondaries when the Cosmic Rays Entering the Earth's Atmosphere 11
1.4 The Schematic of the Emission of Particles from AGNs 15
1.5 The Neutrino Flux of Neutrinos from Different Origins 18
1.6 Deep Inelastic Scattering Feynman Diagram 20
1.7 The Feynman Diagram of Neutrino-Nucleon Charged-Current and Neutral-Current Interaction. 20
1.8 Measurements of the Neutrino-Nucleon Charged-Current Interaction Cross Section at A Few Hundred GeV 23
1.9 The Parton Distribution Functions from HERA I and HERA I+II 23
1.10 The Calculated Neutrino Interaction Cross Section 24
1.11 The Feynman Diagram of an Electron Antineutrino Scattering off an Electron 24

2.1 An Illustration of the Cherenkov Radiation Effect 28
2.2 The Instrumentation of the IceCube Neutrino Observatory 29
2.3 The Schematic of the Component of a DOM 31
2.4 The Schematic of the Data Flow within a DOM 32
2.5 The Overview of the Data Flow in the IceCube Online System 34
2.6 The Event Signatures in IceCube 37
2.7 The Transformation from Waveforms to Pulse Series 38

3.1 The Cascade Level2 Rate for Every Run between May 2011 to May 2015 vs. MJD 43
3.2 Outlier Cleaning for the 2012-2015 Experimental Data 44
3.3 Variable Distributions for the Data and the Monte Carlo at the Cascade Level3 Single Contained Branch 50
3.4 The Polygon Containment Distribution for the Data and the Monte Carlo at the Cascade Level3 Single Contained Branch 51
3.5 Monopod Z Distribution for the Data and the Monte Carlo at the Level 4A 52
3.6 Monopod Energy vs. Qtot_HLC for Data, Corsika and NuGen at level 4B 54
3.7 Monopod Energy vs. TimeSplitPosition for the Data, Corsika and NuGen at level 4C 56
3.8 The Depth Resolution of the Monopod Reconstruction for Cascade Events 57
3.9 Monopod Energy vs. DelayTime for Data, Corsika and NuGen at level4 D 58

3.10 The MaxDomChargeOM Distribution for the Data and the Monte Carlo at Level 4E . . . 60
3.11 Monopod Energy vs. Starting Track Charge for the Data, Corsika and NuGen at level 4F . . . 61
3.12 Variable Distributions for the Data and the Monte Carlo at the Final Level 62
3.13 The Rate at the Final Level of this Selection, the Final Level of the Cascade 2yr Analysis and the Cascade Level3 Single Contain Branch for the Simulations in the Monopod Reconstructed Energy Bins . . . 64
3.14 The Effective Area of ν_e, ν_τ and ν_μ for this Event Selection and the Cascade 2yr Analysis Event Selection . . . 66
3.15 Variable Distribution for the 2011 100% Data, the 2012-2015 10% Data and the Monte Carlo at the Final Level . . . 67
3.16 The Rate at the Final Level of this Selection, the Final Level of the LE Selection and the Cascade Level3 Single Contained Branch for the Simulations in the Monopod Reconstructed Energy Bins . . . 69
3.17 The Rate at the Final Level of the LE + HE selection, the Final Level of the Cascade 2yr Analysis Selection and the Cascade Level3 Single Contained Branch for the Simulations in the Monopod Reconstructed Energy Bins . 70
3.18 The Effective Area of ν_e, ν_τ, and ν_μ for the LE + HE Selection and the Cascade 2yr Analysis Selection . . . 71
3.19 The Depth Dependence of the Absorption and Scattering Parameters of the South Pole Ice . . . 72
3.20 The Monopod Reconstructed Energy vs. the Total Charge for NuE simulation in the Region of -85m < Monopod_Z < -75m and in the Whole Detector . . . 72
3.21 The Event Display of "Eurus" and the Other Three PeV Events . . . 73
3.22 The Energy Resolution for the Special NuE Simulation Injected at the Different Depths in the Dust Layer . . . 74
3.23 A Demonstration of the Decision Tree Algorithm . . . 75
3.24 The Energy Resolution of the GBDT Reconstructed Energy . . . 80
3.25 The Monopod Zenith Resolution of the Dust Layer Events . . . 82
3.26 The Energy Resolution of the Monopod Reconstructed Energy in the Dust Layer Region and the Whole Detector for Events above 100 TeV . . . 83
3.27 The Monopod Reconstructed Depth Distribution of the Unblinded Sample and the Simulation for above 100 TeV . . . 84
3.28 The Reconstructed Energy and Zenith Distribution for the Unblinded Data and the Simulation at the Final Level . . . 85

4.1 The Schematic of the Analysis Method to Measure the Neutrino Interaction Cross Section . . . 88
4.2 The Zenith Angle Dependence of Atmospheric Neutrino Flux at 10 TeV Neutrino Energy . . . 89
4.3 A Simplified Illustration of the Correlation among the Neutrino Energy, the Down-going Events/Up-going Events Ratio and the Neutrino Interaction Cross Section . . . 90
4.4 The Ratio of Down-going Events over Up-going Events vs. Cross Section 91

4.5 Detector Acceptance Rate for the Down-going Events and the Up-going Events in Neutrino Energy Bins 92
4.6 Ratio vs. Neutrino Energy (Asimov) 93
4.7 Cross Section Vs. Neutrino Energy (Asimov) 95
4.8 Neutrino and antineutrino Composition at the Final Level 96
4.9 Weighted Total Cross Section (CSMS) as A Function of Neutrino Energy 97
4.10 The Composition of the Up-going Neutrinos at the detector for all Neutrino Energy Bins 98
4.11 The Ratio of the Down-going Events to the Up-going Events vs. Cross Section Calculated using Monte Carlo Simulations Generated with Three Different Scaling Factors of CSMS Cross Section 99
4.12 Ratio vs. Neutrino Energy for Monte Carlo Simulations Generated with Different Scaling Factors of CSMS Cross Section 100
4.13 Cross Section Vs. Neutrino Energy for Monte Carlo Simulations Generated with Three Different Scaling Factors of the CSMS Cross Section 101

5.1 Relationship between the Reconstructed Variables and the True Variables 102
5.2 Relationship between the Weighted Mean Square Error and the Number of Iteration 107
5.3 Likelihood Ratio used to Determine number of Iteration 108
5.4 The Comparison between the Unfolded True Distribution and the Real True Distribution 109
5.5 The MCMC Sample (for Asimov Data) Number of Events Distribution in the Reconstructed Space 110
5.6 The Unfolded NEvents Posterior Distribution for Asimov Data in True Space after unfolding 111
5.7 The Unfolded Ratio Posterior Distribution for Asimov Data 112
5.8 The Unfolded Ratio Truth Coverage for 5 Years of Livetime 113
5.9 The Unfolded Ratio Truth Coverage for 100 Years of Livetime 114
5.10 The Truth Coverage Rate vs. Expected NEvents for Different Uncertainty Range in Posterior Distribution 114
5.11 The Ratio Truth Coverage vs. the Expected Number of Events in the Down-going Bin and the Up-going Bin 115
5.12 The Unfolded Ratio Truth Coverage for 5 Years of Livetime with Re-calibrated Uncertainty Range for the Last 2 Bins 116

6.1 The H2 30 Simulation to H2 50 simulation ratio in the Reconstructed and True Energy and Zenith Bins 118
6.2 The Reconstructed Zenith and Energy Distribution of the 2011-2015 Unblinded Data, compared with the H2 30 Neutrino Simulation and the H2 50 Neutrino Simulation. 119
6.3 The Angular Acceptance Curves with Different Parameters in Comparison with the H2 50 Model 120
6.4 The Comparison of the Flasher Hole Ice Models with p_2 = -1, 0, 1 in the Reconstructed and True Energy and Zenith Bins 121

6.5 The Systematic Uncertainty Associated with the p_2 Parameter of the Ratio and the Cross Section in the Neutrino Energy Bins tested with the Asimov Data (p_2=0) . . . 122
6.6 The Unfolded and Factor Corrected Ratio of the $p_2 = 2$ Asimov Data using the p_2 = -1, 0, 1 Simulation in Different Neutrino Energy Bins . . . 123
6.7 The Comparison of the Data Set with 10% increase in the Absorption Coefficient of the Ice Model and the Baseline (H2 50) Data Set in the Reconstructed and True Energy and Zenith Bins . . . 123
6.8 The Systematic Uncertainty Associated with the Change in the Absorption Coefficient of the Ratio and the Cross Section in the Neutrino Energy Bins tested with the Asimov Data (H2 50) . . . 124
6.9 The Comparison of the Data Set with 10% increase in the Scattering Coefficient of the Ice Model and the Baseline (H2 50) Data Set in the Reconstructed and True Energy and Zenith Bins . . . 125
6.10 The Systematic Uncertainty Associated with the Change in the Scattering Coefficient of the Ratio and the Cross Section in the Neutrino Energy Bins tested with the Asimov Data (H2 50) . . . 126
6.11 The Unfolded and Factor Corrected Ratio of the Baseline Scattering Asimov Data using the Baseline Scattering and the +10% Scattering Simulation in Different Neutrino Energy Bins . . . 128
6.12 The Comparison of the Different DOM Efficiency Simulation (90%, 95%, 99% (baseline), 108%) in the Reconstructed and True Energy and Zenith Bins . . . 130
6.13 The Systematic Uncertainty Associated with the DOM Efficiency of the Ratio and the Cross Section in the Neutrino Energy Bins tested with the Asimov Data (H2 50) . . . 131
6.14 The Comparison between the Conventional Atmospheric Neutrino Flux Calculated using the NRLMSISE00 model and the U.S. Standard 1976 in the Neutrino Energy and Zenith Bins . . . 132
6.15 The Comparison between the Total Event Rate Calculated with the NRLMSISE00 Conventional Flux and the U.S. Standard 1976 Conventional Flux in the Reconstructed and True Energy and Zenith Bins . . . 133
6.16 The Systematic Uncertainty Associated with the Atmospheric Model of the Ratio and the Cross Section in the Neutrino Energy Bins tested with the Asimov Data (H2 30) . . . 133
6.17 The Comparison between the Self-veto Effect Calculated with Different $E_{\mu,\mathrm{min}}$s and the Event Rate of the Atmospheric Neutrino with the Full CORSIKA simulation in the Reconstructed Energy Bins and in the Neutrino Energy Bins. . . . 134
6.18 The Uncertainty Contour of the Astrophysical Neutrino Flux Parameters and its Impact on the Cross Section in the Neutrino Energy Bins tested with the Asimov Data (H2 30) . . . 136

7.1 The Energy and Zenith Distribution Before (Reconstructed) and After (True) the Unfolding Procedure for the Data and the Simulation . . . 139
7.2 The Unfolded Number of Events Posterior Distribution for the Unblinded Data in the True Space after unfolding . . . 140

7.3 The Unfolded Ratio of the Unblinded Data in Neutrino Energy Bins and its Statistical Uncertainty Estimation 140
7.4 The Cross Section Measurement Result of the Unblinded Data and its Statistical Uncertainty 141
7.5 The Systematic Uncertainty Associated with the p_2 Parameter on the Ratio and the Cross Section in the Neutrino Energy Bins of the Unblinded Data 142
7.6 The Systematic Uncertainty Associated with the Change in the Bulk Ice Scattering Coefficient on the Ratio and the Cross Section in the Neutrino Energy Bins of the Unblinded Data 143
7.7 The Systematic Uncertainty Associated with the Change in the Astrophysical Neutrino Flux Parameters of the Cross Section in the Neutrino Energy Bins of the Unblinded Data 143
7.8 The Cross Section Measurement Result of the Unblinded Data in Comparison with Neutrino-Nucleon Interaction Cross Section Calculations and One Previous IceCube Cross Section Measurement Result 148
7.9 The P-Value Estimation for the Standard Model DIS Cross Section with only Statistical Uncertainty 151
7.10 The P-Value Estimation for the GR Cross Section with both Statistical and Systematic Uncertainty 152
7.11 The P-Value Estimation for the Standard Model DIS Cross Section with both Statistical and Systematic Uncertainty 153

List of Tables

1.1 The Standard Model of Elementary Particles . . . 3
1.2 Properties and Decay Channels of Selected Mesons . . . 13
1.3 The Neutrino Flavor Ratio at the Source and at the Earth for Different Generation Processes . . . 14
1.4 The Integrated Neutrino-Electron Scattering Cross Section at 6.3 PeV . . 25

3.1 The 2011, 2012 and 2013 Cascade Level2 Filter Signal and Background Acceptance Rate . . . 42
3.2 2011-2015 Data Livetime . . . 45
3.3 Cascade Level3 Passing Rate and Branch Rates for the Signal and the Background . . . 45
3.4 The Rate of the Data and the Monte Carlo at the Level3 Single Contained Branch and Level4 A . . . 51
3.5 The Rate of Data and Monte Carlo at Level4 B in Comparison with the Previous Level (Level4 A) . . . 53
3.6 The Rate of the Data and the Monte Carlo at Level 4C in Comparison with the Previous Level (Level 4B) . . . 55
3.7 The Rate of Data and Monte Carlo at Level 4D in Comparison with the Previous Level (Level 4C) . . . 55
3.8 The Rate of Data and Monte Carlo at Level 4E in Comparison with the Previous Level (Level 4D) . . . 59
3.9 The Rate of the Data and the Monte Carlo at Level 4F in Comparison with the Previous Level (Level 4E) . . . 60
3.10 The Rate of the Data and the Monte Carlo at Level 4G (Final Level) in Comparison with the Previous Level (Level 4F) . . . 63
3.11 The Rate of the 2011 100% Data and the 2012-2015 10% Data at the Final Level) . . . 68
3.12 The Depth and Reconstructed Energy by Three Different Method of the Dust Layer Events . . . 81
3.13 The Energy Bin and the Directional Reconstruction Result from the Monopod Reconstruction and the Direct Fit Reconstruction of the Dust Layer Events . . . 82
3.14 The Number of the Down-going Events in All the Reconstructed Energy Bins for the Unblinded Data and the Simulation at the Final Level . . . 86
3.15 The Number of the Up-going Events in All the Reconstructed Energy Bins for the Unblinded Data and the Simulation at the Final Level . . . 86

4.1 The Detector Acceptance Correction Factors for All Neutrino Energy Bins 93
4.2 The Weighted Bin Centers 94

5.1 α Values for the Baseline Unfolding Matrix 104
5.2 The Unfolding Matrix Elements of the Baseline Simulation 106

7.1 The Number of Down-going and Up-going Events in the Neutrino Energy Bins for the Unblinded Data After Unfolding with Statistical Uncertainties 138
7.2 The Cross Section Measurement Result of the 2011-2015 IceCube Cascade Sample and its Statistical Uncertainty 141
7.3 The Cross Section Measurement Result of the 2011-2015 IceCube Cascade Sample and its Systematic Uncertainty 144
7.4 The Cross Section Measurement Result of the 2011-2015 IceCube Cascade Sample with its Statistical Uncertainty, Systematic Uncertainty, and the Combined Uncertainty 144
7.5 The Chemical Composition of the Earth 146
7.6 The Electron Antineutrino Fraction in the Total Astrophysical Neutrino Flux at Earth for Different Astrophysical Source Models 146

Chapter 1

Neutrinos and Interactions

The idea of neutrinos was first postulated by Wolfgang Pauli in 1930 in the attempt to explain the energy and momentum conservation in beta decay:

$$n \rightarrow p^{+} + e^{-} + \bar{\nu}_{e} \tag{1.1}$$

The existence of neutrinos was confirmed by the Cowan-Reines neutrino experiment [1] in 1956, when a positron-electron annihilation coincided with the neutron capture. The neutron and positron are products of the charged current interaction of an electron antineutrino and a proton:

$$\bar{\nu}_{e} + p^{+} \rightarrow n + e^{+} \tag{1.2}$$

In 1962, the products of a charged pion decay were observed in an experiment conducted at Brookhaven National Laboratory. With one of the products being a muon, the other product: the neutrino was believed to be a different kind of neutrino from the product in the beta decay [2]:

$$\pi^{\pm} \rightarrow \mu^{\pm} + (\nu_{\mu}/\bar{\nu}_{\mu}) \tag{1.3}$$

It was expected, after the discovery of the tau lepton [3] in 1975, that each lepton has a corresponding neutrino with the same flavor. However, the first observation of the tau neutrino did not happen until 2000. In the experiment conducted by the DONUT collaboration at Fermilab, the existence of tau neutrinos was confirmed when tau leptons were observed as the only leptons produced at the interaction vertices of the ν_{τ} charged-current interactions [4]. After the discovery of the three flavors of the neutrinos, their properties were studied extensively. In this chapter, we give an overview of the neutrino properties, neutrino sources, and neutrino interactions.

1.1 Neutrino Properties

1.1.1 The Standard Model

The Standard Model is the theory that describes known elementary particles and their interactions. It has been proven effective in explaining most of the data from the high-energy experiments. In the Standard Model, all matter is built from fermions which are elementary particles with half-integer spins. Bosons (elementary particles with integer spins) are the mediators of the interactions among the fermions. There are four types of interactions in the Standard Model: gravitational, electromagnetic, strong, and weak. All known fermions and bosons of the Standard Model are shown in Table 1.1.

Fermions can be further classified as leptons and quarks, according to the charge they carry or the type of interaction they engage in. There are three lepton flavors. Each flavor contains a charged lepton with one negative charge and a neutral lepton with zero charge that is also called a neutrino. As shown in Table 1.1, the three flavors are electron and electron neutrino, muon and muon neutrino, tau and tau neutrino. The mass of the charged lepton increases from the left to the right while the lifetime decreases from the left to the right. In the Standard Model, neutrinos are massless. However, in the later neutrino oscillation experiments, this assumption has proven to be incorrect. Neutrino oscillation will be discussed later in this section. Due to their chargelessness, neutrinos only interact weakly [1], and the interaction is mediated by $W^{\pm}$ or Z bosons. The charged lepton and its corresponding neutrino have the same lepton number while their antiparticles have the opposite sign of the lepton number and charge. In the Standard Model, the lepton number is conserved in weak interactions.

The other half of the fermions are quarks. There are six types of quarks: up, down, charm, strange, top, and bottom. As shown in Table. 1.1, the quarks in the top row all carry $+\frac{2}{3}$ charge and the quarks in the second row all carry -$\frac{1}{3}$ charge. Similarly to the leptons, the mass of the quarks increases from the left to the right while their stability decreases from the left to the right. Quarks do not exist as free particles, instead, they are bound by the strong force which is mediated by the gluon bosons. The quark composites are referred to as hadrons. There are two kinds of common hadrons: baryons and mesons. Baryons consist of three quarks while mesons consist of a quark and antiquark pair. Like leptons, the quarks and antiquarks have the opposite sign in the flavor quantum number and the charge. In a strong interaction, the flavor quantum number is conserved. However, it is not the requirement in the weak interactions. For example, the following weak decay can happen without the flavor quantum number being conserved:

$$\Lambda(uds) -> p^{+}(uud) + \pi^{-}(d\bar{u}). \tag{1.4}$$

[1] Neutrinos are not actually massless, therefore they also interact via gravitational force. However, in comparison with the weak interaction, the strength of the gravitational interaction is more than 20 orders of magnitude weaker.

	Fermions			Bosons	
Quarks	u	c	t	g	H
	d	s	b	γ	
Leptons	e	μ	τ	Z	
	ν_e	ν_μ	ν_τ	W	

TABLE 1.1: The Elementary Particles of the Standard Model.

1.1.2 Neutrino Oscillation

The concept of neutrino oscillation was first brought up by Pontecorvo in 1958 [5]. He proposed that the neutrinos could have masses and therefore the flavor eigenstates are a combination of the mass eigenstates:

$$|\nu_\alpha\rangle = \sum_i U^*_{\alpha i} |\nu_i\rangle \,, \tag{1.5}$$

where $|\nu_\alpha\rangle$ are flavor eigenstates (electron, muon or tau) and $|\nu_i\rangle$ are mass eigenstates (1, 2, or 3). $U_{\alpha i}$ is the neutrino mixing matrix [6]:

$$U = \begin{bmatrix} U_{e1} & U_{e2} & U_{e3} \\ U_{\mu 1} & U_{\mu 2} & U_{\mu 3} \\ U_{\tau 1} & U_{\tau 2} & U_{\tau 3} \end{bmatrix} \tag{1.6}$$

The propagation of the mass eigenstates in time can be written as:

$$|\nu_i(t)\rangle = e^{-iE_i t} \mid \nu_i(0)\rangle \tag{1.7}$$

where $E_i = p + \frac{m_i^2}{2p}$ is the energy of the mass eigenstate, and p is the fixed momentum for all mass eigenstates. When setting $c = 1$, the time travelled can be substituted by the distance propagated (L):

$$|\nu_i(L)\rangle = e^{-ipt} e^{-im_i^2 L/2p} \mid \nu_i(0)\rangle \tag{1.8}$$

Eq. 1.8 shows that different mass eigenstates propagate with different frequencies due to the difference in mass. Therefore it creates the probability of a neutrino of flavor α at time 0 (the time of generation) being observed as flavor β after the propagation of a distance L. This probability can be calculated as [7]:

$$P_{\alpha\to\beta} = |\langle\nu_\beta(L)|\nu_\alpha(0)\rangle|^2 = \left|\sum_i U^*_{\alpha i} U_{\beta i} e^{-im_i^2 L/2p}\right|^2 \tag{1.9}$$

In a simplified case where there are only two flavors, the mixing matrix can be written as:

$$U = \begin{bmatrix} \cos\theta & \sin\theta \\ -\sin\theta & \cos\theta \end{bmatrix} \tag{1.10}$$

Then the probability of the neutrino changing flavor after an L distance propagation is:

$$P_{\alpha\to\beta,\alpha\neq\beta} = \sin^2(2\theta)\sin^2\left(1.27\frac{\Delta m^2 L}{E}\frac{[\text{eV}^2]\,[\text{km}]}{[\text{GeV}]}\right) \tag{1.11}$$

Neutrino oscillation successfully serves as the explanation of the solar neutrino problem [8]. By the standard solar model prediction, the neutrinos emitted from the Sun are mostly the product of the proton-proton chain reaction, and can only be of electron flavor. However, the solar neutrino problem arose when the first measurement of the solar electron neutrino flux turned out to be approximately one-third of the total prediction [8]. This observation fits the prediction of the neutrino oscillation theory, where after a long distance of propagation, the electron neutrinos changed into muon and tau neutrinos. Since the three flavors can change into each other during the propagation, the flavor ratio eventually becomes 1: 1: 1. Being able to set the flavor ratio as 1: 1: 1 is of great importance for this analysis when building the unfolding matrices (c.f. Chapter 5) due to the difference in the interaction kinematics for neutrinos with different flavors.

1.2 Neutrino Sources

Unlike the artificial neutrino sources in accelerator experiments, the neutrinos observed in the IceCube experiment are of cosmic and astrophysical origins. The cosmic rays interact with the nuclei in the Earth's atmosphere upon arrival. The hadrons produced in this process will decay into neutrinos and other products. These neutrinos produced in the Earth atmosphere are called atmospheric neutrinos. They are the predominant neutrinos detected in IceCube in the neutrino energy range of up to tens of TeV. The neutrinos that are generated and accelerated in the same cosmological processes in which the cosmic rays are generated are called astrophysical neutrinos. They are the predominant neutrinos detected in IceCube for the neutrino energy range of 100 TeV and above.

1.2.1 Cosmic Rays

The majority ($\sim 90\%$) of cosmic rays are protons, 9% are alpha particles (helium nuclei), and 1% are heavier nuclei [7]. The fluxes of the primary nuclei are shown in Fig. 1.1.

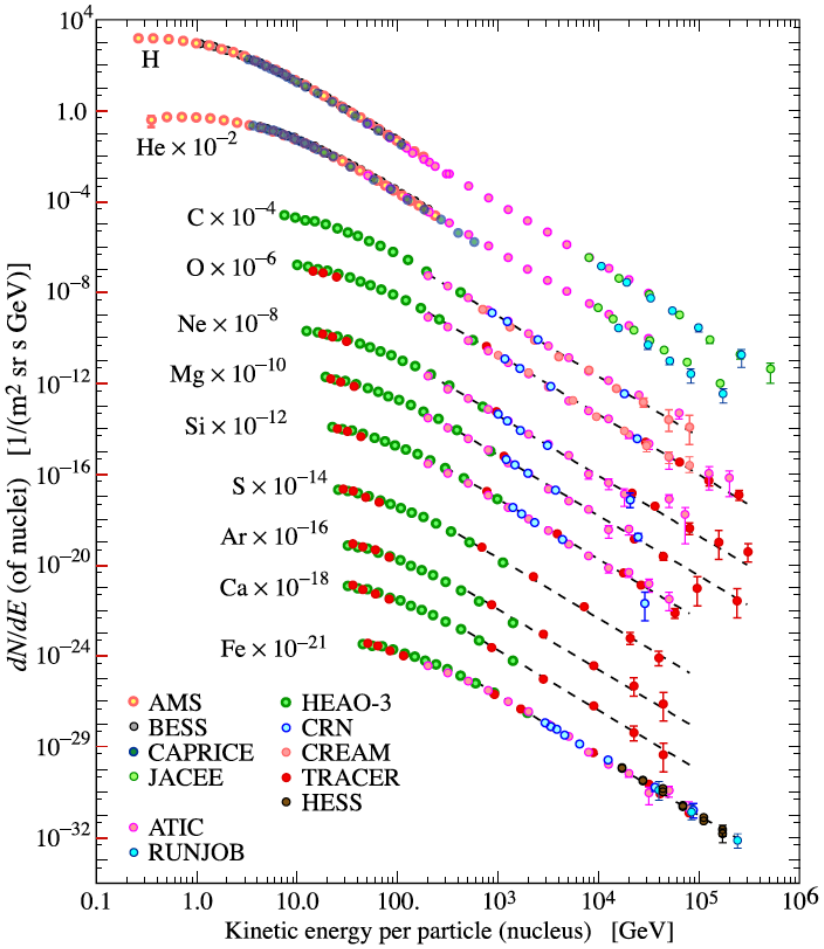

FIGURE 1.1: The flux of the individual primary nuclei in the cosmic rays vs. energy-per-nucleus. The figure is from Ref. [9]

As shown in the figure, the cosmic ray composition is almost the same everywhere in the plotted energy range. The differential intensity of the primary nucleons in this energy range can be described by:

$$I_N(E) \approx 1.8 \times 10^4 (E/\mathrm{GeV})^{-\alpha} \frac{\text{nucleons}}{\mathrm{m^2\,s\,sr\,GeV}}, \tag{1.12}$$

where E is the energy-per-nucleon, and the $\alpha = 2.7$ is the spectral index of the flux of the cosmic rays observed at the Earth [9].

The detection of the cosmic rays can be categorized as *direct detections* and *indirect detections*. Direct detection requires placing the instrument in outer space or very high up in the atmosphere to directly detect the cosmic nuclei before they interact with the

atmosphere. Most of the data points in Fig. 1.1 are the result of direct detection experiments: AMS (Alpha Magnetic Spectrometer) [10], [11] is mounted on the International Space Station; BESS (Balloon-borne Experiment with Superconducting Spectrometer) [12], JACEE (Japanese-American Collaborative Emulsion Experiment) [13], and TRACER (Transition Radiation Array for Cosmic Energetic Radiation) [14] are balloon-borne experiments. Even though the direct detections deliver more accurate results, the limited volume of a balloon, a satellite, or a space station limits the capability of such experiments to probe cosmic rays at higher energies. For the energy range of hundreds of TeV and above, indirect detections are needed.

Indirect detection is a ground-based method that detects cosmic-ray-induced extensive air showers. Ground-based experiments can detect cosmic rays of energies several magnitudes higher than the direct detection experiments. The flux of all the primary nuclei in the cosmic rays in the energy range of 10^{13} eV to 10^{20} eV is shown in Fig. 1.2. Most of the data points in Fig. 1.2 are the result of indirect detection experiments, such as: Kascade (Karlsruhe Shower Core and Array Detector) [15], IceTop-IceCube[16], Telescope Array [17] and Pierre Auger Observatory [18].

The spectrum in Fig. 1.2 shows a special structure. Below ~ 4.5 PeV, the spectral index is 2.7; a spectrum softening happens at around ~ 4.5 PeV (the knee), and the spectral index changes to 3.1. The spectral index has further softened to 3.3 at ~ 400 PeV (the second knee); eventually, the spectrum hardens back to 2.7 at ~ 4 EeV (the ankle) [19]. Beyond $\sim 10^{20}$ eV, a cutoff (the GZK limit) of the cosmic ray spectrum is expected, if cosmic rays are protons [20], [21]. The GZK limit is a theoretical limit that when exceeded, the protons in the cosmic rays start to lose energy from interactions with the microwave background radiation, thus will not be detected.

The acceleration source and mechanism of cosmic rays are also of great interest. To achieve the cosmic ray energy density estimated from the observed cosmic ray flux: $\rho_E \approx 1$ eV/cm^3 [7], the required power to support the cosmic rays throughout the galaxy is:

$$L_{CR} = \frac{V_D \rho_E}{\tau_R} \sim 5 \times 10^{40} \frac{\text{erg}}{\text{sec}}, \tag{1.13}$$

where the V_D is the volume of the galactic disk:

$$V_D = \pi R^2 d \sim \pi (15\text{kpc})^2 (200\text{pc}) \sim 4 \times 10^{66} \text{cm}^3, \tag{1.14}$$

and τ_R is the residence time of the cosmic rays in the volume where the sources are presumably located: $\tau_R \sim 6 \times 10^6$ years.

Such high power could be provided by supernova explosions. For example, the power from a type II supernova ejecting 10 $M_\odot$ mass with $u \sim 5 \times 10^8$ cm/s every 30 years is approximately 3×10^{42} erg/sec.

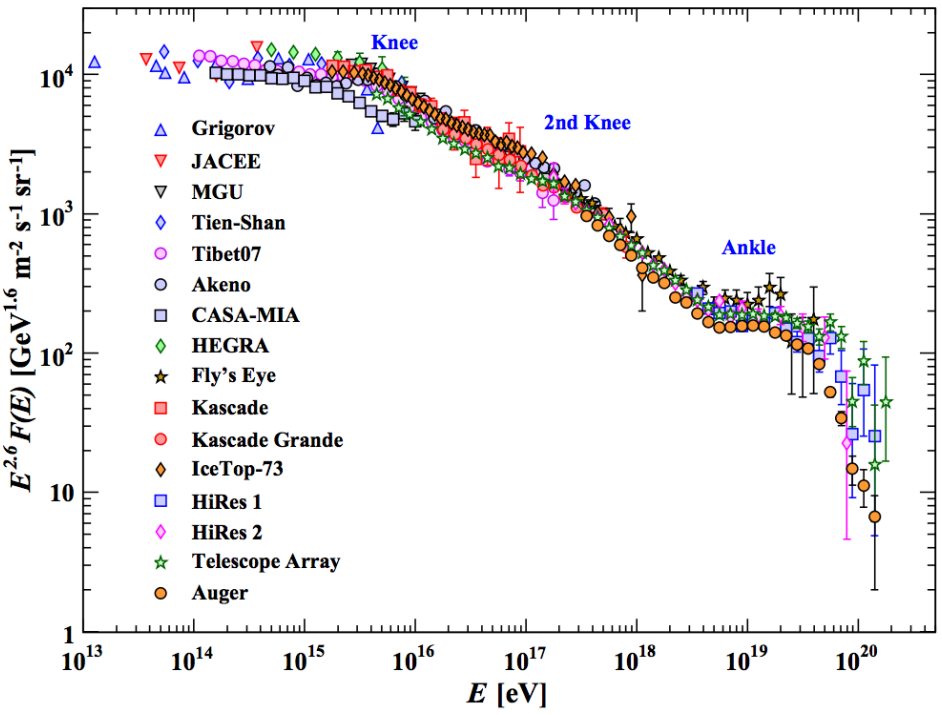

FIGURE 1.2: The flux of the combination of all primary nuclei in cosmic rays vs. energy-per-nucleus. The flux is multiplied by $E^{2.6}$, so that the structures of the knee and the ankle are easier to observe. The figure is from Ref. [9]

The Fermi acceleration mechanism of the supernova shock wave predicts a power-law spectrum of the particles being accelerated. The proportion of the particles of original energy E_0 being accelerated to energy above E is:

$$N(\geq E) \propto \frac{1}{P_{esc}}(\frac{E}{E_0})^{-\gamma}, \tag{1.15}$$

where P_{esc} is the probability that the particle escapes the acceleration region during each encounter. The flux shape of the particles accelerated by the Fermi mechanism matching the flux shape of the observed cosmic rays further suggests that supernova explosions could be one of the acceleration sources [7].

The maximum energy of particles that can be accelerated to via the supernova shock wave is [7]:

$$E_{\max} \leq \frac{3}{20}\,\frac{u}{c}\,Z\,e\,B\,(u\,T_A) \tag{1.16}$$

where u is the velocity of the matter being ejected in the shock wave, $Z\,e$ is the charge of the particle being accelerated, B is the magnetic field, and T_A is the active time of the particles being accelerated.

For a type II supernova ejecting 10 $M_\odot$ mass with $u \sim 5 \times 10^8$ cm/s into the interstellar medium (ISM), the acceleration will keep going until it has ejected all of its own mass. Therefore, T_A can be calculated as:

$$\frac{4}{3}\,\pi\,(u\,T_A)^3 \rho_{\rm ISM} \;=\; M_{\rm ejecta} \tag{1.17}$$

In this case $T_A \approx 1000$ yrs. With the strength of the ISM magnetic field being $B_{ISM} \sim 3\mu$ Gauss, the maximum energy from Eq. 1.16 is:

$$E_{\rm max} \leq \; Z \;\times\; 3 \;\times\; 10^4 {\rm GeV} \tag{1.18}$$

The result in Eq. 1.18 can only account for the acceleration of the cosmic rays up to a few hundred TeV. However, the spectrum in Fig. 1.2 shows that the most energetic cosmic rays observed can reach up to 10^{20} eV. Several scenarios have been proposed to provide an explanation for ultra-high-energy cosmic rays.

Instead of a single supernova, the acceleration could be due to diffusive sources. Ref. [22] suggests that the shock wave from all the supernovae in the galaxy could form a galactic wind that fills the intergalactic medium. For this diffusive source, the velocity of the wind is $u_W = 600$ km/s. The strength of the magnetic field in the intergalactic medium is B $= 0.1\ \mu$ Gauss and the acceleration time is the same as the age of the galaxy: $T_A = 1.5 \times 10^{10}$ years. With the much longer acceleration time, even though the velocity and the strength of the magnetic field are smaller than the single supernova scenario, the maximum energy that could be achieved using Eq. 1.16 is $E_{\rm max} \sim Z \times 3 \times 10^8$GeV which is significantly higher than what's predicted by the single supernova shock. The magnetic field of the galactic wind is likely to be quasi-perpendicular to the propagation direction of the shock which could further increase the upper limit of the accelerated energy [23].

Point sources could also be responsible for the acceleration of the cosmic rays to very high energies. Instead of the long acceleration time, point sources could instead provide very high magnetic fields. A rotating neutron star residing inside the expanding shell of a type II supernova remnant (SNR) could serve as an accelerator. The power of the acceleration could be provided by the rotational energy from an oscillating dipole. However, the power is not emitted as electromagnetic radiation, but as relativistic wind consisting of electrons and positrons [24]. Due to the relativistic nature of the pulsar wind, Eq. 1.16 does not apply. The maximum energy that the particles can be accelerated to under this scheme can be calculated as [25]:

$$E_{\max} \sim \frac{e\, B_* \, R_*^3 \, \Omega^2}{\sqrt{3}\, c^2} \tag{1.19}$$

where B_* is the magnetic field of the neutron star surface, R_* is the radius of the neutron star, and Ω is the angular velocity of the rotation. A sample calculation done using a 10 ms pulsar with $B_* = 10^{12}$ Gauss yields a $E_{\max} \sim 10^5$ TeV.

Another way to provide power for the acceleration is by transferring the gravitational potential energy from the accretion of matter falling back to the neutron star from the shell. A neutron star in a binary system could also accrete matter from its counterpart in the system. Ref. [26] shows that the maximum energy that a particle can be accelerated to in an accretion shock is on the order of 10^7 GeV.

1.2.2 Atmospheric Neutrinos

When the nuclei in the cosmic rays arrive at the Earth atmosphere, they interact with the nuclei in the atmosphere and produce mesons. The flux (N_i) of the produced type i meson can be calculated as [7]:

$$\begin{aligned} \frac{\mathrm{d}N_i(E_i, X)}{\mathrm{d}X} = &-\frac{N_i(E_i, X)}{\lambda_i} - \frac{N_i(E_i, X)}{d_i} \\ &+ \sum_{j=i}^{J} \int_E^{\infty} \frac{F_{ji}(E_i, E_j)}{E_i} \frac{N_j(E_j, X)}{\lambda_j} \mathrm{d}E_j, \end{aligned} \tag{1.20}$$

where λ_i and d_i are the interaction length and the decay length in the air of particle i. $F_{ji}(E_i, E_j)$ represents the particle yield of a type j particle of energy E_j colliding with an air nucleus and producing a type i particle of energy E_i ($E_i < E_j$). X is the slant depth (the distance between the entry point of the particle in the atmosphere and the interaction point).

Mesons produced in the atmosphere will further decay into muons and neutrinos. The most important decay channels are:

$$\pi^{\pm} \to \mu^{\pm} + \nu_{\mu}(\bar{\nu}_{\mu}) \tag{1.21}$$

$$K^{\pm} \to \mu^{\pm} + \nu_{\mu}(\bar{\nu}_{\mu}) \tag{1.22}$$

The decay channel of charged pions listed above has a $\sim 100\%$ branching ratio, and the decay channel of the charged kaons listed above has a $\sim 63.5\%$ branching ratio. Muons from the above decays will further decay and produce more neutrinos:

$$\mu^{\pm} \rightarrow e^{\pm} + \nu_e(\bar{\nu}_e) + \bar{\nu}_\mu(\nu_\mu) \tag{1.23}$$

An illustration of the production of muons and neutrinos from the cosmic rays hitting the Earth atmosphere is shown in Fig. 1.2.

When all the muons produced in the atmosphere decay, the ratio of $(\nu_\mu + \bar{\nu}_\mu)/(\nu_e + \bar{\nu}_e)$ is ~ 2. However, the muon decay length increases with muon energy. When $E_\mu > 2.5$ GeV, the muon decay length grows larger than its production height (~ 15 km) [7], and the ratio of muon neutrinos to electron neutrinos increases.

The flux of the atmospheric muon neutrinos produced from the charged pion and kaon decay can be calculated as:

$$\begin{aligned}\frac{\mathrm{d}N_\nu}{\mathrm{d}E_\nu} \simeq \frac{N_0(E_\nu)}{1 - Z_{NN}}\{&\frac{A_{\pi\nu}}{1 + B_{\pi\nu}\cos\theta E_\nu/\epsilon_\pi} \\ &+ 0.635\frac{A_{K\nu}}{1 + B_{K\nu}\cos\theta E_\nu/\epsilon_K}\}\end{aligned} \tag{1.24}$$

The $N_0(E_\nu)$ in the nucleon flux of the atmosphere. The first term in the bracket is the contribution from the pion decay (Eq. 1.21) with a 100% branching ratio, and the second term is the contribution from the kaon decay (Eq. 1.22) with 63.5% branching ratio. ϵ_i is the critical energy of particle i in the atmosphere. If the energy of particle i is greater than ϵ_i, the interaction of particle i will take over and become dominant instead of the decay of particle i. It is calculated as:

$$\epsilon_i = \frac{m_i c^2 h_0}{c\tau_i}, \tag{1.25}$$

where m_i is the mass of particle i and $c\tau_i$ is its mean life expressed in length. h_0 is the scale height which equals the pressure of the atmosphere divided by the product of the density of the atmosphere with the gravitational constant ($h_0 = \frac{P}{\rho g}$). In the place where the production of the secondary particles of cosmic rays peaks, $h_0 \simeq 6.4$ km. The values of the mean life and the critical energy of some selected mesons in the Earth's atmosphere can be found in Table 1.2.

The $A_{\pi\nu}$ and $B_{\pi\nu}$ in Eq. 1.24 are defined as:

$$A_{\pi\nu} \equiv Z_{N\pi}\frac{(1 - r_\pi)^{\gamma+1}}{(1 - r_\pi)(\gamma + 1)} \tag{1.26}$$

and

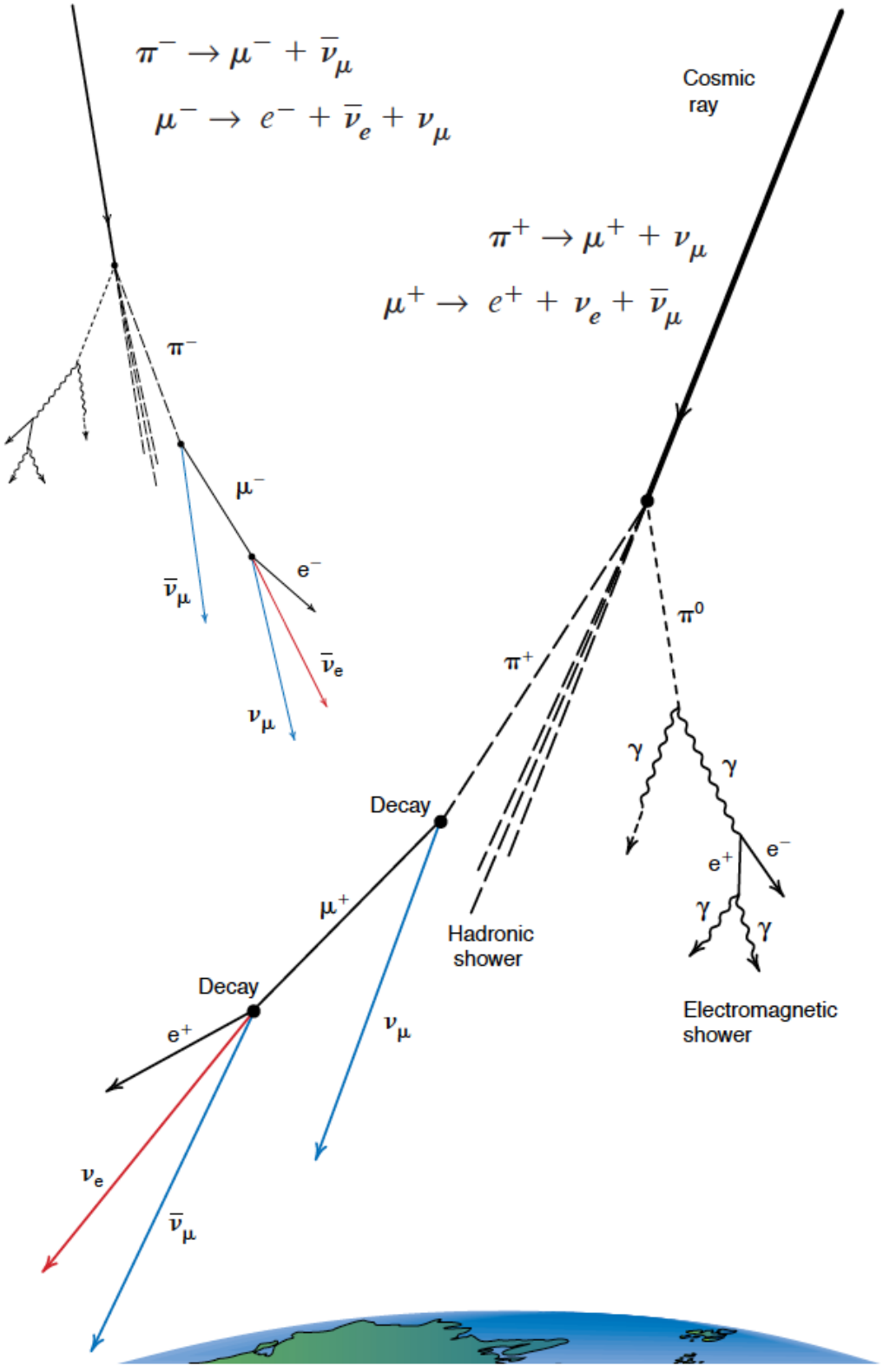

FIGURE 1.3: An illustration of the creation of the secondaries when the cosmic rays enter the Earth's atmosphere. The figure is from Ref. [27].

$$B_{\pi\nu} \equiv \frac{\gamma+2}{\gamma+1}\frac{1}{1-r_\pi}\frac{\Lambda_\pi - \Lambda_N}{\Lambda_\pi \ln(\Lambda_\pi/\Lambda_N)} \tag{1.27}$$

γ is the spectral index of the cosmic ray spectrum $\sim E^{-(\gamma+1)}$. The Z_{ij} is the spectrum-weighted moment of the inclusive cross section for particle j with air to particle i, namely $j + \text{air} \to i$. Λ_i is the attenuation length for particle i in the air. $r_i \equiv m_\mu^2/m_i^2$ is defined as the ratio of the muon mass squared to the particle i mass squared. r_i reflects the decay kinematics, which is different between the pion decay and the kaon decay($r_\pi \simeq 0.573$ and $r_K \simeq 0.046$).

Atmospheric neutrinos generated from charged pion and kaon decays are called conventional atmospheric neutrinos. This part of the atmospheric neutrinos is well understood, and their flux is calculated and calibrated with the atmospheric muon data [28]. As shown in Fig. 4.2, the flux of the conventional atmospheric neutrinos is zenith dependent. In the horizontal direction, the effective depth is larger compared to the vertical direction, thus the higher number of pion and kaon decays.

Once the energy of the primary cosmic rays is much greater than ϵ_K (850 GeV) and ϵ_π (115 GeV), the interactions of pion and kaon take over, and the flux of conventional atmospheric neutrinos falls steeply. However, the critical energies of the heavier charmed mesons (e.g. $D^\pm$, D^0) are much higher. As shown in Table 1.2, the critical energy for D^+ is 37 PeV and some of its decay channels yield neutrinos. Therefore in the energy range of 1 TeV and above, the neutrinos from the decay of charmed mesons become an important part of the atmospheric neutrinos. Due to the short mean life of these heavier mesons, these neutrinos are called prompt atmospheric neutrinos. Since the charmed mesons decay immediately after their generation, the effective depth is irrelevant for the prompt flux. As shown in Fig. 4.2, the prompt component of the atmospheric neutrinos is isotropic. Unlike the well understood conventional counterpart, the flux of the prompt atmospheric neutrinos is calculated with large uncertainties and has not yet been observed. The calculation of the prompt flux involves the charm production from the interaction between the cosmic rays with the air nuclei, and the hadronization of the charm particles [29]. The uncertainties associated with the charm mass, factorization and renormalization scales, and the parton distribution functions could all contribute to the uncertainty in the prompt flux calculation.

1.2.3 Astrophysical Neutrinos

Neutrinos of extraterrestrial origins are called astrophysical neutrinos in contrast to atmospheric neutrinos. In the MeV region, the astrophysical neutrinos are mainly solar neutrinos (neutrinos from the nuclear fusion process in the Sun) and the neutrinos from the neutronisation process in the collapsing core of a supernova:

$$e^- + p \to \nu_e + n \tag{1.28}$$

Particle	Constituent quarks	Mass (MeV)	Mean life	ϵ (GeV)	Decay channels	Branching ratio (%)
π^+	$u\bar{d}$	139.6	7.80 m	115	$\mu^+\nu_\mu$	99.99
					$\mu^+\nu_\mu\gamma$	0.02
					$e^+\nu_e$	0.01
K^+	$u\bar{s}$	493.7	3.71 m	850	$\mu^+\nu_\mu$	63.6
					$\pi^+\pi^0$	20.7
					$\pi^+\pi^-\pi^+$	5.59
					$\pi^0 e^+\nu_e$	5.07
					$\pi^0\mu^+\nu_\mu$	3.35
					$\pi^+\pi^0\pi^0$	1.76
D^+	$c\bar{d}$	1870	312 μm	3.7 $\times 10^7$	$K^0/\bar{K}^0$...	61
					$\mu^+\nu_\mu$...	17.6
					$e^+\nu_e$...	16.1

TABLE 1.2: Properties and decay channels of selected mesons. The table contents are from Ref. [7].

In the higher energy region (TeV and above), the astrophysical neutrinos are generated from the charged pion decays. The pions are generated either in the collisions of high energy protons and protons:

$$p + p \rightarrow \begin{cases} \pi^+ + \text{anything}, & 1/3 \text{ of all cases} \\ \pi^- + \text{anything}, & 1/3 \text{ of all cases} \\ \pi^0 + \text{anything}, & 1/3 \text{ of all cases} \end{cases} \tag{1.29}$$

or from the collisions of high energy protons and gamma-rays:

$$p + \gamma \rightarrow \Delta^+ \rightarrow \begin{cases} \pi^+ + n, & \text{branching ratio: } 1/3 \\ \pi^0 + p, & \text{branching ratio: } 2/3 \end{cases} \tag{1.30}$$

In the case of proton-proton collisions (pp process), the charged pion will decay into a muon and a muon neutrino (Eq. 1.21). If the muon decays as in Eq. 1.23, the flavor ratio of $(\nu_e : \nu_\mu : \nu_\tau)$ at the generation point is (1: 2: 0) for both neutrinos and antineutrinos. If the muon is of high energy and does not decay, this is called the "damped muon mode". Then there will be no electron neutrino produced. The flavor ratio at the source becomes (0:1:0) for both neutrinos and antineutrinos.

In the case of proton photon collisions ($p\gamma$ process), the only particles that will generate neutrinos are π^+s. In the mode where muon decays, the flavor ratio of neutrinos is (1:1:0)

	Flavor ratio at the source $(\nu_e : \nu_\mu : \nu_\tau)$		Flavor ratio at the Earth $(\nu'_e : \nu'_\mu : \nu'_\tau)$	
$pp \to \pi^\pm$	(1:2:0)		(1:1:1)	
w/ damped $\mu^\pm$	(0:1:0)		(4:7:7)	
	ν	$\bar{\nu}$	ν	$\bar{\nu}$
$p\gamma \to \pi^+$	(1:1:0)	(0:1:0)	(14:11:11)	(4:7:7)
w/ damped μ^+	(0:1:0)	(0:0:0)	(4:7:7)	(0:0:0)

TABLE 1.3: The neutrino flavor ratio at the source and at the Earth for different generation processes. The numerical values are from Ref. [30].

while the flavor ratio for the antineutrinos is (0:1:0). In the damped muon mode, the only neutrinos being generated are muon neutrinos, therefore the flavor ratio for neutrinos is (0:1:0) and no antineutrinos are generated.

After neutrino propagation from the source to the Earth, the flavor ratio can be calculated according to the oscillation theory. The flavor ratios for different modes are shown in Table 1.3. Different astrophysical neutrino generation models will result in different flavor ratio predictions for neutrinos and antineutrinos at the Earth. This means that if the flavor ratio at the Earth can be measured, the puzzle of neutrino generation process can be solved.

In IceCube, the neutrino events are detected through their interactions in the ice. Over most of the energy range, the dominant neutrino interaction is neutrino-nucleon deep inelastic scattering. For neutral current interactions, the event signatures are indistinguishable among all the flavors. In the charged current interactions, the electron neutrino events and tau neutrino events are also hard to separate below 1 PeV. IceCube also cannot distinguish neutrinos from antineutrinos. Therefore, the flavor ratio cannot be directly measured.

However, at 6.3 PeV, the electron antineutrino-electron scattering cross section has a significant peak which is much higher than the DIS cross section at the same energy range (c.f. Sec. 1.3.2). The analysis presented in this dissertation has the potential to measure the proportion of the electron antineutrino in the total astrophysical neutrino flux by measuring the total interaction cross section in that energy range (c.f. Sec. 7.4.1). The $\bar{\nu}_e$ proportion can be used as an indicator of the neutrino generation process as shown in Table 7.6.

The neutrino generation process is typically associated with the type of the sources. Among the popular neutrino source candidates, Active Galactic Nucleus (AGN) jets and Gamma-Ray Bursts (GRBs) are associated with the $p\gamma$ process, and starburst galaxies are associated with the pp process.

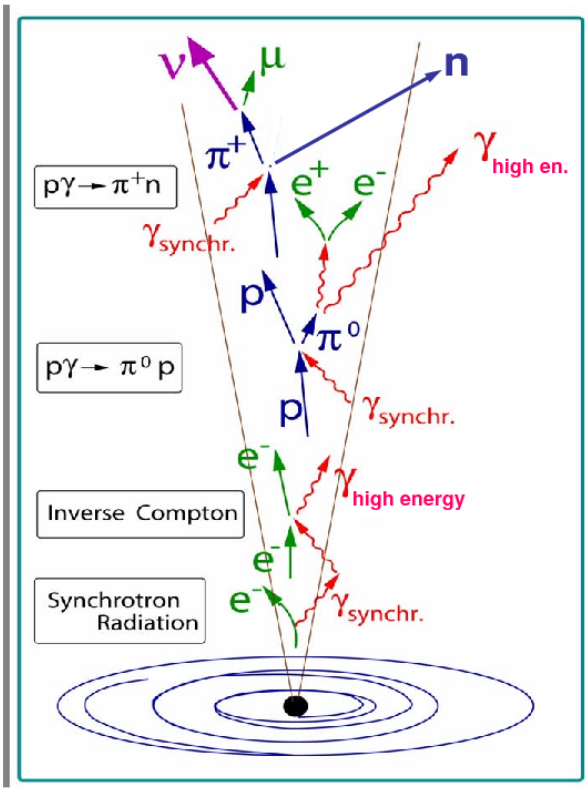

FIGURE 1.4: The schematic of the emission of particles from AGNs. The plot is from Ref. [31].

Active Galactic Nucleus

An active galactic nucleus is the extremely luminous core of a galaxy [7]. Among all the galaxies, only a few percents of them are the hosts to AGNs. The AGNs are powered by the gravitational energy released from the accretion of matter into a black hole located in the center of the galaxy. Near the center of the AGNs, the high energetic relativistic electrons are accelerated by strong magnetic fields. These electrons will produce synchrotron photons, and they can interact with the synchrotron photons through inverse-Compton scattering to produce higher energy photons. The high-energy photons can interact with the high-energy protons (Eq. 1.30) and produce neutrinos. The whole process will generate a stream of high-energy particles, which are emitted from the center of AGNs as a jet perpendicular to the accretion disk of the central black hole. The schematic of the particle emission is shown in Fig. 1.4.

The AGNs can be categorized as *radio-loud* AGNs and *radio-quiet* AGNs by the criterion of whether or not a notable radio jet is detected. Approximately 15% of the AGNs are radio-loud. When the direction of the jet from a radio-loud AGN points towards the

Earth, it is called a *blazar*. The Fermi Large Area Telescope has published the second catalog of AGNs [32] which is used by the IceCube collaboration to search for a potential source of the observed astrophysical neutrinos. The analysis was performed on 3 years (2009 - 2011) of IceCube muon neutrino sample [2], and no significant source from the catalog was identified [33].

On September 22$^{\text{nd}}$, 2017, IceCube detected a $\sim$ 290 TeV muon neutrino which coincided with the γ-ray flare detected by the Fermi-LAT experiment of a blazar TXS 0506+056 in space and time [34]. The flare has also been observed in radio, optical and x-ray signals. Due to this discovery, IceCube investigated 9.5 years of astrophysical neutrino samples and found the evidence for an excess of high-energy neutrino events in the time range of September 2014 to March 2015 from the direction of TXS 0506+056 [35]. This was the first observation suggesting that blazars are sources of astrophysical neutrinos and accelerators for cosmic rays.

Gamma-Ray Bursts

Gamma-Ray Bursts (GRBs) are high-energy transient events with an energy emission of 10^{51} to 10^{54} erg/s [36]. The duration of GRBs ranges from ms to 1000 s with peaks at 2 s and 20 s [37]. They are proposed to be one of the sources of high-energy cosmic rays [38]. GRBs can be categorized as long GRBs (t > 2s) and short GRBs (t < 2s). The long GRBs are believed to be associated with the black hole generation from the collapsing core of a massive star [39], while the short GRBs are likely to be the products of the merger of a binary system: for example, two neutron stars (NS-NS) or a neutron star and a black hole (NS-BH) [40], [41].

The spectrum of the GRB emission follows a double broken power law [42]:

$$N(E) \propto \begin{cases} E^{-\alpha} \exp(-E/E_0) & E < E_0 \\ E^{-\beta} & E > E_0 \end{cases} \tag{1.31}$$

In Eq. 1.31, α is smaller than β and E_0 is burst specific. Typically, $\alpha \approx 1$ and $\beta \approx 2$ [43].

With the development of the GRB, the plasma of photons, electrons, and baryons in the center of the GRB expand relativistically under the radiation pressure. The particles inside the GRB are accelerated to relativistic velocities. In this process, the relativistic protons interact with the high energy photons and produce pions which later will decay into neutrinos. A large fraction of the burst energy is transferred to the produced neutrinos so that the neutrino energy can reach up to 10^{14} eV [44].

After the detection of the gravitational wave emission from the merger of a binary neutron star (GW170817) by the Advanced LIGO and Advanced Virgo observatories [45], the ANTARES, IceCube, and Pierre Auger Observatories performed a search for possible

[2]The track-like event signature from the charged-current interaction of muon neutrinos provides a good directional resolution which is essential to identify the direction of the source.

GeV - EeV neutrinos associated with this GRB. No neutrino was found within the ±500 s time window of the event in the direction of the event [46].

IceCube has performed another more comprehensive search for potential neutrino emissions from GRBs with 7 years of muon neutrino sample [47]. 1172 GRBs with information acquired from Gamma-ray Coordinates Network (GCN) and the Fermi Gamma-ray Burst Monitor (GBM) database [48], [49] have been studied, and no significant correlation is found between the neutrinos and the GRB events.

Starburst Galaxies

Starburst galaxies (SBGs) or star-forming galaxies (SFGs) are galaxies with a much higher star formation rate (SFR) than the average SFR of galaxies at a similar redshift [50]. The disk density of SBGs ($\Sigma_g > 0.1$ g/cm [51]) and the magnetic field of SBGs ($B \sim 1$ mG [52]) are typically much higher than the normal galaxies ($\Sigma_g \approx 0.003$ g/cm^2, $B \sim 5$ μG for the Milky Way).

The majority of the star formation activities at redshift $z \sim$2 happens in transient starburst events which are usually triggered by galaxy mergers. In these activities, the relativistic protons are injected into the starburst interstellar medium and collide with the interstellar nucleons. This hadronic process (pp) will lead to the production of charged and neutral pions (Eq. 1.29) which will lead to a neutrino production.

When assuming the neutrinos are from the same sources that are also responsible for the cosmic-ray production and the size of the sources is not much larger than the mean-free-path of the pion production, an upper bound (Waxman-Bahcall upper bound) for the neutrinos flux produced by the pion decay [53], [54] can be set by the cosmic-ray observations:

$$E_\nu^2 \Phi_\nu < E_\nu^2 \Phi_\nu^{WB} = 5 \times 10^{-8} \mathrm{GeV cm^{-2} s^{-1} sr^{-1}} \tag{1.32}$$

Ref. [55] shows that the radio observations of SBGs suggest a lower limit on the neutrino flux which is in the order of Φ_ν^{WB} for the energy range of a few GeV to $\sim$ 300 TeV, and this lower limit of neutrino flux could exceed the Waxman-Bahcall upper bound at higher energies:

$$E_\nu^2 \Phi_\nu \propto E_\nu^{-0.15 \pm 0.1} \tag{1.33}$$

A study performed on 3 years of IceCube data [56], [57] placed a strong upper limit on the spectral index ($E_\nu^{-\gamma}$) of the hadronic sources, $\gamma <$ 2.1 - 2.2 [58].

The neutrino fluxes from different origins are shown in Fig. 1.5. Different sources produce neutrinos of different spectrums and in different energy ranges. The cosmological neutrinos are the relic neutrinos generated during the Big Bang. Their energy is believed

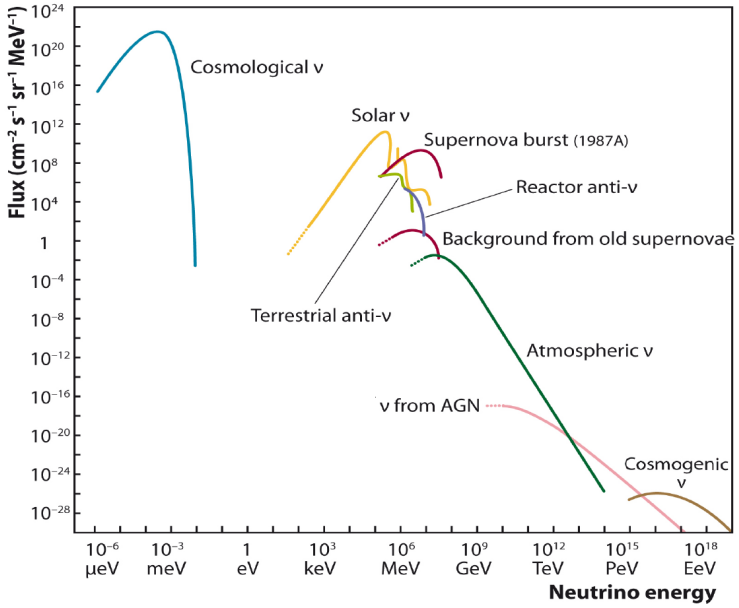

FIGURE 1.5: The neutrino flux of neutrinos from different origins. The plot is from Ref. [31].

to be in the order of meV. The cross section of the relic neutrinos are very low, so they are yet to be detected.

In this analysis, we use neutrinos in the energy range of 6 TeV to 10 PeV. The major contribution of the neutrinos used in the cross section measurement is of astrophysical origins.

1.3 Neutrino Interactions

1.3.1 Deep Inelastic Scattering

Deep Inelastic Scattering (DIS) is a process in which a high-energy lepton is scattered by a hadron with part of the lepton's energy transferred to the hadron. Due to the very high energy, the wavelength of the lepton is smaller than the size of the hadron, thus allowing for the ability to probe the hadron structure. In the final state, a scattered lepton and hadrons are produced.

Figure 1.6 shows the kinematics of a DIS process. The 4-momentum of the injected lepton is p with a relativistic energy E and 3-momentum $\overrightarrow{p}$. The 4-momentum of the scattered lepton is p' with a relativistic energy E' and 3-momentum $\overrightarrow{p}'$. The 4-momentum of the hadron is P. Since the target is fixed, the relativistic energy of the hadron is its mass M and the 3-momentum is 0. The 4-momentum transferred to the hadron is the 4-momentum q of a virtual exchange boson. q can be calculated using momentum conservation at the top vertex of the interaction as:

$$-Q^2 \equiv q^2 \;=\; (p - p')^2 \;=\; (E - E')^2 - (\overrightarrow{p} - \overrightarrow{p}')^2 \tag{1.34}$$

Q^2 is defined as $-q^2$ to be a positive variable since q^2 is negative:

$$Q^2 \approx 4EE' \sin^2 \frac{\theta}{2} \tag{1.35}$$

Use momentum conservation at the bottom vertex of the interaction:

$$P \cdot q = M(E - E') = Mv, \tag{1.36}$$

the invariant mass W of the hadrons in the final state can be calculated as:

$$W^2 = (P + q)^2 = M^2 + 2P \cdot q + q^2 = M^2 + 2Mv - Q^2 \tag{1.37}$$

The Bjorken x variable is defined as:

$$x = \frac{-q^2}{2P \cdot q} = \frac{Q^2}{2M \cdot q} = \frac{Q^2}{2Mv} \tag{1.38}$$

In the case of elastic scattering, $W = M \;\rightarrow\; 2Mv = Q^2 \;\rightarrow\; x = 1$. In the case of inelastic scattering, $W > M \;\rightarrow\; 2Mv - Q^2 > 0 \;\rightarrow\; x < 1$. Therefore the range of the Bjorken x is from 0 to 1. In the Quark Parton Model infinite-momentum frame, it is the fraction of a proton's momentum carried by the parton the lepton scattered off.

Another important variable in a DIS process is defined as:

$$y = \frac{E - E'}{E} = \frac{v}{E} \tag{1.39}$$

It is the fraction of the energy of the injected lepton transferred to the nucleon.

The majority of the neutrino interactions in the IceCube detector are neutrino-nucleon deep inelastic scatterings. There are two types of ν-N DIS: the charged-current interaction and the neutral-current interaction. The charged-current interaction is mediated by a W boson, and the interaction products are a charged lepton and a hadronic shower. The neutral-current interaction is mediated by a Z boson, and the interaction products are a neutrino and a hadronic shower. The Feynman diagrams of these two types of interactions are shown in Fig. 1.7.

The differential cross section of the charged-current interaction between a neutrino (antineutrino) and an isoscalar nucleon ($N \equiv \frac{n+p}{2}$) can be written as [59]:

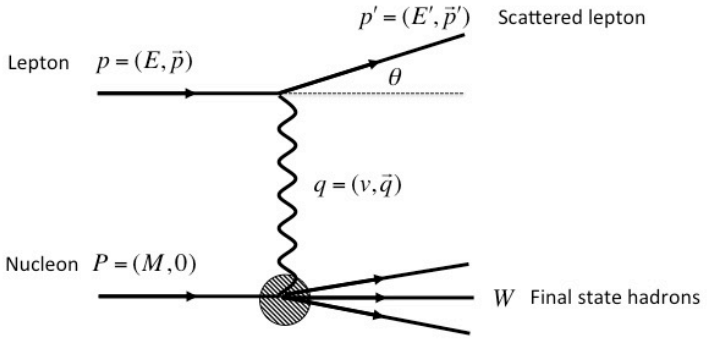

FIGURE 1.6: Deep Inelastic Scattering Feynman Diagram.

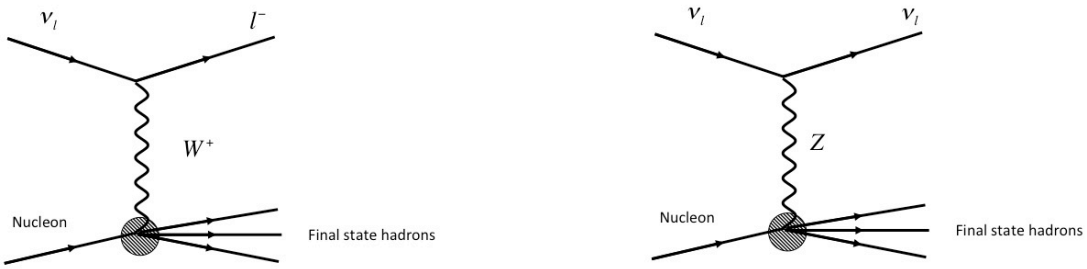

FIGURE 1.7: The Feynman diagram of neutrino-nucleon charged-current (left) and neutral-current (right) interaction.

$$\frac{d^2\sigma(\nu_l N \to l^- X)}{dxdy} = \frac{2G_F^2 ME}{\pi}(\frac{M_W^2}{Q^2+M_W^2})^2[xq(x,Q^2) + x\bar{q}(x,Q^2)(1-y)^2], \tag{1.40}$$

$$\frac{d^2\sigma(\bar{\nu}_l N \to l^+ X)}{dxdy} = \frac{2G_F^2 ME}{\pi}(\frac{M_W^2}{Q^2+M_W^2})^2[xq(x,Q^2)(1-y)^2 + x\bar{q}(x,Q^2)], \tag{1.41}$$

where $G_F = 1.16632 \times 10^{-5}$ GeV^{-2} is the Fermi constant [59], M_W is the mass of the W boson = 80.379 GeV, and $q(x,Q^2)$, $\bar{q}(x,Q^2)$ are parton distribution functions:

$$q(x,Q^2) = \frac{u_v(x,Q^2) + d_v(x,Q^2)}{2} + \frac{u_s(x,Q^2) + d_s(x,Q^2)}{2} + s_s(x,Q^2) + b_s(x,Q^2) \tag{1.42}$$

$$\bar{q}(x,Q^2) = \frac{u_s(x,Q^2) + d_s(x,Q^2)}{2} + c_s(x,Q^2) + t_s(x,Q^2), \tag{1.43}$$

where the subscripts v and s represent valence quarks (determine the hadron's quantum numbers) and sea quarks (virtual quark-antiquark pairs), and u, d, s, b, c, t are the quark distribution for the quark of the marked flavor [59].

The differential cross section of the neutral-current interaction between a neutrino (antineutrino) and an isoscalar nucleon can be written as [59]:

$$\frac{d^2\sigma(\bar{\nu}_l N \to \bar{\nu}_l X)}{dxdy} = \frac{2G_F^2 ME}{\pi}(\frac{M_Z^2}{Q^2+M_Z^2})^2[xq^0(x,Q^2)(1-y)^2 + x\bar{q}^0(x,Q^2)], \tag{1.44}$$

$$\frac{d^2\sigma(\nu_l N \to \nu_l X)}{dxdy} = \frac{2G_F^2 ME}{\pi}(\frac{M_Z^2}{Q^2+M_Z^2})^2[xq^0(x,Q^2) + x\bar{q}^0(x,Q^2)(1-y)^2], \tag{1.45}$$

where M_Z is the mass of the Z boson, and the parton distribution functions are:

$$\begin{aligned} q^0(x,Q^2) = [&\frac{u_v(x,Q^2) + d_v(x,Q^2)}{2} + \frac{u_s(x,Q^2) + d_s(x,Q^2)}{2}](L_u^2 + L_d^2) \\ &+ [\frac{u_s(x,Q^2) + d_s(x,Q^2)}{2}](R_u^2 + R_d^2) + \\ &[s_s(x,Q^2) + b_s(x,Q^2)](L_d^2 + R_d^2) + [c_s(x,Q^2) + t_s(x,Q^2)](L_u^2 + R_u^2) \end{aligned} \tag{1.46}$$

$$\bar{q}^0(x,Q^2) = [\frac{u_v(x,Q^2)+d_v(x,Q^2)}{2} + \frac{u_s(x,Q^2)+d_s(x,Q^2)}{2}](R_u^2+R_d^2) + [\frac{u_s(x,Q^2)+d_s(x,Q^2)}{2}](L_u^2+L_d^2)+ [s_s(x,Q^2)+b_s(x,Q^2)](L_d^2+R_d^2) + [c_s(x,Q^2)+t_s(x,Q^2)](L_u^2+R_u^2), \quad (1.47)$$

where

$$L_u = 1 - \frac{4}{3}x_W \qquad L_d = -1 + \frac{2}{3}X_w \quad (1.48)$$

$$R_u = -\frac{4}{3}x_w \qquad R_d = \frac{2}{3}x_W \quad (1.49)$$

are the chiral couplings and $x_W = \sin^2\theta_W = 0.2312$ [9] is the weak mixing parameter .

According to the neutrino DIS cross section equations listed above, the neutrino-nucleon cross sections have a linear relationship with the neutrino energy in the energy range of a few hundred GeV and below (as shown in Fig. 1.8). This is verified by the direct measurements of the νN cross section in the fixed target experiments. The results of these measurements are shown in Fig. 1.8.

As shown in Fig. 1.8, the direct measurements of neutrino-nucleon cross section performed in the fixed-target experiments can only reach to $E_\nu \sim 350$ GeV due to the limited ability to generate high-energy neutrinos. However, with the parton distribution functions (PDFs) at small x, the neutrino-nucleon cross section at high energies can be calculated using Eq. 1.40, 1.41, 1.44, 1.45.

The PDFs are process-independent. Hadron-Elektron-Ringanlage (HERA) was a particle accelerator based in the Deutsches Elektronen-Synchrotron (DESY). During its operation time, it collected valuable data to fit the PDFs at very small x using ep scattering. The PDFs calculated using HERA data are shown in Fig. 1.9.

HERAPDF1.5 enabled the calculation of the neutrino-nucleon DIS interaction cross section up to 10^{12} GeV in Ref. [62] (CSMS). The calculated result is shown in Fig. 1.10. In this dissertation, a direct measurement of the neutrino interaction cross section using high-energy astrophysical neutrinos will be presented. The result of this measurement will be compared with multiple cross section calculations including CSMS (c.f. Sec. 7.4.2).

1.3.2 Glashow Resonance

The neutrino-electron interaction cross sections is typically much smaller than the neutrino-nucleon interaction cross section due to the much smaller mass of the electrons compared to the nucleons. An exception is at around 6.3 PeV, the resonant formation of the W^- boson from electron antineutrino-electron scattering [64]. At this energy, the resonance cross section is much larger than the neutrino-nucleon cross section. The Feynman diagram of this interaction is shown in Fig. 1.11.

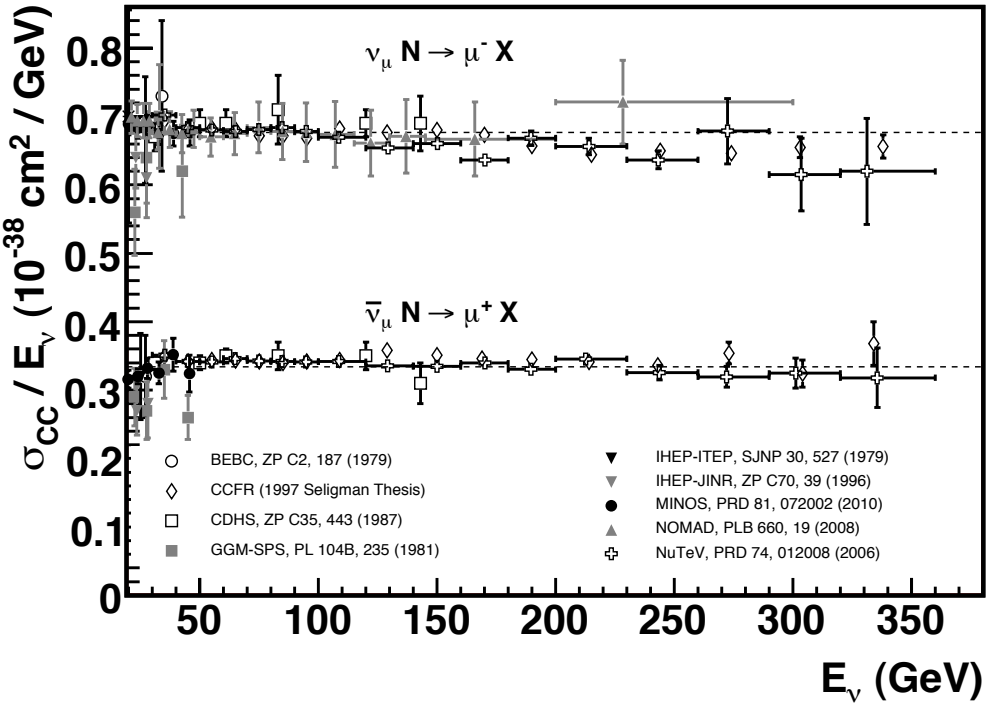

FIGURE 1.8: Measurements of the neutrino and antineutrino charged-current interaction cross section divided by the neutrino energy as a function of the neutrino energy in the energy range of a few hundred GeV. The dashed lines indicated the averaged cross section to the neutrino energy ratio for neutrino interactions and antineutrino interactions: $\sigma^\nu/E_\nu = (0.677 \pm 0.014) \times 10^{-38}\text{cm}^2/\text{GeV}$ and $\sigma^{\bar{\nu}}/E_\nu = (0.334 \pm 0.008) \times 10^{-38}\text{cm}^2/\text{GeV}$ [60]. The plot is from Ref. [61].

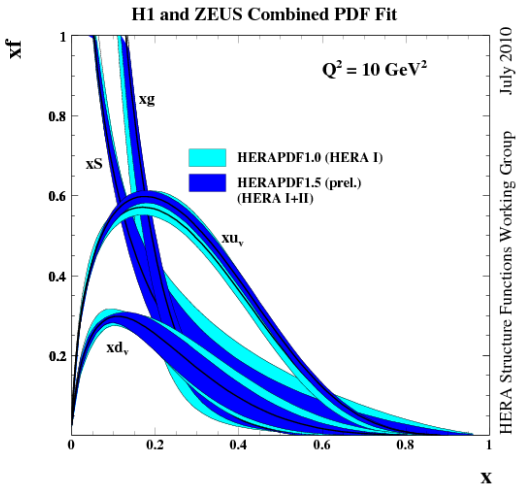

FIGURE 1.9: The parton distribution functions fit to HERA I+II data (HERAPDF1.5) and HERA I data (HERAPDF1.0). The plot is from Ref. [63].

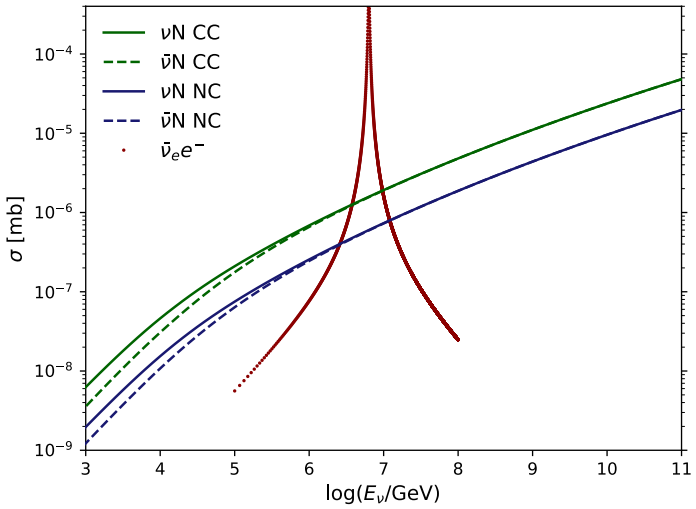

FIGURE 1.10: The calculated neutrino interaction cross section. The DIS interaction is calculated using HERAPDF1.5 by Ref. [62] and the Glashow Resonance cross section calculation is from Ref. [64].

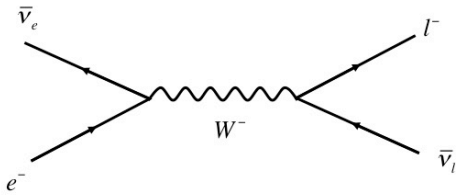

FIGURE 1.11: The Feynman diagram of an electron antineutrino scattering off an electron. Only the leptonic decay channels of the W^- boson is shown in the plot.

Reaction Channel	σ [cm^2]
$\bar{\nu}_e e \to \bar{\nu}_e e$	5.38×10^{-32}
$\bar{\nu}_e e \to \bar{\nu}_\mu \mu$	5.38×10^{-32}
$\bar{\nu}_e e \to \bar{\nu}_\tau \tau$	5.38×10^{-32}
$\bar{\nu}_e e \to$ hadrons	3.41×10^{-31}
$\bar{\nu}_e e \to$ anything	5.02×10^{-31}

TABLE 1.4: The integrated neutrino-electron scattering cross sections at 6.3 PeV. The numbers in the table are from Ref. [59].

The products of $\bar{\nu}_e e$ scattering can be leptonic and hadronic. The energy of the recoiling lepton is $E' = yE$. The differential cross section of the $\bar{\nu}_e e$ scattering with the leptonic decay of the mediating W^- boson can be calculated as [59]:

$$\frac{d^2\sigma(\bar{\nu}_e e \to \bar{\nu}_e e)}{dy} = \frac{G_F^2 mE}{2\pi}[\frac{R_e^2}{(1+2mEy/M_Z^2)^2} + |\frac{L_e}{1+2mE_y/M_Z^2} + \frac{2}{1-2mE/M_W^2 + i\Gamma_W/M_W}|^2(1-y)^2] \tag{1.50}$$

$$\frac{d^2\sigma(\bar{\nu}_e e \to \bar{\nu}_\mu \mu)}{dy} = \frac{G_F^2 mE}{2\pi}\frac{4(1-y)^2[1-(\mu^2-m^2)/2mE]^2}{(1-2mE/M_W^2)^2 + \Gamma_W^2/M_W^2} \tag{1.51}$$

The differential cross section of the $\bar{\nu}_e e$ scattering with the hadronic decay of the mediating W^- boson can be calculated as [59]:

$$\frac{d^2\sigma(\bar{\nu}_e e \to \text{hadrons})}{dy} = \frac{d^2\sigma(\bar{\nu}_e e \to \bar{\nu}_\mu \mu)}{dy} \cdot \frac{\Gamma(W \to \text{hadrons})}{\Gamma(W \to \mu\bar{\nu}_\mu)} \tag{1.52}$$

In the equations above, m is the mass of the target electron $m = 0.51$ MeV/c^2 and μ is the muon mass $\mu = 105.66$ MeV/c^2. L_e and R_e are the left-handed and right-handed chiral couplings of the Z^0 to e: $L_e = 2\sin^2\theta_W - 1$ and $R_e = 2\sin^2\theta_W$, and Γ_W is the W decay width: $\Gamma_W \approx 2.08$ GeV.

The branching ratio of the products of the electron antineutrino-electron scattering depends on the branching ratio of W^- boson decay. The cross section of the different reaction channels of the neutrino-electron scattering at 6.3 PeV is shown in Table 1.4. Each leptonic decay channel has the same branching ratio of $\sim 10.7\%$ and the hadronic channel has the branching ratio of $\sim 67.9\%$.

The total electron antineutrino-electron scattering cross section ($\bar{\nu}_e e \to$ anything) as a function of neutrino energy is shown in Fig. 1.10. A peak of the Glashow Resonance manifests at around 6.3 PeV. In the energy range of below 1 PeV and above 10 PeV the neutrino-electron interaction cross section is negligible compared to the neutrino-nucleon interaction cross section. In this thesis, we will measure for the first time, a combined νN

and $\bar{\nu}_e e$ cross section. The fraction of $\bar{\nu}_e e$ events is sensitive to the astrophysical neutrino generation process (pp or $p\gamma$) as discussed in Sec. 1.2.3.

Chapter 2

The IceCube Detector

As discussed in the previous chapter there is evidence that neutrinos of extraterrestrial origins are generated in association with the high-energy cosmic rays. Due to their charge-free and weakly interacting nature, neutrinos can travel through the space from their sources to the Earth without being deflected or absorbed. Thus they are the ideal messenger pointing back to their sources.

In order to detect astrophysical neutrinos, at least one-cubic-kilometer size in detection volume is required. In this chapter, we will discuss the principle of the neutrino detection, and their detection in the IceCube detector. The chapter will cover the instrumentation of the detector, the data acquisition and processing, the neutrino interaction event signature and reconstruction, and Monte Carlo simulations.

2.1 Neutrino Detection

Neutrino detection in the IceCube detector is realized by the detection of the Cherenkov radiation of the charged secondary particles from neutrino interactions. When a charged particle passes through a dielectric media with a velocity that is greater than the phase velocity of the light in that media, an electromagnetic radiation is emitted. This radiation is called the Cherenkov radiation.

An illustration of the Cherenkov radiation forming is shown in Fig. 2.1. When the velocity of the charged particle is greater than the phase velocity of the light in the media, the light can not overpass the particle, therefore a wavefront is formed. The propagation direction of the radiation is indicated by the up-right-pointing arrow in the right plot of Fig. 2.1. The emission angle can be calculated as:

$$\cos\theta_c = \frac{ct/n}{vt} = \frac{c}{vn} = \frac{1}{n\beta}, \tag{2.1}$$

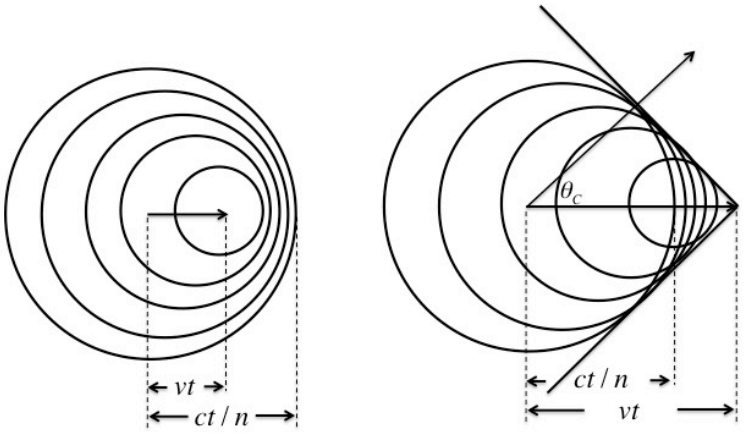

FIGURE 2.1: An illustration of the Cherenkov radiation effect. In the left plot: $v < c/n$, the condition for the Cherenkov radiation is not fulfilled. In the right plot: $v > c/n$, the condition for the Cherenkov radiation is fulfilled. The plot is reproduced from Fig. 2.1 in Ref. [65].

where n is the refractive index of the material [1] and β is the relative velocity compared to the speed of light in vacuum: $\beta = \frac{v}{c}$.

The number of photons emitted per unit length per unit energy of a particle with charge ze is [60]:

$$\frac{\mathrm{d}^2N}{\mathrm{d}E\mathrm{d}x} = \frac{\alpha z^2}{\hbar c}\sin^2\theta_c = \frac{\alpha z^2}{\hbar c}(1 - \frac{1}{\beta^2 n^2(E)}), \tag{2.2}$$

where α is the fine structure constant and $\hbar$ is the Dirac constant.

By substituting E with $\frac{2\pi c\hbar}{\lambda}$ ($\mathrm{d}E$ becomes $\frac{2\pi c\hbar}{\lambda^2}\mathrm{d}\lambda$), the above equation can be written as:

$$\frac{\mathrm{d}^2N}{\mathrm{d}\lambda\mathrm{d}x} = \frac{2\pi\alpha z^2}{\lambda^2}(1 - \frac{1}{\beta^2 n^2(\lambda)}) \tag{2.3}$$

[1] The refractive indices for water and ice are 1.333 and 1.309 respectively (evaluated at sodium D line: 598.2 nm).

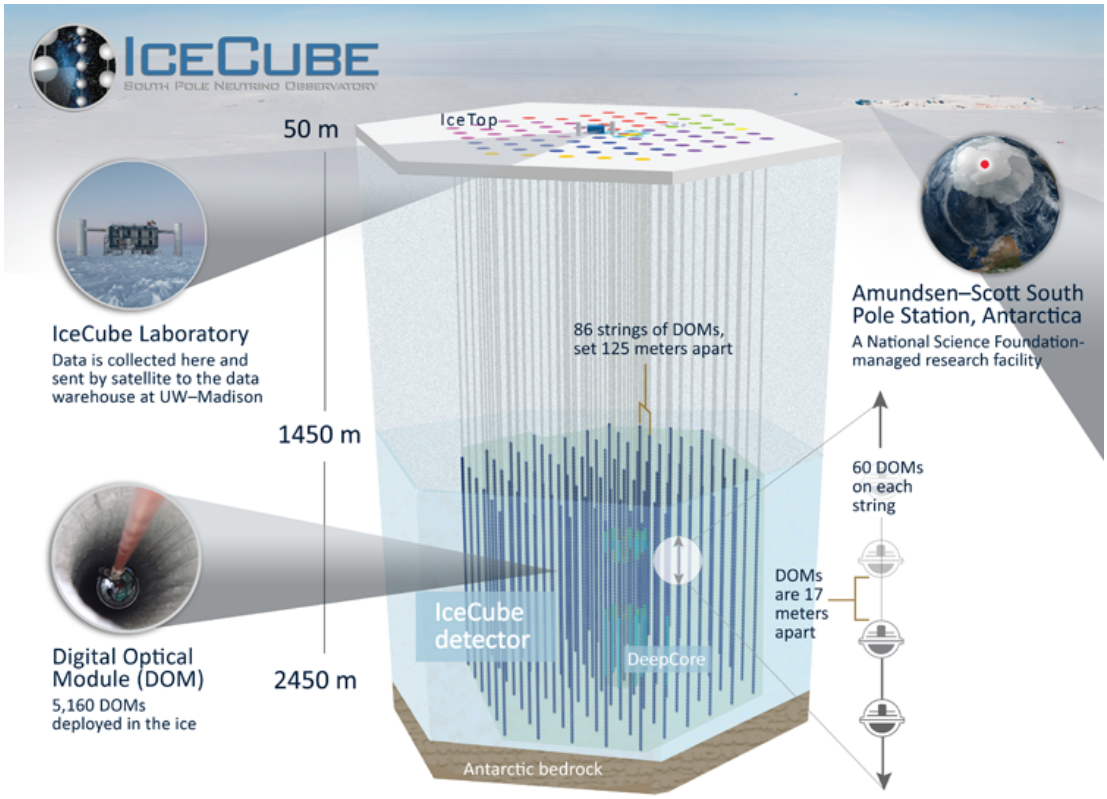

FIGURE 2.2: The instrumentation of the IceCube Neutrino Observatory. Image credit: the IceCube Collaboration.

The total number of photoelectron ($N_{\text{p.e.}}$) observed by a certain device with the photon detection efficiency ($\epsilon(\lambda)$) in the wavelength range ($[\lambda_{\min}, \lambda_{\max}]$), after the charged particle traveled the length (L), can be calculated as:

$$N_{\text{p.e.}} = L 2\pi\alpha z^2 \int_{\lambda_{\min}}^{\lambda_{\max}} \frac{\epsilon(\lambda)\sin^2\theta_c(\lambda)}{\lambda^2} \mathrm{d}\lambda \tag{2.4}$$

The photomultiplier tubes (PMTs) used in IceCube are sensitive to the wavelength range of 300 nm - 700 nm [66]. The photon detection efficiency is $\sim 25\%$ [67].

2.2 IceCube Instrumentation

The IceCube Neutrino Observatory is a one-cubic-kilometer size detector located in the ice of the geographic South Pole. It is capable of detecting neutrinos over a broad energy range from GeV to EeV. IceCube detector consists of two sections: the in-ice array and Ice Top. The collected data is processed in the IceCube laboratory (ICL) located at the surface on the ice. The instrumentation of the detector is shown in Fig. 2.2.

In-Ice Array

The IceCube in-ice array consists of 5160 digital optical modules (DOMs) for the detection of the Cherenkov photons. The DOMs are deployed on 86 vertical strings between 1450 m and 2450m in the Antarctic ice using the method of hot water drilling. Each in-ice string hosts 60 DOMs. The primary 78 strings form a hexagonal footprint and are placed 125 m apart from each other. The DOMs on the primary strings are placed 17 m apart. The spacing of the primary strings is suitable for the detection of neutrinos in the energy range of O(TeV) - O(PeV).

The other 8 strings are called the Deep Core strings. A deep core string has 10 DOMs deployed between 1900 m and 2000 m with the DOM-to-DOM spacing of 10 m and 50 DOMs deployed between 2100 m and 2450 m with the spacing of 7 m [68]. Such design is to avoid the so-called *"dust layer"* [69] region (2000 m - 2100 m) where there is a significant increase in the scattering and absorption coefficient in the ice. The top 10 DOMs of the deep core strings also serve as a veto cap to reject the penetrating atmospheric muons from cosmic rays. The much denser DOM placing in the deep core strings shifted the energy sensitivity of the detection to 10 GeV $\sim$ 100 GeV. The physics topic can be performed with deep core strings are neutrino oscillations [70], nonstandard neutrino interactions [71], dark matter detection [72], neutrino emission from core-collapse supernovae [73], and more.

IceTop

IceTop [74] consists of 162 ice-filled tanks located in 81 stations in the vicinity of the footprint of the IceCube in-ice array on the surface of the antarctic ice. Its primary goal is to detect cosmic ray air showers. Each station hosts two tanks that are 10 m apart with ice filled to a height of 0.9 m. Eight extra stations are placed in the center of the IceTop in the vicinity of the footprint of the Deep Core strings. Within each ice-filled tank, there is one "high-gain" DOM (5×10^6) and one "low-gain" DOM (10^5) to increase the dynamic range of the air shower detection. IceTop is sensitive to air showers induced by the cosmic rays with primary energy of PeV to EeV, and the inner denser tanks are sensitive to the cosmic rays with primary energy of $\sim$ 100 TeV. Besides the detection of cosmic ray air showers, IceTop also serves as the veto cap for the in-ice array to alert the system for any down-going muons.

The IceCube Laboratory

The IceCube Laboratory (ICL) is the central operation building located in the center of the footprints of the in-ice array at the surface. All the in-ice cables that connect the in-ice DOMs and the servers are grouped into two groups and are connected into the servers through the two cable towers on the two sides of the ICL. A picture of the ICL is shown in Fig. 2.2. ICL is the host of computers that are responsible for the data acquisition process and the online filtering process. The building is kept at a constant temperature of 18 °C.

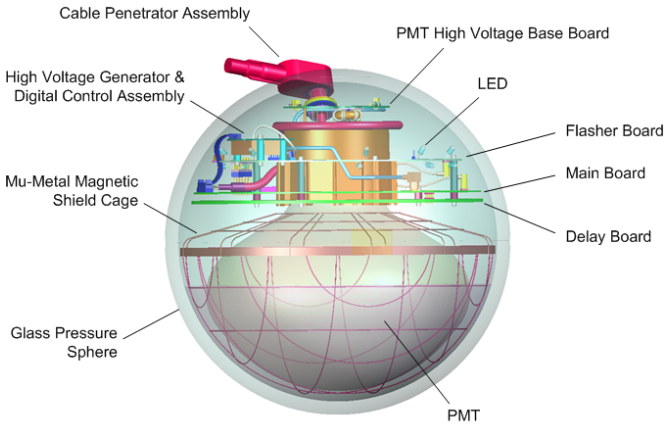

FIGURE 2.3: The schematic of the component of a DOM. The figure is from Ref. [67].

Digital Optical Module

The Digital Optical Modules (DOMs) are used for the data acquisition process in IceCube. Each DOM contains a downward-facing PMT [75] with the size of 10" diameter and several circuit boards all wrapped in a spherical glass housing. The schematic of the structure of a DOM is shown in Fig. 2.3.

The DOMs are wired in direct connection with their above and below neighbor for local coincidence (LC) photon signal (hits) detection. When a DOM and its nearest neighbors or next-to-nearest neighbors are hit within a time window of $\pm 1\,\mu$s, it is called an LC hit. The hits are called Hard Local Coincidence (HLC) hits when the LC conditions are met and are otherwise called Soft Local Coincidence (SLC) hits. The HLC hits indicate multiple photons being detected and thus saved in full details. The SLC hits are more likely to be noise hits that are not associated with charged particles, therefore only a timestamp and minimal information is saved.

The control center of a DOM is the main board. The main board manages a series of tasks including the digitization of the PMT waveforms using the Analog Transient Waveform Digitizer (ATWD) and fast Analog-to-Digital Converter (fADC), the communication with the data acquisition (DAQ) system, the calibration of the internal DOM clock, and the communication with the neighbor DOMs of local coincidence pulses.

The schematic of the data flow within a DOM is shown in Fig. 2.4. The waveform collected by the PMT is passed through a discriminator (Single Photoelectron (SPE) discriminator for the in-ice DOMs and Multiple Photoelectron (MPE) discriminator for the IceTop DOMs), and digitized by the ATWD. The digitized waveform is then sent to the DAQ (c.f. Sec. 2.3) with the time and charge information. Only if the LC pulse is detected and the discriminator threshold is passed, is the full waveform data included in the transmission to the DAQ.

The recording period of the ATWD is 427 ns with a 3.3 ns sampling period. It covers the light emission within tens of meters of the DOM. The detection of the photons generated further away from the DOM is cover by the fADC which samples continuously with a 25

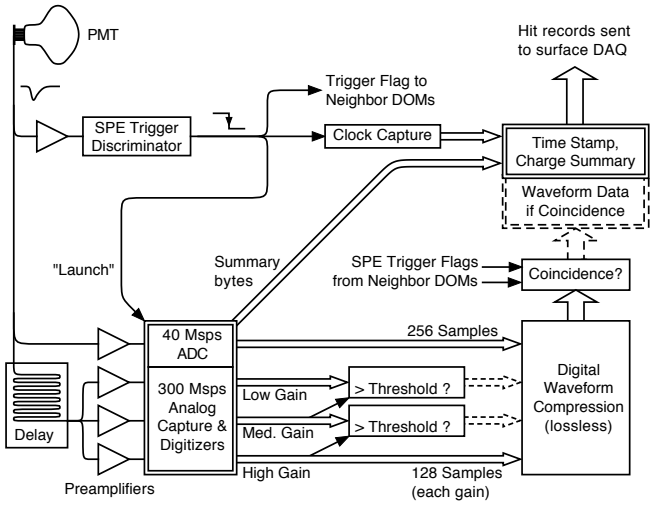

FIGURE 2.4: The schematic of the data flow within a DOM. The figure is from Ref. [76].

ns sampling period and an interval of 6.4 μs is saved after the launch. Each main board contains two ATWDs working in alternations to minimize the dead time. The median dead time for the in-ice DOMs is 6.6 $\times 10^{-3}\%$ [76].

Each DOM also has a Flasher Board which consists of 12 LEDs. Except for the "color DOMs" (cDOMs), all the other LEDs emit light with the wavelength of 405 ± 5 nm which is close to the wavelength (300 nm) the DOMs are most sensitive to at temperature of -20 °C. The 12 LEDs are arranged in a circle on the flasher board in pairs. The pairs are spaced 60° apart with one LED pointing 10.7° downwards and the other 51.6° upwards. The choice of the angle is to have the downward pointing LED emit light horizontally and the upward pointing LED emit light in the direction of 48° [2] away from the upward direction after the refraction through the DOM glass and the ice.

16 cDOMs are evenly deployed on String 79 (in the center of the detector) and String 14 (at the edge of the detector). Each cDOM also contains 12 LEDs in 6 pairs with even spacing in a circle on the flasher board. On each flasher board of a cDOM, there are three pairs of 370 nm and 340 nm LEDs and three pairs of 340 nm and 505 nm LEDs. All of the cDOMs' LEDs are pointing outward horizontally.

By measuring the controlled light emitted by the LEDs in the DOMs, we study the response time of the DOMs, measure the position of the DOMs, measure the optical properties of the ice [3], and calibrate the direction and energy reconstruction algorithms.

[2] This angle is close to the Cherenkov angle in ice.

[3] The scattering and absorption property of the ice is shown in Fig. 3.19

2.3 Data Acquisition and Processing

Data Flow Overview

As discussed in Sec. 2.2, hits are classified as HLC hits or SLC hits according to whether or not they fulfill the location coincidence condition. All the hits are readout to the computers in the ICL through the data acquisition system (DAQ). The HLC hits are checked for causal relationships by examining the temporal and sometimes spatial correlations among them. A set of triggers are applied to the data to reduce the data volume. All the hits (SLC included) within a certain time window of a trigger are integrated into an event which is the output of the DAQ. Since the vast majority of the triggered events are atmospheric muons, the DAQ data rate is between 2.5 KHz to 2.9 kHz due to the seasonal variation. The median rate is 2.7 kHz which translates to a data volume of 1 TB/day.

About 25 physics filters, which are designed for different physics analysis purposes are applied on the DAQ events to select a subset ($\sim 15\%$) that can be fitted in the allowed bandwidth of the satellite. The events that pass any filter are transferred to the Northern Hemisphere through a satellite connection, and all the events (including the ones failed all the filters) are stored on the local disks which are shipped north at the end of the season.

The data-taking periods are chosen to be 8 hours. The data acquisition process is not interrupted by the run transition. The experiment control and monitoring can be conducted via the IceCube Live software system, and the low-latency communications for the experiment control are managed by the IceCube Messaging System (I3MS). An IceCube detector year starts around May each year. The detector configuration and the settings of the online filters can be changed annually before the start of a new data collection year if needed. A demonstration of the data flow is shown in Fig. 2.5.

Data Acquisition System

The Data Acquisition System (DAQ) includes String Hubs, Triggers, Event Builder, Secondary Builders and a Command and Control server [76]. It is designed to detect the hit patterns that potentially result from particle interactions, and bundle the hits to events before transferring them to Processing and Filtering (PnF).

The first layer of the DAQ is the StringHub. The StringHub contains two parts: the front end Omicron, and the back end Sender [76]. Omicron collects all the data from the DOMs including the calibration and monitoring data as well as the physics data. It organizes the hits from all the DOMs by time and then sends them over to the Sender. The HLC and SLC hits are temporarily stored in the HitSpool disk cache. The Sender sends the condensed HLC hits to the triggers. The condensed HLC hits contain the information about the hit time, the DOM number and the trigger remark. If a time interval is determined by the triggers, the Event Builder will request the information of all the hits within the interval from the Senders.

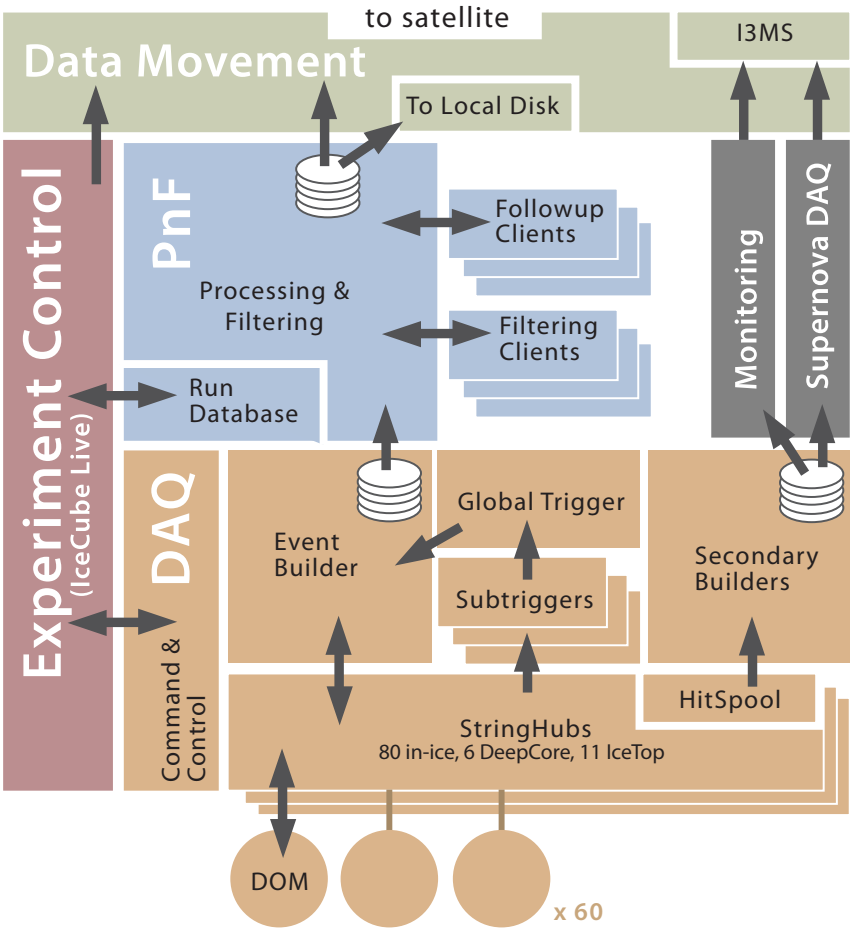

FIGURE 2.5: The overview of the data flow in the IceCube online system. The figure is from Ref. [76].

The triggers are designed to select HLC hits that potentially result from particle interaction by using their spacial and temporal correlations. The fundamental trigger is called the Simple Multiplicity Trigger (SMT). It requires at least N HLC hits within an n μs time window. N and n are location specific. For the in-ice DOMs, $N = 8$ and $n = 5$. For the denser DeepCore DOMs, the sensitive energy range is smaller, therefore $N = 3$ and $n = 2.5$ are also smaller. For the IceTop DOMs, $N = 6$ and $n = 5$ [76]. When the condition of the SMT is met, the trigger will go on until there is a time window where there are no HLC hits recorded.

Some triggers have a more relaxed multiplicity requirement and are compensated by a requirement in spacial correlation. The Volume Trigger requires a certain number (N) of the HLC hits detected within a cylinder of radius r and height h of each hit DOM within a time window of n μs. The String Trigger requires the hits to be within a certain number (M) of adjacent vertical DOMs. As it is for the SMT, r, h, N, and n are different for the in-ice DOMs and the IceTop DOMs.

There are other triggers like the Slow Particle (SLOP) trigger that is designed to select hits that may be induced by a subrelativistic heavy particle, the Fixed Rate Trigger (FRT) that reads out all the hits within a 10 ms time window at a certain frequency, and the Minimum Bias trigger reads out one out of every N HLC hits.

All the trigger data are eventually merged into the Global Trigger, where all the individual trigger information is still intact without having overlapped events that pass multiple triggers. The Global Trigger then passes the triggered time window to the Event Builder which requests the information for all hits within the time window from the StringHubs. The hits will be bundled into an event with the trigger data by the Event Builder before being sent to the Processing and Filtering (PnF) system. The total time from the photons being detected by the PMTs in the DOMs to the event being ready to be picked up by the PnF is 5 seconds [76].

Online Processing and Filtering

The task of the online Processing and Filtering (PnF) is to further reduce the size of the data to accommodate the satellite allowance ($\sim$ 100 GB/day).

Before running the event reconstruction algorithms, the digitized DOM waveforms of the triggered events are calibrated. The information of geometry, calibration, and detector status (GCD) is data-taking run specific. The GCD information is not only used online, but also used offline when more sophisticated event reconstruction algorithms are being performed on the filtered data in the North. Therefore all the GCD files are stored in a database.

The information in an event used in the online reconstruction is the time and amplitude of the waveform. The PnF compresses this information into the Super Data storage and Transfer (SuperDST) format which reduces the data volume to 9% of the original waveform. Various reconstruction results such as the energy, direction, interaction vertex, and the goodness of the fit are used by about 25 filters to select events that are potentially interesting for physics analyses. Around 15% of the triggered events pass at least one of the filters. The online filter that is relevant to this analysis is the cascade level2 filter which is described in Sec. 3.1. Some of the filters that are targeting astrophysical neutrino signals also produce real-time alerts [77]. When an event passes one of these filters, it could be potentially produced in an astrophysical phenomenon (e.g. GRBs) that is time sensitive. These astrophysical events usually also produce other signals like gamma-ray or gravitational waves that can be observed by other astrophysics observatories. Therefore a real-time alert enables timely follow-up observations.

Finally the filtered events and their SuperDST version of the DOM information are transferred to the North via satellite at the rate of $\sim$ 90 GB/day. All the triggered events and their SuperDST DOM information ($\sim$ 170 GB/day) are stored as the long-term archive as well as the raw data files with the uncalibrated waveforms for all the DOMs in all events.

The information such as the rates of DOM readouts, the rate of the triggers and filters are used in the IceCube Live monitoring system. The IceCube Live system allows the shift

taker to monitor the real-time data taking processing from any computer with internet connection in the North.

2.4 Event Signature and Reconstruction

Event Signature

There are three major event signatures in IceCube: a cascade, a track, and a double-bang. The light propagation and the detector DOM response of these event signatures are shown in Fig. 2.6. The color coding indicates the relative time when the DOMs detect the light: red is early in time and blue is late in time. The size of the "bubble" in the right column of Fig. 2.6 is proportional to the amount of the charge observed by that DOM: the bigger the size of the "bubble", the more charge it observed.

The cascade signature is induced by ν_e charged-current interactions, "low-energy" ν_τ charged-current interactions and neutral current interactions of neutrinos of all flavors. It is related to the electromagnetic or hadronic shower generated in the interactions. A ν_e charged-current interaction produces an electron. Due to the very small mass, the electron is scattered around the interaction vertex and creates an electromagnetic shower, thus the cascade signature. A ν_τ charged-current interaction produces a tau lepton. A low-energy tau lepton decays almost instantaneously after its production and creates a hadronic shower. When the energy of the ν_τ is less than 1 PeV, the decay vertex of the tau lepton is close to the vertex of the ν_τ interaction. The two hadronic showers cannot be distinguished from one another. When a neutral current interaction happens, the products are an out-going neutrino and a hadronic shower.

The muon track signature is induced by ν_μ charged-current interactions. A muon is much heavier than an electron and has a longer lifetime than a tau lepton. After the production, it propagates in a straight line and loses energy before it decays. Therefore it leaves a track signature. A down-going muon track that starts outside the detector is primarily induced by cosmic rays which are the background for the neutrino analyses. The more reliable ν_μ signals are either the ones starting within the detector or the ones from the up-going direction since the up-going cosmic ray induced muons are absorbed by the Earth.

The double-bang signature which is yet to be observed, is induced by very high-energy ν_τ charged-current interactions. As discussed before, the tau lepton is produced in a ν_τ charged-current interaction. When the energy of the primary neutrino is high enough, the tau lepton will also carry higher energy that allows it to travel further before it decays. Due to the large spacing (125 m) between the IceCube in-ice arrays, it requires the decay vertex of the tau lepton to be several hundred meters apart from the interaction vertex of the ν_τ for the two cascades to be separable. Therefore only ν_τ with PeV energies can induce such a signature. Due to the repaid falling spectrum of astrophysical neutrinos, the event count at the PeV energy level is very low.

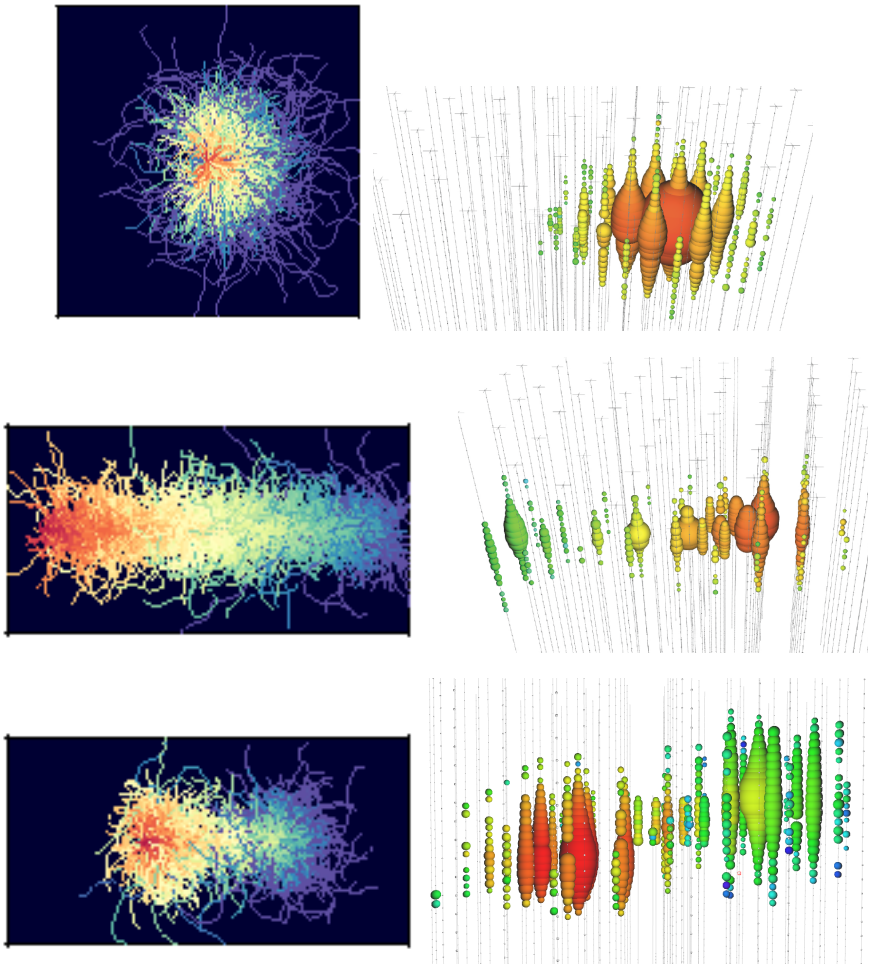

FIGURE 2.6: The event signatures in IceCube. The left column shows the light propagation and the right column shows the corresponding DOM response in the detector. The top row is the cascade signature. The middle row is the track signature. The bottom row is the double-bang signature. Image credit: the IceCube Collaboration.

Event Reconstruction

Different event topologies require different event reconstruction methods. In this analysis, only the cascade sample is used to produce the final result. Among all the reconstruction methods for the cascade sample, *Monopod* [78] is the one that produces the reconstructed result with the best resolution in a reasonable amount of time, thus can be applied on large scale of data. Some other cascade reconstruction methods such as *CascadeLlhVertexFit* [79] (c.f. Sec. 3.3) produces faster and less accurate results. Their reconstruction results are usually used in the early level event selection to distinguish cascade-like events from track-like events based on the goodness of fit, since these algorithms are based on a cascade topology assumption. These reconstruction results can also be used as the seed for Monopod to reduce the time needed for converge.

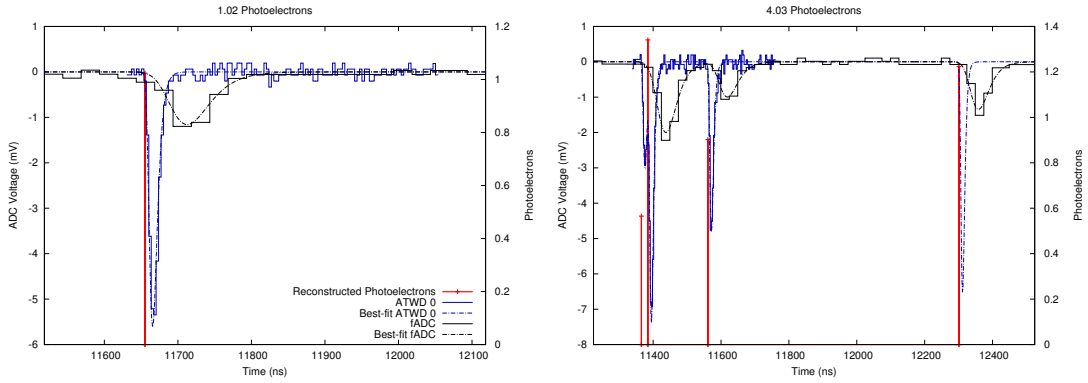

FIGURE 2.7: An illustration of the unfolding of the waveforms. The left plot shows a simple waveform case where one photoelectron is detected. The right plot shows a more complicated waveform case where multiple photoelectrons are detected. The plots are from Ref. [78].

Monopod is a likelihood-based algorithm. The input of Monopod is a pulse series represented by the observed number of photons and their time of observation in the DOMs. The number of photons is obtained by applying a non-negative linear simultaneous unfolding method on the digitized waveforms [78]. An illustration of the unfolding method is shown in Fig. 2.7.

A series of light propagation in the South Pole ice sheet [80], [69] from a broad range of deposited energy is simulated [81] by using the LED calibration data. This simulation is used as a template to be compared with the photon observations (k_i as the number of photons observed by DOM$_i$) in an event. The likelihood for the true light deposit being λ_i while the observation being k_i is:

$$L_i = \frac{\lambda_i^{k_i}}{k_i!} \cdot e^{-\lambda_i} \tag{2.5}$$

The true number of photons observed by DOM$_i$ from a cascade event with the true deposited energy E, the true position (x_0, y_0, z_0) and the true direction (θ_0, ϕ_0) can be calculated as:

$$\lambda_i = E\ \Lambda_i(x_0, y_0, z_0, \theta_0, \phi_0) + \rho_{i,0}, \tag{2.6}$$

where Λ_i is the expected number of photons produced per unit energy for DOM$_i$ and ρ_0 is the expected number of noise photons. Λ_i depends on the position of the DOM, the vertex of the event and the direction of the event. It can be numerically calculated using the template simulation with the application of a multi-dimensional spline fit [81].

The combined log likelihood for all the DOMs can be calculated as:

$$\ln L = \sum_{i \in \text{DOMs}} k_i \ln(E\Lambda_i + \rho_{i,0}) - (E\Lambda_i + \rho_{i,0}) - \ln(k_i!) \tag{2.7}$$

Maximizing the log likelihood with respect to E yields the reconstruction result for the deposited energy and all the other variables that determine Λ_i: $x', y', z', \theta', \phi'$. The maximization is done by calculating the gradient with respect to E, therefore the term $\ln(k_i!)$ will disappear. This is useful because the unfolding of the digitized waveform allows the result k_i to be non-integer.

The photons observed by each DOM can be further binned in time intervals. Adding this information in Eq. 2.7 will result in a small increase in the energy resolution in the single-source case. This application is more important in the multi-source case, as well as the PMT saturation case where only parts of the waveform can be used.

2.5 Monte Carlo Simulation

Monte Carlo simulation is an important part of the IceCube experiment. It is used extensively in the data analysis process. The major components of the simulation chain are:

- **Generators**: produce primary particles (neutrinos or charged particles) from the positions at the edge of the Earth. The generation of the particles is either done with simulating the reactions or with a flux spectrum.
- **Propagators**: propagate the particles to the effective volume of the detector. When the up-going particles are propagated through the Earth, certain interactions are simulated with the frequency according to the cross section. If the secondary neutrinos are produced, these neutrinos are further propagated to the detector. Due to the small neutrino interaction cross section, if the interactions within the effective volume of the detector are also simulated according to the cross section, much more neutrinos need to be generated to get enough statistics for the neutrino interactions within the detector. Therefore, all particles are forced to interact inside the detector volume and are assigned a weight according to the cross section.
- **Light injectors**: generate the certain amount of photoelectrons observed by each PMT when an interaction happens. The light injector takes the information of the event topology, the event deposited energy, and the photonics table [81] to calculate the number of photoelectrons that needs to be simulated.
- **Detector simulation**: simulate the detector responses to the photoelectrons simulated in the previous step. The detector responses include the digitization of the waveform, applying the trigger criteria, and applying the filters.

The neutrino simulation in IceCube is done with the *Neutrino-Generator (NuGen)* [82]. NuGen is based on the All Neutrino Interaction Generator (ANIS). NuGen uses the cross section table with the most up-to-date PDF: CSMS [62]. The choice of using NuGen instead of ANIS is to accommodate the data structure of IceCube.

When the interaction produces a muon inside the detector volume or within the reach of the detector volume, the energy loss of the muon track is simulated using the *Muon Monte Carlo (MMC)* [83]. In the case where two neutrinos reach the detector at the same time, for example, the charged-current interaction of a ν_τ primary neutrino in the Earth could produce a tau lepton that later decays into two neutrinos, the likelihood of both neutrinos interact in the detector volume is negligibly small, therefore NuGen randomly chooses one to interact based on the interaction probability of both neutrinos. When calculating the interaction probability, the target in the detector volume is the ice (H_2O). When the neutrinos are being propagated through the Earth, the target density is calculated using the *Preliminary Reference Earth Model (PREM)* [84].

The atmospheric muon simulation is done with the *Cosmic Ray Simulations for Kascade (CORSIKA)* [85] and the *MuonGun* [65]. CORSIKA simulates the extensive air showers produced when the cosmic rays enter the Earth's atmosphere. The primary particles in CORSIKA are the five most abundant nuclei in the cosmic rays: H, He, N, Al, Fe. From the air showers, the most pronounced background is the yielded single muons and muon bundles. The background distributions are crucial in the development of the event selection. However, simulating the full chain of air shower with CORSIKA is very computationally expensive. After applying the event selection (c.f. Chapter 3) on the simulation and experimental datasets, the background rate is very low. Using CORSIKA simulation to test the background rejection rate is not practical. Therefore a less time-consuming simulation is used in this stage.

At the final level of the most analyses focused on neutrinos, the major background is single muons. *MuonGun* is the simulation that injects single muons at the edge of the detector with the production rate calculated from CORSIKA. Without having to run the full air shower simulation, MuonGun can simulate single muons at a much faster rate. It needs to be kept in mind that even though MuonGun simulation works well at the final level to describe the data, its distribution fails to match the data at earlier levels because it doesn't have the muon bundles.

Chapter 3

Event Selection

The major background for this analysis is muons induced by cosmic rays when entering the atmosphere. IceCube detects these muons at a relatively much higher rate of 2.7 kHz [76], and several hundred atmospheric neutrinos per day [86]. Twenty-five online filters are designed for different physics analysis purposes and run at the South Pole. They reduce the triggered event rate to $\sim 15\%$ in order to accommodate the bandwidth of the satellite transformation while the rest of the data are kept on tape at the South Pole and shipped to the North annually [76]. In this analysis, we are interested in the cascade-like events for their good energy resolution, therefore the cascade level2 online filter is chosen(c.f. Sec. 3.1). Due to the limited computational power at the South Pole, the online filters can only perform simple direction and energy reconstructions. After the data are transmitted to the North, an offline filter - the cascade level3 filter (c.f. Sec. 3.2) is run on the data to further select the cascade-like events and compute variables that will be used for the final selection. The online and offline filters are designed and run by the collaboration to provide a starting point for analyses that use this kind of events.

Starting from the cascade level3 single contained branch (c.f. Sec. 3.2), we develop event selections that target the cascade-like events at the high energies (above 60 TeV). Only 10% of the experimental data is used to develop unbiased event selections. This 10% of the experimental data will be referred to as "burn sample" in the following content. Only after the event selection is developed, the rest 90% of the experimental data can be viewed by the analyzer. The rest 90% of the experimental data will be referred to as "unblinded sample" in the following content. The procedure of viewing the unblinded sample is called "unblinding" in the IceCube Collaboration. This analysis uses five years of IceCube data from 2011 to 2015. The 2011 data analysis utilizes the event selection from Ref. [87]. The 2012-2015 data was unblinded using the event selection developed with the burn sample of the 2012-215 data and the 100% of 2011 data. The 100% 2011 unblinded data provides enough statistics to develop the event selections without biasing the new 2012-2015 event selection. The event selection developed here has achieved a 20% increase in the signal efficiency compared to the event selection from Ref. [87]. Eventually, the 2011 final level sample from Ref. [87] and the 2012-2015 final level sample developed here are combined with the 2012-2015 final level sample selected using the event selection from Ref. [88], which targets the energy range below 60 TeV reconstructed energy. Both data sets are used in this analysis to measure the neutrino interaction cross section.

3.1 Cascade Level2

3.1.1 Cascade Level2 Filter Passing Rate

The cascade level2 filter is one of the online filters run at the South Pole after the trigger level. The filter settings change at most once a year. In the data collection period of this analysis, there are three different settings of the cascade level2 filter. The 2011 filter is applied on the 2011 data, the 2012 filter is applied on the 2012 data, while the 2013 filter is applied on the 2013-2015 data. When the filters are designed, the filter performances are studied on Monte Carlo simulations. ν_e simulation generated with the NuGen is used for the estimation of the signal passing rate for the filters. The passing rate of the astrophysical neutrinos is estimated using a single power law

$$\Phi_{astro} = \Phi_0 \times (E_\nu/100\text{TeV})^{-\gamma} \tag{3.1}$$

where $\gamma = 2$ and Φ_0 is a normalization factor that is dataset-specific . The acceptance rate of the atmospherical neutrinos is estimated using the weight calculated with the Honda model [28]. The acceptance rate for the 2011,2012 and 2013 cascade level2 filter is shown in Table 3.1. The numbers in the table come from the IceCube internal Trigger Filter Transmission (TFT) proposals (Ref. [89], [90], [91]).

Year	Corsika	$E^{-2}\nu_e$	Atm. $\nu_e(Honda)$
2011	1.1 %	84 %	51 %
2012	1.29 %	88.7 %	71.7 %
2013	1.34 %	89.3 %	70.8 %

TABLE 3.1: The 2011, 2012, and 2013 cascade level2 filter acceptance rate for astrophysical neutrinos, atmospherical neutrinos and atmospherical muons (Ref. [89], [90], [91]).

Figure 3.1 shows the cascade level2 rate of every run in the data taking period of May 2011 to May 2015. The x-axis is the Modified Julian Date (MJD) when the run was started, scaled to the year of 2013 for comparison. Every data point represents a run which is the unit of IceCube data collection. A run typically lasts 8 hours. The color of the points corresponds to different detector years. Every detector year begins around May of each calendar year and ends around May of the next calendar year.

As shown in Fig. 3.1, the cascade level2 rate for each detector year is not flat. At this filter level, the data is dominated by the atmospheric muons. The production of the atmospheric muons is closely correlated with the condition of the atmosphere. In May, June, and July, the antarctic winter, the atmosphere above the South Pole is less dense, which leads to fewer muon productions compared to the antarctic summer (December, January, February). This results in the seasonal fluctuation of the cascade level2 rate. At this filter level, the data is in equivalent to the CORSIKA prediction. Table 3.1 shows

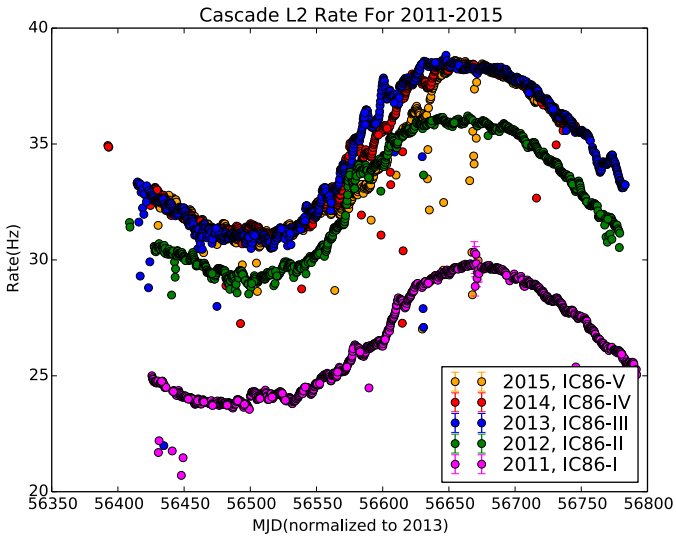

FIGURE 3.1: The cascade level2 rate of every run between May 2011 to May 2015 vs. their MJD scaled to 2013.

that in 2012 and 2013, the cascade level2 filter has a higher passing rate for CORSIKA and Fig. 3.1 shows a higher rate in the experimental data of 2012-2015 compared to 2011. This difference among the data from different years only exists in the background dominated level. In Sec. 3.5, we will show that at the final level where the background contribution to the data sample is less than 10%, the rate among the data from different years are consistent, therefore it is possible to use the simulation from one year (instead of different simulation datasets for every year) in the following parts of this analysis.

3.1.2 Experimental Data Good Runs

After the cascade level2 filter, we selected "good runs" for the higher level filters. Only runs with all 86 strings in the configuration are selected, and rare outliers were removed. The cascade level2 rate vs. RunID plots for the 2012-2015 data before and after the rare outlier removal are shown in Fig. 3.2. The RunID correlates with the time the run took place, therefore the plot shows a similar seasonal fluctuation as in Fig. 3.1. The 2011 run cleaning was done in Ref. [87].

In summary, 32 runs corresponding to 26.3 hours of the data collection time were removed as outliers from 2012-2015. After the rare outlier removal, the livetime of the data for individual years used in this analysis in shown in Table 3.2.

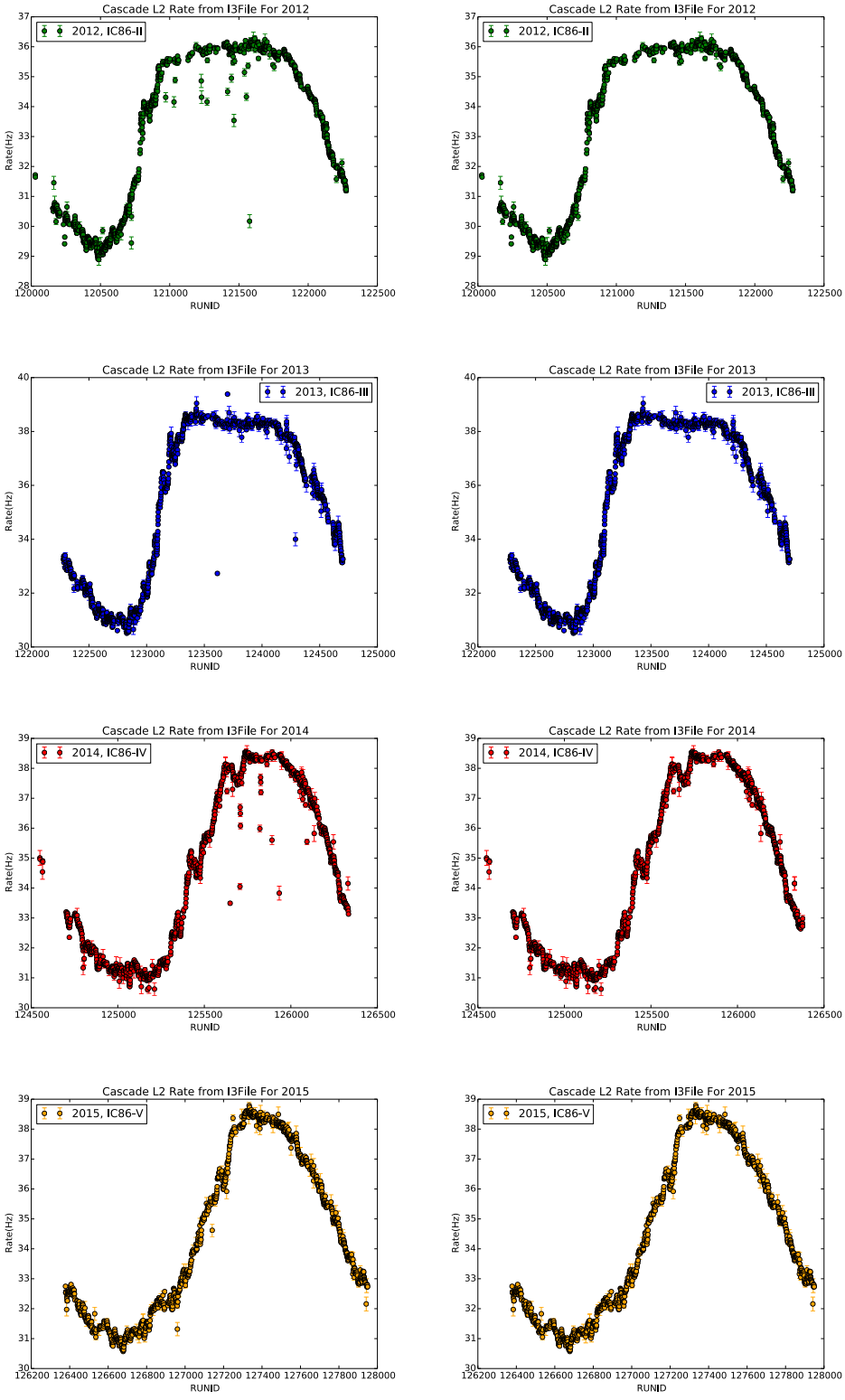

FIGURE 3.2: The cascade level2 rate vs. RunID for 2012 (top) - 2015 (bottom), before (left) and after (right) the rare outlier removal.

	90% [Day]	10% (burn sample) [Day]	Total [Day]
2011	301.47	31.04	332.51
2012	296.70	32.64	329.34
2013	316.96	33.67	350.63
2014	325.40	34.33	359.73
2015	321.22	36.54	357.76
Total			1729.97

TABLE 3.2: 2011-2015 data livetime

3.2 Cascade Level3

The cascade level3 filter is one of the offline filters that are implemented in the North (Wisconsin IceCube Particle Astrophysics Center) on the data after the transmission. It is designed to further reduce the background rate while keeping a high neutrino signal efficiency. After the selection, the selected cascade-like events are classified into three different categories: the single contained branch, the single un-contained branch, and the coincidence (double) contained branch. An event can be classified as either a single event or a coincident event depending on if it can be split into sub-events according to its topology [1]. The single events are further classified into two categories: the contained branch and the un-contained branch according to the position of the first hit in the cleaned pulse series of the event. If the depth of the first hit is within ± 430 m from the center of the detector, it belongs to the single contained branch, otherwise, it belongs to the single un-contained branch. The cascade level3 filter settings are updated at most once a year. In the data collection season 2011-2015, the cascade level3 filter setting has remained the same which means all the data used in this analysis are processed with the 2011 cascade level3 filter. The rate of the three cascade level3 branches and the passing rate for the filter is shown in Table 3.3. The numbers in the table are from Ref. [92].

	Corsika	$E^{-2}\nu_e$	Atm. $\nu_e(Honda)(E_\nu > 1\text{TeV})$
L2 Rate (Hz)	14.25	29.74 $\times 10^{-7}$	6.58 $\times 10^{-5}$
L3 Rate (Hz)	0.159	14.26 $\times 10^{-7}$	2.59 $\times 10^{-5}$
Passing Rate (L3/L2)	1.1%	47.9%	39.4%
L3 Single Cont. Rate (Hz)	0.103	9.63 $\times 10^{-7}$	2.39 $\times 10^{-5}$
L3 Single UnCont. Rate (Hz)	0.025	4.63 $\times 10^{-7}$	0.19 $\times 10^{-5}$
L3 Double Cont. Rate (Hz)	0.032	0.0037 $\times 10^{-7}$	0.00073 $\times 10^{-5}$

TABLE 3.3: Cascade level3 passing rate for the signal and the background. The numbers in the table are from Ref. [92]. Only the L3 single contained branch is used for this analysis.

[1] When two hits are: 1. on the same string and not further than z DOMs apart; 2. the horizontal distance between the hits is less than r meters; 3. happen within a time window, they are considered to belong to the same sub-event.

3.3 Level 4

In this analysis, the next level selection level4 (c.f. Sec. 3.3) is developed on the cascade level3 single contained branch, due to the good energy resolution of the single contained events. As shown in Table 3.3, after selecting the single contained branch of the cascade level3, the sample is still dominated by the background ($\sim 10^4$ more than the signal). An event selection is developed based on the single contained branch of the cascade level3 to provide a background free sample above the reconstructed energy 60 TeV while achieving an $\sim 80\%$ signal efficiency compare to the cascade level3 single contained branch.

The method of this event selection is a series of straight cuts. The cuts are developed with IceCube 2013 neutrino (ν_e, ν_μ, ν_τ) simulations generated with NuGen [82], and the 2011 background simulations generated by CORSIKA [85]. The fluxes used in the simulations are:

- **Conventional Neutrino Flux**: The conventional atmospheric neutrinos are produced by charged pion and kaon decay. HKKMS06 [28] with corrections to account for the knee in the cosmic-ray spectrum as well as the atmospheric self-veto effect [93] are used for the conventional flux calculation. A normalization factor of 0.85 [87] is also applied.
- **Prompt Neutrino Flux**: The prompt atmospheric neutrinos are produced by heavier meson decay. ERS [94] with corrections to account for the knee in the cosmic-ray spectrum as well as the atmospheric self-veto effect [93] are used for the prompt flux calculation. A normalization factor of 0.5 [87] is used to mimic the latest theoretical prediction BERSS [29]. In the development of the event selection, ERS is used instead of BERSS since the normalization factors and the astrophysical neutrino flux spectrum index used in this event selection are calculated using ERS [87]. After the event selection, a new fit is performed on the selected sample [88]. The rest part of this analysis will use the updated fit result from Ref. [88] and BERSS for the prompt flux.
- **Astrophysical Neutrino Flux** A single, unbroken power-law (as shown in Eq. 3.1) with the normalization parameter= 2.3 and the spectrum index = 2.67 is assumed [87].
- **Atmospheric Muon Background (CORSIKA)** Ref. [95] is used to calculate the flux of the atmospheric muons.

The experimental data used for developing the cuts are 100% for the 2011 data and 10% for the 2012-2015 data.

3.3.1 Variable Definition

The variables used in this event selection are defined as below:

Monopod Variables

Reconstruction results of the 4-iteration Monopod [78] [65] cascade reconstruction are used in this event selection. They consist of Monopod Energy, Monopod Z (depth) and Monopod Zenith.

SPEFit Zenith

The reconstructed zenith angle from the 16-iteration SPEFit [96] reconstruction is used in the event selection. The SPEFit is a fit-based reconstruction run at the cascade level3 assuming a track hypothesis. For track events, SPEFit has better zenith resolution than Monopod.

Starting Track Charge

A full sky scan is performed to collect any out-going charge from the Monopod reconstructed vertex that is disconnected from the cascade itself. If a muon is produced during the interaction (ν_μ charged-current interaction or the decay of a tau lepton as the product of a ν_τ charged-current interaction), it will create a track leaving the vertex of the interaction. This variable helps remove such background events.

Cascade Llh

The cascade log likelihood is the reduced log likelihood of the CascadeLlhVertexFit [79]. CascadeLlhVertexFit is a fit-based reconstruction run at the cascade level2 assuming a cascade hypothesis, and the reduced log likelihood indicates how well the data fits to the hypothesis.

Delay Time

Each event has a Monopod reconstructed vertex and a Monopod reconstructed vertex time t_{reco}. The time of the first hit of DOM$_i$ is t_i. For the cascade events, assuming the reconstructed vertex is the interaction vertex, the first hits on the DOMs are from the photons emitted from the reconstructed vertex. If there is no scattering in the ice, t_i can be calculated as:

$$t_i = t_{reco} + d_i/c_{ice}, \tag{3.2}$$

where d_i is the distance between the reconstructed vertex and the DOM$_i$ and c_{ice} is the speed of light in ice.

In reality, there is scattering in the ice, therefore it takes longer than $t_{reco} + d_i/c_{ice}$ for the DOM$_i$ to receive the first hit. The difference between the t_i and $t_{reco} + d_i/c_{ice}$, is the delay time of DOM$_i$:

$$dt_i = t_i - t_{reco} - d_i/c_{ice} \tag{3.3}$$

The delay time of an event is the smallest value among all the delay time of all DOMs with hits.

$$\text{DelayTime} = \min_{i \in \text{all DOMs with hits}} (dt_i) \tag{3.4}$$

For a true signal cascade event, the reconstructed vertex is the interaction vertex. The DelayTime should always be greater than or equal to zero due to causality. Since the reconstruction can only recover the interaction vertex within a limited resolution, small negative deviations can occur. For a background track event, instead of photons emitting from one interaction vertex, the photons are emitted along the track the muon travels. Therefore, hits in some DOMs happen before the reconstructed vertex time. This leads to a small negative DelayTime value.

TimeSplitPosition

The mean time is defined as the charge-weighted mean time over all the pulses in the pulses series.

$$t_{mean} = \frac{\sum_{i \in \text{pulse series}} Q_i \times t_i}{\sum_{i \in \text{pulse series}} Q_i} \tag{3.5}$$

where Q_i is the charge of pulse i and t_i is the time of pulse i. The pulse series is then split into two halves. The first half contains pulses that occur before the mean time and the second half contains pulses that occur after the mean time. The CascadeLlhVertexFit reconstruction is run on each half separately. The distance between the two reconstructed vertices of the two halves is the TimeSplitPosition.

For a true signal cascade event, the photons are emitted from the interaction vertex in all directions. The time split should separate the pulse series of a cascade event into two almost concentric spheres. Therefore the TimeSplitPosition of a cascade event should be small. For a background track event, the photons propagate in one direction, resulting in an elongated shape. The time split would cut the track into two no-overlapping halves, therefore the TimeSplitPosition of a track event ends up being large.

Qtot_HLC

Hard Local Coincidence (HLC) hits occur when two of the neighboring or next-to-nearest neighboring DOMs are both hit by photons within a time window of ± 1 μs [76]. Qtot_HLC is the total charge of the pulse series that only contains HLC hits (excluding the hits on Deep Core DOMs), and it is correlated with the deposited energy of the interaction. Choosing HLC hits will largely eliminate noise hits. Deep Core has a much denser DOM

distribution compared to the rest of IceCube, which means the same amount energy deposited will result in a higher total charge among Deep Core DOMs than the normal IceCube DOMs. Taking the charges of the Deep Core DOMs into account would cause a bias in its correlation with the deposited energy, therefore they are excluded.

MaxDomChargeOM

The MaxDomChargeOM is the DOM number of the DOM that sees the most of the light in the event. In a cascade event, such DOM should be close to the interaction vertex.

DepthofFirstHit

The DepthofFirstHit is the depth of the first hit in a cleaned pulse series. The depth of the first hit will be closer to the reconstructed vertex for a cascade event than a track event.

Fig. 3.3 shows the distribution of the data and the Monte Carlo at the cascade level3 single contained branch in different variables. In the plots, Monte Carlo simulations include the conventional atmospheric neutrino flux, the prompt atmospheric neutrino flux, the astrophysical neutrino flux (c.f. 3.3), and cosmic-ray muon background. As shown in these plots, the data is dominated by the background at the high energy range ($E_{reco} > 60$ TeV), and not very well described by the Monte Carlo (shown in the top-left plot in Fig. 3.3).

3.3.2 Level 4A: Polygon Cut

The cascade events that happen at the edge of the detector are harder to reconstruct and have a poor energy resolution. There is also higher background contamination at the edge of the detector. Hence it is important to implement a containment cut. The containment cut in the cascade level3 is based on the position of the first hit in a cleaned pulse series of an event. Due to the large data rate at level2, the hit-based cut is effective in eliminating the obvious background, but not sufficient by itself. To further ensure the selected events are contained events, we introduce a cut on the Polygon containment variable. This cut selects events with the Monopod reconstructed vertex within the IceCube polygon. The distribution of the polygon containment variable is shown in Fig. 3.4. The selection criteria for this level is:

$$\text{Polygon Containment} == 1 \tag{3.6}$$

The rates for data and simulations after the level4 A cut are shown in Table 3.4, in comparison with the previous level - Level3 SC [2].

[2]The rate of the MC at Level3 SC is different from the rate of the MC at level3 SC in Table 3.3 due to the difference in the MC dataset used in calculating these rates.

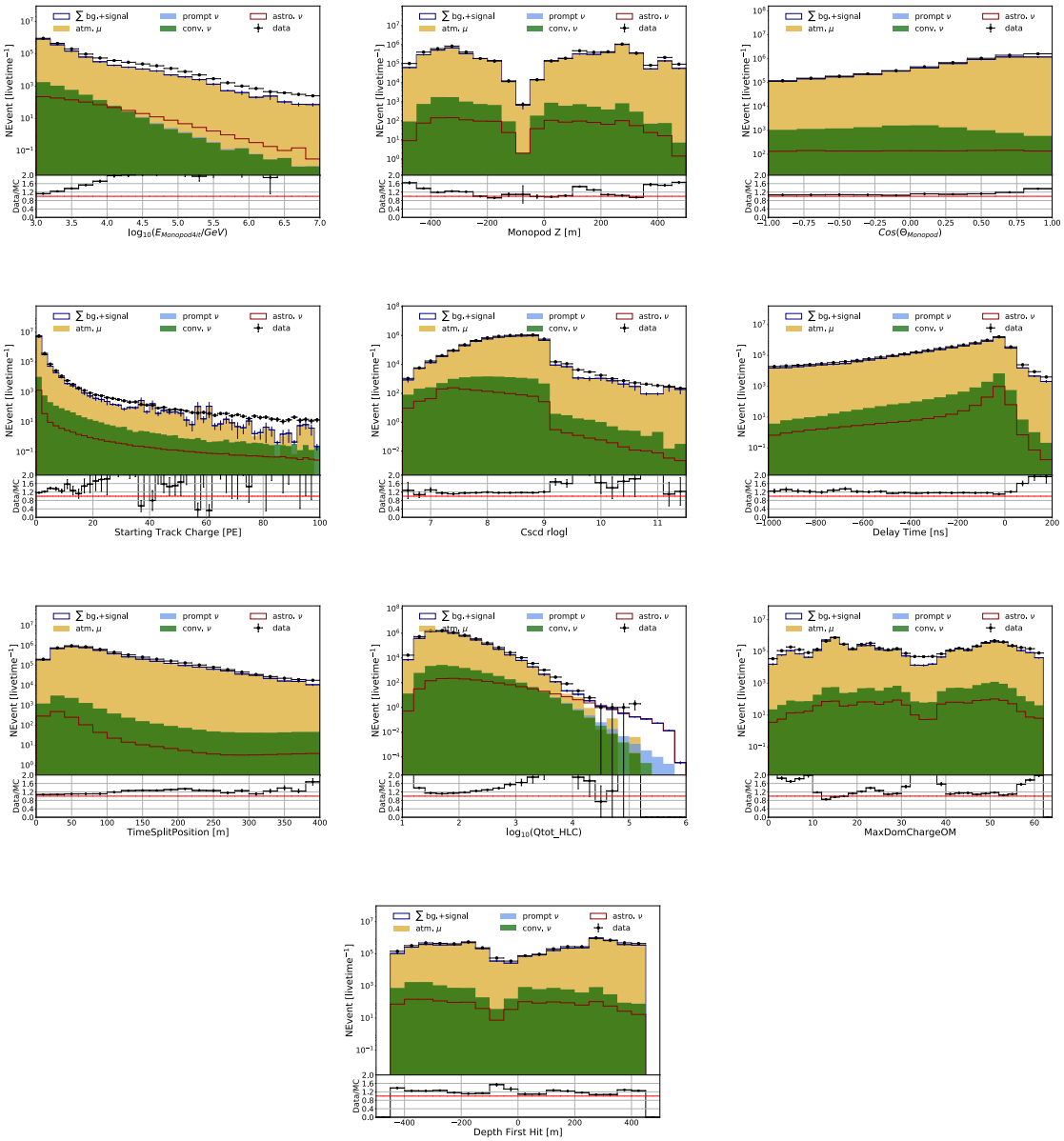

FIGURE 3.3: Variable distributions for the data and the Monte Carlo at the cascade level3 single contained branch. From the top to the bottom, the left to the right are: Monopod Energy, Monopod Z, cos(Monopod Zenith), Starting Track Charge, Cscd Llh, Delay Time, Time Split Position, Qtot_HLC, MaxDomChargeOM, and Depth First Hit.

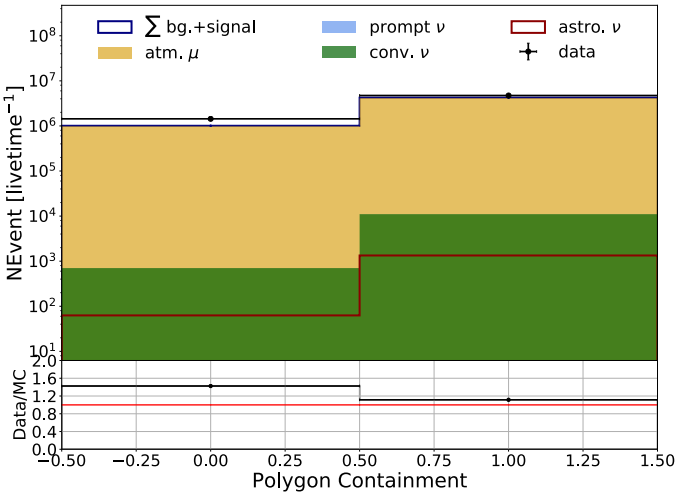

FIGURE 3.4: The Polygon Containment distribution for the data and the Monte Carlo at the cascade level3 single contained branch.

	Level3 SC [mHz]	Level 4A [mHz]	L 4A/ L3 SC
Data	152.02 ± 0.06	116.63 ± 0.05	76.7%
CORSIKA	129.12 ± 0.54	104.31 ± 0.50	80.8%
NuMu (conv)	0.2387 ± 0.0005	0.2234 ± 0.0004	93.6%
NuE (conv)	(5.039 ± 0.005) $\times 10^{-2}$	(4.842 ± 0.005) $\times 10^{-2}$	96.1%
NuMu (astro)	(5.718 ± 0.008) $\times 10^{-3}$	(5.338 ± 0.008) $\times 10^{-3}$	93.4%
NuE (astro)	(1.691 ± 0.001) $\times 10^{-2}$	(1.624 ± 0.001) $\times 10^{-2}$	96.0%
NuTau (astro)	(1.188 ± 0.002) $\times 10^{-2}$	(1.139 ± 0.002) $\times 10^{-2}$	95.9%
NuMu (prompt)	(4.422 ± 0.008) $\times 10^{-4}$	(4.111 ± 0.007) $\times 10^{-4}$	93.0%
NuE (prompt)	(1.4154 ± 0.0009) $\times 10^{-3}$	(1.3564 ± 0.0009) $\times 10^{-3}$	95.8%
Sum MC	129.44 ± 0.54	104.62 ± 0.50	80.8%

TABLE 3.4: The rate of the data and the Monte Carlo at the level3 single contained branch and level4 A.

3.3.3 Level 4B: Monopod Z Cut

The level4 B cut is used to further constrain the containment requirement. The position of the center of the detector is at (x_c, y_c, z_c) = (0 m, 0 m, 0 m). The detector covers the depth from - 500 m to + 500 m. The distribution of Monopod reconstructed depth (z) after the level 4A cut for the data and the Monte Carlo is shown in Fig. 3.5. The selection criteria for this level is:

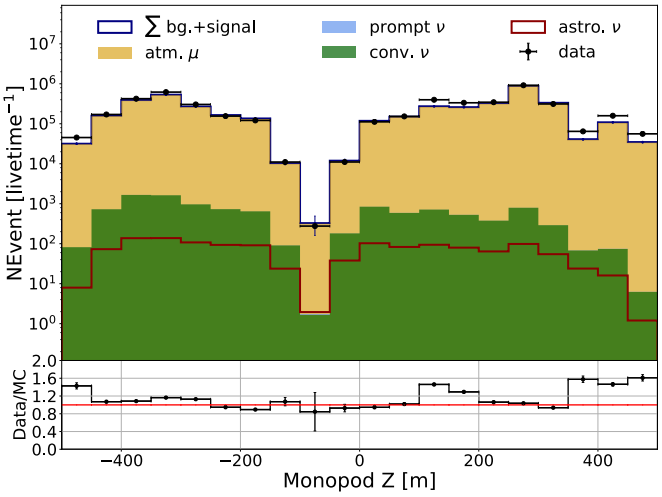

FIGURE 3.5: Monopod Z distribution for the data and the Monte Carlo at level 4A.

$$|\text{Monopod\_z}| < 450\text{m} \tag{3.7}$$

The events with 450< |Monopod_z| <500 are considered "partially contained" events. Their vertex is within the detector volume, but not the entire event. A dedicated event selection [97] is developed to select partially contained neutrinos to enhance the effective area in the very high energy range. In this analysis, we'll only focus on fully contained events.

The rate for data and simulations after the level 4B are shown in Table 3.5, in comparison with the previous level - level 4A.

3.3.4 Level 4C: Qtot_HLC Cut

As described in Sec. 3.3.1, Qtot_HLC is the total charge of the HLC hits in a cleaned pulse series. The higher the total charge, the more energetic the event is. Therefore, it should be positively correlated with the reconstructed energy. As shown in Fig. 3.6 (top left and right), in the Monopod reconstructed energy vs. Qtot_HLC distribution of the background events (Corsika) and the data, which is background dominated at this level, there is a considerable amount of events with a low total charge but a relatively high reconstructed energy. These events are mis-reconstructed events and should be removed from the final level sample. To best determine the boundary for applying the cut, a quantity called "signal significance" is introduced. It is calculated using the equation below:

	Level 4A [mHz]	Level 4B [mHz]	L 4B/L 4A
Data	116.63 ± 0.05	113.74 ± 0.05	97.5%
CORSIKA	104.31 ± 0.50	102.42 ± 0.49	98.2%
NuMu (conv)	0.2234 ± 0.0004	0.2205 ± 0.0004	98.7%
NuE (conv)	$(4.842 \pm 0.005) \times 10^{-2}$	$(4.794 \pm 0.005) \times 10^{-2}$	99.0%
NuMu (astro)	$(5.338 \pm 0.008) \times 10^{-3}$	$(5.256 \pm 0.008) \times 10^{-3}$	98.5%
NuE (astro)	$(1.624 \pm 0.001) \times 10^{-2}$	$(1.605 \pm 0.001) \times 10^{-2}$	98.8%
NuTau (astro)	$(1.139 \pm 0.002) \times 10^{-2}$	$(1.126 \pm 0.002) \times 10^{-2}$	98.8%
NuMu (prompt)	$(4.111 \pm 0.007) \times 10^{-4}$	$(4.046 \pm 0.007) \times 10^{-4}$	98.4%
NuE (prompt)	$(1.3564 \pm 0.0009) \times 10^{-3}$	$(1.3398 \pm 0.0009) \times 10^{-3}$	98.8%
Sum MC	104.62 ± 0.50	102.72 ± 0.49	98.2%

TABLE 3.5: The rate of data and Monte Carlo at level4 B in comparison with the previous level (level4 A).

$$\text{Signal Significance} = \frac{N_{signal}}{\sqrt{N_{signal} + N_{background}}} \tag{3.8}$$

The signal significance distribution in the Monopod reconstructed energy vs. the total charge grid is shown in Fig. 3.6 (bottom right).

The level 4C cut is designed to remove the events whose reconstructed energy is much higher than the total charge. However, it is undesirable to remove events with a high total charge nevertheless. Therefore the selection criteria for this level is chosen as below: it checks if the reconstructed energy and the total charge are positively correlated unless the total charge is higher than 1000 Photo Electron (P. E.).

$$\log_{10}(\text{Monopod\_Energy/GeV}) < \log_{10}(\text{Qtot\_HLC/P.E.}) + 1.6 \quad \text{or} \quad \text{Qtot\_HLC} > 1000 \text{ P.E.} \tag{3.9}$$

Note that the selection only removes events with a low total charge and high reconstructed energy, but not events with a high total charge that are mistakenly reconstructed to a lower energy. This is because the occurrence of the latter case is much lower compared to the former case, and in principle, the events with a high total charge should be kept.

The selected area is indicated with the blue lines in Fig. 3.6. Fig. 3.6 (top left and right) shows that this cut removes mis-reconstructed events in the background sample. At the mean time, the removed region has a much lower signal significance compared to the kept region (shown in Fig. 3.6 (bottom right)).

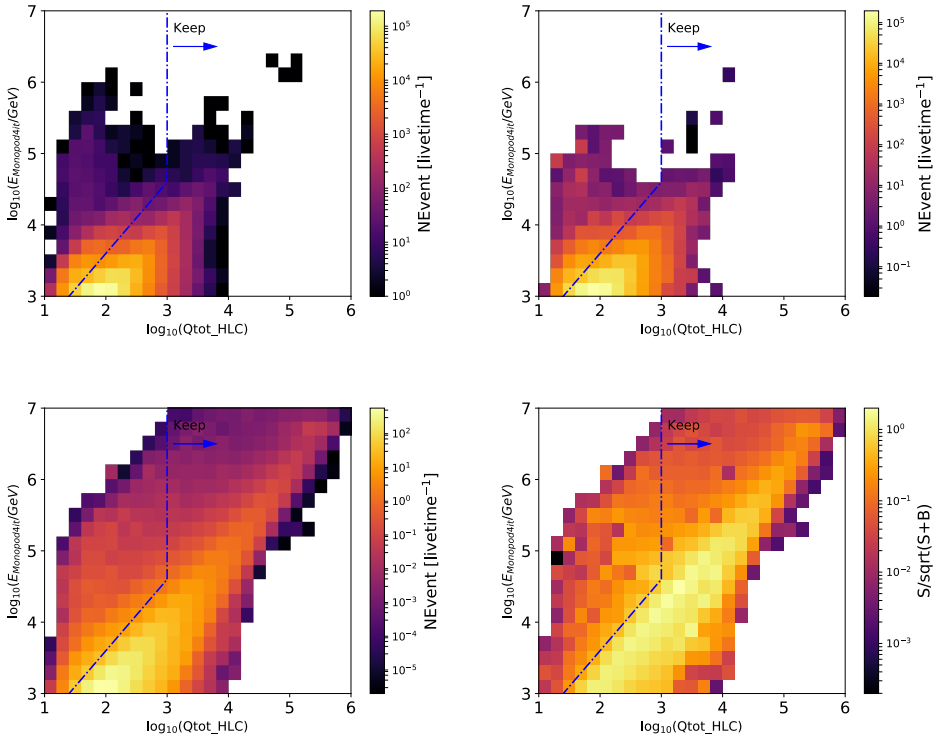

FIGURE 3.6: Monopod Energy vs. Qtot_HLC at level 4B: data (top left), Corsika (top right), and NuGen (bottom left). The bottom right plot is the signal significance distribution in Monopod Energy vs. Qtot_HLC grid. The blue arrow indicates the area being kept in the level 4C cut.

The rate for the data and the simulations after the level 4C are shown in Table 3.6, in comparison with the previous level - level 4B.

3.3.5 Level 4D: TimeSplitPosition Cut

As discussed in Sec. 3.3.1, the TimeSplitPosition for a cascade event is much smaller than it is for a track event, therefore it is better to keep events with a small TimeSplitPosition. By observing the 2-D histogram of the Monopod reconstructed energy and the TimeSplitPosition for signal events (the bottom left plot in Fig. 3.7), one could see that the two variables have a negative correlation. The design of the level 4D cut follows the similar idea of the level 4C cut: remove the events that don't follow the negative correlation between the Monopod reconstructed energy and the TimeSplitPosition and keep events with a small TimeSplitPosition (≤ 60) nevertheless. The cutting criteria for level4 D are :

	Level 4B [mHz]	Level 4C [mHz]	L 4C/L 4B
Data	113.74 ± 0.05	111.16 ± 0.05	97.7%
CORSIKA	102.42 ± 0.49	100.86 ± 0.49	98.5%
NuMu (conv)	0.2205 ± 0.0004	0.2180 ± 0.0004	98.9%
NuE (conv)	$(4.794 \pm 0.005) \times 10^{-2}$	$(4.752 \pm 0.005) \times 10^{-2}$	99.1%
NuMu (astro)	$(5.256 \pm 0.008) \times 10^{-3}$	$(5.133 \pm 0.007) \times 10^{-3}$	97.6%
NuE (astro)	$(1.605 \pm 0.001) \times 10^{-2}$	$(1.561 \pm 0.001) \times 10^{-2}$	97.2%
NuTau (astro)	$(1.126 \pm 0.002) \times 10^{-2}$	$(1.097 \pm 0.001) \times 10^{-2}$	97.4%
NuMu (prompt)	$(4.046 \pm 0.007) \times 10^{-4}$	$(3.935 \pm 0.007) \times 10^{-4}$	97.2%
NuE (prompt)	$(1.3398 \pm 0.0009) \times 10^{-3}$	$(1.3005 \pm 0.0009) \times 10^{-3}$	97.1%
Sum MC	102.72 ± 0.49	101.16 ± 0.49	98.5%

TABLE 3.6: The rate of the data and the Monte Carlo at level 4C in comparison with the previous level (level 4B).

$$\log_{10}(\text{Monopod\_Energy/GeV}) < (-0.01 \times \text{TimeSplitPosition/m} + 1.6) \quad \text{or} \quad \text{TimeSplitPosition} \leq 60\text{m} \tag{3.10}$$

The rate for the data and the simulations after the level 4D cut are shown in Table 3.7, in comparison with the previous level - level 4C.

	Level 4C [mHz]	Level 4D [mHz]	L 4D/L 4C
Data	111.16 ± 0.05	87.84 ± 0.05	79.0%
CORSIKA	100.86 ± 0.49	82.25 ± 0.44	81.5%
NuMu (conv)	0.2180 ± 0.0004	0.1800 ± 0.0004	82.6%
NuE (conv)	$(4.752 \pm 0.005) \times 10^{-2}$	$(3.889 \pm 0.005) \times 10^{-2}$	81.8%
NuMu (astro)	$(5.133 \pm 0.007) \times 10^{-3}$	$(4.438 \pm 0.007) \times 10^{-3}$	86.5%
NuE (astro)	$(1.561 \pm 0.001) \times 10^{-2}$	$(1.378 \pm 0.001) \times 10^{-2}$	88.3%
NuTau (astro)	$(1.097 \pm 0.001) \times 10^{-2}$	$(0.966 \pm 0.001) \times 10^{-2}$	88.0%
NuMu (prompt)	$(3.935 \pm 0.007) \times 10^{-4}$	$(3.387 \pm 0.007) \times 10^{-4}$	86.1%
NuE (prompt)	$(1.3005 \pm 0.0009) \times 10^{-3}$	$(1.1578 \pm 0.0008) \times 10^{-3}$	89.0%
Sum MC	101.16 ± 0.49	82.50 ± 0.44	81.6%

TABLE 3.7: The rate of data and Monte Carlo at level 4D in comparison with the previous level (level 4C).

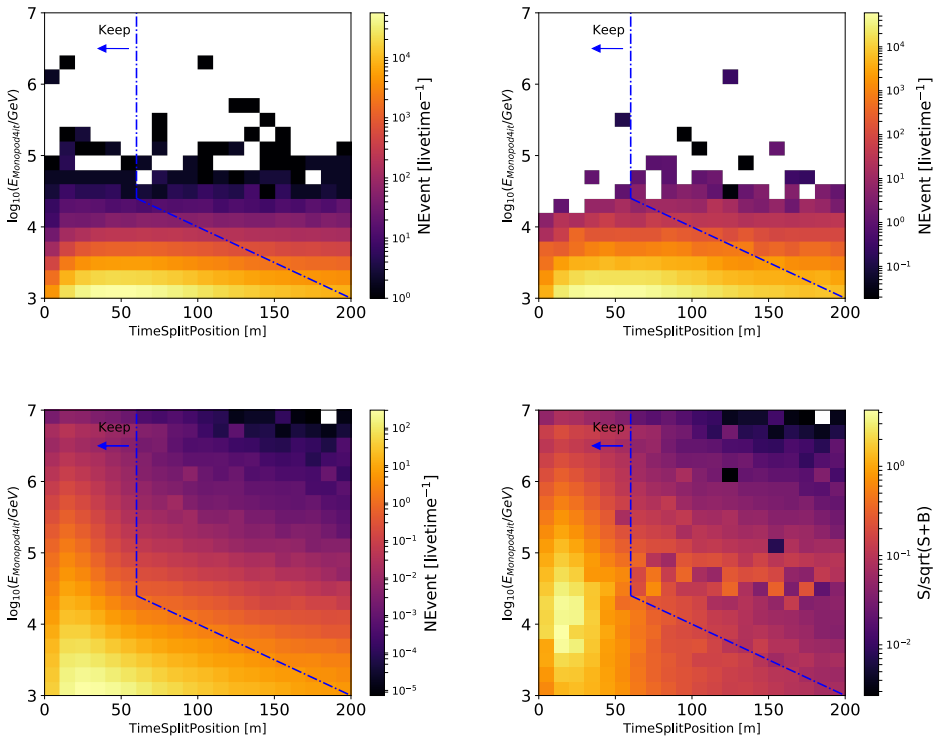

FIGURE 3.7: Monopod Energy vs. TimeSplitPosition at level 4C: data (top left), Corsika (top right), and NuGen (bottom left). The bottom right is the signal significance distribution in Monopod Energy vs. TimeSplitPosition grid. The blue arrow indicates the area being kept in the level 4D cut.

3.3.6 Level 4E: Delay Time Cut

The DelayTime of an event is the minimum delay time of all the DOMs that see hits in an event. A DOM's delay time is defined as the time difference between the first hit seen in the DOM and the time a photon takes to directly travel from the reconstructed vertex to the DOM subtracted. If the cascade hypothesis is true, the DelayTime of an event is always positive. Otherwise, it is negative (c.f. Sec. 3.3.1). Even though by design this variable has a great separation power between the cascade events and the track events, the imperfect performance of the pulse cleaning process would lead to an unexpected value of the DelayTime.

In the 2011 data sample, we observed several cases where the events look like cascade events in the event display and are suggested as cascade events by all the other variables, but their DelayTime values are all small negative numbers. In these events, some hits were found much earlier than in the cascade itself. The dis-connectivity in both space and time from the cascade events suggests these hits are not part of the cascades, but just noise hits. The noise hits not being removed from the pulses series leads to a small negative value of the DelayTime of these events.

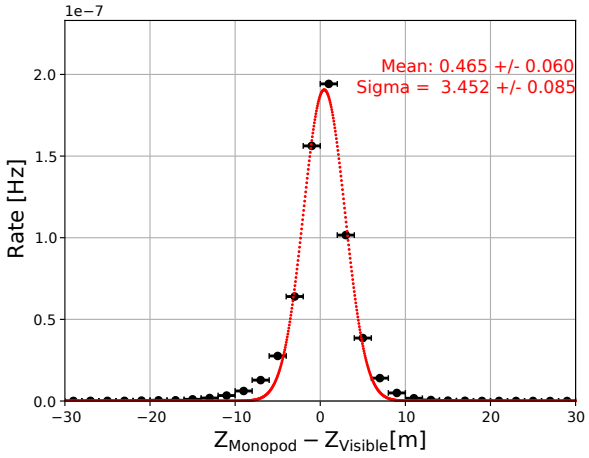

FIGURE 3.8: The depth resolution of the Monopod reconstruction for cascade events. The resolution is calculated using the NuE simulation at the final level with the reconstructed energy greater than 1TeV.

Since no better pulse-cleaning algorithm is available, extra caution needs to be taken when applying cuts on the DelayTime. In this event selection, the DelayTime cut is only applied to the events that are likely to be track events indicated by the other variables. The criteria of an event being indicated as a track event are listed as below:

- **Monopod_Energy $\leq$ 600 TeV**
- **Down-going**:

$$\cos(\text{Zenith}_{\text{reco}}) \geq 0.2 \tag{3.11}$$

  The choice of the zenith reconstruction depends on whether the event is more cascade-like or more track-like. The Monopod reconstructed zenith is used for the former case and the SPEFit reconstructed zenith is used for the latter. As shown in Fig. 3.8, the cascade events have a good depth resolution ($\sigma_z \sim 3$ m). The depth of the first hit for a cascade event should be the depth of its vertex. If the following condition holds, it is unlikely to be a cascade event:

$$|\text{DepthFirstHit} - \text{Monopod\_z}| > 15 \text{ m} \tag{3.12}$$

  Therefore, if Eq. 3.12 holds the SPEFit reconstructed zenith is used for the judge of the direction of the event, otherwise, the Monopod reconstructed zenith is used.

- **The event falls in the limbo between the signal and the background**: if 2 out of 3 of the following conditions are fulfilled:
  - CascadeLlh > 7.5
  - TimeSplitPosition > 40 m
  - $|\text{DepthFirstHit} - \text{Monopod\_z}| > 15$ m,

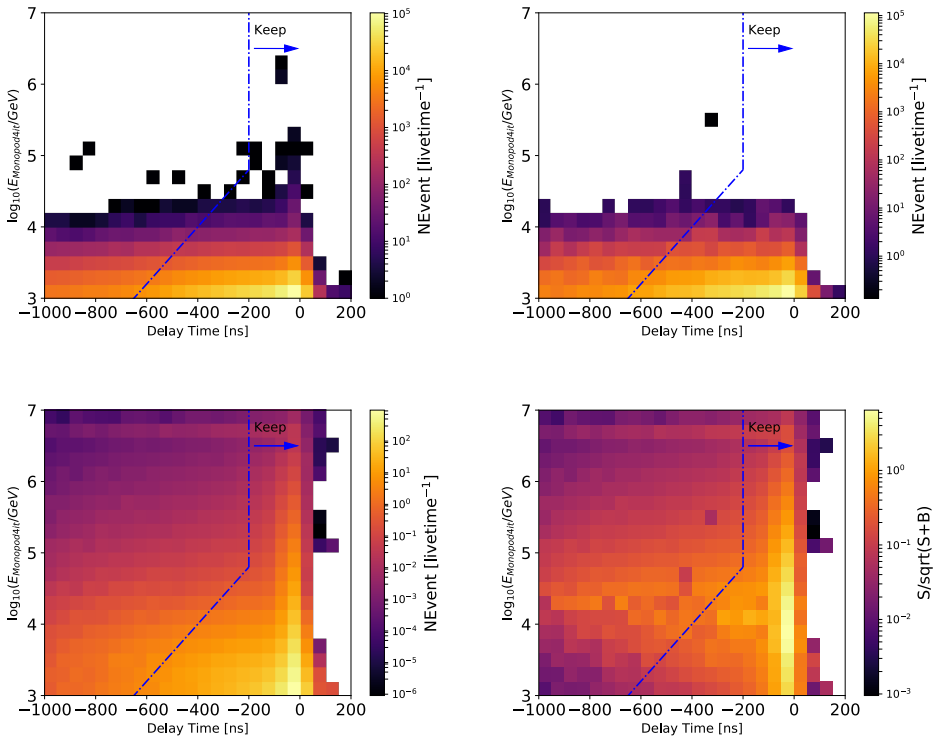

FIGURE 3.9: Monopod Energy vs. DelayTime at level 4D: data (top left), Corsika (top right), and NuGen (bottom left). The bottom right plot is the signal significance distribution in Monopod Energy vs. DelayTime grid. The blue arrow indicates the area being kept for the level 4E cut.

We applied the cut on the DelayTime as described below:

$$\log_{10}(\text{Monopod\_Energy/GeV}) < 4 \times 10^{-3} \times \text{DelayTime/m} + 5.6 \quad \text{or} \quad \text{DelayTime} > -200 \text{ m} \tag{3.13}$$

The 2D distributions of the Monopod Energy and the DelayTime for the data and the simulation, as well as the signal significance at level 4D, are shown in Fig. 3.9. The rate for the data and the simulations after the level 4E are shown in Table 3.8, in comparison with the previous level - level 4D.

3.3.7 Level 4F: MaxDomChargeOM Cut

The level 4F utilizes the MaxDomChargeOM variable, the DOM number of the DOM contains the most of the charge in an event. When the DOM contains the most of the charge is located at the top or at the bottom of the detector, it becomes harder to identify if the event is a track or a cascade, thus the removal of such events. The optical modules

	Level 4D [mHz]	Level 4E [mHz]	L 4E/ L 4D
Data	87.84 ± 0.05	78.58 ± 0.04	89.4%
CORSIKA	82.25 ± 0.44	74.85 ± 0.42	91.0%
NuMu (conv)	0.1800 ± 0.0004	0.1788 ± 0.0004	99.3%
NuE (conv)	$(3.889 \pm 0.005) \times 10^{-2}$	$(3.881 \pm 0.005) \times 10^{-2}$	99.8%
NuMu (astro)	$(4.438 \pm 0.007) \times 10^{-3}$	$(4.382 \pm 0.007) \times 10^{-3}$	98.7%
NuE (astro)	$(1.378 \pm 0.001) \times 10^{-2}$	$(1.373 \pm 0.001) \times 10^{-2}$	99.6%
NuTau (astro)	$(0.966 \pm 0.001) \times 10^{-2}$	$(0.962 \pm 0.001) \times 10^{-2}$	99.6%
NuMu (prompt)	$(3.387 \pm 0.007) \times 10^{-4}$	$(3.356 \pm 0.007) \times 10^{-4}$	99.1%
NuE (prompt)	$(1.1578 \pm 0.0008) \times 10^{-3}$	$(1.1537 \pm 0.0008) \times 10^{-3}$	99.6%
Sum MC	82.50 ± 0.44	75.10 ± 0.42	91.0%

TABLE 3.8: The rate of data and Monte Carlo at level 4E in comparison with the previous level (level 4D).

on the IceCube strings (String Number < 79) and the DeepCore strings (String Number ≥ 79)are numbered from the top to the bottom as 1-60. While the top DOMs of the IceCube strings are at the edge of the detector, due to the location of the DeepCore strings [76], their top DOMs are well contained in the detector. Therefore the cutting criteria for the level 4F cut is described as below:

$$\textbf{Keep} \begin{cases} \text{MaxDomChargeOM} < 58, & \text{if String No.} \geq 79. \\ 5 \leq \text{MaxDomChargeOM} < 58, & \text{if String No.} < 79 \text{ and Monopod\_E} \geq 50 \text{ TeV}. \\ 9 \leq \text{MaxDomChargeOM} < 58, & \text{if String No.} < 79 \text{ and Monopod\_E} < 50 \text{ TeV}. \end{cases} \tag{3.14}$$

The distribution of the maxDomChargeOM at the level 4E is shown in Fig. 3.10. After the cut is applied, the rate for the data and the simulations are shown in Table 3.9, in comparison with the previous level - level 4E.

3.3.8 Level 4G (Final Level): Starting Track Charge Cut

The starting track events consist of a hadronic cascade and a track starting from the origin of the cascade. If the track is generated within the cascade, its energy will be smaller then the cascade's energy. Therefore, compared to a track event, a starting track event appears to be more like a cascade event than a track event in the variable distributions. To distinguish the starting tracks from the real cascades, the Starting Track Charge variable is used. When a cascade event is very energetic, with many photons propagating outwards, some of the photons from the shower part might get mistaken as photons from a starting track. To prevent losing highly energetic events, the cut on the Starting Track Charge has a limit on the Monopod energy: when the Monopod energy is higher than

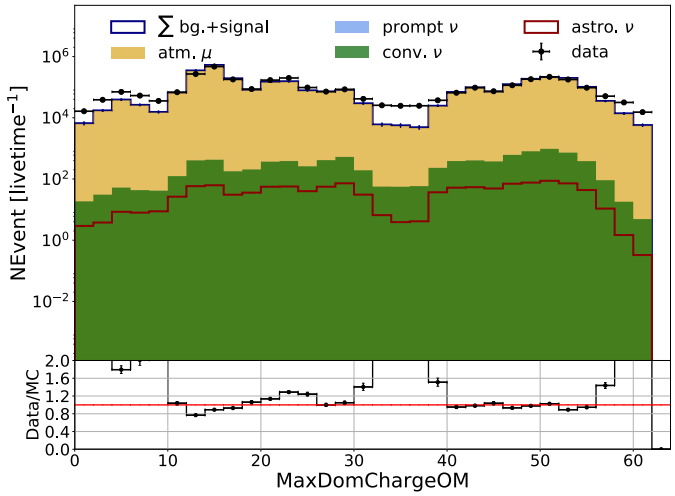

FIGURE 3.10: The MaxDomChargeOM distribution for the data and the Monte Carlo at level 4E.

	Level 4E [mHz]	Level 4F [mHz]	L 4F/L 4E
Data	78.58 ± 0.04	73.96 ± 0.04	94.1%
CORSIKA	74.85 ± 0.42	72.84 ± 0.42	97.3%
NuMu (conv)	0.1788 ± 0.0004	0.1767 ± 0.0004	98.8%
NuE (conv)	$(3.881 \pm 0.005) \times 10^{-2}$	$(3.842 \pm 0.005) \times 10^{-2}$	99.0%
NuMu (astro)	$(4.382 \pm 0.007) \times 10^{-3}$	$(4.309 \pm 0.007) \times 10^{-3}$	98.3%
NuE (astro)	$(1.373 \pm 0.001) \times 10^{-2}$	$(1.354 \pm 0.001) \times 10^{-2}$	98.6%
NuTau (astro)	$(0.962 \pm 0.001) \times 10^{-2}$	$(0.948 \pm 0.001) \times 10^{-2}$	98.5%
NuMu (prompt)	$(3.356 \pm 0.007) \times 10^{-4}$	$(3.294 \pm 0.006) \times 10^{-4}$	98.2%
NuE (prompt)	$(1.1537 \pm 0.0008) \times 10^{-3}$	$(1.1367 \pm 0.0008) \times 10^{-3}$	98.5%
Sum MC	75.10 ± 0.42	73.08 ± 0.42	97.3%

TABLE 3.9: The rate of the data and the Monte Carlo at level 4F in comparison with the previous level (level 4E).

600 TeV, the cut is not applied. The selection criteria for the level 4G cut is described as below:

$$\log_{10}(\text{Monopod\_Energy/GeV}) > 0.1 \times \text{StartingTrackCharge/P.E.} + 4.4$$
$$\text{or} \quad \text{StartingTrackCharge} \leq 4 \text{ P.E.}$$
$$\text{or} \quad \text{Monopod\_Energy} > 600 \text{ TeV}$$

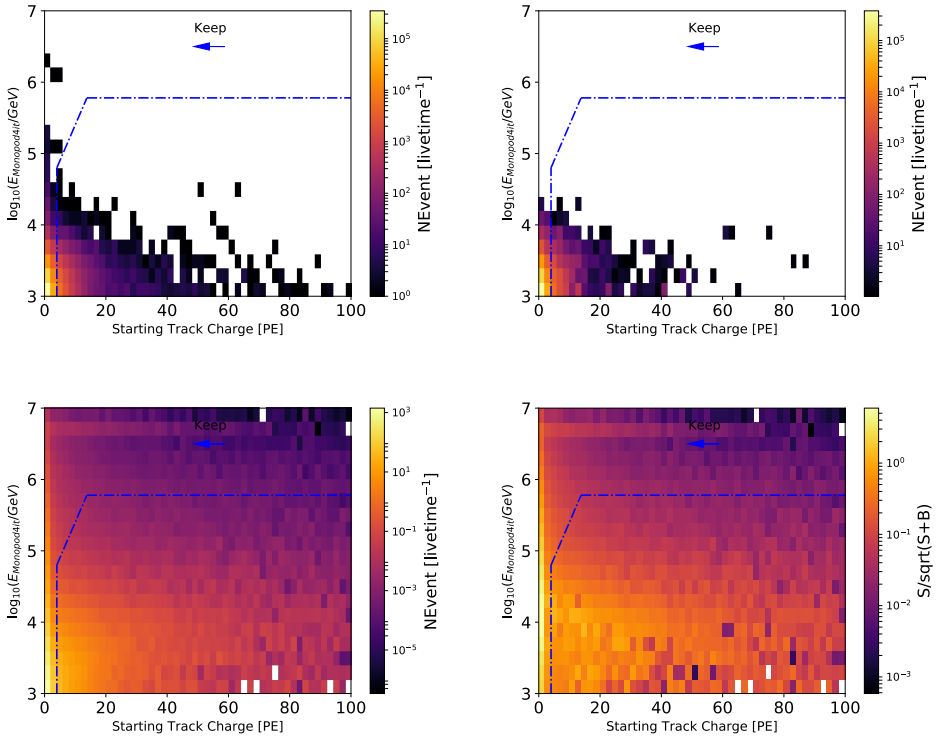

FIGURE 3.11: Monopod Energy vs. Starting Track Charge at level 4F: data (top left), Corsika (top right), and NuGen (bottom left). The bottom right plot is the signal significance distribution in Monopod Energy vs. Starting Track Charge grid. The blue arrow indicates the area being kept for the Level4 F cut.

The distribution of the Starting Track Charge variable at the level 4F is shown in Fig. 3.11. After the cut is applied, the rate for the data and the simulations are shown in Table 3.10, in comparison with the previous level - level 4F. The agreement in the rate of the data and the Monte Carlo results in a significant improvement compared to the starting point of the event selection (level 3SC).

The distributions of variables are shown in Fig. 3.12. In the top left plot (the reconstructed energy distribution), the agreement between the data and the Monte Carlo events become much better compared to the cascade level3, and the sample is background free above 60 TeV.

3.4 Signal Efficiency, Background Rejection and Effective Area

To study the event selection's effectiveness, three variables are used: the signal efficiency, the background rejection and the effective area. In this section we will compare these

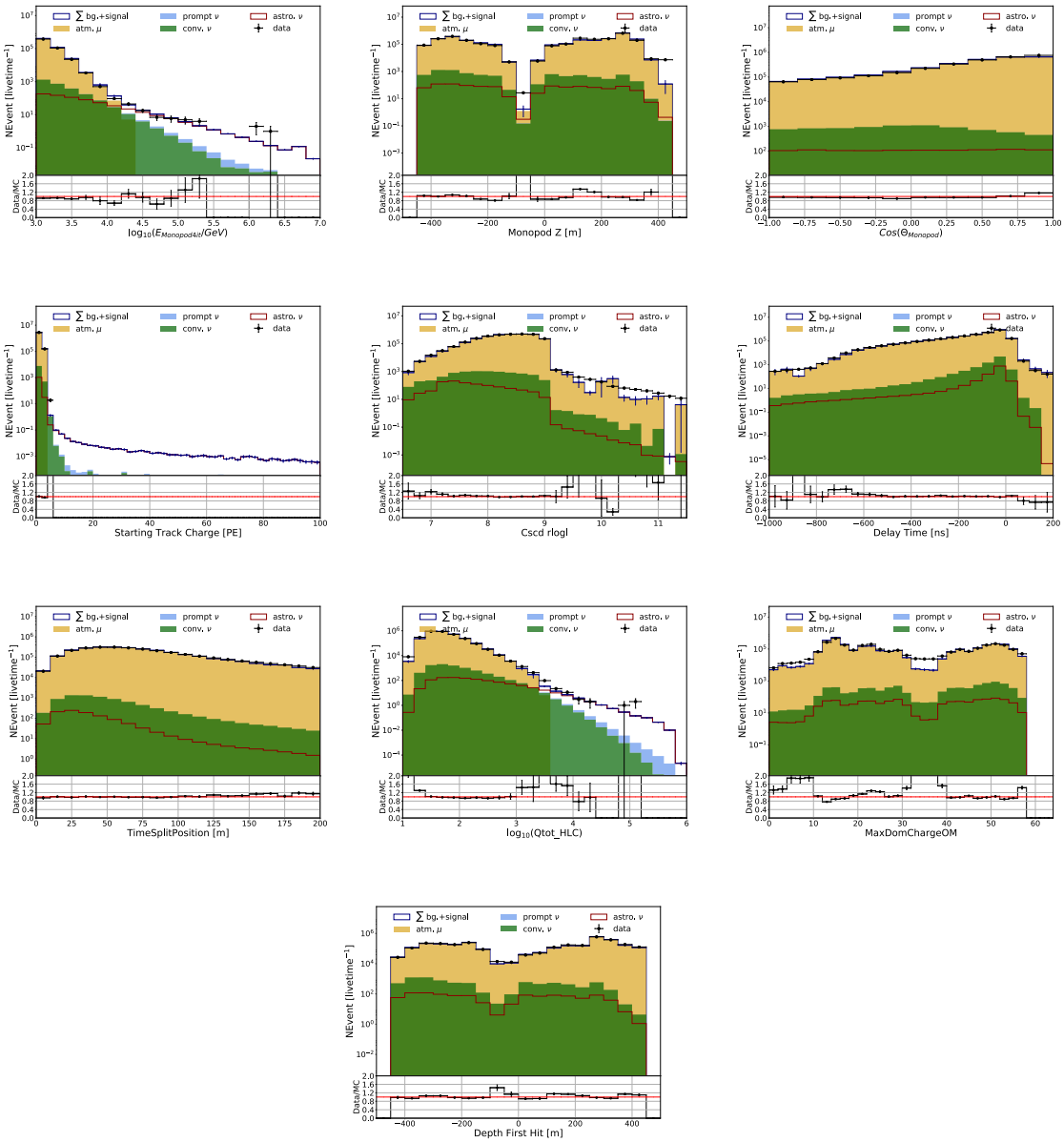

FIGURE 3.12: Variable distributions for the data and the Monte Carlo at the final level. From the top to the bottom, the left to the right are: Monopod Energy, Monopod Z, cos(Monopod Zenith), Starting Track Charge, Cscd Llh, Delay Time, Time Split Position, Qtot_HLC, MaxDomChargeOM, Depth First Hit.

	Level 4F [mHz]	Level 4G (final level) [mHz]	L 4G/L 4F
Data	73.96 ± 0.04	72.95 ± 0.04	98.6%
CORSIKA	72.84 ± 0.42	71.92 ± 0.42	98.7%
NuMu (conv)	0.1767 ± 0.0004	0.1635 ± 0.0004	92.5%
NuE (conv)	(3.842 ± 0.005) $\times 10^{-2}$	(3.839 ± 0.005) $\times 10^{-2}$	99.9%
NuMu (astro)	(4.309 ± 0.007) $\times 10^{-3}$	(3.821 ± 0.006) $\times 10^{-3}$	88.7%
NuE (astro)	(1.354 ± 0.001) $\times 10^{-2}$	(1.351 ± 0.001) $\times 10^{-2}$	99.8%
NuTau (astro)	(0.948 ± 0.001) $\times 10^{-2}$	(0.938 ± 0.001) $\times 10^{-2}$	98.9%
NuMu (prompt)	(3.294 ± 0.006) $\times 10^{-4}$	(2.866 ± 0.006) $\times 10^{-4}$	87.0%
NuE (prompt)	(1.1367 ± 0.0008) $\times 10^{-3}$	(1.1345 ± 0.0008) $\times 10^{-3}$	99.8%
Sum MC	73.08 ± 0.42	72.15 ± 0.42	98.7%

TABLE 3.10: The rate of the data and the Monte Carlo at level 4G (final level) in comparison with the previous level (level 4F).

three variables for the event selection developed in this analysis versus the one for the cascade 2yr analysis [87] [3].

3.4.1 Signal Efficiency and Background Rejection

The signal efficiency is defined as the signal rate at the final level divided by the rate at the starting level (the cascade level 3SC). The signal efficiency in the Monopod reconstructed energy bins is shown in the top two plots and the bottom left plot of Fig. 3.13. Figure 3.13 shows the efficiency of this event selection in comparison with the event selection of the cascade 2yr analysis. For the main signal of these two analyses: electron and tau neutrinos, this event selection is $\sim$ 30% higher in the signal efficiency than the cascade 2yr analysis in all energy ranges. Note that the cascade 2yr analysis has a very low efficiency below 10 TeV. This is because it is designed to select relatively high energy events (above 10 TeV), and it has a cut on the reconstructed energy from a different cascade reconstruction at 10 TeV. For muon neutrinos, the signal efficiencies for the two event selections are similar.

The background rejection is reflected by the rate of the passing background rate at the final level. The rate of the background simulation CORSIKA at the final level for the two selections and at the cascade level3 single contained branch are shown in the bottom right plot of Fig. 3.13. The plot shows that the cascade 2yr analysis is more efficient at reducing background, however above 60 TeV both event selections have no background. Since this event selection targets a reconstructed energy range above 60 TeV and the

[3]The cascade 2yr analysis is an analysis using the cascade sample in 2010-2011 IceCube data to measure the astrophysical neutrino flux. A dedicated event selection targeting the cascade sample was developed for the analysis and was the most up-to-date cascade event selection before this one. The event selection developed in this analysis aims to gain more signal efficiency compare to the cascade 2yr analysis.

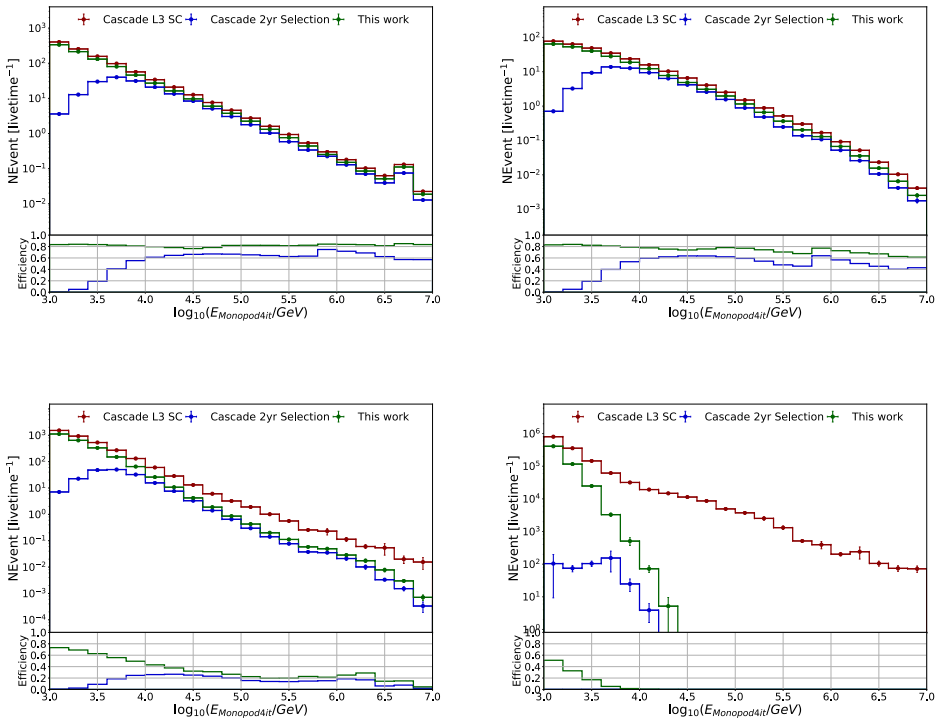

FIGURE 3.13: The rate at the final level of this selection, the final level of the cascade 2yr analysis and the cascade level3 single contain branch for the simulations in the Monopod reconstructed energy bins. Top left: NuE, top right: NuTau, bottom left: NuMu, bottom right: CORSIKA. The bottom half of every plot is the passing rate of the two selections.

reconstructed energy range of below 60 TeV is covered by the dedicated low energy event selection developed in Ref. [88], the higher passing rate of the background below 60 TeV in this event selection is not a concern.

3.4.2 Effective Area

The detection volume for the IceCube detector is fixed. However, different event selections will result in different efficiencies and different fiducial volumes for the accepted neutrino events. To better compare the selection efficiencies and to enable a comparison with other detectors, the effective area is introduced. The effective area is the size of an area which is 100% efficient for detecting neutrinos. It is evaluated using the NuGen simulation [82].

In reality, most of the neutrinos pass through the detector without any interactions and the astrophysical neutrino flux has a relatively soft index [88]. It would be inefficient to simulate neutrinos in the same manner. In the NuGen simulation, neutrinos are generated with a harder spectrum so that the higher energy neutrinos are well represented and all the neutrinos are forced to interact inside the detector. Each neutrino is also

assigned a corresponding weight according to the interaction cross section. This weight is called *OneWeight*. With OneWeight, the physical rates of the neutrinos interacted in the detector can be recovered. OneWeight is calculated using the formula below:

$$\text{OneWeight} = \frac{P_{int}}{E^{-\gamma}} \cdot \int_{E_{min}}^{E_{max}} E^{-\gamma} dE \cdot Area \cdot \Omega[\text{GeV} \cdot \text{cm}^2 \cdot \text{sr}], \tag{3.15}$$

where P_{int} is the total interaction probability weight, $E^{-\gamma}$ is the generated energy spectrum of neutrinos, E_{min} and E_{max} define the energy range of the neutrino generation, Area is the generation surface, and Ω is the generation solid angle.

The effective area is calculated using the equation below:

$$\text{EffectiveArea} = 10^{-4} \cdot \text{OneWeight} \cdot \frac{1}{\text{TotalGeneratedEvents}} \cdot \frac{1}{4\pi \cdot \text{EnergyBinWidth}} [\text{m}^2] \tag{3.16}$$

where the EnergyBinWidth is the bin width of the energy bin whose effective area is being calculated. The effective area is expressed in the unit of m^2 and the unit of OneWeight is cm^2, therefore a factor of 10^{-4} is applied.

The effective area of ν_e, ν_τ and ν_μ for this event selection are shown in Fig. 3.14, in comparison with the Cascade 2yr analysis event selection. Fig. 3.14 shows that for ν_e and ν_τ, the effective area of this event selection is at $\sim 30\%$ higher than the Cascade 2yr analysis event selection, and for ν_μ, it's $\sim 40\%$ higher.

3.5 Cross Year Comparison

The data from each year in the 2011-2015 collection are compared. Table 3.11 shows the rate of the 2011-2015 data at the final level for the whole energy range and for the reconstructed energy range of above 60 TeV. The table shows that the event rates are consistent within statistical uncertainties for all years. Figure 3.15 shows the variable distributions for the five years separately, compared to the Monte Carlo simulation results. The distribution plots show that the data from the five years are consistent for both the event rates and the variable distributions. The consistency across years justified the use of the Monte Carlo simulation from a single year (2013).

3.6 Merging with the Low Energy Event Selection

As stated at the beginning of this chapter, the event selection described in this dissertation is designed to achieve a high signal efficiency and a low background passing rate for the

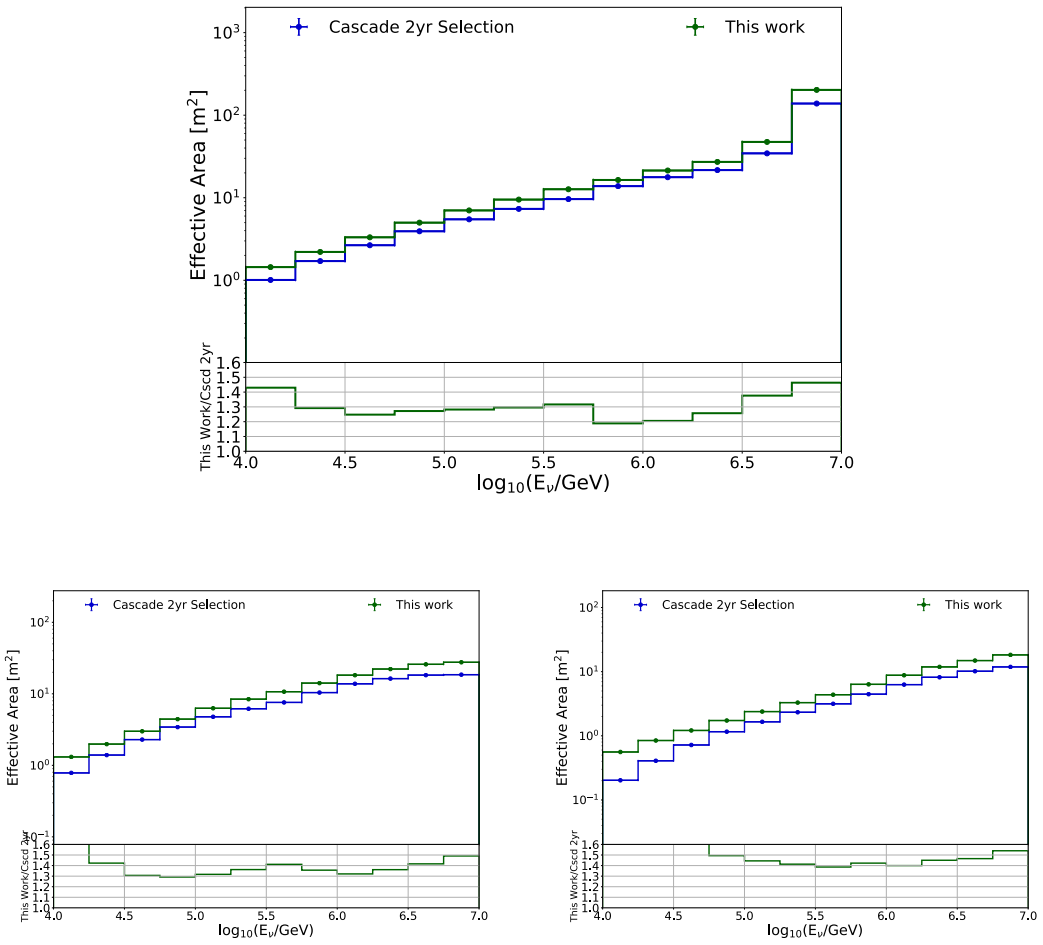

FIGURE 3.14: The effective area of ν_e (top), ν_τ (bottom left) and ν_μ (bottom right) for this event selection compared to the cascade 2yr analysis event selection.

reconstructed energy range above 60 TeV as shown in Fig. 3.13. For lower energy events, a dedicated low energy (LE) event selection was developed and applied [88].

To reasonably compare the signal efficiency of the LE event selection and the high energy (HE) event selection developed in this thesis, the comparison is done in a low background region. As shown in the middle plot in the third row in Fig. 3.12, the background dominates the region of the total charge below 1000 P. E. Therefore, to compare the LE and the HE event selection, an extra cut as below is applied.

$$\text{Qtot\_HLC} > 1000\text{P. E.} \tag{3.17}$$

The comparison of the signal efficiency and the background passing rate between the LE and the HE selection after the cut on the total charge is applied is shown in Fig. 3.16.

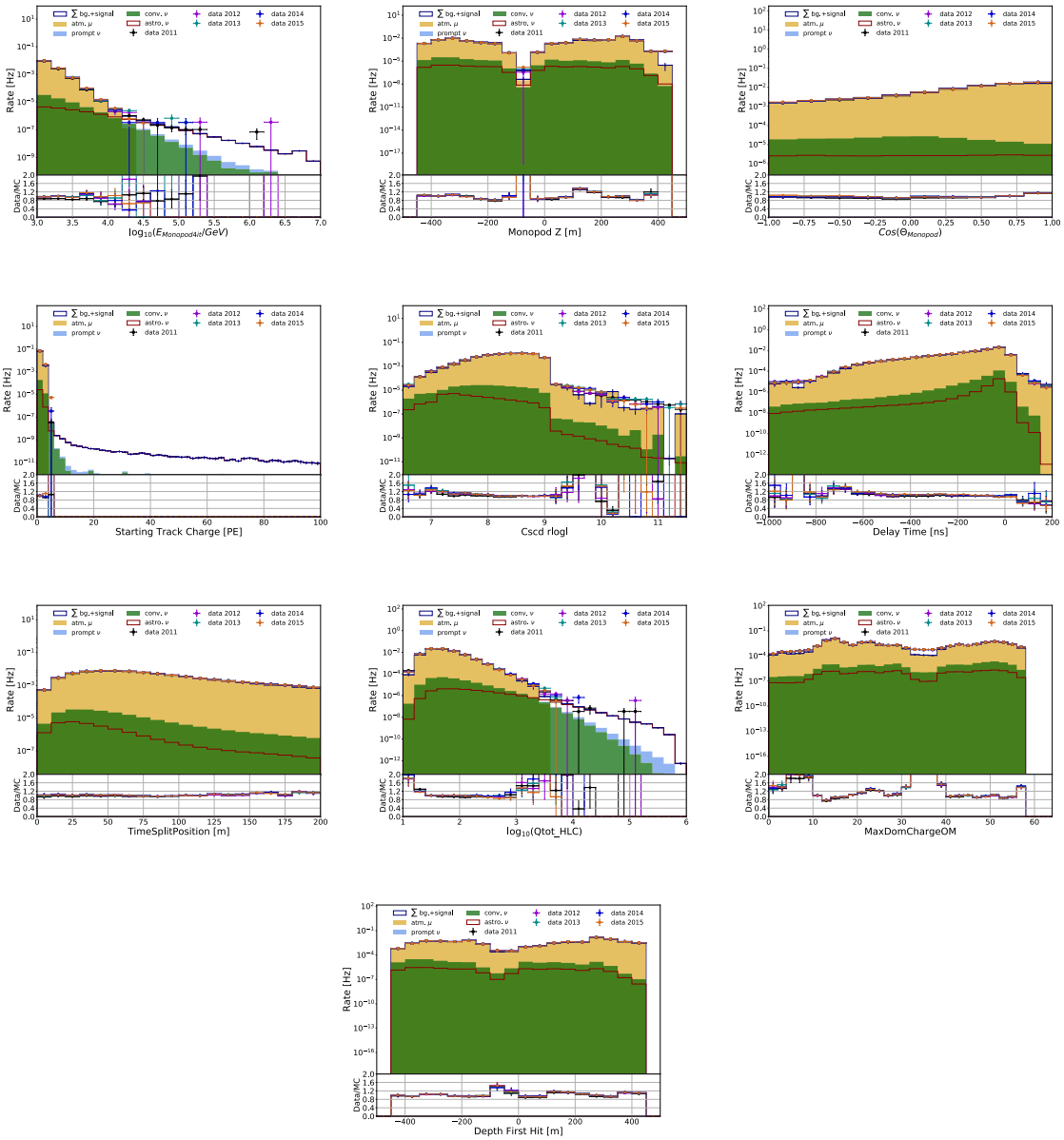

FIGURE 3.15: Variable distribution for the 2011 100% data, the 2012-2015 10% data and the Monte Carlo at the final level. From top to bottom, left to right are Monopod Energy, Monopod Z, cos(Monopod Zenith), Starting Track Charge, Cscd Llh, Delay Time, Time Split Position, Qtot_HLC, MaxDomChargeOM, Depth First Hit.

	Final Level (all) [mHz]	Final Level (>60TeV) [μHz]
2011 (100%)	70.99 ± 0.05	453 ± 126
2012 (10%)	72.76 ± 0.16	709 ± 501
2013 (10%)	73.61 ± 0.16	1031 ± 595
2014 (10%)	73.81 ± 0.16	337 ± 337
2015 (10%)	73.22 ± 0.15	0

TABLE 3.11: The rate of the 2011 100% data and the 2012-2015 10% data at the final level.

The plots show that below 60 TeV (indicated by the vertical black line in the plots), the LE selection has a higher signal efficiency and a lower background passing rate in the region below 60 TeV, while the HE selection has a higher signal efficiency and is background free in the region above 60 TeV. To maximize the advantages of the two event selections, the sample is separated into two parts: the LE selection is applied on events with reconstructed energy below 60 TeV and the HE selection is applied on events with reconstructed energy above 60 TeV. These two parts constitute the final sample for this analysis.

The selection efficiency of the LE and HE combined selection is shown in Fig. 3.17. The plots show that the LE + HE selection has a $\sim$ 20% higher signal efficiency and a much lower background passing rate compared to the cascade 2yr analysis. Fig. 3.18 also shows that the effective area of the LE + HE selection is least 20% larger than the cascade 2yr analysis.

3.7 Unblinded Sample

With the demonstration of the data and the Monte Carlo agreement and the study of the signal efficiency and the background rejection rate, the event selection developed in this dissertation is proven to be effective. These cuts are applied on all events in 2012-2015 and the results are then "unblinded". After unblinding, we found 402 cascade events with reconstructed energy above 10 TeV among which three events are above 1 PeV. The three PeV events are the highest energy cascade events found in IceCube so far. Their reconstructed energies are 2.00 PeV, 1.04 PeV, and 1.14 PeV. The event view of these three events are shown in the top right, the bottom left, and the bottom right plot in Fig. 3.21.

In the unblinded sample, we also found several events with the interaction vertices located in the "dust layer". We will show that using the conventional cascade reconstruction method (Monopod) on these events will lead to a bias in the reconstructed energy. In the next section, we will discuss a special energy reconstruction developed for this analysis using the boosted decision tree for events located in the dust layer.

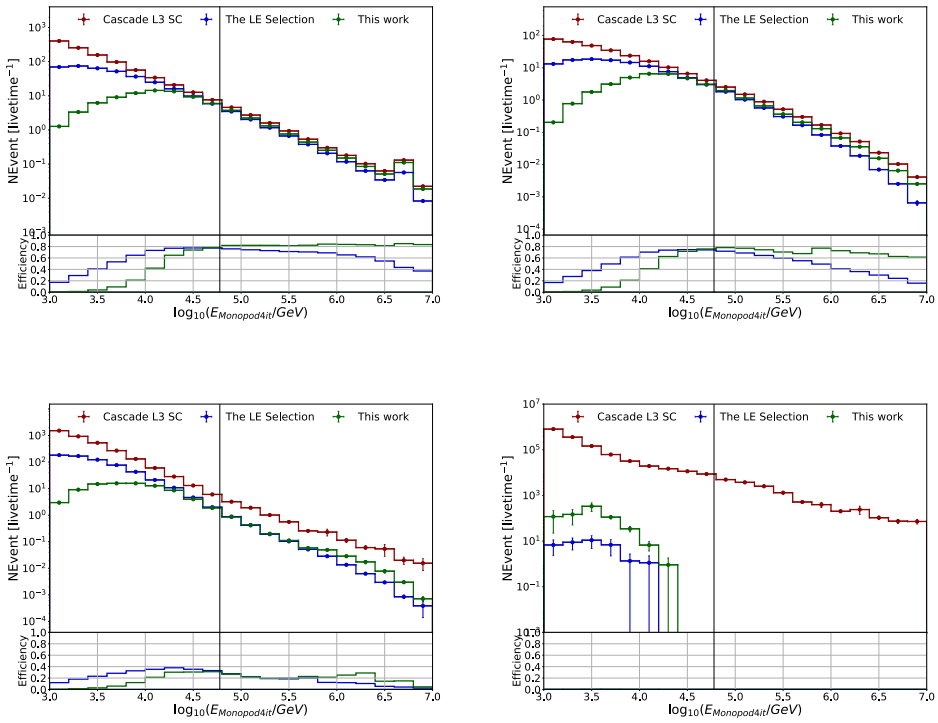

FIGURE 3.16: The rate of the final level of this selection, the final level of the LE selection and the cascade level3 single contained branch for the simulations in the Monopod reconstructed energy bins. Top left: ν_e, top right: ν_τ, bottom left: ν_μ, bottom right: cosmic-ray background (CORSIKA). The lower half of each plot is the passing rate of the two selections as a function of the reconstructed energy. The vertical black line is at the reconstructed energy of 60 TeV.

3.7.1 Dust Layer Events

The two most important parameters used to describe the optical properties of the ice are the absorption coefficient and the scattering coefficient. The absorption coefficient a describes the average travel distance of a photon before the absorption $(1/a)$, and the scattering coefficient b describes the average distance between the successive scatterings $(1/b)$ [69]. These two parameters of the glacial ice in which the IceCube detector is built, to first order change with the increase of the depth of the ice.

Figure 3.19 shows the depth dependence of the absorption (left) and the scattering (right) parameters. The black line comes from the SPICE LEA [98] [4] model which is used for the Monte Carlo simulations. Both parameters have a spike between a depth of 2000 m to 2050 m. The area around the spike is called the "dust layer". It is caused by the volcanic dust from the time that layer of the glacier was formed. Due to the short scattering

[4]SPICE LEA is the newer ice model compared to SPICE MIE. It has included the slight azimuthal dependence of the ice properties in the model which yields a better description of the calibration data compared to SPICE MIE.

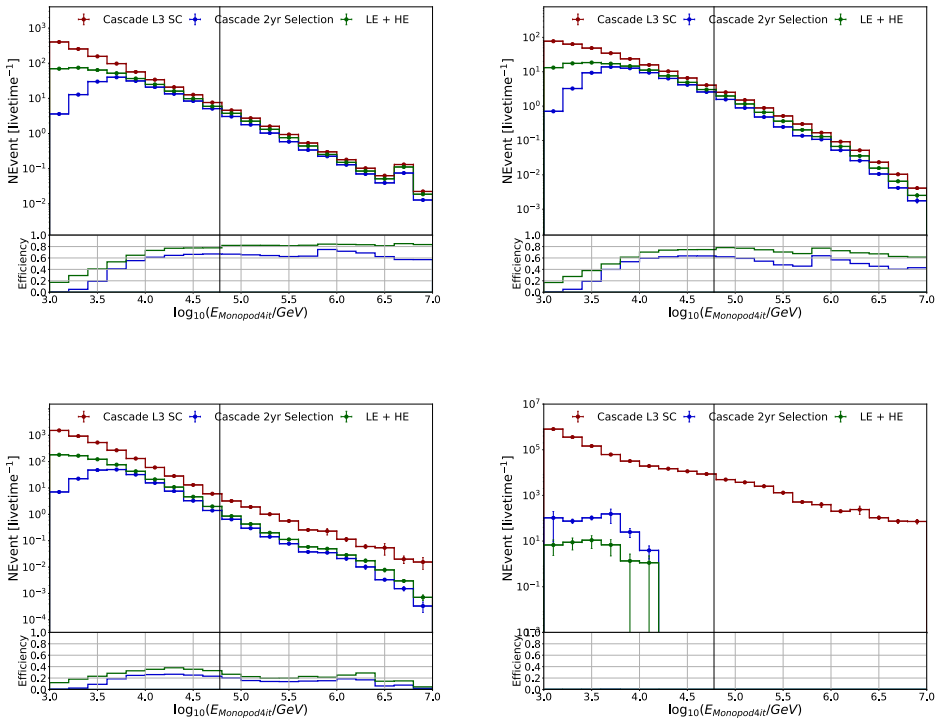

FIGURE 3.17: The rate of the final level of the LE + HE selection, the final level of the Cascade 2yr analysis selection and the cascade level3 single contained branch for the simulations in the Monopod reconstructed energy bins. Top left: ν_e, top right: ν_τ, bottom left: ν_μ, bottom right: cosmic-ray background (CORSIKA). The lower half of each plot is the passing rate of the two selections as a function of the reconstructed energy. The vertical black line is at the reconstructed energy of 60 TeV.

and absorption distance in the dust layer, the photons are less likely to reach the DOMs further away from the interaction vertex compared to the case when the same interaction was to happen in the clearer layer of the ice.

With the spike in the scattering and absorption coefficient, the reconstructed energy of the events located in the dust layer is biased when they are reconstructed using the Monopod reconstruction. The optical properties used in Monopod only correspond to those from clean ice. Therefore the dust layer region is almost always removed in other event selections. For example, the High Energy Starting Events (HESE) [56] is an analysis based on a veto-based event selection that uses the dust layer as the veto region to ensure the purity of the events located in the effective volume of the detector at the cost of a loss of some statistics from events located in the dust layer. One of the big advantages of the event selection developed in this dissertation is that it includes the dust layer in the effective volume without losing the background free feature in the high energy region. Keeping the dust layer significantly increases the signal efficiency in the high energy region. After unblinding, there are some interesting cascade events found in the final sample that are not in the HESE sample [57], [99], [100]. Among these events, there are five high-energy events located in the dust layer. The most energetic event is named

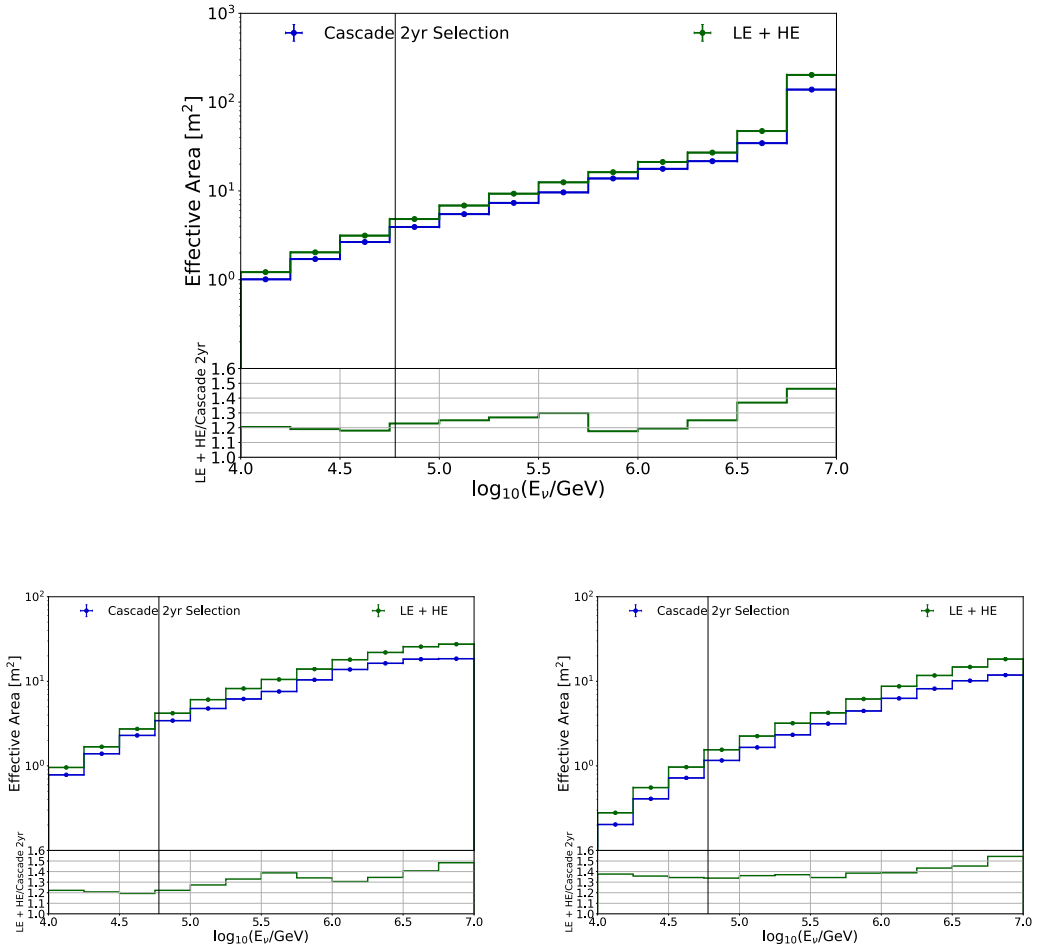

FIGURE 3.18: The effective area of ν_e (top), ν_τ (bottom left) andν_μ (bottom right) for the LE + HE selection, in comparison with the cascade 2yr analysis selection.

as "Eurus". It is an event detected on August 8$^{\text{th}}$, 2013 with RunID: 122819 and Event ID: 44356016. Some of its variables regarding the reconstructed energy are:

- Monopod_Z = - 82 m
- Monopod_Energy = 2.06×10^6 GeV
- Qtot_HLC = 2047 P.E.

As shown in the right plot of Fig. 3.20, in order for an event to get a reconstructed energy as 2 PeV, at least ten times more than 2000 P.E. of the total charge need to be observed by the DOMs if the event occurred in the clear part of the ice. In the dust layer, as shown in the left plot of Fig. 3.20, the total charges of the majority of the PeV events are around a few thousand P. E. in the region of -85m < Monopod_Z < -75m.

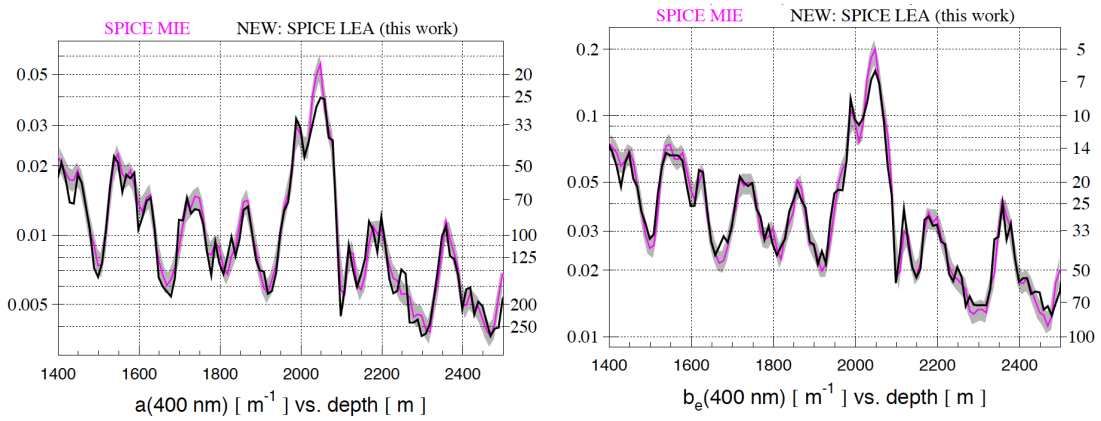

FIGURE 3.19: The depth dependence of the absorption (left) and scattering (right) parameters of the South Pole Ice. The parameters of two ice models are plotted: SPICE MIE [69] (magenta) and SPICE LEA [98] (black). The figure is from Ref [98].

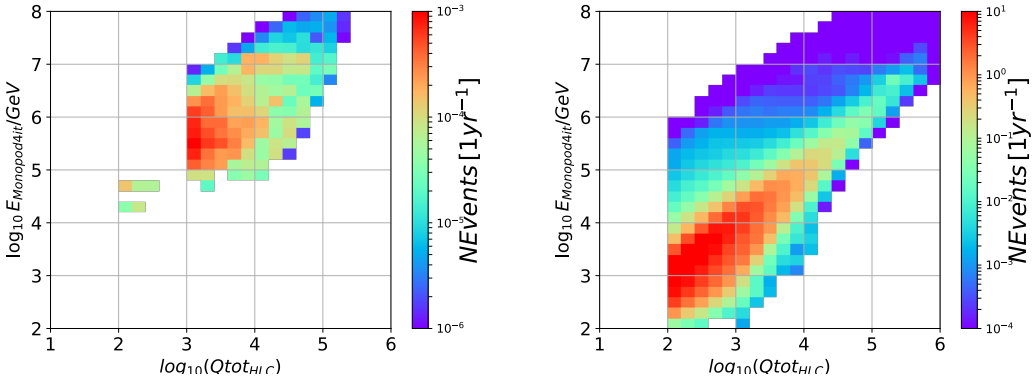

FIGURE 3.20: The Monopod reconstructed energy vs. the total charge for NuE simulation in the region of -85m < Monopod_Z < -75m (left) and in the whole detector (right).

The event display of "Eurus" is shown in Fig. 3.21 (top left). It is in comparison with the other three most energetic cascade events observed by IceCube so far: "Bert" (1.04 PeV), "Ernie" (1.14 PeV) [56], and "BigBird" (2.00 PeV) [57]. The interaction vertices of "Bert", "Ernie" and "BigBird" are outside of the dust layer; therefore, much more charges from these interactions are observed by the DOMs. In comparison, the total amount of observed charge for "Eurus" is much smaller due to the interaction vertex being located in the dust layer.

The center of the detector is located at 1950 m in depth. The Monopod reconstructed depth (Monopod_Z) is in the detector coordination system. This means the reconstructed interaction vertex of "Eurus" is located at the depth of around 2032 m. As shown in Fig. 3.19, it is in the region where the absorption length and the scattering length are much shorter than for the rest of the detector.

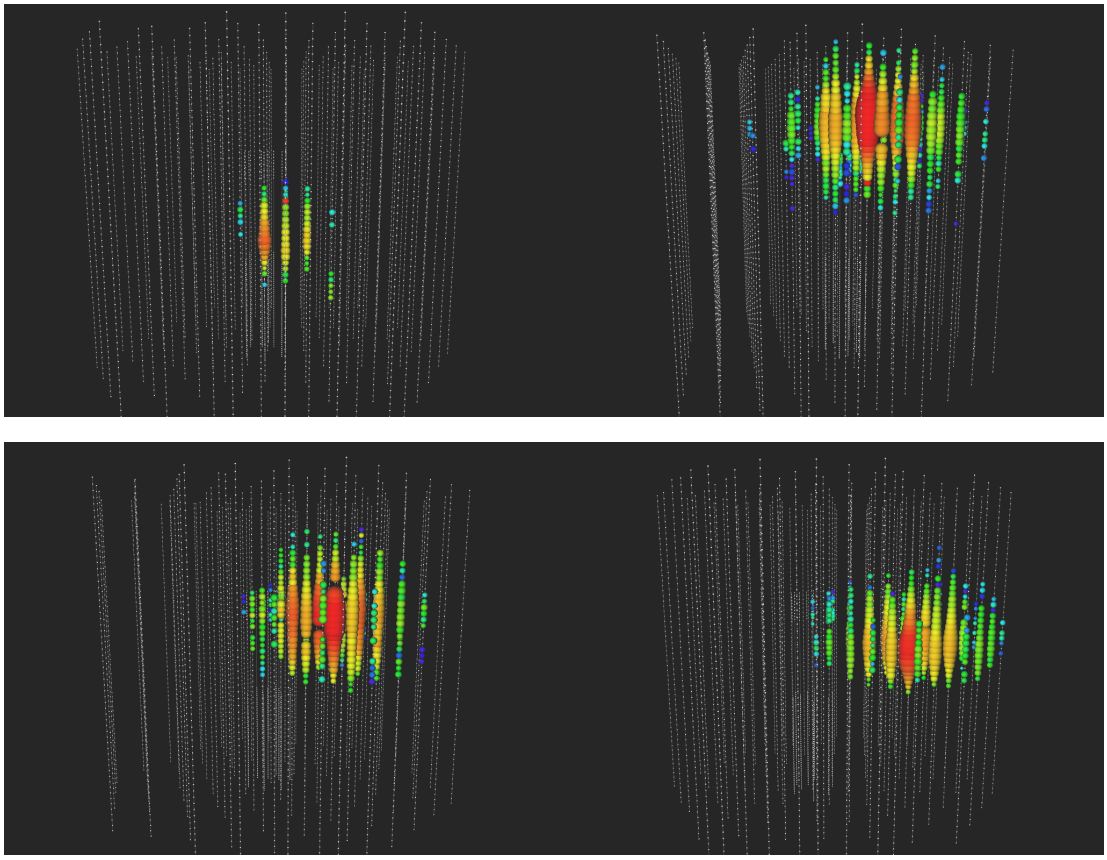

FIGURE 3.21: The event display of "Eurus" (top left), and "BigBird" (top right), "Bert" (bottom left), and "Ernie" (bottom right). Except for "Eurus", "BigBird", "Bert", and "Ernie" are located outside the dust layer with reconstructed energy of 2.00 PeV, 1.04 PeV, and 1.14 PeV respectively.

Since the dust layer region is $\sim 10\%$ of the whole detector, and the energy range of interest is at the high end, the standard simulation datasets do not provide enough statistics to study the energy resolution for these events. Therefore a dedicated simulation dataset is generated. This dataset is generated with the SPICE 3.2 ice model which is the newest generation of the ice model. The SPICE 3.2 model is fitted with more extensive LED ("Flasher") data. It uses a more refined method for adding corrections to the absorption and the scattering coefficients and provides a better description of the South Pole ice properties compared to the SPICE LEA model [98]. In this simulation, only electron neutrinos with neutrino energy of 500 TeV, 1 PeV, and 1.5 PeV are generated. The injection depths are set to -65 m, -70 m, -75 m, and -80 m. In Fig. 3.22, the resolution of this special simulation is plotted for different injection depths. As shown in the plot, the events in the dust layer have a $\sim 100\%$ bias in energy reconstruction. This means the deposited energy of 'Eurus' is overestimated by the Monopod reconstruction. To account for this bias and recover the true deposited energy, a machine learning algorithm called the *Gradient Boosted Decision Trees* (GBDT) has been used [101].

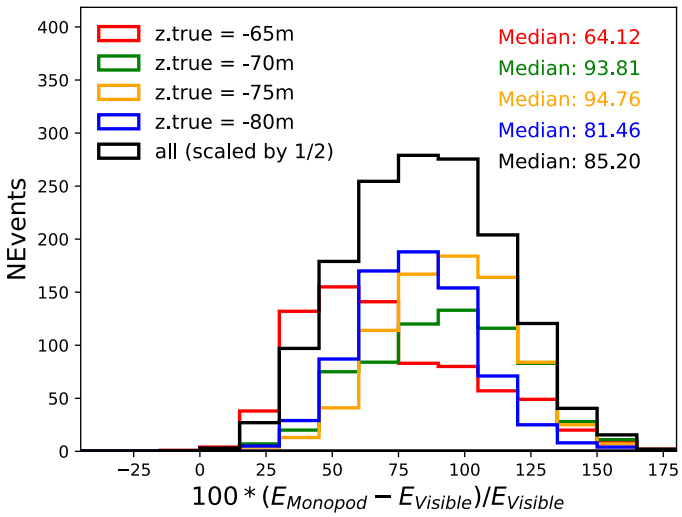

FIGURE 3.22: The energy resolution for the special NuE simulation injected at the different depths in the dust layer.

3.7.2 Dust Layer Events Energy Reconstruction using Gradient Boosted Decision Trees

Decision Tress - Regression

A regression task is to find a model $f(\mathbf{X})$ to estimate y when $\mathbf{X}$ is given. When solving such problems using decision trees, the variable space is partitioned into M different regions $R_1, R_2, ...R_M$, and in each region, a simple model (usually a constant) is fitted [102]. Then the model $f(\mathbf{X})$ can be expressed as

$$f(\mathbf{X}) = \sum_{m=1}^{M} c_m I(\mathbf{X} \in R_m), \tag{3.18}$$

where $I(\mathbf{X} \in R_m)$ is an indicator function which equals to 1 when $\mathbf{X} \in R_m$, otherwise it equals to 0.

A simple example of a 2D variable space partition is shown in Fig. 3.23. The variable space is first split at $X_2 = s_1$. The region of $X_2 < s_1$ is further split at $X_1 = s_2$: when $X_1 < s_2$, it's region R_1, otherwise it's region R_2. The region of $X_2 \geq s_1$ is further split at $X_1 = s_3$: when $X_1 \geq s_3$, the region is R_3, otherwise the region is split at $X_2 = s_4$: when $X_2 < s_4$, it's region R_4, otherwise it's region R_5. The partition of the variable space is shown in the left plot of Fig. 3.23. The right plot of Fig. 3.23 is the corresponding tree diagram of the partition. The testing data will go through the conditions on each tree node and be assigned to a certain tree leaf in the last layer. Each region is modeled with

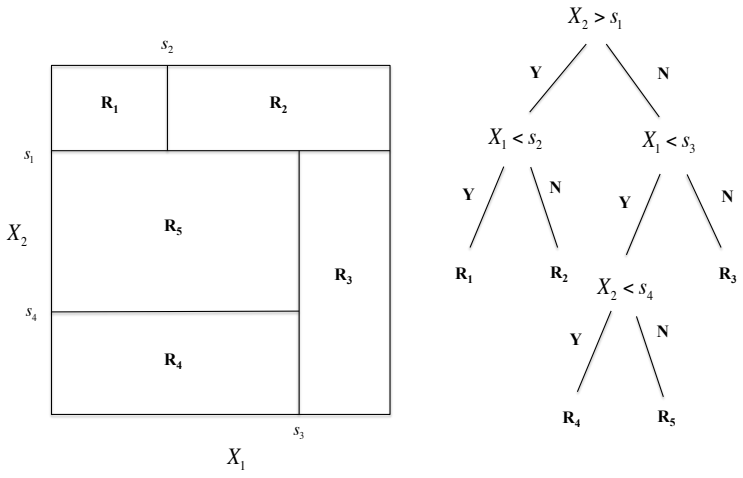

FIGURE 3.23: A demonstration of the decision tree algorithm. The left plot shows a partition of the variable space. The right plot shows the corresponding decision tree of the partition in the left plot.

a constant c_m which will be the y estimation of the testing data that are assigned to this region.

To build such a model, a training data set of N observations $(\mathbf{X}_i, y_i)$ is needed. The best way to estimate c_m is to minimize the sum of the squared errors:

$$\sum_{\mathbf{X}_i \in R_m} (y_i - f(\mathbf{X}_i))^2 \tag{3.19}$$

The solution to Eq. 3.19 is the average of y_i in region R_m

$$\hat{c}_m = \text{ave}(y_i | \mathbf{X}_i \in R_m) \tag{3.20}$$

At each node, a variable j and a threshold s are to be elected for the partition. The partition will split the space into two parts:

$$R_a(j, s) = \{\mathbf{X}_i | \mathbf{X}_{ij} < s\} \text{ and } R_b(j, s) = \{\mathbf{X}_i | \mathbf{X}_{ij} \geq s\} \tag{3.21}$$

j and s are chosen to minimize the sum squared error of both R_a and R_b after the split:

$$\sum_{\mathbf{X}_i \in R_a(j,s)} (y_i - \hat{c}_a)^2 + \sum_{\mathbf{X}_i \in R_b(j,s)} (y_i - \hat{c}_b)^2 \tag{3.22}$$

where $\hat{c}_a$ and $\hat{c}_b$ are estimated using Eq. 3.20.

Continuation of the partitioning will certainly reduce the sum squared error of the training sample. In the extreme case, each region would contain only one event, reducing the sum squared error to zero. However, this will lead to overfitting. The ultimate goal of training the decision tree is to perform classification/ regression on the testing sample. When the overfitting happens, the performance on the training sample is good but not on the testing sample. To prevent overfitting, some stopping rules of the partition are applied. The commonly seen stopping rules are the maximum depth of the tree, the minimum reducetion of the sum squared error, and the minimum data points on a leaf [102].

Gradient Boosted Decision Trees

Boosting is a powerful tool in machine learning which was first implemented as "AdaBoost" in Ref. [103]. It is an iterative procedure that combines multiple weighted "weak" trees to produce a "strong" output. In each iteration, the difference between the output of the previous tree and the target value will be compensated by the current tree. If a total number of M iterations is to be performed, the tree at m iteration is constructed as:

$$f_m(\mathbf{X}) = f_{m-1}(\mathbf{X}) + h_m(\mathbf{X}) \tag{3.23}$$

where $h(\mathbf{X})$ is fitted to the residual:

$$y - f_{m-1}(\mathbf{X}) \tag{3.24}$$

In the gradient boosting, the first tree is initialized to an optimal constant model that minimizes the loss function L [102]:

$$f_0(\mathbf{X}) = \arg\min_\gamma \sum_{i=1}^{N} L(y_i, \gamma), \tag{3.25}$$

where N is the size of the training sample.

At each iteration, $h_m(\mathbf{X}_i)$ is fitted to minimize the loss function:

$$f_m(\mathbf{X}) = f_{m-1}(\mathbf{X}) + \arg\min_{h_m \in \mathcal{H}} [\sum_{i=1}^{N} L(y_i, f_{m-1}(\mathbf{X}_i) + h_m(\mathbf{X}_i))]. \tag{3.26}$$

Computing h_m in each step of Eq. 3.26 is computationally expensive. Therefore it is calculated in the greedy fashion [104]: the steepest descent (the negative gradient) is used for the minimization. For every event, a *pseudo-residual* is calculated as:

$$r_{im} = -\left[\frac{\partial L(y_i, f(\mathbf{X}_i))}{\partial f(\mathbf{X}_i)}\right]_{f=f_{m-1}}. \tag{3.27}$$

A regression tree $h_m(\mathbf{X})$ is fitted to these *pseudo-residuals* using the training set $\{(\mathbf{X}_i, r_{im})\}_{i=1}^{n}$. In Ref. [105], a method of finding $h_m(\mathbf{X})$ is proposed. When the variable space is partitioned in to J_m regions at m iteration: $R_{jm}, j = 1, 2, ..., J_m$, $h_m(\mathbf{X})$ can be calculated using Eq. 3.18

$$h_m(\mathbf{X}) = \sum_{j=1}^{J_m} c_{jm} I(\mathbf{X} \in R_{jm}) \tag{3.28}$$

For each region R_{jm}, a weight of $h_m(\mathbf{X})$ is calculated as

$$\gamma_{jm} = \arg\min_{\gamma} \sum_{\mathbf{X}_i \in R_{jm}} L(y_i, f_{m-1}(\mathbf{X}_i) + \gamma c_{jm}). \tag{3.29}$$

Since γ_{jm} is the weight of h_m in region R_jm, c_{jm} can be merged to γ_{jm} by calculating γ_{jm} using the equation below:

$$\gamma_{jm} = \arg\min_{\gamma} \sum_{\mathbf{X}_i \in R_{jm}} L(y_i, f_{m-1}(\mathbf{X}_i) + \gamma). \tag{3.30}$$

Finally, we have

$$f_m(\mathbf{X}) = f_{m-1}(\mathbf{X}) + \sum_{j=1}^{J_m} \gamma_{jm} I(\mathbf{X} \in R_{jm}) \tag{3.31}$$

The total number of regions J determines the allowance of the interactions between the variables in the model. There are interactions between up to J-1 variables allowed, therefore when $J = 2$, no interactions between variables exist. Ref. [102] suggests that $4 \leq J \leq 8$ is usually a good choice for most of the boosting tasks and within the range, the choice of J has little effect on the result. The case when J is greater than 10 is rarely needed.

Apart from the stopping rules in the single decision tree, there are some other parameters in the boosted decision trees that can help prevent overfitting as well. One of them is the number of trees (iterations) M in the boosting process. With the increase of M, the value of the training sample's loss function will decrease, but this will also potentially lead to overfitting.

The "learning rate" of the process can also be used to prevent overfitting. The learning rate parameter l is add in Eq. 3.31, so that it becomes:

$$f_m(\mathbf{X}) = f_{m-1}(\mathbf{X}) + l \cdot \sum_{j=1}^{J_m} \gamma_{jm} I(\mathbf{X} \in R_{jm}) \tag{3.32}$$

Eq. 3.31 is equivalent to having $l = 1$. Typically having $l < 0.1$ can greatly improve the performance of the boosting method compare to the case where $l = 1$ [102]. However, to achieve such performance when having a relatively low learning rate, more iterations (larger M) will be needed. This will result in an increase of the computing time.

Dust Layer Events energy Reconstruction with XGBoost

The regression task in this chapter is to reconstruct the deposited (visible) energy of the events in the dust layer. To complete this regression task, certain variables ($\mathbf{X}$) need to be selected to feed the boosted decision trees (BDT). From Fig. 3.22, we know that even though for the dust layer events there is a bias between the Monopod reconstructed energy and the visible energy, they are still correlated. Therefore the monopod reconstructed energy is a good variable to feed the BDT. Since the problem starts with events being in the dust layer, it is obvious that the interaction vertex is important in this task. Events being in the different locations of the dust layer results in different biases between the Monopod reconstructed energy and the visible energy. This can be interpreted as the closer to the center of the dust layer the larger the bias, and the closer to the edge of the dust layer the smaller the bias. The total charge is also a major factor that could indicate the visible energy. As shown in Fig. 3.20, in both the dust layer region and the rest of the detector, there is a correlation between the total charge and the Monopod reconstructed energy. The difference is the correlation is different in the two regions. The last variable that could be of importance is the direction (zenith θ and azimuth ϕ) of the event.

In summary, the variables used in the regression BDT are:

- Monopod_Energy

- Monopod_X
- Monopod_Y
- Monopod_Z
- Qtot_HLC
- Monopod_Zenith

The implementation of the GBDT used in this analysis is XGBoost [101]. The loss function used in the boosting method is the *root mean square error* (rmse) which can be expressed as the equation below:

$$\sqrt{\frac{\sum_{i=i}^{N}(\hat{y}_i - y_i)^2}{N}}, \tag{3.33}$$

where N is the size of the training sample, $\hat{y}_i$ is the prediction value for sample i and y_i is the true value for sample i.

Some other settings of the GBDT are:

- Tree Depth: 5
- Number of Trees: 3000
- Minimum Loss Function Reduction: 0
- Minimum Data Points on a Leaf: 1
- Learning Rate: 0.1

To perform this regression task, an electron neutrino simulation dataset with SPICE 3.2, energy spectral index of -1.5 and the primary neutrino energy range of 5TeV - 10PeV has been produced. In total 7000 files were generated with each file containing 10000 events. This simulation set was processed to the final level of the event selection used in this analysis.

Since all the dust layer events are in the high energy region (the low energy event selection has an anti-dust-layer cut implemented [88]), only the simulated events with a Monopod reconstructed energy of above 10 TeV are selected in the training and testing process. A depth selection is also implemented by selecting simulated events for training and testing. The correlation between the training variables and the visible energy is different in the clear ice compared to the dust layer. With the thickness of the dust layer being $\sim 1/10$ of the clear ice, the majority of the events are located in the clear ice. Without the depth selection for the training and testing sample, the GBDT will be guided to find the correlation between the training variables and the visible energy in the clear ice instead of the dust layer. Therefore it is necessary to apply the depth cut in training/testing sample selection.

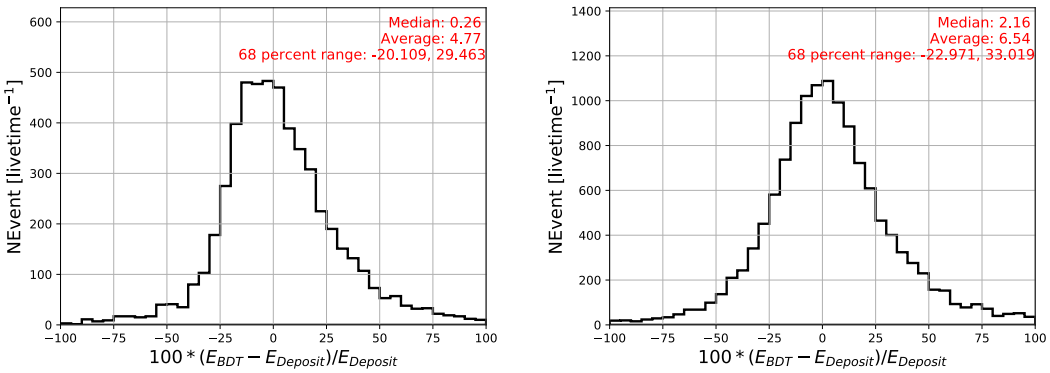

FIGURE 3.24: The energy resolution of the GBDT reconstructed energy: in the depth range from -60 m to -90 m (left), and in the depth range from -100 m to - 140 m (right). The median, average and 68 % confidence interval is labeled in the plot.

After the selection conditions are applied, 50% of the selected simulated events are randomly picked as the training sample and the rest are used for testing. For the simulated events, the visible energy is used as the regression target y. According to the depth distribution of the five dust layer events (as shown in Table. 3.12), two GBDTs are built: one for the regression task of events within the depth of -60 m to -90 m and the other for the regression task of events within the depth of -100 m and -140 m. The resolutions of the GBDT reconstructed energy on the testing sample for the two GBDTs are shown in Fig. 3.24. The bias of the GBDT reconstruction is less than 3%, which is a great improvement compared to the bias ($\sim$ 100%) of the monopod reconstructed energy shown in Fig. 3.22. The resolution (68 % confidence interval) of the GBDT reconstructed energy is around 20 % $\sim$ 30%, which is higher than the monopod energy resolution (15 %) of the cascade events in the clear ice [76]. Considering the difficulty of reconstructing the dust layer events, this energy resolution is acceptable.

The result of the GBDT reconstructed energy for the five most energetic dust layer events are shown in Table 3.12. Also shown are the reconstructed results from an alternative CPU intensive event reconstruction using the direct event re-simulation (Direct Fit) [106]. Direct Fit simulates events with different sets of energy, direction, vertex location, and returns as a result the one that is the most similar to the real event by comparing the likelihood described in Ref. [107]. One of the disadvantages of Direct Fit is that it is much more time consuming compared to GBDT. Once the GBDT is trained it can produce the test result for new data in O(1) time.

Table 3.12 shows that the reconstructed results by the two very different methods are consistent for all but one event ("Zephyrus"). This verified the effectiveness of the GBDT results.

Some investigations on "Zephyrus" are performed to understand the failure of its reconstruction with GBDT. Most of the variables used in the GBDT are the Monopod reconstructed result. The Monopod setting used in this analysis is the recommended setting by the collaboration and has been tested to provide good results. Furthermore,

Detector Year	Run ID Event ID	Name	Depth (in IceCube coordination system)	(Biased) Monopod Energy	GBDT Energy	Direct Fit Energy
2013	122819 44356016	Eurus	-82 m	2 PeV	$0.78\ \text{PeV}^{+0.20\ \text{PeV}}_{-0.17\ \text{PeV}}$	0.77 PeV
2012	122144 80391638	Campbell	-126 m	548 TeV	$0.49\ \text{PeV}^{+0.15\ \text{PeV}}_{-0.12\ \text{PeV}}$	0.47 PeV
2012	120730 25304985	Zephyrus	-75 m	473 TeV	$368\ \text{TeV}^{+92\ \text{TeV}}_{-83\ \text{TeV}}$	186 TeV
2011	118432 67932074	Ophelia	-118 m	235 TeV	$174\ \text{TeV}^{+52\ \text{TeV}}_{-43\ \text{TeV}}$	157 TeV
2014	125741 1771788	Bob	-118 m	178 TeV	$158\ \text{TeV}^{+47\ \text{TeV}}_{-39\ \text{TeV}}$	126 TeV

TABLE 3.12: The depth, monopod reconstructed energy, GBDT energy and the direct fit energy of the five most energetic dust layer events. The uncertainty of the Direct Fit reconstructed energy is $\sim 15\%$.

the reconstructed result should not depend on the setting of the reconstruction method. A few tests were run with different settings. Some of the test results show consistency with the Direct Fit result. This suggests that this event probably has some features that make it sensitive to the reconstruction settings. In this case, the reconstruction result of Direct Fit is likely to be more trustworthy. Therefore the reconstructed result of the Direct Fit is used for the five dust layer events in this analysis.

In each energy bin, the sample is separated into two groups: the down-going group and the up-going group. This separation is done on the reconstructed zenith angle. If the reconstructed zenith angle of an event is smaller than 90 degrees, it is considered down-going, otherwise up-going. As shown in Fig. 3.25, the bias in the monopod zenith reconstruction of the dust layer events is small, and the resolution (spread) is relatively large. However, the zenith bin size used in this analysis is 90 degree which is larger than the zenith resolution even for the dust layer events.

To study this point, the monopod reconstructed direction and the direct fit reconstructed direction for the five most energetic dust layer data events and their energy bin allocation is shown in Table 3.13. Three of the five events have the same reconstructed direction (up or down) using the Monopod reconstruction and the Direct Fit reconstruction. The two events that have the opposite reconstructed direction from the methods belong to the same energy bin and the opposite zenith bins. The means the event distribution in the reconstructed energy and zenith 2-D grids are the same when using the Monopod

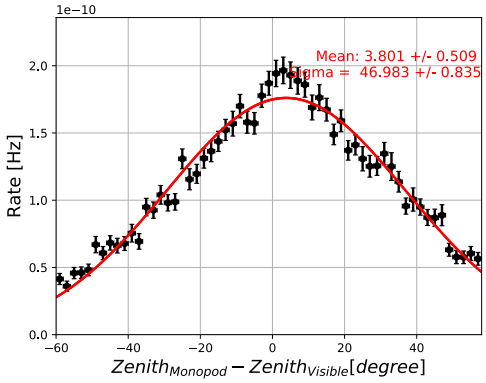

FIGURE 3.25: The Monopod zenith resolution calculated using the ν_e simulation in the above 100 TeV reconstructed energy range, within the depth of [-60 m, -140m].

reconstruction and the Direct Fit reconstruction, therefore the choice of the reconstruction method will not affect the result of this analysis.

Name	Energy Bin [log(E/GeV)]	Monopod Direction	Direct Fit Direction
Eurus	5.4-6.2	Up	Up
Campbell	5.4-6.2	Down	Down
Zephyrus	4.6-5.4	Down	Down
Ophelia	4.6-5.4	Down	Up
Bob	4.6-5.4	Up	Down

TABLE 3.13: The energy bin and the directional reconstruction result from the Monopod reconstruction and the Direction Fit reconstruction of the dust layer events. The binning in the reconstructed energy will be discussed in Chapter 4.

The energy reconstruction using the Direct Fit is only performed on the dust layer events in the final experimental data sample, but not on the simulation sample. This is because the information on the simulation datasets used in this analysis is in the unfolding process (c.f. Chapter 5). In this process, all events in a particular energy and zenith bin are used regardless of their interaction position. Even though the Monopod reconstructed energies of the dust layer events are biased (as shown in Fig. 3.26), the amount of the dust layer events is much smaller compare to the total number of events in the whole detector. The resolution of the Monopod reconstructed energy for the whole detector is shown in the right plot of Fig. 3.26. The bias in the Monopod reconstructed energy for the whole detector is almost zero and the uncertainty of the reconstruction is also much smaller than the uncertainty in the Monopod reconstruction for the dust layer events [5].

[5]The reason for the existence of the $\sim$ 5% bias is not related to the dust layer events but rather the mismatch between the hole ice model used in the simulation and the Monopod reconstruction. The hole ice model used in the simulation is the Hole Ice 30 (scattering length of 30 cm) which is closer to the experimental data than the Hole Ice 50 (scattering length of 50 cm) (c.f. Sec. 6.1.1). With better

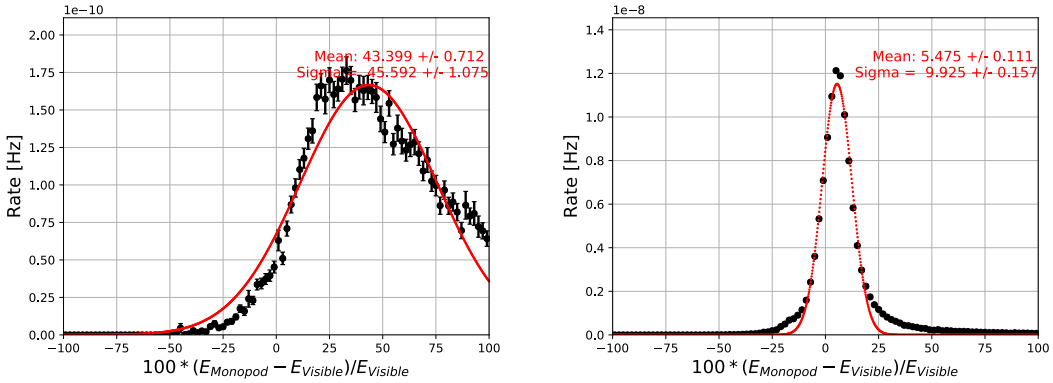

FIGURE 3.26: The energy resolution of the monopod reconstructed energy in the dust layer region (left) and the whole detector (right). Both Plots are made with events above 100 TeV Monopod reconstructed energy from NuE simulation.

Therefore when calculating the unfold matrix, the bias effect from the dust layer events is negligible.

While the dust layer events contribute little to the total number of events in the simulation, the situation is slightly different in the experimental data. For example, in the energy bin of $[10^{5.4}, 10^{6.2}]$ (see Chapter 4 for the detail on the binning), there are four events in total in the unblinded sample with two inside of the dust layer and two outside. The contribution of the dust layer events at high energy is not negligible in the experimental data, therefore it is necessary to correct the bias in the Monopod reconstructed energy of the dust layer events in the experimental data. Even though the data has a higher contribution from the dust layer events, this is not completely unexpected. Figure 3.27 shows the Monopod reconstructed depth distribution of the unblinded sample and the simulation for the reconstructed energy range above 100 TeV. In the dust layer region, the event rate of the experimental data is higher than the simulation, however, it is still within a 1 σ uncertainty. The higher contribution from the dust layer events in the final data sample is likely to be a statistical fluctuation instead of a mismatch between the data and the simulation.

3.7.3 Final Level Contained Cascade Five Years Data Sample Statistic

The final sample used in this analysis consists of two parts:

- The 2012-2015 data unblinded with the high energy event selection developed in this analysis and the low energy event selection developed in Ref. [88], merged at the reconstructed energy of 60 TeV

understanding of the South Pole ice, the simulation has been updated to Hole Ice 30 but the table used in the Monopod reconstruction has yet to be updated from the Hole Ice 50 ice model.

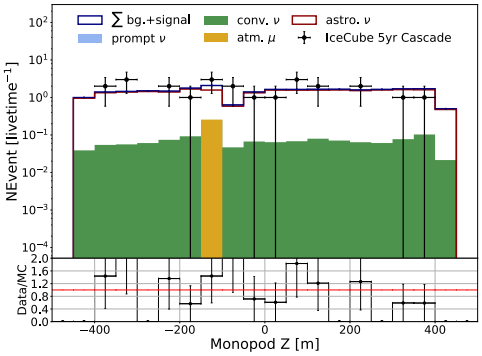

FIGURE 3.27: The Monopod reconstructed depth distribution of the unblinded sample and the simulation for above 100 TeV reconstructed energy.

- The 2011 data unblinded with the event selection developed by the previous two-year contained cascade analysis [87]

After unblinding, the data and simulation statistics in all the reconstructed energy bins (with the correction of the dust layer events in the data sample as discussed in the previous section) used in this analysis are shown in Table 3.14 (the reconstructed down-going sample) and Table 3.15 (the reconstructed up-going sample). The astrophysical neutrino flux index, normalization, and the atmospherical neutrino flux normalization used to in the calculation of the neutrino simulation statistics are from Ref. [88], which utilized the same event sample as in this analysis. The values are shown below:

- Astrophysical neutrino flux index: -2.5,
- Astrophysical neutrino flux normalization: 1.59,
- Conventional atmospherical neutrino flux normalization: 1.05,
- Prompt atmospherical neutrino flux normalization: 9.66 $\times 10^{-}5$

The background estimation is done using the MuonGun simulation [65] (c.f. Sec. 2.5).

The event distribution in the reconstructed energy and zenith for the unblinded data and the simulation at the final level are shown in Fig. 3.28. The top plot is the reconstructed energy distribution for all the events, with the four bins of the measurement result indicated by the dashed lines. The bottom plot is the reconstructed zenith distribution for all the events with the reconstructed energy above $10^{3.8}$ GeV. These two plots show a good data/MC agreement for the variables (the reconstructed energy and zenith) used in this analysis.

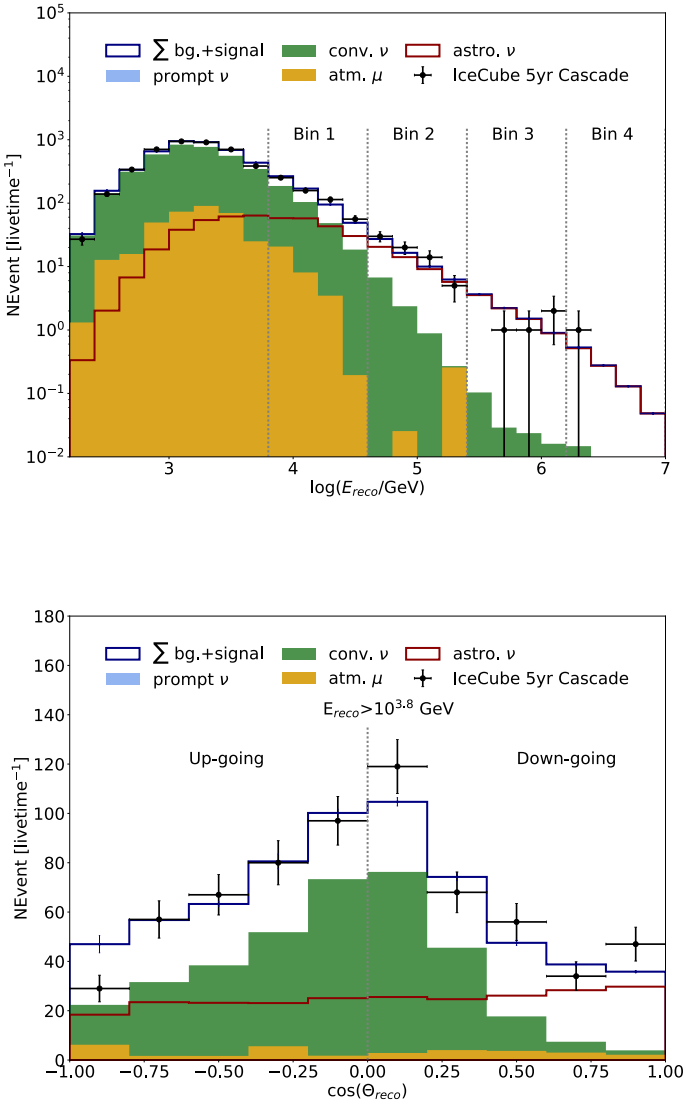

FIGURE 3.28: The reconstructed energy (top) and zenith (bottom) distribution for the unblinded data and the simulation at the final level. The bottom plot only includes the events with the reconstructed energy greater than $10^{3.8}$ GeV.

Energy Range [log(E_{reco}/GeV)]	2.2 - 3.0	3.0 - 3.8	3.8 - 4.6	4.6 - 5.4	5.4 - 6.2	6.2 - 7.0
Data	256	942	274	46	3	1
MuonGun	41(8)	129(17)	16(2)	0	0	0
NuMu (conv)	124(4)	478(9)	106(2)	3.2(1)	0.08(2)	0.006(3)
NuE (conv)	51(1)	183(1)	39.8(1)	1.482(6)	0.0217(2)	1.26(3)e-4
NuMu (astro)	0.43(1)	7.02(6)	10.40(5)	2.75(2)	0.504(7)	0.066(2)
NuE (astro)	1.79(2)	33.5(1)	52.31(6)	17.08(3)	3.48(1)	0.98(1)
NuTau (astro)	1.34(3)	23.8(1)	35.4(1)	10.44(4)	1.72(1)	0.174(3)
NuMu (prompt)	6.7(2)e-6	7.16(9)e-5	5.20(6)e-5	6.3(2)e-6	4.1(3)e-7	3.9(9)e-8
NuE (prompt)	3.14(4)e-5	5.01(2)e-4	4.870(7)e-4	7.35(2)e-5	4.33(2)e-6	1.70(3)e-7
Sum MC	220(9)	854(19)	260(3)	35.0(1)	5.81(2)	1.23(1)

TABLE 3.14: The number of the down-going events for all the reconstructed energy bins for the unblinded data and simulation at the final level. The Monopod reconstructed energy is used for all the simulation and data events except for the dust layer events in the experimental data, in which case the Direct Fit reconstructed energy is used.

Energy Range [log(E_{reco}/GeV)]	2.2 - 3.0	3.0 - 3.8	3.8 - 4.6	4.6 - 5.4	5.4 - 6.2	6.2 - 7.0
Data	954	1997	306	23	1	0
MuonGun	38(7)	130(18)	17(4)	0.3(2)	0	0
NuMu (conv)	717(10)	1471(13)	164(2)	4.1(1)	0.048(5)	0.014(8)
NuE (conv)	182(1)	381(1)	47.6(1)	1.486(5)	0.0196(1)	1.22(4)e-4
NuMu (astro)	3.10(4)	17.3(1)	9.15(7)	1.66(2)	0.236(7)	0.031(2)
NuE (astro)	12.07(6)	79.0(2)	49.18(6)	10.92(2)	1.507(6)	0.215(5)
NuTau (astro)	9.06(9)	57.2(3)	33.0(1)	6.72(5)	0.81(1)	0.081(3)
NuMu (prompt)	5.74(8)e-5	3.14(2)e-4	1.34(1)e-4	1.36(2)e-5	5.5(3)e-7	4(1)e-8
NuE (prompt)	2.20(1)e-4	1.483(3)e-3	8.39(1)e-4	1.236(3)e-4	6.08(3)e-6	1.68(2)e-7
Sum MC	961(12)	2136(22)	320(4)	25.2(2)	2.62(1)	0.34(1)

TABLE 3.15: The number of the up-going events for all the reconstructed energy bins for the unblinded data and the simulation at the final level. The Monopod reconstructed energy is used for all the simulation and data events except for the dust layer events in the experimental data, in which case the Direct Fit reconstructed energy is used.

Chapter 4

Analysis Method

In this dissertation, we introduce a novel analysis method developed to measure flux independent neutrino interaction cross section [108]. The method utilizes the Earth absorption effect to measure the cross section. The schematic of the analysis method is shown in Fig. 4.1. The neutrino sample is divided into two groups: down-going and up-going. With the increase of neutrino energy and interaction cross section, more up-going neutrinos are absorbed by the Earth while the down-going neutrinos remain unaffected. By calculating the ratio of the down-going neutrinos to the up-going neutrinos in each neutrino energy bin, the corresponding neutrino interaction cross section can be calculated. The idea was first brought up by D. Hooper in Ref. [108], as a theoretical calculation without taking into consideration reconstruction and detector effects. In this chapter, we will discuss the analysis method in detail, and show how to realize the experimental measurement from a theoretical idea.

4.1 An Overview of the Analysis Method

IceCube detects neutrinos from all directions. The neutrinos from the southern hemisphere (down-going) directly reach the detector. The number of the down-going neutrino events detected in IceCube can be expressed as

$$N(E_\nu, down) = \Phi_{down}(E_\nu) \times Acpt_{down}(E_\nu) \times \sigma(E_\nu) \times A^{3/2} \times n \tag{4.1}$$

where $\Phi_{down}(E_\nu)$ is the neutrino flux from the Southern hemisphere, $Acpt_{down}(E_\nu)$ is the detector acceptance rate for the down-going events, $\sigma(E_\nu)$ is the neutrino interaction cross section, A is the neutrino effective area and n is the density of the targets that can interact with a neutrino.

The neutrinos from the Northern hemisphere (up-going) travel through the Earth. When the neutrinos pass through matter with density n_E, the interaction length can be calculated using the formula below [108]:

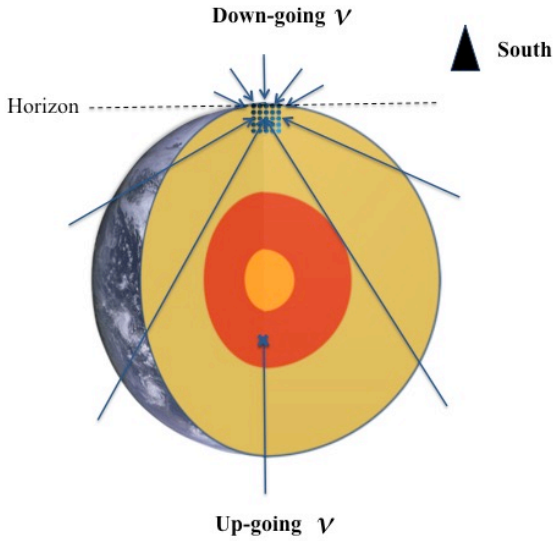

FIGURE 4.1: The schematic of the analysis method to measure the neutrino interaction cross section.

$$l = (\sigma(E_\nu) \times n_E)^{-1} \tag{4.2}$$

When the interaction length is smaller than the distance that a neutrino needs to travel to reach the detector, the neutrino will be absorbed by the Earth before it can reach the detector. The number of the up-going neutrino events detected in IceCube can be expressed as:

$$N(E_\nu, up) = \Phi_{up}(E_\nu) \times Acpt_{up}(E_\nu) \times (1 - Absp(\sigma(E_\nu))) \times \sigma(E_\nu) \times A^{3/2} \times n \tag{4.3}$$

where $\Phi_{up}(E_\nu)$ is the neutrino flux from the northern hemisphere, $Acpt_{up}(E_\nu)$ is the detector acceptance rate for the up-going events, and $Absp(\sigma(E_\nu))$ is the fraction of the up-going neutrinos absorbed by the Earth.

In this analysis, we form a ratio of the number of down-going events to the number of up-going events:

$$\begin{aligned} R(E_\nu) &= \frac{N(E_\nu, down)}{N(E_\nu, up)} \\ &= \frac{\Phi_{down}(E_\nu) \times Acpt_{down}(E_\nu) \times \sigma(E_\nu) \times A^{3/2} \times n}{\Phi_{up}(E_\nu) \times Acpt_{up}(E_\nu) \times (1 - Absp(\sigma(E_\nu))) \times \sigma(E_\nu) \times A^{3/2} \times n} \end{aligned} \tag{4.4}$$

$\sigma(E_\nu)$, A and n are the same in the denominator and the numerator, thus canceled out. The neutrino flux is a combination of the atmospheric flux and the astrophysical flux. The conventional part of the atmospheric neutrino flux is produced by charged pion and kaon decays and is modeled with HKKMS06 [28]. The prompt part of the atmospheric neutrino flux is produced by heavier meson decays and is modeled by BERSS [29]. The conventional atmospheric neutrino flux is symmetric around the horizon ($\theta = 90°$). The prompt atmospheric neutrino flux is isotropic. Fig. 4.2 shows the zenith distribution of the atmospheric neutrino flux for neutrino energy of 10 TeV. We assume that the astrophysical neutrino flux is isotropic as well since current data does not indicate is it anisotropic [88].

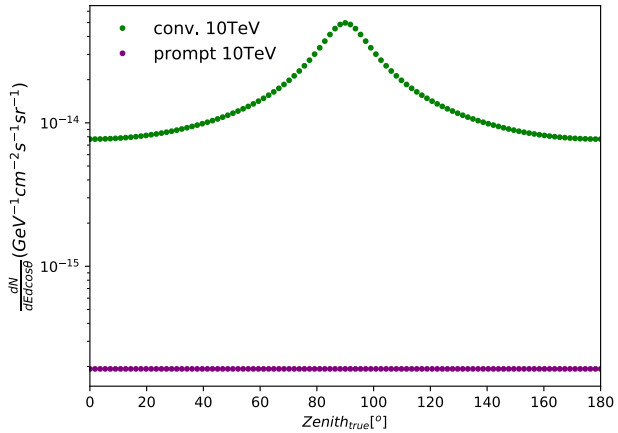

FIGURE 4.2: The zenith angle dependence of the atmospheric neutrino flux at 10 TeV neutrino energy.

With the isotropic astrophysical neutrino flux assumption, the flux of the down-going neutrinos and the up-going neutrinos are the same ($\Phi_{down}(E_\nu) = \Phi_{up}(E_\nu)$). The ratio of the number of the down-going events to the number of the up-going events then becomes:

$$R(E_\nu) = \frac{N(E_\nu, down)}{N(E_\nu, up)} = \frac{Acpt_{down}(E_\nu)}{Acpt_{up}(E_\nu) \times (1 - Absp(\sigma(E_\nu)))} \tag{4.5}$$

Once the ratio is corrected for the detector acceptance effect (c.f. Sec. 4.3.1), the ratio only depends on the neutrino interaction cross section.

The neutrino interaction cross section, neutrino energy and the ratio of down-going events to up-going events have the relationship shown in Fig. 4.3. In the experiment, we reconstruct the deposited energy and zenith angle of the neutrinos. The mapping between the reconstructed energy and the true neutrino energy, the reconstructed zenith angle and the true zenith angle using the unfolding method is discussed in detail in the next chapter. After the mapping, neutrino events are assigned in neutrino energy bins. In each neutrino energy bin, they are separated into two groups according to their true zenith angle: down-going and up-going. In each neutrino energy bin, the ratio $R(E_\nu)$ of the down-going events to the up-going events is calculated. Thus we are able to obtain the

relationship between the ratio dependence on the neutrino energy, which is shown as the green curve in Fig. 4.3.

The ratio ($R(\sigma)$) increases with the increase in the interaction cross section; the higher the cross section, the shorter the interaction length, the more events get absorbed by the Earth. The relationship between the ratio and the cross section can be obtained by using Monte Carlo simulations (c.f. Sec. 4.2) and is shown as the purple curve in Fig. 4.3.

From the two projections $R(E_\nu)$ and $R(\sigma)$ on a 3D curve, we can construct the third projection $\sigma(E_\nu)$ which is shown as the red curve in Fig. 4.3.

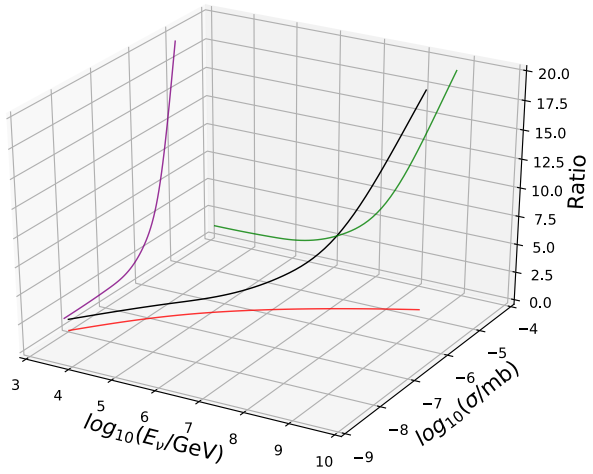

FIGURE 4.3: A simplified illustration of the correlation among the neutrino energy, the down-going events/up-going events ratio and the neutrino interaction cross section. The green curve represents the ratio vs. the neutrino energy, the purple curve represents the ratio vs. the cross section, and the red curve represents the goal of this analysis: the cross section vs. the neutrino energy.

4.2 Ratio Versus Cross Section

All-sky neutrinos of all flavors are simulated with the total DIS (charged-current interactions and neutral current interactions [1])cross section range from 10^{-9} mb to 10^{-4} mb using NuGen [82]. The Earth density model used in the simulation is PREM [84]. No detector effects are included in this simulation, therefore the only factor that contributes to the difference between the number of the down-going events and the number of the up-going events is the cross section. The simulated events are grouped in cross section bins with a bin size of 0.2 in logarithm space $-9 < \log_{10}(\sigma/\text{mb}) < -4$. In each cross section bin, the events are divided into two groups: down-going and up-going. The ratio of down-going events to up-going events in each cross section bin is calculated and a spline

[1] The ratio vs. cross section curve generated with neutrino-nucleon DIS interaction simulations reflects the Earth absorption effect of nucleon targets. The same curve can also be used to measure the total cross section (including the $\bar{\nu}_e e$ scattering (Glashow Resonance) cross section) with a scaling factor for the target density. (c.f. Sec. 7.4.1)

fit is applied to create a smooth curve connecting all the data points, as shown in Fig. 4.4. In this process, no relationship between the cross section and the neutrino energy is assumed, thus no bias is introduced when using the ratio vs. cross section curve.

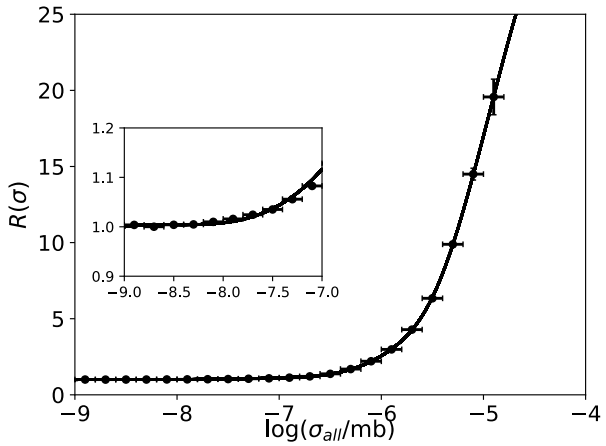

FIGURE 4.4: The ratio of the down-going events to the up-going events vs. the cross section.

4.3 Ratio Versus Neutrino Energy

4.3.1 Detector Acceptance Effect Correction Factor

As seen in Eq. 4.5, the ratio of the down-going events to the up-going events also depends on the detector acceptance. The difference between the acceptance rate for the down-going events and the up-going events is due to the self-veto effect [109], [93] and the difference in the selection efficiency. The self-veto effect means an atmospheric neutrino will be removed from the analysis since it is accompanied by a muon produced from the same cosmic ray shower. The effect only exists in the down-going atmospheric neutrinos, since all the up-going atmospheric muons will get absorbed by the Earth.

To correct for these effects, we introduce the correction factor, which is calculated as the acceptance rate for the up-going events divided by the acceptance rate for the down-going events:

$$CF(E_\nu) \equiv \frac{Acpt_{up}(E_\nu)}{Acpt_{down}(E_\nu)}, \tag{4.6}$$

where the acceptance rates are calculated as the number of events for a certain direction at the final level divided by the number of events at the generated level without any detector effects for that direction:

$$Acpt_{up}(E_\nu) = \frac{NEvents(E_\nu, up, final)}{NEvents(E_\nu, up, gen)} \tag{4.7}$$

$$Acpt_{down}(E_\nu) = \frac{NEvents(E_\nu, down, final)}{NEvents(E_\nu, down, gen)} \tag{4.8}$$

The upper part of Fig. 4.5 shows the neutrino energy distribution for the down-going events and the up-going events at the generated level and at the final level. Both astrophysical neutrino flux and the atmospheric neutrino flux are included. The lower part of Fig. 4.5 shows the acceptance rates for down-going and up-going events calculated using Eq. 4.8 and Eq. 4.7.

With the acceptance rates, the correction factors (CFs) are calculated using Eq. 4.6 and listed in Table 4.1.

After applying the correction factor, Eq. 4.5 becomes:

$$R(E_\nu) = \frac{N(E_\nu, down)}{N(E_\nu, up)} \times CF(E_\nu) = \frac{1}{1 - Absp(\sigma(E_\nu))} \tag{4.9}$$

This ratio only reflects the Earth absorption effect and is used for the cross section determination.

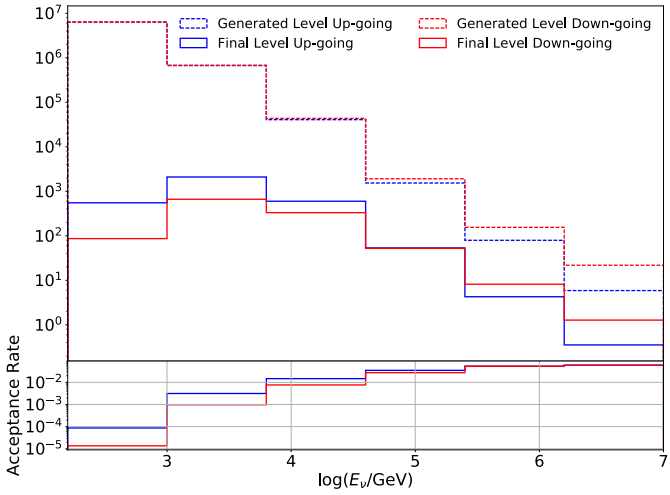

FIGURE 4.5: Upper part: the neutrino energy distribution for the down-going events and the up-going at the generated level and at the final level. Lower part: the detector acceptance rate for the down-going events and the up-going events in neutrino energy bins.

$log_{10}(E_\nu/GeV)$	2.2-3.0	3.0-3.8	3.8-4.6	4.6-5.4	5.4-6.2	6.2-7.0
Correction Factor	6.395	3.219	1.928	1.278	1.024	1.026

TABLE 4.1: The detector acceptance correction factors for all the neutrino energy bins.

4.3.2 Ratio Versus Neutrino Energy for Asimov Data

Using the neutrino energy distribution [2] for down-going and up-going events, the correction factor and Eq. 4.9, the ratio in neutrino energy bins can be calculated.

Asimov data [110] is the distribution according to the Monte Carlo expectation. The expectation for $N(E_\nu, down)$ and $N(E_\nu, up)$ was calculated using the simulation and a livetime of 5 years. We use the following astrophysical neutrino flux:

$$\Phi_{astro} = \Phi_0 \times (E_\nu/100 \text{ TeV})^{-\gamma}, \tag{4.10}$$

where $\Phi_0 = 1.59 \times 10^{-18}$ GeV^{-1}s^{-1}sr^{-1}cm^{-2} and γ=2.50. The normalization and spectral index are the best fit result from Ref. [88].

The ratio $R(E_\nu)$ from Asimov data is shown in Fig. 4.6.

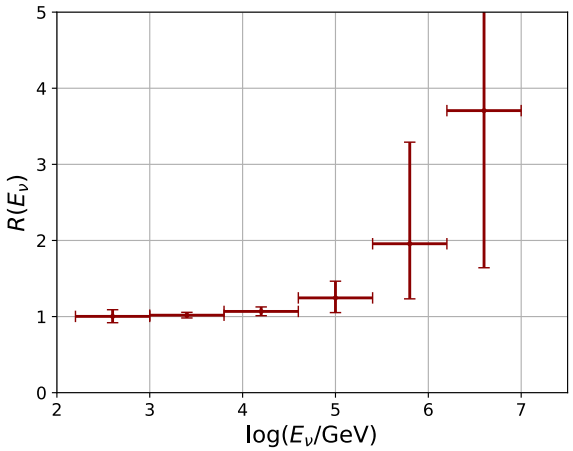

FIGURE 4.6: Ratio vs. neutrino energy for Asimov data (5 years of livetime).

4.4 Cross Section Versus Neutrino Energy

4.4.1 Cross Section vs. Neutrino Energy for Asimov Data

We use the ratio $R(E_\nu)$ from Asimov data (as shown in Fig. 4.6) to find the corresponding cross section $\sigma(E_\nu)$ according to Fig. 4.4. The cross section vs. the neutrino energy

[2] The mapping from the reconstructed space to the true space see Chapter 5

$log_{10}(E_\nu/GeV)$	2.2-3.0	3.0-3.8	3.8-4.6	4.6-5.4	5.4-6.2	6.2-7.0
Bin Center Value	$2.826^{+0.001}_{-0.001}$	$3.446^{+0.002}_{-0.002}$	$4.133^{+0.004}_{-0.006}$	$4.916^{+0.011}_{-0.015}$	$5.734^{+0.001}_{-0.017}$	$6.513^{+0.010}_{-0.015}$

TABLE 4.2: The weighted bin centers.

correlation for Asimov data is shown in Fig. 4.7.

As shown in Fig. 4.4, for small values of cross section, the Earth absorption effect is negligible. Therefore, below a certain cross section value, the ratio will always be 1, implying no up-going neutrinos are absorbed by the Earth. As a result, there are an equal number of events in the down-going and the up-going region. Here, the method reaches its limit. The ratio for the first neutrino energy bin (150 GeV to 1 TeV) in Fig. 4.6 is close to 1. For the above reasons, the ratio in the first bin is not informative. As a result, it is omitted in Fig. 4.7.

The bin centers chosen for the data points display in Fig. 4.7 are the weighted average neutrino energy for all the events in the neutrino energy range. It is calculated as:

$$E_{center} = \frac{\sum_j E_j \times W_j}{\sum_j W_j} \tag{4.11}$$

The weighted bin centers and their uncertainties are shown in Table 4.2. Here the best fit value is calculated using the fit result of the astrophysical flux in Fig. 6.18 (left) alongside the atmospheric flux. The statistical uncertainty is associated with the 68% C. L. contour of the astrophysical flux shown in Fig. 6.18 (left).

Asimov data is the expectation from Monte Carlo simulation which is simulated using the CSMS [62] cross section. Fig. 4.7 shows that the measured neutrino energy dependence of the neutrino cross section is consistent with the CSMS cross section.

4.4.2 Neutrino to Antineutrino Ratio

There are two components of the neutrino flux: the astrophysical component and the atmospheric component. The astrophysical flux is the same for neutrinos and antineutrinos, and the same for all neutrino flavors (assuming a (1:1:1) flavor ratio at Earth). The atmospheric flux is different for neutrinos and antineutrinos. It is also different for ν_e and ν_μ. The compositions of the two components are different due to the difference in the selection efficiencies for different neutrino flavors. For the same neutrino flavor, the selection efficiency is the same for neutrinos and antineutrinos.

The selection efficiency for a given neutrino flavor is defined as:

$$f_{\nu_i}(E_\nu) = \frac{NEvents_{final,\nu_i}(E_\nu)}{NEvents_{gen,\nu_i}(E_\nu)} \tag{4.12}$$

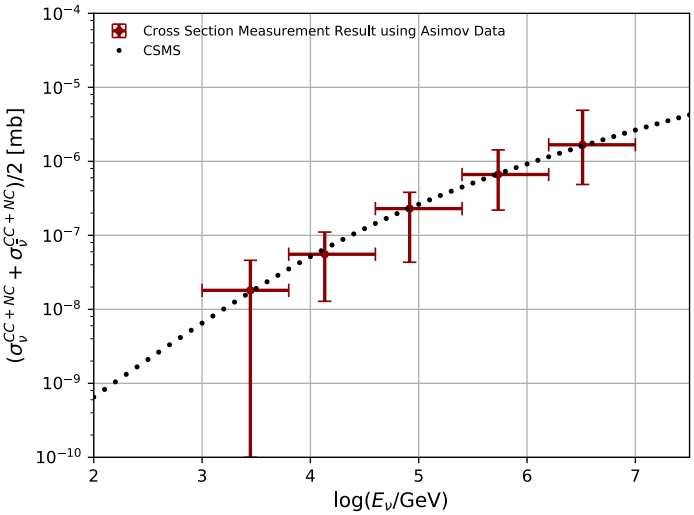

FIGURE 4.7: Cross section vs. neutrino energy for Asimov data (5 years of livetime).

where

$$
\begin{aligned}
&NEvents_{gen,\nu_i}(E_\nu) = \\
&\sigma_\nu(E_\nu) \times 2\pi \int_{-1}^{1} [d\Phi_{\nu,astro}(E_\nu)/dE_\nu + d\Phi_{\nu_i,atm}(E_\nu,\theta_\nu)/dE_\nu] dcos(\theta_\nu) + \\
&\sigma_{\bar{\nu}}(E_\nu) \times 2\pi \int_{-1}^{1} [d\Phi_{\nu,astro}(E_\nu)/dE_\nu + d\Phi_{\bar{\nu}_i,atm}(E_\nu,\theta_\nu))/dE_\nu] dcos(\theta_\nu)
\end{aligned}
\tag{4.13}
$$

is the number of events for that neutrino flavor at the generated level. The number of events for that neutrino flavor at the final level can be expressed as:

$$
\begin{aligned}
&NEvents_{final,\nu_i}(E_\nu) = \\
&f_{\nu_i}(E_\nu) \times \{\sigma_\nu(E_\nu) \times 2\pi \int_{-1}^{1} [d\Phi_{\nu,astro}(E_\nu)/dE_\nu + d\Phi_{\nu_i,atm}(E_\nu,\theta_\nu)/dE_\nu] dcos(\theta_\nu) + \\
&\sigma_{\bar{\nu}}(E_\nu) \times 2\pi \int_{-1}^{1} [d\Phi_{\nu,astro}(E_\nu)/dE_\nu + d\Phi_{\bar{\nu}_i,atm}(E_\nu,\theta_\nu)/dE_\nu] dcos(\theta_\nu)\}
\end{aligned}
\tag{4.14}
$$

The weighted average total neutrino cross section is:

$$
\bar{\sigma}(E_\nu) = \frac{\sigma_\nu(E_\nu) \sum_i [f_{\nu_i}(E_\nu) \times \Phi_{\nu_i}(E_\nu)] + \sigma_{\bar{\nu}}(E_\nu) \sum_i [f_{\nu_i}(E_\nu) \times \Phi_{\bar{\nu}_i}(E_\nu)]}{\sum_i [\Phi_{\nu_i}(E_\nu) + \Phi_{\bar{\nu}_i}(E_\nu)] \times f_{\nu_i}(E_\nu)}
\tag{4.15}
$$

where σ_ν is the total cross section for neutrinos, $\sigma_{\bar{\nu}}$ is the total cross section for antineutrinos.

$$\Phi_{\nu_i}(E_\nu) = 2\pi \int_{-1}^{1} [d\Phi_{\nu,astro}(E_\nu)/dE_\nu + d\Phi_{\nu_i,atm}(E_\nu,\theta_\nu)/dE_\nu] dcos(\theta_\nu) \tag{4.16}$$

is the total flux for neutrinos with flavor i and

$$\Phi_{\bar{\nu}_i}(E_\nu) = 2\pi \int_{-1}^{1} [d\Phi_{\nu,astro}(E_\nu)/dE_\nu + d\Phi_{\bar{\nu}_i,atm}(E_\nu,\theta_\nu))/dE_\nu] dcos(\theta_\nu) \tag{4.17}$$

is the total flux for antineutrinos with flavor i.

Figure 4.9 shows the composition of neutrino and antineutrino at the final level ($\sum_i [f_{\nu_i}(E_\nu) \times \Phi_{\nu_i}(E_\nu)]$ and $\sum_i [f_{\nu_i}(E_\nu) \times \Phi_{\bar{\nu}_i}(E_\nu)]$) as a function of neutrino energy. The lower part of the plot shows the neutrino to antineutrino ratio.

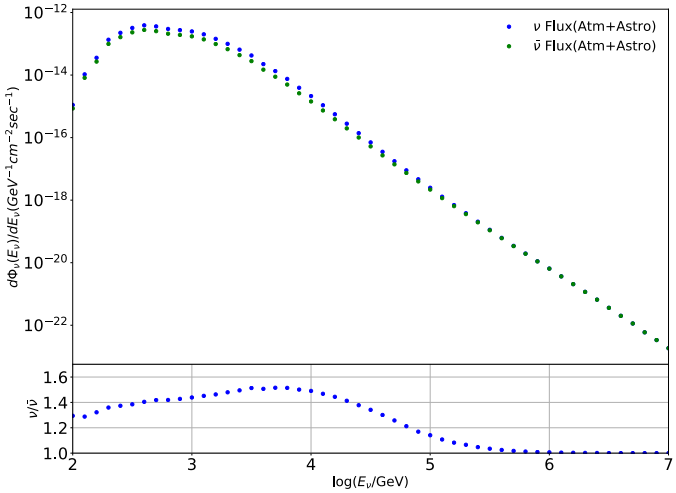

FIGURE 4.8: Neutrino and antineutrino composition at the final level.

The weighted total cross section (the sum of the charged-current interaction cross section and the neutral current interaction cross section averaged over neutrinos and antineutrinos according to their ratio) with neutrino to antineutrino ratio = 1:1 and the neutrino energy dependent neutrino to antineutrino ratio is shown in Fig. 4.9. The maximum difference between the two weighted total cross sections is less than 5%. For simplicity, the neutrino to antineutrino ratio being 1:1 is used when calculating the weighted total cross section in comparison with the experimental result.

4.5 Tau Regeneration

With the increase of cross section, it is more likely for up-going neutrinos to interact in the Earth. When the charged-current interaction of a tau neutrino occurs, a tau lepton

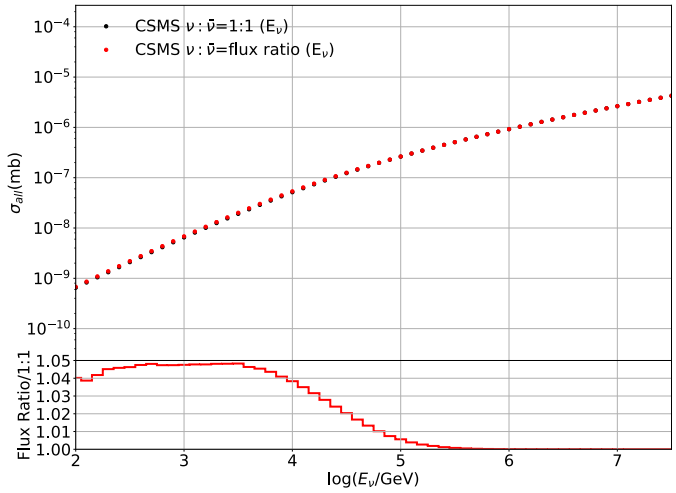

FIGURE 4.9: Weighted total cross section (CSMS) as a function of neutrino energy.

will decay into neutrinos which will have some probability of reaching the detector from below.

$$\tau^- \longrightarrow \nu_\tau + W^- \longrightarrow \nu_\tau + e^- + \bar{\nu_e} \tag{4.18}$$

$$\longrightarrow \nu_\tau + \mu^- + \bar{\nu_\mu} \tag{4.19}$$

If these product neutrinos reach the detector and interact there, they will have lower neutrino energy compared to the original tau neutrino that interacted in the Earth.

The number of the up-going events reaching the detector with the neutrino energy E_1 without any interactions in the Earth is:

$$N_{up,atDetector,no-inter}(E_1) = N_{up,atEarth}(E_1) \times (1 - abs(\sigma(E_1))) \tag{4.20}$$

The number of the up-going events with the neutrino energy E_1 that interact when passing through the Earth is:

$$N_{up,inter}(E_1) = N_{up,atEarth}(E_1) \times abs(\sigma(E_1)) \tag{4.21}$$

The products of these interactions can be neutrinos (from neutral current interactions or ν_τ charged current interactions). These neutrinos will carry a lower energy E_2 compared to their parent neutrinos that interacted in the Earth. Therefore the neutrinos that reach the detector with energy E_2 consist of two parts: the neutrinos that reached the Earth with energy E_2 and go through the Earth without any interactions:

$$N_{up,atDetector,no-inter}(E_2) = N_{up,atEarth}(E_2) \times (1 - abs(\sigma(E_2))), \tag{4.22}$$

and the neutrinos that reached the Earth with a higher energy E_1, interacted in the Earth and produced new neutrinos from the interactions with energy E_2. The number of neutrinos from the second part is proportional to the number of events that reached the Earth with E_1.

$$N_{up,atDetector}(E_1 \to E_2) \sim N_{up,atEarth}(E_1) \times abs(\sigma(E_1)) \tag{4.23}$$

$$N_{up,atDetector}(E_2) = N_{up,atDetector,no-inter}(E_2) + N_{up,atDetector}(E_1 \to E_2) \tag{4.24}$$

In this binned analysis, when E_2 belongs to a lower energy bin, due to the fast falling spectrum, the down-feed effect is very small.

$$N_{up,atDetector,no-inter}(E_2) \gg N_{up,atDetector}(E_1 \to E_2) \tag{4.25}$$

Figure 4.10 is a demonstration the down-feed effect. The red part indicates the down-feed effect: the primary neutrinos' energy comes from a higher energy bin than the secondary neutrino's energy.

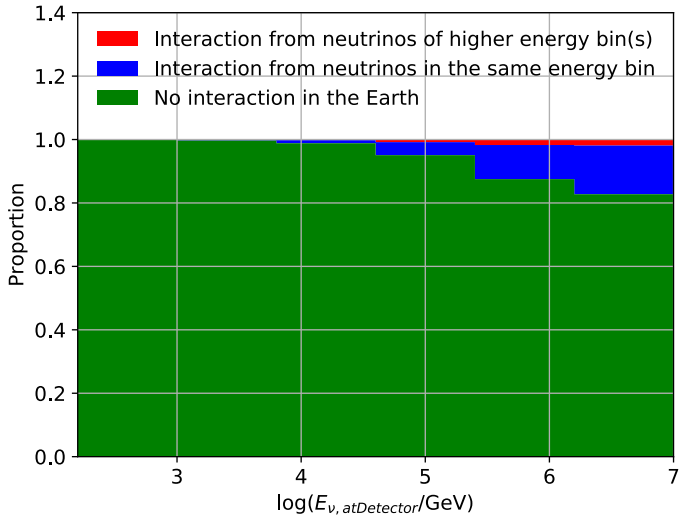

FIGURE 4.10: The composition of the up-going neutrinos at the detector: the green part is the proportion that goes through the Earth without any interactions; the blue part is the proportion that interacts in the Earth and produces a secondary neutrino with a lower energy that is in the same energy bin as the primary neutrino energy; the red part is the proportion that interacts in the Earth and produces a secondary neutrino whose primary neutrino's energy belongs to a higher energy bin compare to the secondary neutrino's energy.

Some proportion of neutrinos interact in the Earth and produce a secondary neutrino that reaches the Earth. This process is cross section dependent. When creating the ratio vs. cross section curve, these events are taken into consideration: the number of up-going neutrino in a certain cross section bin includes the events that have interactions in the Earth. Therefore the down-feed effect is accounted for in this analysis.

4.6 Validation Study with ν_τs

To test the validity of the analysis method, three sets of ν_τ simulations are simulated using NuGen [82] with the Standard Model cross section scaled by 0.2, 1, and 5 respectively. The Standard Model cross section used is the CSMS [62] calculation. The 5*CSMS simulation is used to calculate the ratio vs. cross section curve ($R(\sigma)$).

The ratio vs. cross section curve is independent of the cross section dependence on the neutrino energy ($\sigma(E_\nu)$). In Fig. 4.11, the ratio vs. cross section curves ($R(\sigma)$) generated with 1×CSMS, 0.2×CSMS and 5.0×CSMS simulation are plotted. The three curves are consistent within the statistical uncertainties. Due to the same neutrino energy range used for the simulations, the 0.2×CSMS and 1.0×CSMS curves run out of statistics at a lower cross section value compared to the 5×CSMS curve. For the same reason, at the low cross section values, the 5×CSMS curve does not have enough statistics. Since this test covers cross section values up to 10^{-5} mb, the 5×CSMS simulation is used to generate the ratio vs. cross section curve. In principle, provided enough statistics and a large enough energy range for the simulation, a simulation generated with any cross section table can be used to calculate the ratio vs. cross section curve.

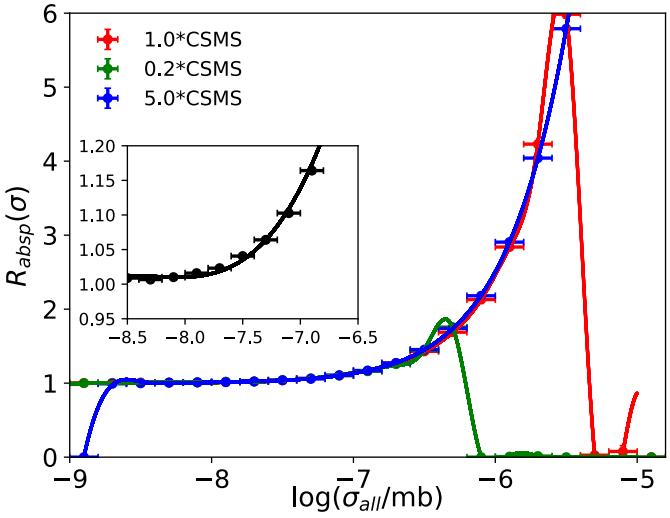

FIGURE 4.11: The ratio of the down-going events to the up-going events vs. cross section, calculated using Monte Carlo simulations generated with three different scaling factors of CSMS cross section.

For the purpose of testing the analysis method, true neutrino energy is used [3]. For each simulation dataset, the events are assigned into different neutrino energy bins and separated into down-going group and up-going group. The ratio vs. neutrino energy curve for the three datasets are shown in Fig. 4.12. The 5*CSMS (blue) curve in Fig. 4.11 is used to calculate the corresponding cross section value for each ratio in Fig. 4.12.

The resulting cross section for the three simulation datasets is shown in Fig. 4.13, showing consistency with the cross section used in the generation of the simulations. The only mismatch is in the first energy bin of the 0.2×CSMS data set. This is due to the insensitivity of this method towards the low cross section value. As shown in Fig. 4.11, for cross section values smaller than $\sim 10^{-8.5}$ mb, the ratio is always consistent with 1, which means no Earth absorption effect. This indicates the method is insensitive for small cross section values.

This test has shown that using the event distributions in neutrino energy and zenith bins, the neutrino interaction cross section as a function of neutrino energy can be measured using this method.

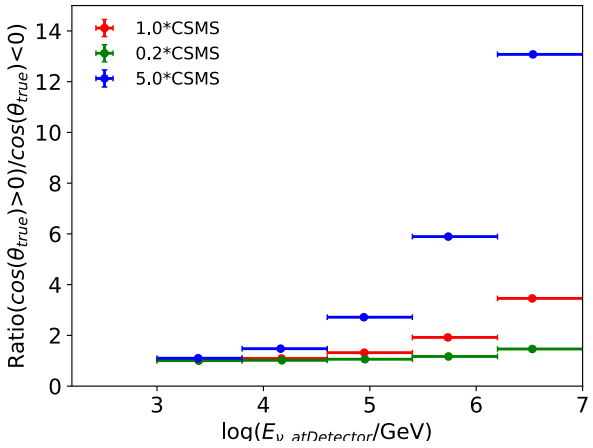

FIGURE 4.12: Ratio (after the application of the detector correction factors) vs. neutrino energy for Monte Carlo simulations generated with three different scaling factors of CSMS cross section.

[3]The validation test of the mapping from the reconstructed energy to the true neutrino energy for different underlying cross section and energy relationships is shown in Chapter 5

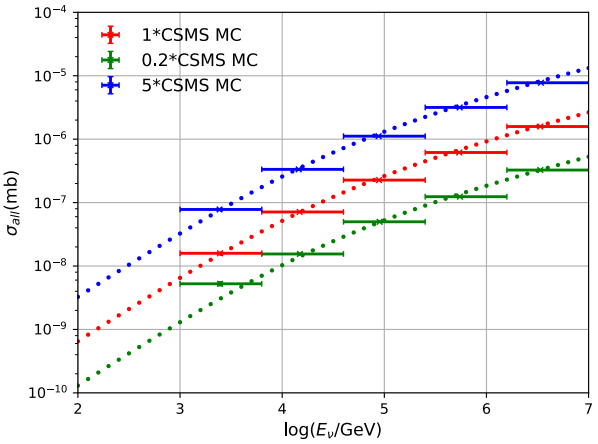

FIGURE 4.13: Cross section (indicated by the data points) vs. neutrino energy for Monte Carlo simulations generated with three different scaling factors for the CSMS cross section. Dotted lines indicated the corresponding scaled CSMC cross section's neutrino energy dependence.

Chapter 5

Unfolding

The goal of this analysis is to measure the neutrino energy dependent neutrino interaction cross section. The variables measured in the experiment are the reconstructed variables. In ν_e and ν_τ charged-current interactions, the interacting neutrino deposits almost all of its energy in the detector. However, in ν_μ charged-current interactions and all neutral current interactions, the out-going particle carries a fraction of the primary neutrino energy. Therefore, the deposited energy is smaller than the primary neutrino energy (as shown in Fig. 5.1 (left) where the off-diagonal events are mostly with a reconstructed energy smaller than the neutrino energy). There is also reconstruction effect: for cascade events, the energy resolution is $\sigma_E \sim 15\%$, and the zenith resolution is $\sigma_\theta \sim 10^o - 15^o$. These factors will result in a difference between the reconstructed variables and the true variables. For mapping from the reconstructed space to the true space, we introduce the unfolding method. In this analysis we are interested in the data distribution in a 2D (energy, zenith) grid; therefore we unfold these two variables simultaneously.

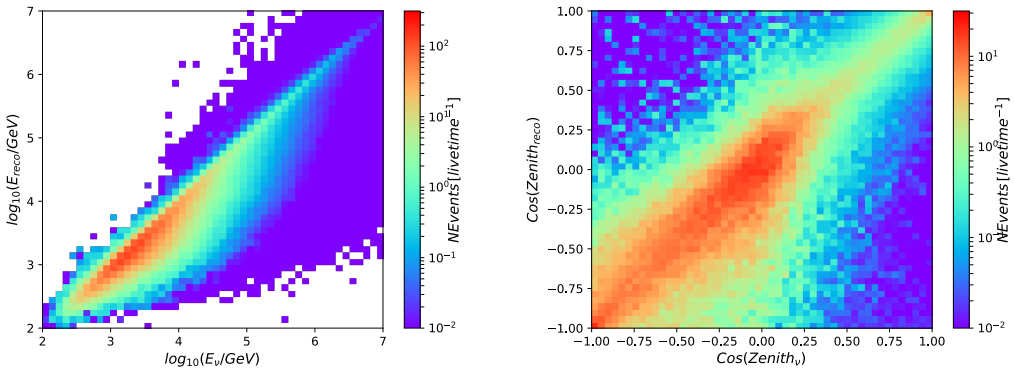

FIGURE 5.1: Reconstructed energy vs. neutrino energy (left) and reconstructed zenith vs. true zenith (right) for the neutrino-induced cascades.

5.1 Iterative Unfolding

After a dedicated study of many different unfolding methods and the regularization methods (to balance the variance and the bias of the unfolded result) associated with them, Iterative Unfolding [111] has been chosen for this analysis.

5.1.1 Iterative Unfolding Method

Iterative unfolding is based on Bayes' Theorem. The probability of having reconstructed energy R_j given true energy T_i ($P(R_j|T_i)$) is known (the detector response matrix or the unfolding matrix), and the probability of having true energy T_i given reconstructed energy R_j ($P(T_i|R_j)$) is of interest. The equation connects the two probabilities is:

$$P(T_i|R_j) = \frac{P(R_j|T_i)P(T_i)}{P(R_j)} \tag{5.1}$$

$$P(R_j) = \sum_i P(R_j|T_i)P(T_i), P(T_i) = \frac{N(T_i)}{\sum_i N(T_i)} \tag{5.2}$$

where $N(T_i)$ is the number of events in true bin i. In this analysis, it is the number of events in a certain neutrino energy and true zenith bin. Note that we know $P(R_j|T_i)$ because of the kinematic of interactions. For neutrinos with different flavors, the kinematic is different. For example, ν_e charged-current interaction will deposit almost all the energy into the detector while ν_μ charged-current interaction will result in an out-going muon which carries away a certain amount of the primary neutrino energy. Therefore in this analysis, we need to assume a ν_e: ν_μ: ν_τ = 1: 1: 1 flavor ratio to calculate the detector response matrix (unfolding matrix). After plugging Eq. 5.2 into Eq. 5.1, Eq. 5.1 becomes:

$$P(T_i|R_j) = \frac{P(R_j|T_i)N(T_i)}{\sum_i P(R_j|T_i)N(T_i)} \tag{5.3}$$

The goal of the unfolding is to obtain the distribution in true space ($N(T)$) according to the distribution in reconstructed space ($N(R)$). At the beginning of the iteration, the Monte Carlo truth is chosen to be the initial $N(T)$ ($N(T_i)^{(0)}$ in the equation below), the first iteration is expressed as following:

$$P(T_i|R_j)^{(0)} = \frac{P(R_j|T_i)N(T_i)^{(0)}}{\sum_i P(R_j|T_i)N(T_i)^{(0)}} \tag{5.4}$$

After acquiring the $P(T_i|R_j)^{(0)}$ from the first iteration, we calculate the truth distribution after the first iteration, $N(T_i)^{(1)}$:

$$N(T_i)^{(1)} = \sum_j P(T_i|R_j)^{(0)}N(R_j)/\alpha_j \tag{5.5}$$

where

$$\alpha_j = \sum_j P(R_j|T_i) \tag{5.6}$$

corrects for acceptance losses. α is the sum of all the reconstruction probabilities, given a certain range in true space. Theoretically, it should be 1. However, due to the limited size of the unfolding range. α can be smaller than 1. Therefore it is necessary to have this term in the denominator to correct for the acceptance losses. For example, the current unfolding energy range is from 150 GeV to 10 PeV [1] for both reconstructed energy and neutrino energy. If there are events with true neutrino energy within this range and after reconstruction, they fall outside this range, α would be smaller than 1. The α values for the unfolding matrix built with the baseline simulation are listed in the table below.

Energy Range [log(E_ν/GeV)]	2.2-3.0	3.0-3.8	3.8-4.6	4.6-5.4	5.4-6.2	6.2-7.0
up-going	0.997	0.999	1.000	0.999	0.999	0.995
down-going	0.999	1.000	1.000	0.999	0.999	0.991

TABLE 5.1: The α values for the unfolding matrix built with the baseline simulation.

For the k+1 th iteration:

$$P(T_i|R_j)^{(k)} = \frac{P(R_j|T_i)N(T_i)^{(k)}}{\sum_i P(R_j|T_i)N(T_i)^{(k)}} \tag{5.7}$$

$$N(T_i)^{(k+1)} = \sum_j P(T_i|R_j)^{(k)} N(R_j)/\alpha_j \tag{5.8}$$

The energy binning used in this analysis is in the common logarithm space ($\log_{10}(E/\text{GeV})$) from 2.2 to 7.0 with the bin size 0.8. The zenith binning used is [0°, 90°] (down-going) and [90°,180°] (up-going). The same binning is used for both reconstructed space and true space.

$P(R_{2j}|T_{2i})$ represents the probability of an up-going event with true energy i (i th energy bin) gets reconstructed as up-going with reconstructed energy j (j th energy bin).

$P(R_{2j+1}|T_{2i})$ represents the probability of an up-going event with true energy i (i th energy bin) gets reconstructed as down-going with reconstructed energy j (j th energy bin).

$P(R_{2j}|T_{2i+1})$ represents the probability of a down-going event with true energy i (i th energy bin) gets reconstructed as up-going with reconstructed energy j (j th energy bin).

[1] Even though the measured cross section is in the energy range of 6 TeV to 10 PeV, it is still necessary to unfold in the whole energy range (150 GeV to 10 PeV) where events are observed, since the events in the lower reconstructed energy bins may have a higher primary neutrino energy. For the measured result, in the energy range of 150 GeV to 6 TeV there are large systematic uncertainties and the cross section over this energy range is too small to be sensitive to this analysis method; therefore the result doesn't have physical meaning.

$P(R_{2j+1}|T_{2i+1})$ represents the probability of a down-going event with true energy i (i th energy bin) gets reconstructed as down-going with reconstructed energy j (j th energy bin).

The above probability of $P(R|T)$s are the elements of the unfolding matrix. The unfolding matrix elements of the baseline simulation are listed in the table below.

5.1.2 Iteration Optimization

With the increase in the number of iterations, the bias of the result (the difference between the unfolded value and the true value) decreases while the variance of the result increases. We want the bias to be small, so that the choice of the initial distribution in true space ($N(T)^{(0)}$) in Eq. 5.4 will have a minimal effect on the result. We also want a relatively small variance so that the result is stable against statistical fluctuations. Therefore, it is crucial to determine the optimum number of iterations.

The goal is to balance between the variance and the bias. Usually weighted Mean Square Error (MSE) is used to quantify these two variables:

$$MSE' = \frac{Var + Bias^2}{NEvents} \tag{5.9}$$

Figure 5.2 shows the change of MSE' with the number of iterations. Ideally, we should choose the stop time so that the MSE' is the global minimum (average over all bins), as indicated by the vertical dotted line in the right plot of Fig. 5.2. This way we have a good balance between the bias and the variance. However, in reality, we have no information on the true distribution; therefore we can not calculate MSE' (since we can not calculate the bias).

The method used to determine the optimal number of iterations is from Ref. [111]. During the first few iterations, the bias decreases rapidly. After a certain number of iterations, the bias reduction becomes negligible and the variance keeps increasing. To find this point, we introduce a log likelihood ratio to quantify the bias. Even though the true distribution is unknown, we could recalculate the reconstructed distribution ($N_{iter}(R)$) after every iteration using Eq. 5.8:

$$N_{iter}(R_i) = N(R_i)^{(k+1)} = \sum_j P(R_i|T_j) N(T_j)^{(k+1)} \tag{5.10}$$

A log likelihood ratio can then be calculated using the equation below to quantify the difference between the reconstructed distribution from the unfolding and the real reconstructed distribution. This log-likelihood also reflects the difference between the true distribution from the unfolding and the real true distribution. Therefore, we set a critical value for the log likelihood. Once this critical value is reached, the interaction should stop.

			True											
			2.2-3.0		3.0-3.8		3.8-4.6		4.6-5.4		5.4-6.2		6.2-7.0	
			Up	Down	Up	Down	Up	Down	Up	Down	Up	Down	Up	Down
Reco	2.2-3.0	Up	8.9e-1	3.1e-1	1.8e-1	4.1e-2	8.9e-3	1.8e-3	9.8e-4	1.2e-5	2.9e-4	1.2e-5	3.4e-5	0
		Down	7.8e-2	6.5e-1	1.4e-2	7.2e-2	8.1e-4	2.6e-3	2.9e-5	1.4e-4	0	3.2e-6	0	0
	3.0-3.8	Up	2.9e-2	1.9e-2	7.1e-1	3.0e-1	4.2e-1	1.3e-1	5.2e-2	9.9e-3	1.1e-2	1.2e-3	3.2e-3	1.6e-4
		Down	2.1e-3	2.0e-2	9.4e-2	5.8e-1	7.7e-2	2.6e-1	1.3e-2	2.5e-2	2.2e-3	5.3e-3	3.7e-4	1.7e-3
	3.8-4.6	Up	0	0	2.0e-3	1.1e-3	3.9e-1	1.2e-1	3.6e-1	7.1e-2	7.6e-2	7.4e-3	2.3e-2	2.5e-3
		Down	0	0	2.7e-4	2.6e-3	9.7e-2	4.8e-1	1.0e-1	3.3e-1	1.8e-2	7.2e-2	8.9e-3	2.8e-2
	4.6-5.4	Up	0	0	0	0	1.3e-3	5.7e-4	3.7e-1	5.2e-2	2.5e-1	2.7e-2	7.2e-2	6.8e-3
		Down	0	0	0	0	2.9e-4	2.0e-3	8.8e-2	5.1e-1	7.9e-2	2.8e-1	3.2e-2	9.8e-2
	5.4-6.2	Up	0	0	0	0	8.1e-6	5.2e-7	2.6e-3	1.3e-3	4.2e-1	5.5e-2	2.3e-1	3.6e-2
		Down	0	0	0	0	1.4e-5	0	1.8e-3	4.3e-3	1.3e-1	5.4e-1	1.1e-1	2.9e-1
	6.2-7.0	Up	0	0	0	0	0	0	3.1e-4	6.9e-6	4.8e-3	3.4e-3	3.6e-1	6.6e-2
		Down	0	0	0	0	0	0	9.7e-5	9.9e-7	3.5e-3	6.2e-3	1.4e-1	4.6e-1

TABLE 5.2: The unfolding matrix elements of the baseline simulation: the probability of a reconstructed value given a certain true value.

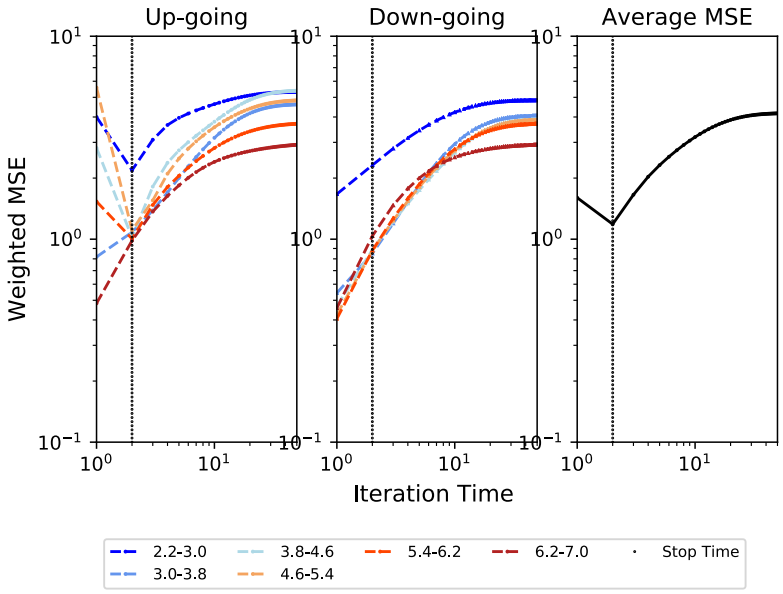

FIGURE 5.2: Relationship between the MSE' and the number of iterations according to simulations: for the up-going events (left), for the down-going events (middle). Different lines indicate different energy bins. The average MSE' for all the energy and zenith bins is shown on the right.

$$-2\ln(\frac{LLH}{LLH_{true}}) = -2 \times (\sum_i [N_{ori}(R_i)\ln(N_{iter}(R_i)) - N_{iter}(R_i)] - \sum_i [N_{ori}(R_i)\ln(N_{ori}(R_i)) - N_{ori}(R_i)]) \tag{5.11}$$

To find the critical value, we use the original distribution in the reconstructed space $N_{ori}(R)$ as the expectation of a Poisson distribution to sample $N_{sam}(R)$ 100,000 times. For each sampling, we calculate the log likelihood ratio:

$$-2\ln(\frac{LLH}{LLH_{true}}) = -2 \times (\sum_i [N_{sam}(R_i)\ln(N_{ori}(R_i)) - N_{ori}(R_i)] - \sum_i [N_{sam}(R_i)\ln(N_{sam}(R_i)) - N_{sam}(R_i)]) \tag{5.12}$$

The log likelihood ratio distribution is shown in the left plot of Fig. 5.3. The critical value is chosen to be the point corresponds to a p-value of 0.5. Once the likelihood valued for an iteration is smaller than the critical value, we use twice the number of iterations as the optimum number of iterations. The reason for choosing this p-value is that the increase of p-value gets slower with the increase of iteration time. It's hard to determine when it gets to 1 (see the right plot of Fig. 5.3). Therefore we choose the iteration time when p-value is close to 0.5, which is easier to determine since that's when the likelihood

ratio drops fastest. We then multiply this number by 2 as the number of iterations to run. The vertical dotted line, which indicates the number of iterations in Fig. 5.2 is determined using the method described above. Figure 5.2 shows that we are able to find the number of iterations where the MSE' is at its global minimum.

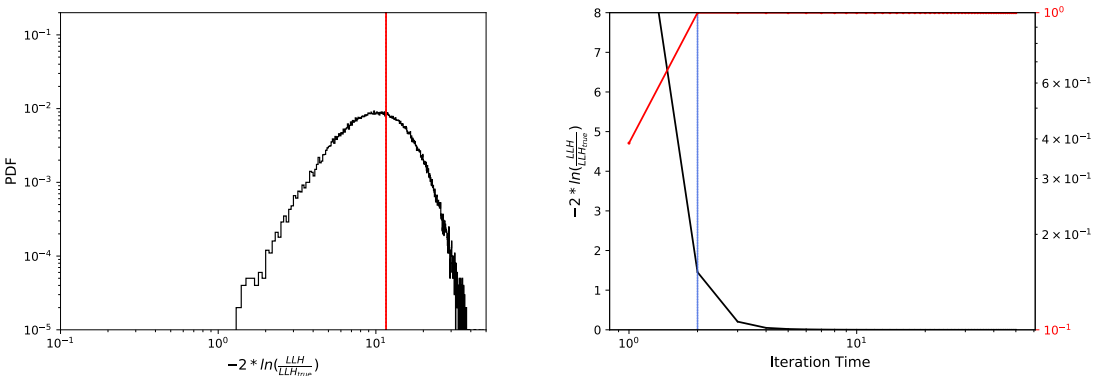

FIGURE 5.3: Left: the distribution of the likelihood ratio calculated using Eq. 5.12. Right: the likelihood ratio (left y-axis) vs. the number of iterations and p-value (right y-axis) vs. the number of iterations.

A test has been done to show that the above method will give an unbiased result. Three sets of ν_τ events were simulated using NuGen [82] with the Standard Model CSMS cross section [62] scaled by 0.2, 1 and 5 respectively. The 5×CSMS simulation is used to build the unfolding matrix. The reconstructed distribution of the other two sets of simulation are used as the input to unfold. The unfolded true distribution of three sets of simulation using the same matrix built with the 5×CSMS simulation are shown in comparison to their real true distributions in Fig. 5.4. The lower plot of Fig. 5.4 shows the ratio of the unfolded true value and the real true value. Even when the data set being unfolded and the data set used for building the matrix have orders of magnitudes of difference in the event distribution, the unfolding method is able to recover the true distribution with almost zero bias. This test proves that in the real experiment, the true distribution of the observed data can be recovered using an unfolding matrix built with the simulation using the Standard Model cross section regardless of what the actual values of the cross section might be.

5.2 Uncertainty Estimation

5.2.1 Markov Chain Monte Carlo

Since the unfolding method is involved, directly calculating the uncertainty on the unfolded number of events using error propagation is overly complicated. Instead, Markov Chain Monte Carlo (MCMC) is used for the statistical uncertainty estimation. An uniform prior in logarithm space from 10^{-10} to 10^{10} is chosen. The same prior and its range

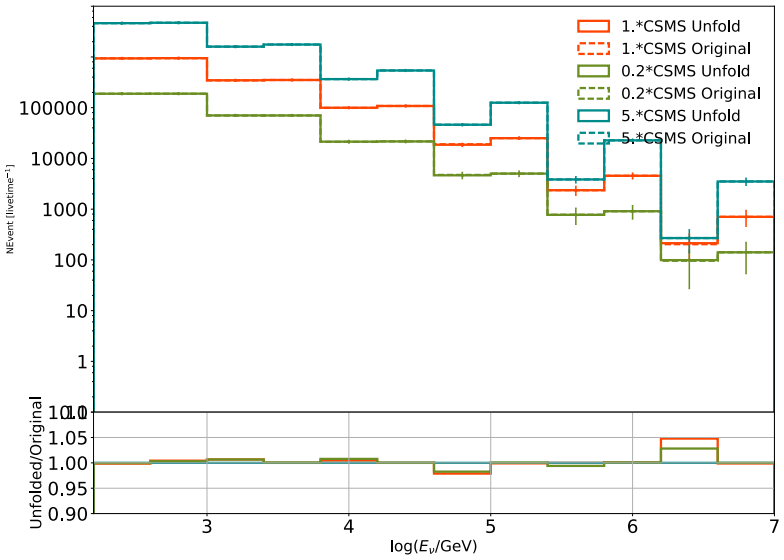

FIGURE 5.4: The unfolded true distribution and the real true distribution. The $2i$-1 th and $2i$ th bins are over the same energy range, with $2i$-1 th bin representing the up-going region and $2i$ th bin representing the down-going region.

are used for all the bins to avoid any bias caused by the assumption for the expected number of events in a bin. The broad range (10^{-10} to 10^{10}) ensures coverage of all possible events given the experimental livetime (5 years) for this analysis. The probability distribution function using Poisson statistics on our observations from the reconstructed space is used to calculate the likelihood for the MCMC. 20,000 samples are simulated using MCMC. The first 10% of the simulated samples are discarded to ensure that the samples used have reached an equilibrium state. The sample distribution from Asimov data (Monte Carlo expectation) for all reconstructed energy and zenith bins are shown in Fig. 5.5.

All samples from MCMC are unfolded with the procedure described above. Then we obtain the posterior distributions for the true space for true neutrino energy and true zenith bins, as shown in Fig. 5.6. The vertical black lines in Fig. 5.6 indicate the central values of the unfolded result. They are the result of directly unfolding the observed reconstructed distribution. The colored lines in Fig. 5.6 indicate the 68% statistical uncertainty range for the unfolded result. The uncertainty range is calculated based on the posterior distribution: 16% in both tails of the distribution are marked as the edges of the uncertainty range. This uncertainty range should correspond to 68% of the truth coverage which will be discussed in the next section.

In this analysis, the ratio of down-going events to up-going events as a function of neutrino energy is needed to calculate the corresponding cross section. After unfolding, we have the number of events for the down-going region and the up-going region in each neutrino energy bins. After applying the correction factor (c.f. Sec. 4.3.1), we obtain the ratio in

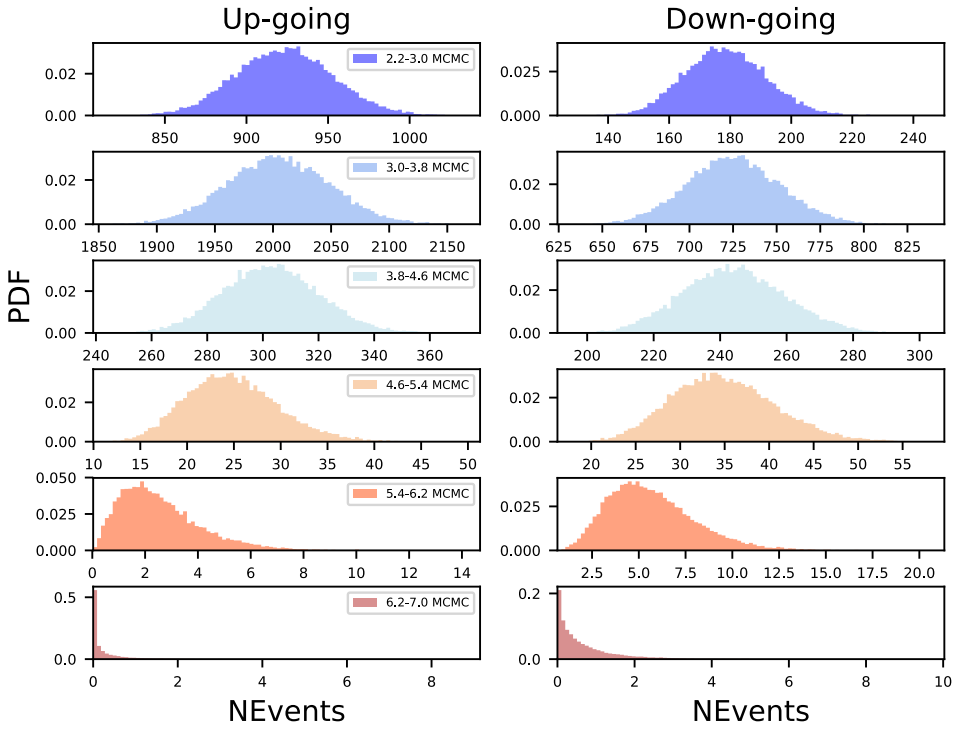

FIGURE 5.5: The MCMC sample (for Asimov data) number of events distribution in the reconstructed space for all reconstructed energy and zenith bins.

each neutrino energy bin. The statistical uncertainty estimation of the unfolded ratio is done the same way as the statistical uncertainty estimation for the unfolded number of events described in the proceeding paragraph: using MCMC to sample according to the observed reconstructed distributions. For each sample, the ratio in the neutrino energy bins after unfolding is calculated. The posterior distributions of the ratio for Asimov data in the neutrino energy bins are shown in Fig. 5.7.

5.2.2 Truth Coverage Test

After choosing a method to estimate the statistical uncertainty, it is important to test the truth coverage of the method. A truth coverage test is a test to exam if the statistical uncertainty estimated by a certain method can cover the true value given the statistical fluctuations.

The ratios in neutrino energy bins from Asimov data are used as the true values (shown as the horizontal black lines in Fig. 5.8). Asimov data is used as the expectation of the Poisson distribution sampled 100 times over the reconstructed space to serve as the statistical fluctuations. The set of ratios for each sample is calculated from unfolding and their statistical uncertainties (68%) are estimated using MCMC as described above

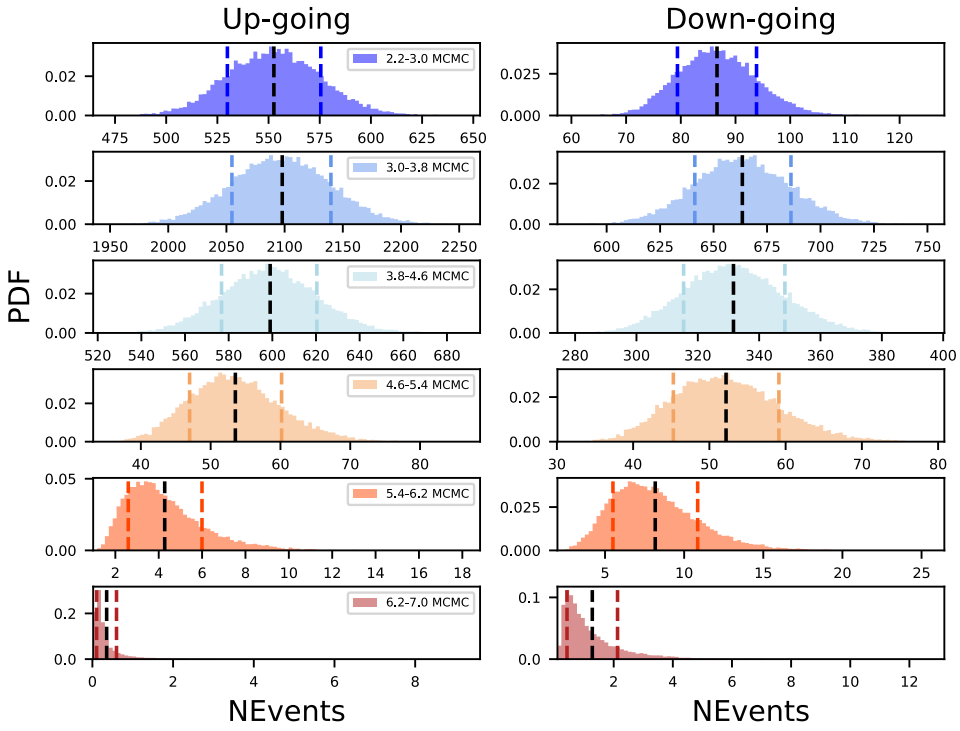

FIGURE 5.6: The unfolded number of events posterior distribution for Asimov data in the true space for true neutrino energy and true zenith bins. The vertical black lines indicate the central values. The vertical colored lines indicate the 68% statistical uncertainty range.

(represented by the colored data points with error bars in Fig. 5.8). The green data points in all energy bins are the ones do not correspond to the true value within the estimated uncertainty while the other colors do cover the true value within the estimated uncertainty. Since the 68% range is chosen as the uncertainty, the truth coverage for this test should be approximately 68%.

As shown in Fig. 5.8, for the first three bins, the truth coverage is $\sim$ 68%. However, for the last two bins, the truth coverage is significantly lower (the bin of $\log_{10}$(E/GeV): 2.2-3.0 is omitted as described in Sec. 4.4.1). The loss in coverage for the last two bins can be explained by low statistics: the second to last bin contains $\sim$ 8 events and the last bin contains $\sim$ 1 event according to the Asimov data with 5 years of livetime. When the livetime of the Asimov data is increased to 100 years, the truth coverages in all the bins become $\sim$ 68%, as shown in Fig. 5.9.

To compensate for the insufficient truth coverage in the low statistics bins, a re-calibration is needed for those bins. As shown in Fig. 5.10 (left), when there are enough statistics, the range used in the posterior distribution to estimate the uncertainty is the same with the corresponding truth coverage. When the statistics are low, as shown in Fig. 5.10 (right), the truth coverage is always lower than the corresponding uncertainty range in

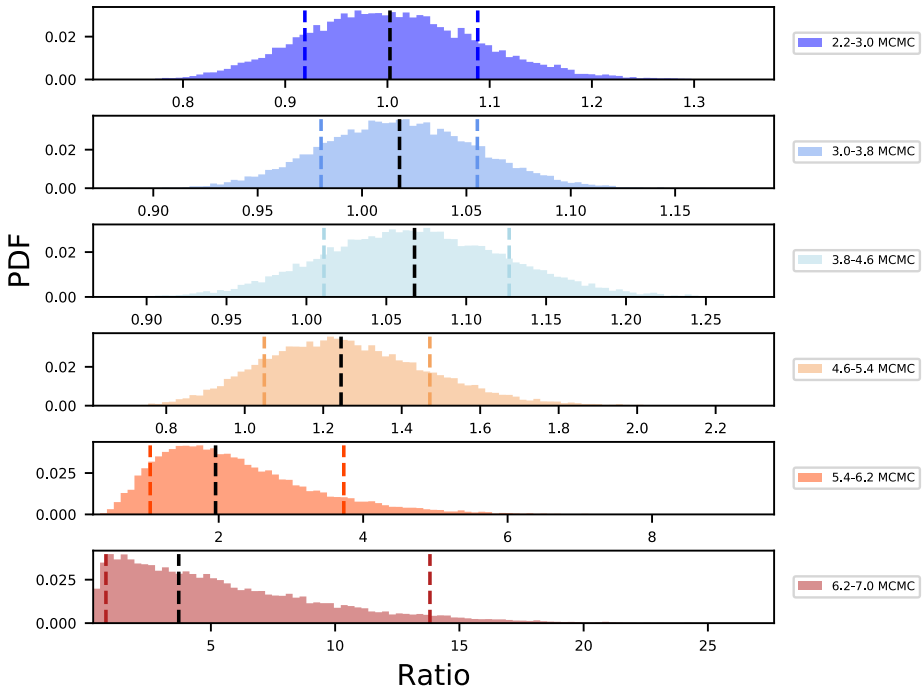

FIGURE 5.7: The unfolded ratio posterior distribution for Asimov data in neutrino energy bins. The vertical black lines indicate the central value and the vertical colored lines indicate the 68% statistical uncertainty range.

the posterior distribution. To maintain a 68% truth coverage (indicated by the horizontal black lines in Fig. 5.10), a larger range in the posterior distribution is needed for the uncertainty estimation. Figure 5.10 shows that for the second to last bin, where there are $\sim$ 8 events, using 80% as the range for the uncertainty estimation will result in a truth coverage of at least 68%. However, for the last bin where the total number of events is smaller than 1, a finer scan is needed to perform the study.

In Fig. 5.10, the expected number of events is altered by changing the livetime which means the number of events in the down-going bin and the up-going bin are modified by the same scaling factor. In Fig. 5.11, the ratio truth coverage is calculated for the different combinations of the number of events in the down-going bin and the up-going bin for the case where both of them are smaller than 1. Figure 5.11 shows that with a 90% range in the posterior distribution taken as the uncertainty estimation, it is guaranteed to have a truth coverage of at least 68% for the very low statistics case.

After re-calibrating the second to last bin with a 80% and the last bin with a 90% range in the posterior distributions for the uncertainty estimation, the truth coverages for all the bins have reached 68% as shown in Fig. 5.12.

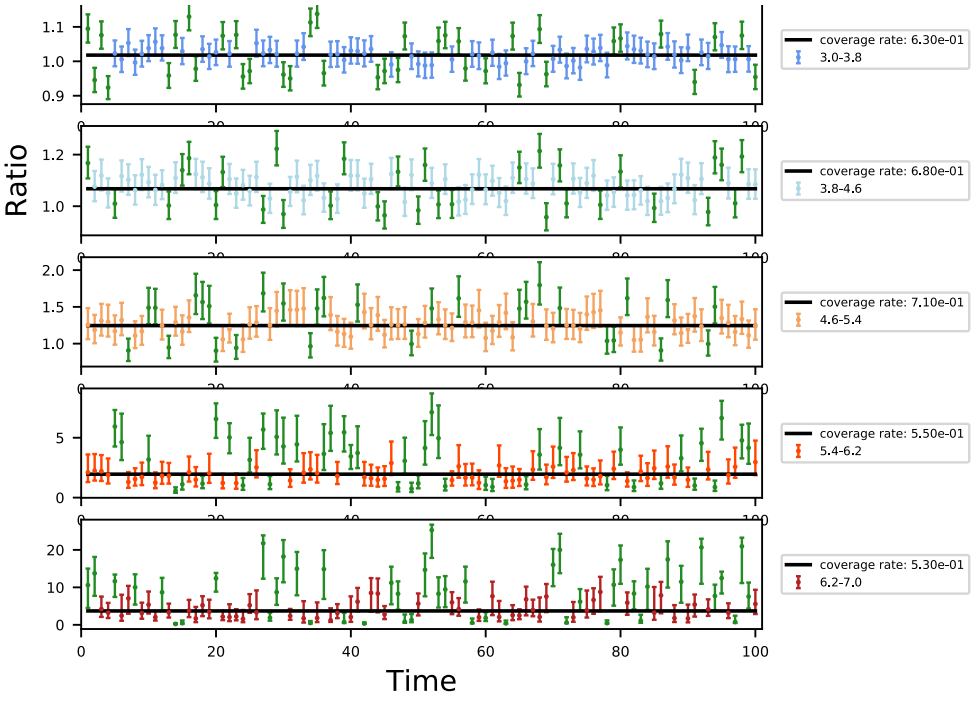

FIGURE 5.8: The unfolded ratio truth coverage for 5 years of livetime: horizontal black lines indicate the true ratio for each neutrino energy bin; the colored data points are the ratio and its uncertainty from each Poisson resample. The green data points do not cover the true value while other colors do cover the true value.

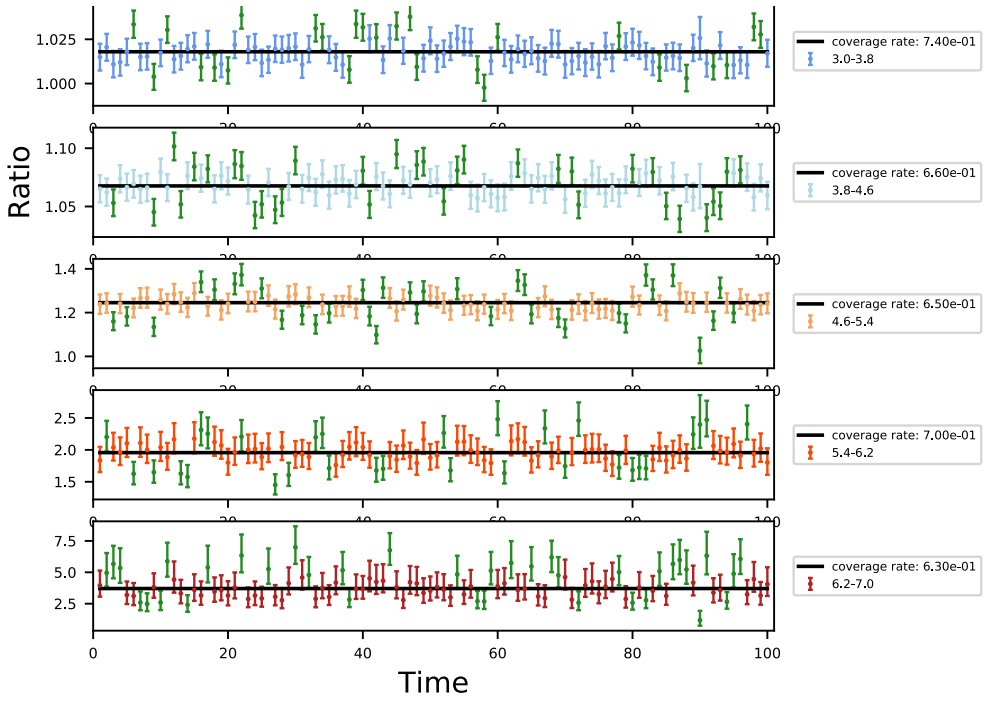

FIGURE 5.9: The unfolded ratio truth coverage for 100 years of livetime: horizontal black lines indicate the true ratio for each neutrino energy bin; the colored data points are the ratio and its uncertainty from each Poisson resample. The green data points do not cover the true value while other colors do cover the true value.

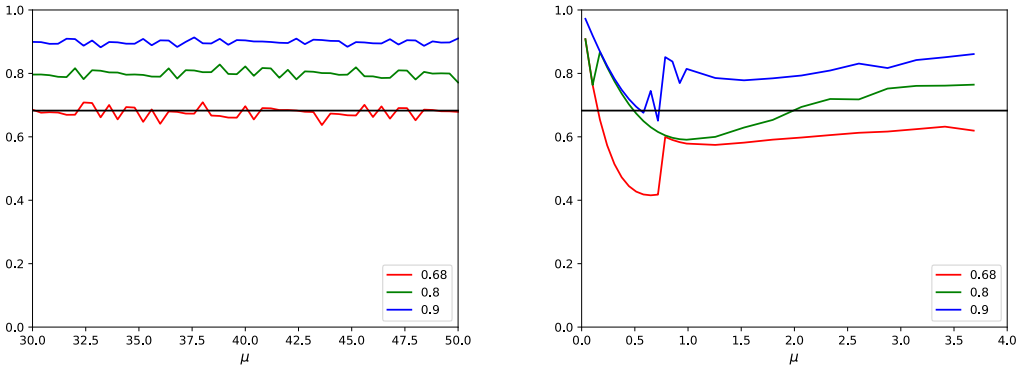

FIGURE 5.10: The truth coverage rate vs. the expected number of events (μ) for different uncertainty ranges in the posterior distribution: the case of enough statistics (left), the case of low statistic case (right). The y-axis is the truth coverage rate and the x-axis is the expected number of events. Different colored lines correspond to the different ranges in posterior distribution when estimating the statistical uncertainties.

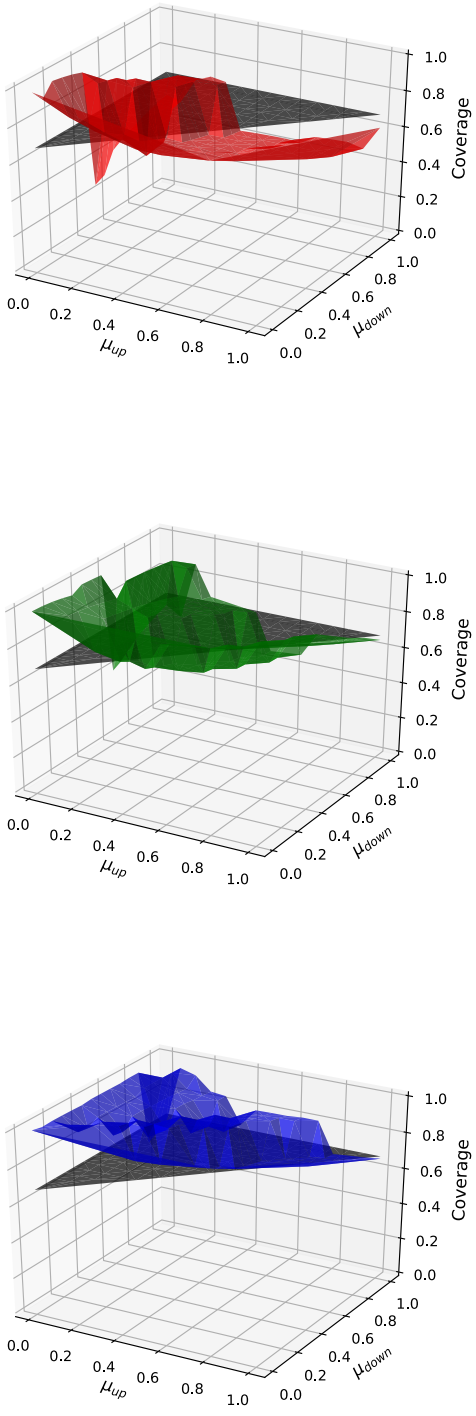

FIGURE 5.11: The ratio truth coverage vs. expected number of events in the down-going bin and the up-going bin of a low statistics case: (top) 68% range in the posterior distribution for the uncertainty estimation, (middle) 80% range in the posterior distribution for the uncertainty estimation, (bottom) 90% range in the posterior distribution for the uncertainty estimation. The black plane indicates the 68% truth coverage plane in the 2D plot.

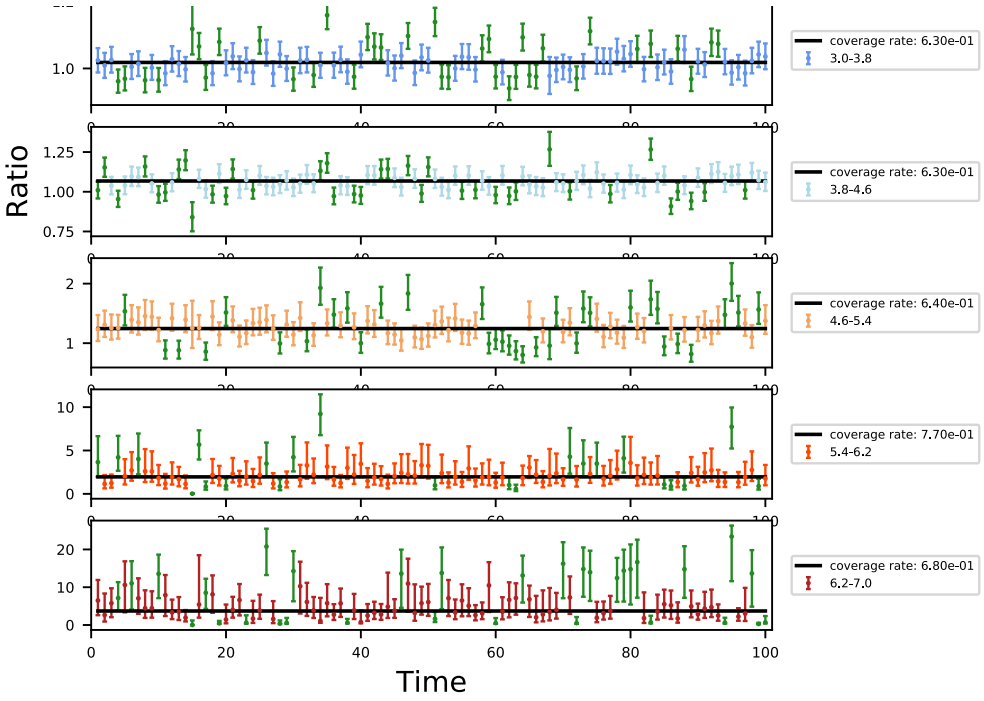

FIGURE 5.12: The unfolded ratio truth coverage for 5 years of livetime with recalibrated uncertainty ranges for the last 2 bins.

Chapter 6

Systematic Uncertainties

Besides the statistical uncertainties, one must also take systematic uncertainties into consideration when estimating the total uncertainty for the result. In this analysis, systematic uncertainties come from the environment, such as the ice property of the South Pole ice and the Earth composition model; the apparatus, such as the DOM efficiency, and the analysis techniques such as the self-veto effect for atmospheric neutrinos. In this chapter, we will discuss how these systematic effects affect the result of this analysis, and how to estimate the total systematic uncertainty on the final result. To study these systematic effects, simulation datasets with the change of corresponding systematic parameters are generated. These systematic datasets are generated for neutrinos of all three flavors and have the same generation spectrum, energy range, and statistics as the baseline simulation.

6.1 The Ice Property of the South Pole Ice

From the emission point (such as neutrinos interactions vertices) to their receiver DOMs, photons travel through the South Pole ice. The probability of these photons getting scattered or absorbed depends on the ice property which is described by parameters like the absorption coefficient (the average distance to absorption) and the scattering coefficient (the average distance between successive scatters of photons) [69]. Such parameters are crucial for creating Monte Carlo simulations and event reconstructions. The IceCube calibration has done dedicated studies on the ice property by using the LED calibration system [69]. These studies provide an estimation of the uncertainty of the ice property parameters. In this section, we will discuss the systematic effects from the three most important parameters of the ice properties: hole ice scattering, absorption, and bulk ice scattering.

6.1.1 Hole Ice Scattering

To deploy the DOMs and the cables into the South Pole Ice, 86 vertical holes were drilled using hot-water jet [76]. After the deployment, the hot water around the DOMs refroze

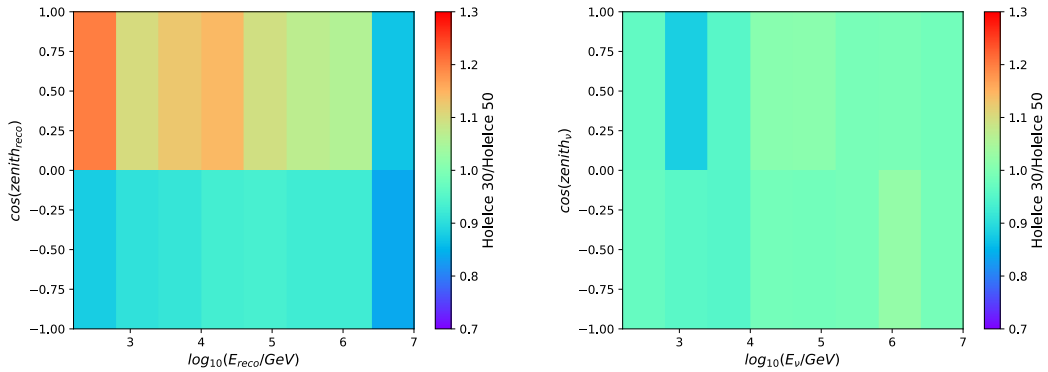

FIGURE 6.1: H2 30 simulation/ H2 50 simulation in the reconstructed (left) and the neutrino (right) energy and zenith bins for all flavors at the final event selection level.

into ice, and formed a 30 cm radius cylinder around the IceCube strings. Compared to the pristine glacial ice (bulk ice), the refreeze ice (hole ice) contains residual air bubbles that increase the light scattering [69]. Historically the hole ice model was built based on the study done for the AMANDA detector [112] (H2 model) and is characterized by the scattering length in the hole ice.

Here we study two different H2 Hole Ice models: the scattering length of 30 cm (H2 30) and the scattering length of 50 cm (H2 50). As shown in Fig. 6.1, when changing the scattering length in the hole ice, the difference between the two models in the true energy and zenith bins is small (less than a few percents) while the change in the reconstructed energy and zenith bins is rather large ($\sim 10\%$).

In this analysis, the variable distributions from the simulated datasets contribute to two parts of the analysis procedure. The first part is the calculation of the detector acceptance correction factor (c.f. Sec. 4.3.1). The distribution of the neutrino energy and the true zenith angle are used in Eq. 4.7 and Eq. 4.8. The second part is the calculation of the unfolding matrix (c.f. Chapter 5). The unfolding matrices map from the reconstructed space to the true space where both the distribution of the simulated datasets in the reconstructed variables and in the true variables are used. Therefore, applying different unfolding matrices and correction factors calculated with different systematic simulation datasets will yield results on the cross section systematic uncertainties.

For a long time, the H2 50 model was the default baseline model. The systematic datasets with different scattering/absorption lengths (c.f. Sec. 6.1.2 and Sec. 6.1.3) and DOM efficiencies (c.f. Sec. 6.2) are simulated based on H2 50. This means the hole ice model used in all the systematic datasets is the H2 (50) model while the other systematic parameters are being changed.

H2 30 model was originally introduced as a hole ice scattering systematic dataset. However, the study done in [88] showed that when fitting the simulation to the experimental data the goodness of fit of the H2 30 model was better than for the H2 50 model. Fig.

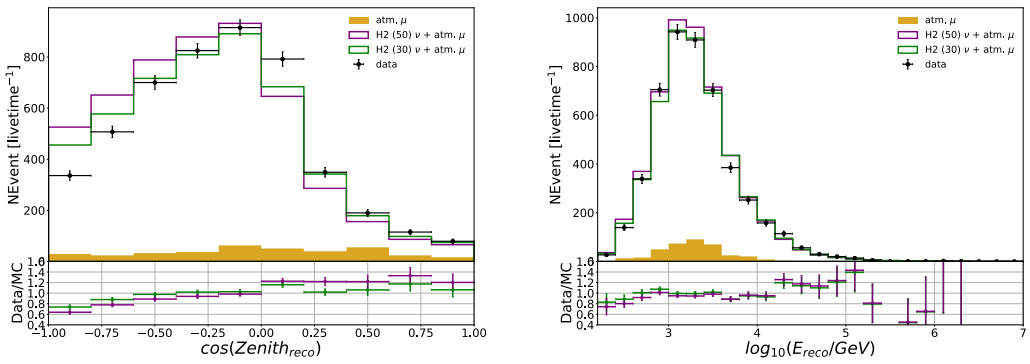

FIGURE 6.2: The reconstructed zenith and energy distribution of the 2011-2015 unblinded data, compared with the H2 (30) neutrino simulation and the H2 50 neutrino simulation.

6.2 also shows that the H2 30 model describes the experimental data better in the reconstructed zenith and energy distribution. Therefore, the H2 30 hole ice model is chosen to be the baseline of this analysis. Since the H2 30 model fits the experimental data much better than the H2 50 model, the difference between the two hole ice scattering lengths is not considered as a part of the systematic effect on the hole ice model.

Now we will discuss how the systematic uncertainty associated with the hole ice effect is estimated. With the recent study done on the IceCube flasher data [69], a new method (Flasher Hole Ice model) to parameterize the hole ice model with the angular acceptance effect of the DOMs was proposed [113], [114]. The angular acceptance effect of the DOMs is that the probability of the acceptance of a photon has directional dependence. In this new model, there are two parameters used to describe the relationship between the acceptance and the incoming direction. The model can be expressed as the equation below:

$$\begin{aligned}\text{Angular Acceptance} = 0.34(1 + 1.5\cos\eta - \cos^3\eta/2) + p \cdot \cos\eta(\cos^2\eta - 1)^3 \\ + p_2 \cdot \exp(10(\cos\eta - 1.2))\end{aligned} \tag{6.1}$$

The change in the p and p_2 parameters in Eq. 6.1 can be used to quantify the systematic effect of the hole ice model. The angular acceptance curves calculated with different combinations of the p and p_2 parameters are shown in Fig. 6.3. The plot shows that when changing p, the change of the curve is not significant while changing p_2 causes a much more noticeable change on the curve. Therefore, the variation of p_2 is chosen to describe the systematic effect on the hole ice model.

It is suggested by the IceCube collaboration that the reasonable range of p_2 for the systematic uncertainty estimation is from -1 to +1, while $p_2 = 0$ is served as the baseline for the flasher hole ice model. The comparison of p_2 = -1 and $p_2 = 1$ to $p_2 = 0$ simulation in the reconstructed energy and zenith bins and the true energy and zenith bins is shown

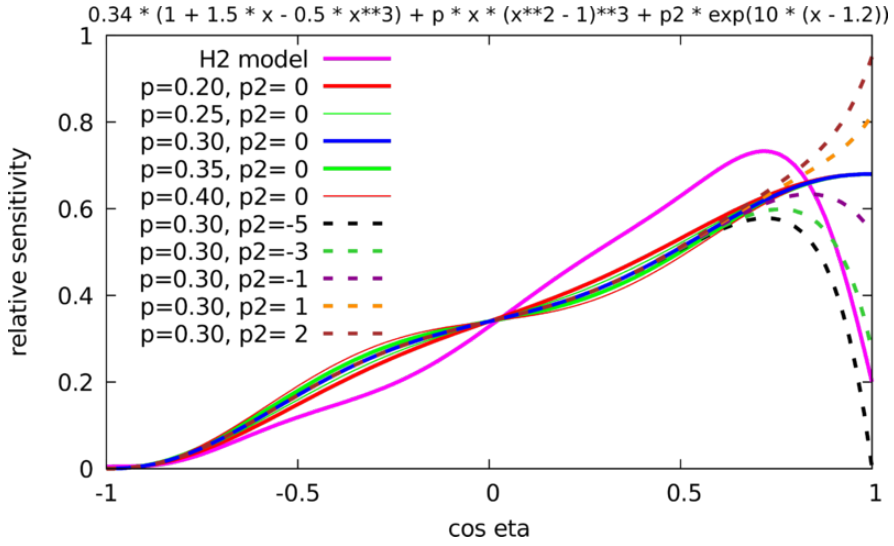

FIGURE 6.3: The angular acceptance curves with different parameters in comparison with the H2 50 model. The plot is from Ref. [114]

in Fig. 6.4. The plots show a consistency in the distribution of the true space [1]. In the reconstructed space, the plots show that the $p_2 = 1$ simulation turns to have a bias towards the up-going direction and the $p_2 = -1$ turns to have a bias towards the down-going direction compared to the $p_2 = 0$ simulation. The bias in the directional reconstruction affects the result for the down/up ratio unfolded with the systematic datasets.

To study the uncertainty associated with the change of p_2 in the cross section measurement, the p_2=0 simulation is used as the Asimov dataset and all the three p_2 variation datasets (p_2=-1, 0, 1) are used to calculate the unfolding matrices and the correction factors to be applied on the Asimov data, respectively. The ratio of the down-going to the up-going events in the neutrino energy bins of the Asimov dataset after the application of unfolding and the factor correction using the different systematic datasets are shown in Fig. 6.5 (left). The corresponding cross section in the neutrino energy bins is shown in Fig. 6.5 (right) where the red band indicates the systematic uncertainty range associated with the change of p_2 in the Asimov test.

To implement the calculation of the p_2 hole ice systematic uncertainty in this analysis, ideally, the simulations of p_2 variations with the 30 cm hole ice scattering length should be used. However, since the discovery that our data is better described by the H2 30 model is very recent, it was not feasible to produce all systematic datasets with H2 30 as a baseline model. To extrapolate the systematic effects to the H2 30 model, which is being used as the baseline of this analysis, the assumption that the systematic effects on the H2 50 model are the same with the effects on the H2 30 model is adopted.

The systematic effect from the change of p_2 parameter on the H2 50 simulation in each neutrino energy bin is shown in Fig. 6.6. Assuming the change in the ratio from $p_2 = 0$

[1] The inconsistency in the top left bins in the top right plot is due to the statistical fluctuations of the simulation in the low energy bins.

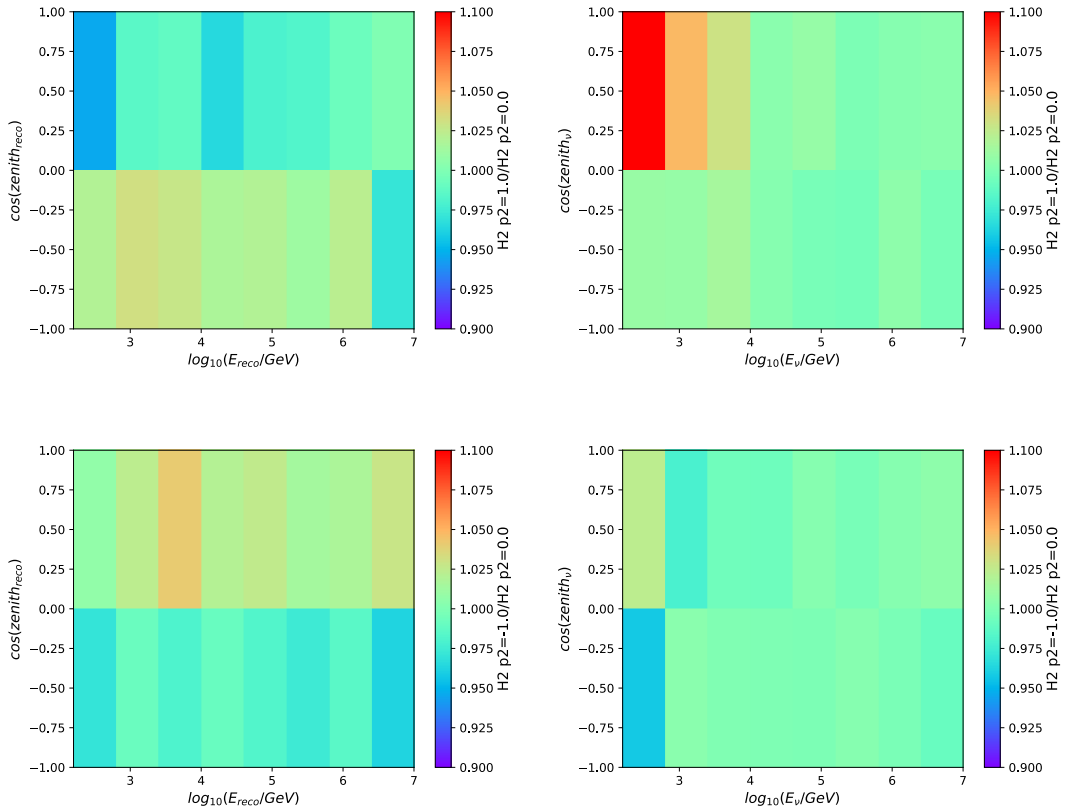

FIGURE 6.4: The ratio of the number of events from the Flasher Hole Ice (p_2 = 1) simulation to the number of events from the Flasher Hole Ice (p_2 = 0) simulation in the reconstructed (top left) and the neutrino (top right) energy and zenith bins for events with all flavors at the final event selection level. The ratio of the number of events from the Flasher Hole Ice (p_2 = -1) simulation to the number of events from the Flasher Hole Ice (p_2 = 0) simulation in the reconstructed (bottom left) and the neutrino (bottom right) energy and zenith bins for events with all flavors at the final event selection level.

to $p_2 = 1$ has the same rate for the H2 50 model and the H2 30 model, the ratio in each neutrino energy bin for the H2 30 model when $p_2 = 1$ can be calculated as:

$$\text{Ratio}_{30,p_2=1}(\text{Bin}_i) = \frac{\text{Ratio}_{50,p_2=1}(\text{Bin}_i)}{\text{Ratio}_{50,p_2=0}(\text{Bin}_i)} \times \text{Ratio}_{30,p_2=0}(\text{Bin}_i) \tag{6.2}$$

Similarly, the ratio in each neutrino energy bin for the H2 30 model when p_2 = -1 can be calculated in the same way as:

$$\text{Ratio}_{30,p_2=-1}(\text{Bin}_i) = \frac{\text{Ratio}_{50,p_2=-1}(\text{Bin}_i)}{\text{Ratio}_{50,p_2=0}(\text{Bin}_i)} \times \text{Ratio}_{30,p_2=0}(\text{Bin}_i) \tag{6.3}$$

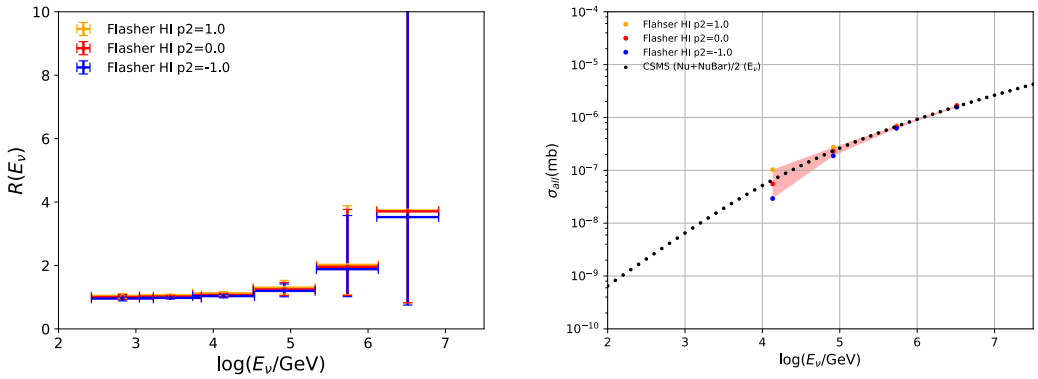

FIGURE 6.5: The systematic uncertainty associated with the p_2 parameter on the ratio ($R(E_\nu)$) (left) and the cross section (right) in the neutrino energy bins, tested with the Asimov data ($p_2 = 0$). The data points of different colors represent the simulation result from the unfolding matrices built with the simulations utilizing different p_2 parameters. The statistical uncertainties are not shown in the right plot.

In this way, the uncertainty due to the H2 30 model can be studied using the systematic simulation of the H2 50 model. The systematic uncertainty associated with the hole ice effect on the cross section measurement result is discussed in Sec. 7.3.2.

6.1.2 The Absorption Length Uncertainty in the South Pole Ice (Bulk Ice)

The bulk ice at the South Pole is modeled with the scattering and absorption coefficient. To study the systematic effect associated with the bulk ice scattering and absorption characteristic, three neutrino simulation datasets of all flavors are generated respectively: 10% increase in the scattering coefficient, 10% increase in the absorption coefficient and 7% decrease in both the scattering coefficient and the absorption coefficient [2].

To study the systematic effect associated with the absorption coefficient, the 10% increase in the absorption coefficient dataset and its relative "baseline" (H2 50) simulation was used. The comparison of +10% absorption simulation and the "baseline" simulation in the reconstructed energy and zenith bins and the true energy and zenith bins are shown in Fig. 6.7. The plots show a consistency in the distribution in the true space. In the reconstructed space, the +10% absorption dataset does not have a noticeable preference in the directional reconstruction compared to the bias caused by changing the p_2 parameter of the hole ice scattering (see Fig. 6.4).

The H2 50 with the baseline value of the absorption coefficient is used as the Asimov data. The unfolding matrices and the correction factors calculated with the datasets simulated with the +10% absorption coefficient, the baseline absorption coefficient, and the -7% absorption and scattering coefficient are applied on the Asimov data. The unfolded and

[2]The hole ice scattering model used in all these simulations is H2 50.

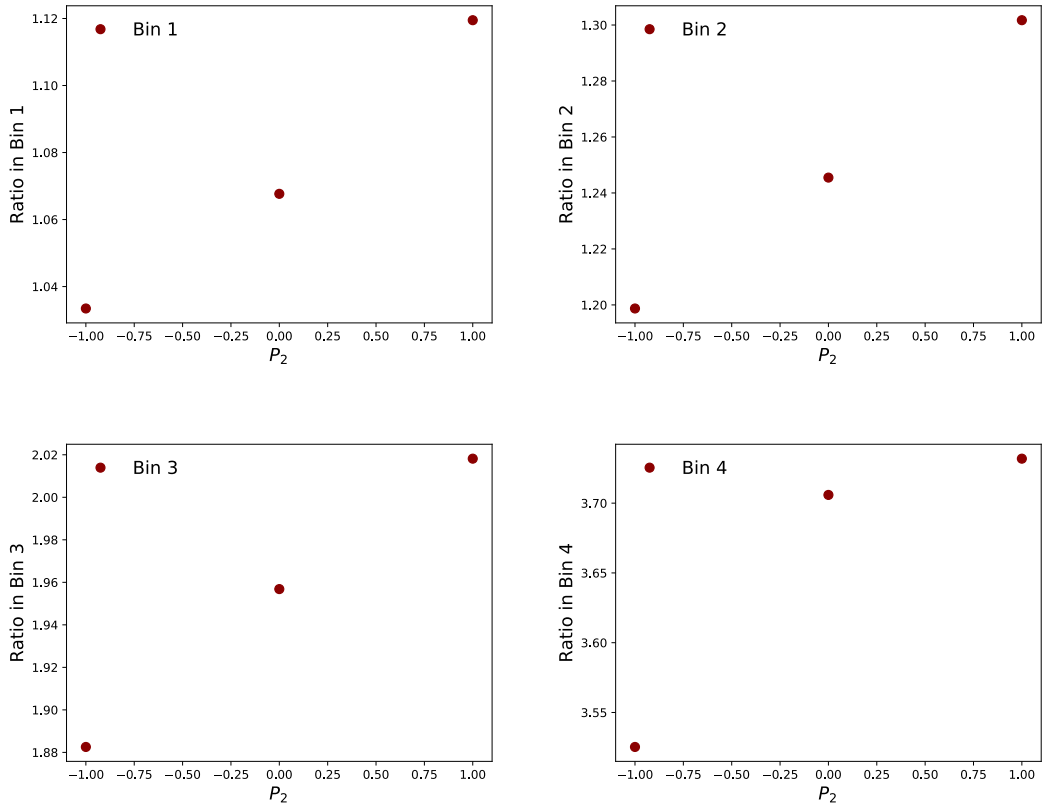

FIGURE 6.6: The unfolded and factor corrected ratio of the $p_2 = 0$ Asimov data using the p_2 = -1, 0, 1 H2 50 simulation in different neutrino energy bins.

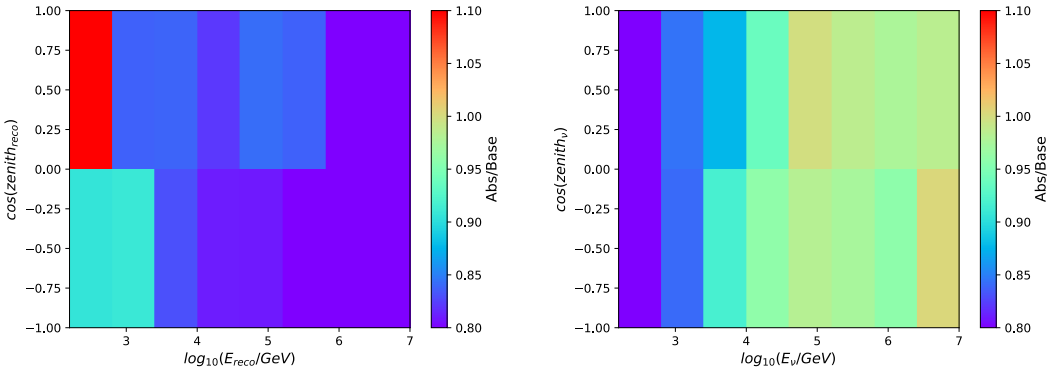

FIGURE 6.7: The 10% increase in the absorption coefficient simulation/baseline (H2 50) simulation in the reconstructed (left) and the neutrino (right) energy and zenith bins for all flavors at the final event selection level.

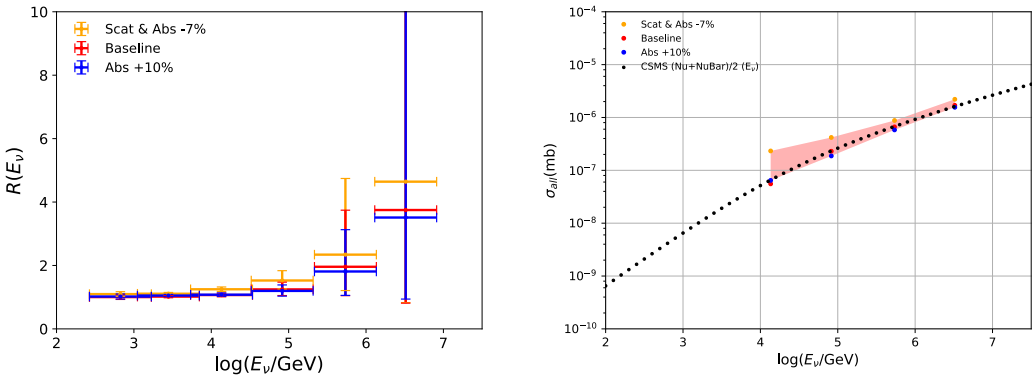

FIGURE 6.8: The systematic uncertainty associated with the change on the absorption coefficient in the bulk ice on the ratio ($R(E_\nu)$) (left) and the cross section (right) in the neutrino energy bins tested with the Asimov data (H2 50). The data points of different colors represent the simulation result from the unfolding matrices built with the simulation utilizing different variations on the absorption coefficient. The statistical uncertainties are not shown in the right plot.

corrected ratios of the Asimov data in the neutrino energy bins are shown in Fig. 6.8 (left) and the corresponding cross sections are shown in Fig. 6.8 (right). The plots show that the cross section result from the absorption baseline simulation and the +10% absorption simulation are consistent, while the cross section result from the -7% scattering and absorption simulation are inconsistent with the other two. This observation suggests that the increase/decrease in the absorption coefficient will have little effect on the cross section measurement, thus can be neglected for the systematic uncertainty estimation. The difference between the cross section result processed with the -7% scattering and absorption simulation and the baseline simulation is likely to be caused by a change in the scattering coefficient.

6.1.3 The Scattering Length Uncertainty in the South Pole Ice (Bulk Ice)

To study the systematic effect associated with the scattering coefficient, a 10% increase in the scattering coefficient dataset and its relative "baseline" (H2 50) simulation is used. The comparisons of +10% scattering simulation and the "baseline" simulation in the reconstructed energy and zenith bins and the true energy and zenith bins are shown in Fig. 6.9. The plots show a consistency in the distribution in the true space. In the reconstructed space, the +10% scattering dataset reconstruction has a noticeable preference in the direction, which likely affects the cross section.

The Asimov test uses the baseline of the scattering coefficient (H2 50) simulation as the input data. The unfolding matrices and the correction factors calculated with the dataset simulated with the +10% scattering coefficient, baseline scattering coefficient, and -7% absorption and scattering coefficient are applied on the Asimov data. The unfolded and

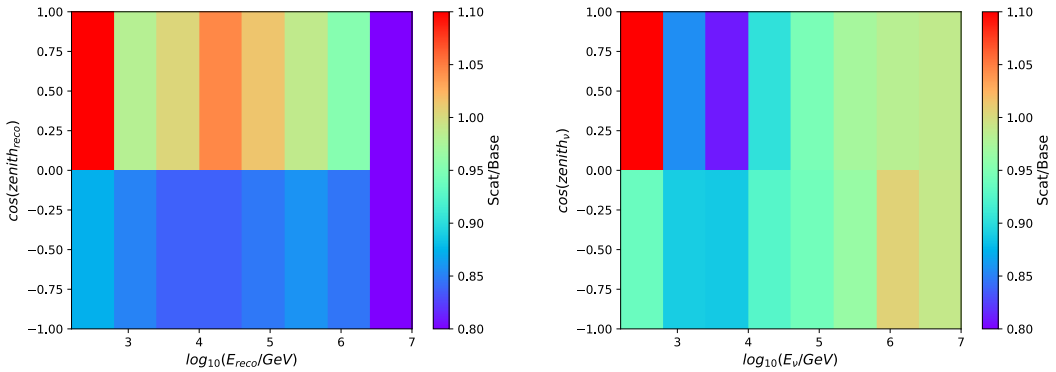

FIGURE 6.9: The 10% increase in the scattering coefficient simulation/baseline (H2 50) simulation in the reconstructed (left) and the neutrino (right) energy and zenith bins for neutrinos of all flavors at the final event selection level.

corrected ratios of the Asimov dataset in the neutrino energy bins are shown in Fig. 6.10 (left) and the corresponding cross sections are shown in Fig. 6.10 (right). The plots show that the change in the scattering coefficient does have an impact on the cross section result.

The fact that the seemingly small systematic uncertainties in the ratio in the lower energy bins is translated into larger systematic uncertainties for the cross section and the relatively large systematic uncertainties in the ratio in the high energy bins is translated into smaller systematic uncertainties for the cross section can be explained by Fig. 4.4. Fig. 4.4 shows that the ratio increases slowly with the increase of the cross section, when the cross section value is small and the curve becomes more steep for large cross section values. This indicates that for small cross section values, the little change in the ratio can be mapped into to relatively large change in the cross section value while for large cross section values the relatively large change in the ratio could only be mapped into a small change in the cross section value.

As shown in Fig. 6.10, the lower limit on the systematic uncertainty associated with the scattering coefficient for the first data point is infinity. This is due to the fact that the ratio in the first energy bin is smaller than 1 when unfolded with the +10% scattering coefficient simulation. Figure 4.4 shows that when the cross section is smaller than a certain value the ratio stays at $\sim$1 regardless of the change in the cross section value. This feature suggests that when the ratio is smaller than 1, the method can not determine the corresponding cross section, and the cross section can have any value below the threshold.

Since the change in the scattering coefficient is likely to have an impact on the cross section, it is taken into consideration when estimating the systematic uncertainty. The variation range of the scattering coefficient proposed by the IceCube collaboration is (-10%, +10%). The current available simulated datasets are the baseline simulation (H2 50), the scattering coefficient +10% simulation, and the scattering and absorption coefficient -7% simulation. To extrapolate the -10% scattering coefficient, only the first two datasets are used.

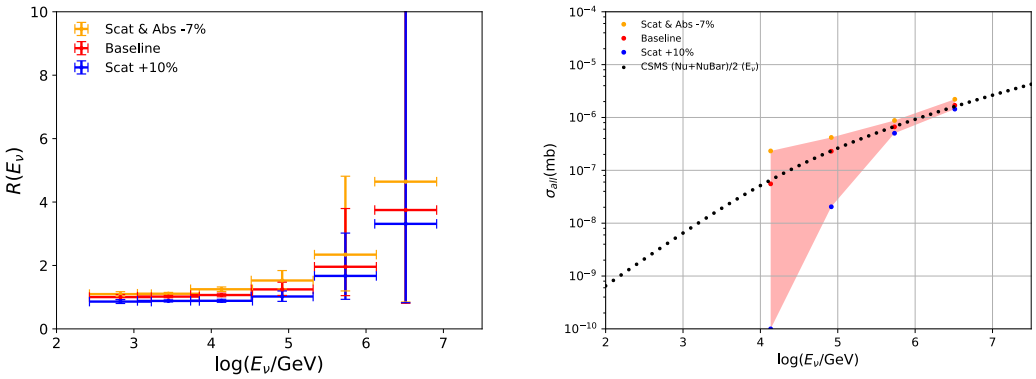

FIGURE 6.10: The systematic uncertainty associated with the change on the scattering coefficient on the ratio ($R(E_\nu)$) (left) and the cross section (right) in the neutrino energy bins tested with the Asimov data (H2 50). The data points of different colors represent the simulation result from the unfolding matrices built with the simulation utilizing different variations on the scattering coefficient. The statistical uncertainties are not shown in the right plot.

The unfolded and factor corrected ratios ($R(E_\nu)$) in each neutrino energy bin of the Asimov data using the baseline simulation and the +10% scattering simulation are shown in Fig. 6.11. The baseline scattering is factorized as 100% and the +10% scattering as 110%. Assuming the change of the ratio due to the change in the scattering percentage follows a linear relationship, it can be expressed as the equation below.

$$\frac{\text{Ratio}_{scat,x,50}}{\text{Ratio}_{scat,1.0,50}} = x \times A + B \tag{6.4}$$

There are two data points to Eq. 6.4 : 1.0 and 1.0, which can be used to solve for A and B:

$$\begin{cases} \frac{\text{Ratio}_{scat,1.0,50}}{\text{Ratio}_{scat,1.0,50}} = 1.0 \times A + B \\ \frac{\text{Ratio}_{scat,1.1,50}}{\text{Ratio}_{scat,1.0,50}} = 1.1 \times A + B \end{cases} \tag{6.5}$$

The solution to Eq. 6.5 is:

$$\begin{cases} A = (\frac{\text{Ratio}_{scat,1.1,50}}{\text{Ratio}_{scat,1.0,50}} - 1)/0.1 \\ B = 1 - A \end{cases} \tag{6.6}$$

Once A and B are calculated, the ratio for -10% (90%) scattering can be calculated using Eq. 6.4 with x substituted by 0.9.

$$\frac{\text{Ratio}_{scat,0.9,50}}{\text{Ratio}_{scat,1.0,50}} = 0.9 \times A + B \tag{6.7}$$

Above are the extrapolations of the H2 50 model simulations. Due to the lack of the bulk ice scattering variation systematic datasets of the H2 30 model, we can extrapolate the effect from the H2 50 simulations. Assuming the variation of the bulk ice scattering coefficient has the same effect on H2 30 simulation and H2 50 simulation, the change in ratio for both hole ice models follows the same linear relationship:

$$\frac{\text{Ratio}_{scat,x,30}}{\text{Ratio}_{scat,1.0,30}} = x \times A + B \tag{6.8}$$

Therefore, the +10% (110%) scattering and the -10% (90%) scattering effect of the H2 30 baseline can be calculated as:

$$\text{Ratio}_{scat,x,30} = \text{Ratio}_{scat,1.0,30} \times (x \times A + B) \tag{6.9}$$

6.2 The Detector Response - the Relative DOM Efficiency

Apart from the systematic effect associated with the ice properties, the DOM efficiency can potentially have an effect as well. The true relative DOM efficiency (ϵ_0) depends on the rate of light detection. Assuming an event deposits E_0 energy into the detector, the number of photons (n_0) observed by the DOMs can be expressed as:

$$n_0 = C\epsilon_0 E_0 \tag{6.10}$$

where C is a known constant involving the transformation from the deposited energy to photons. It also includes the absolute PMT photon detection efficiency, quantum and photon collection efficiency, and other effects. The energy reconstruction is a process used to reconstruct the deposited energy from the observed photons:

$$E_{reco} = \frac{n_0}{C\epsilon} \tag{6.11}$$

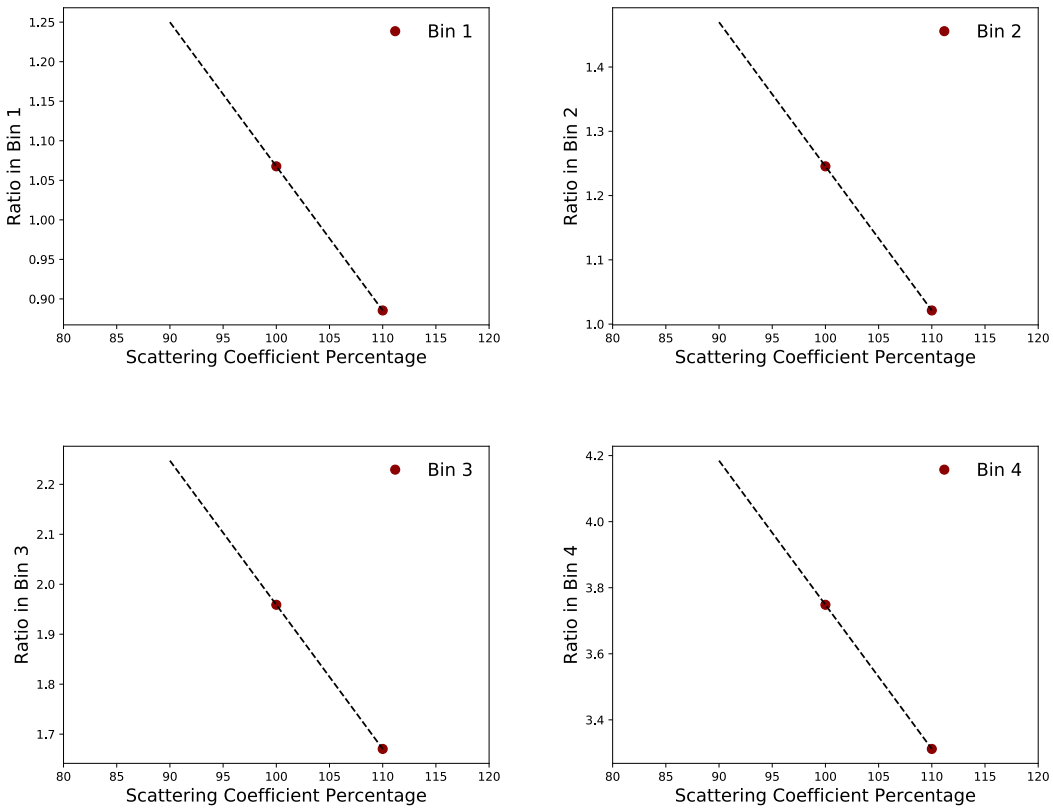

FIGURE 6.11: The unfolded and factor corrected ratio of the baseline scattering Asimov data using the baseline scattering and the +10% simulation in different neutrino energy bins. (H2 50)

where ϵ is the relative DOM efficiency we assumed for the DOMs. If $\epsilon = \epsilon_0$, the reconstructed energy will be relatively accurate. When $\epsilon < \epsilon_0$, the reconstructed energy will be overestimated and vice versa.

The ϵ used in the IceCube analyses is 99%, and it also represents the relative DOM efficiency used in the baseline simulation. The uncertainty on the relative DOM efficiency measured by the IceCube collaboration is $\pm$ 9%. Systematic simulation datasets are generated with 90%, 95%, and 108% relative DOM efficiency, respectively [3].

The comparison between the relative DOM efficiency systematic simulations and the baseline (99%) simulation are shown in Fig. 6.12. When the relative DOM efficiency in the simulation is smaller than that the assumed for the relative DOM efficiency (99%) in the reconstruction, the rate in the reconstructed energy and direction bins are smaller than the baseline simulation and vice versa. This is expected based on Eq. 6.10 and 6.11.

The event rates are comparable for all the DOM efficiency simulations except in the low neutrino energy bins. This difference is due to the threshold effect of the event

[3]The hole ice scattering model used in these simulations are all H2 50

selection. When $\epsilon_0 < \epsilon$, the reconstructed energy of a certain event is smaller than when $\epsilon_0 = \epsilon$. Therefore, it may not be able to pass some reconstructed-energy-related cut in the systematic simulation while it passes such selection in the baseline simulation.

The change in the reconstructed and true distributions associated with the change of the DOM efficiency is mostly homogenous. The change of DOM efficiency does not bring a bias in the reconstructed direction. Therefore it is likely that the change of the DOM efficiency will have little impact on the cross section result.

The Asimov test uses the baseline of the DOM efficiency (99%) simulation as the input data. The unfolding matrices and the correction factors calculated with the dataset simulated with the DOM efficiency of 90%, 95%, 99%, and 108% are applied on the Asimov data. The unfolded and corrected ratios of the Asimov data in the neutrino energy bins are shown in Fig. 6.13 (left) and the corresponding cross sections are shown in Fig. 6.13 (right). The plots show that the change in DOM efficiency has very little impact on the cross section result as we predicted. Therefore the systematic uncertainty associated with the DOM efficiency is neglected.

6.3 The Earth Atmosphere

The major systematic effect associated with the Earth atmosphere comes from two parts: the conventional atmospheric neutrino flux and the self-veto effect that exists in both the conventional and the prompt atmospheric neutrino fluxes. In this section, these effects will be discussed and estimated.

6.3.1 The Conventional Atmospheric Neutrino Flux

The conventional atmospheric neutrino flux used in this analysis is calculated using the Honda Model [28] which utilized the U.S. Standard 1976 [115] atmosphere model. The calculation does not take into consideration of the South Pole location of the IceCube detector and the fact that the atmosphere above the South Pole is much cooler compared to the rest of the Earth. It also does not take into consideration of the seasonable fluctuation of the atmospheric temperature.

To make a more realistic estimation of the conventional atmospheric neutrino flux, the NRLMSISE00 [116] model was used. The NRLMSISE00 model is an empirical atmospheric model that models the temperature and the density of the atmosphere. Since the experimental data used in this analysis were collected continuously for five years, in the conventional flux calculation, the atmospheric data used are the average between winter and the summer seasons.

The newly calculated conventional neutrino flux for electron neutrinos, electron antineutrinos, muon neutrinos, and muon antineutrinos are shown in Fig. 6.14 in comparison with the original conventional neutrino flux. The plots show that the flux calculated using the more accurate model does show a difference from the one calculated using the

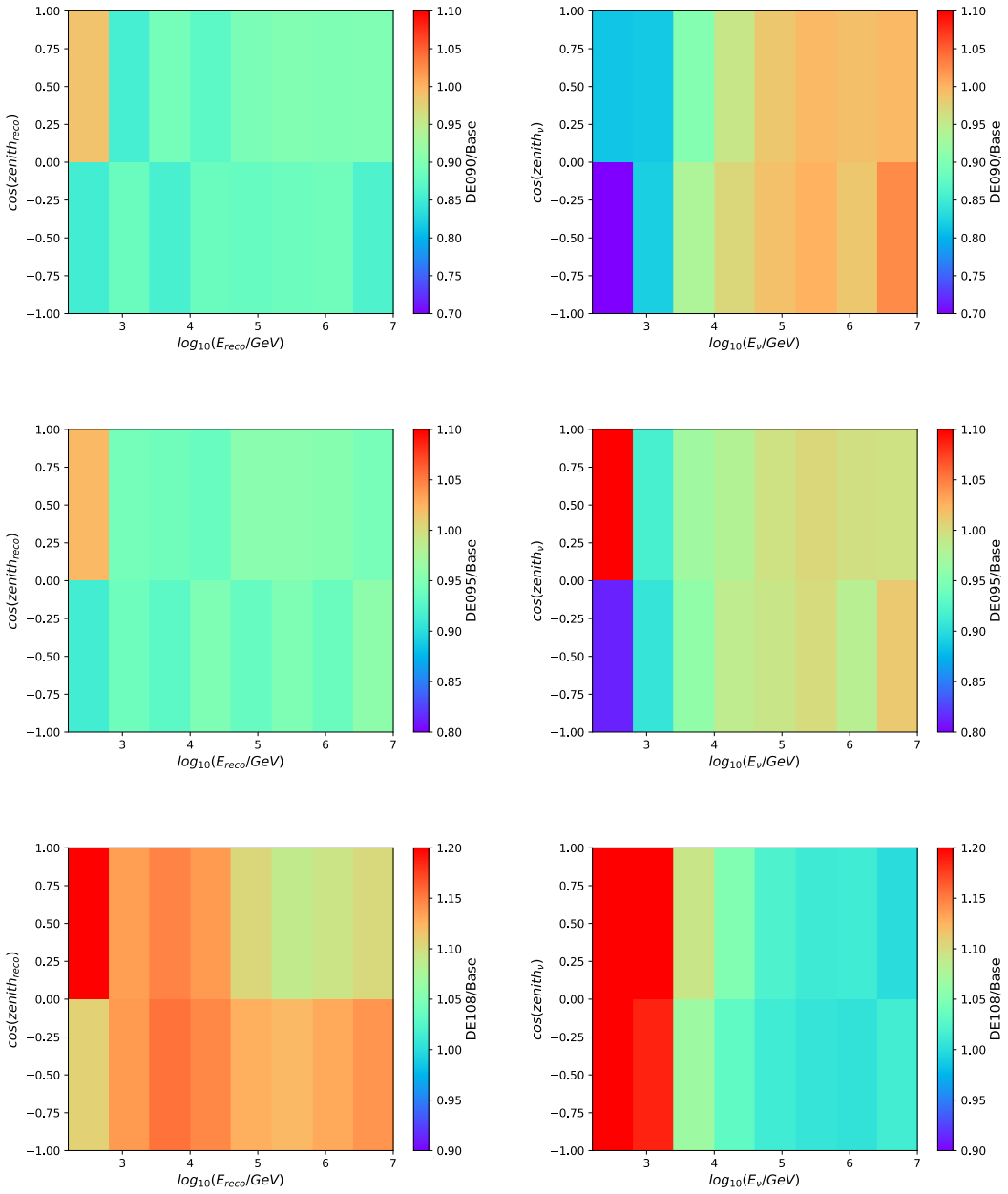

FIGURE 6.12: DOM efficiency = 90% simulation/ DOM efficiency = 99% simulation in the reconstructed (top left) and the neutrino (top right) energy and zenith bins for neutrinos of all flavors at the final event selection level. DOM efficiency = 95% simulation/ DOM efficiency = 99% simulation in the reconstructed (middle left) and the neutrino (middle right) energy and zenith bins for neutrinos of all flavors at the final event selection level. DOM efficiency = 108% simulation/ DOM efficiency = 99% simulation in the reconstructed (bottom left) and the neutrino (bottom right) energy and zenith bins for neutrinos of all flavors at the final event selection level.

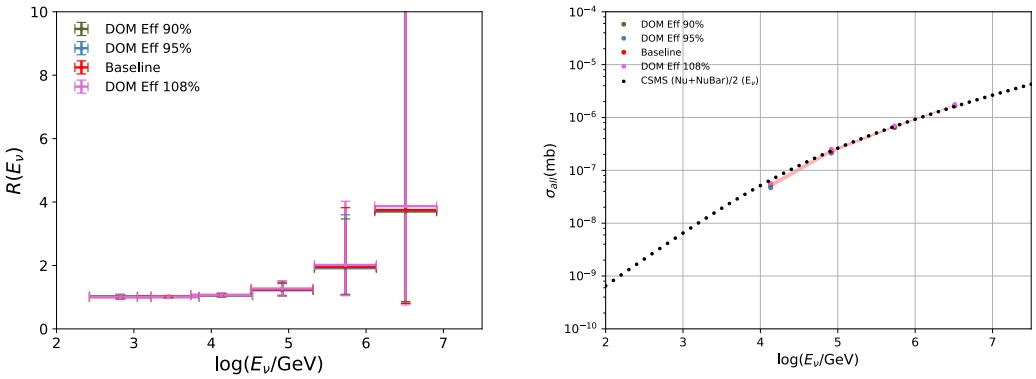

FIGURE 6.13: The systematic uncertainty associated with the relative DOM Efficiency on the ratio ($R(E_\nu)$) (left) and the cross section (right) in the neutrino energy bins tested with the Asimov data (H2 50). The data points of different colors represent the simulation result from the unfolding matrices built with the simulation utilizing different relative DOM efficiencies. The statistical uncertainties are not shown in the right plot.

older model. The difference is relatively small (a few percents) and is mainly located in the up-going region.

The small difference in the conventional flux calculations indicates that the impact of using the updated atmospheric model might be small on this analysis. The total event rates of the baseline simulation (H2 30) for neutrinos of all flavors at the final event selection level are calculated with the NRLMSISE00 conventional flux and the U.S. Standard 1976 conventional flux respectively with all the other parameters (the astrophysical neutrino flux, the prompt atmospheric neutrino flux, the normalization of the fluxes) kept the same. The comparison between the two total rates is shown in Fig. 6.15.

It is expected that the difference between the total rates are mostly in the low energy region where the conventional neutrino flux dominates. In the high energy region, where the astrophysical neutrino flux dominates, the difference between the conventional neutrino flux will have little impact on the total event rate. Even in the low energy region, the difference is smaller than 2%.

The Asimov test uses the baseline simulation (H2 30) with the conventional flux calculated with the U.S. Standard 1976 model as the Asimov data. The Asimov data was treated with unfolding matrices and the correction factors calculated using event rates from the two atmospheric models respectively. The unfolded and corrected ratios of the Asimov data in the neutrino energy bins are shown in Fig. 6.16 (left) and the corresponding cross sections are shown in Fig. 6.16 (right). The systematic uncertainty associated with the atmospheric model is very small, thus neglected.

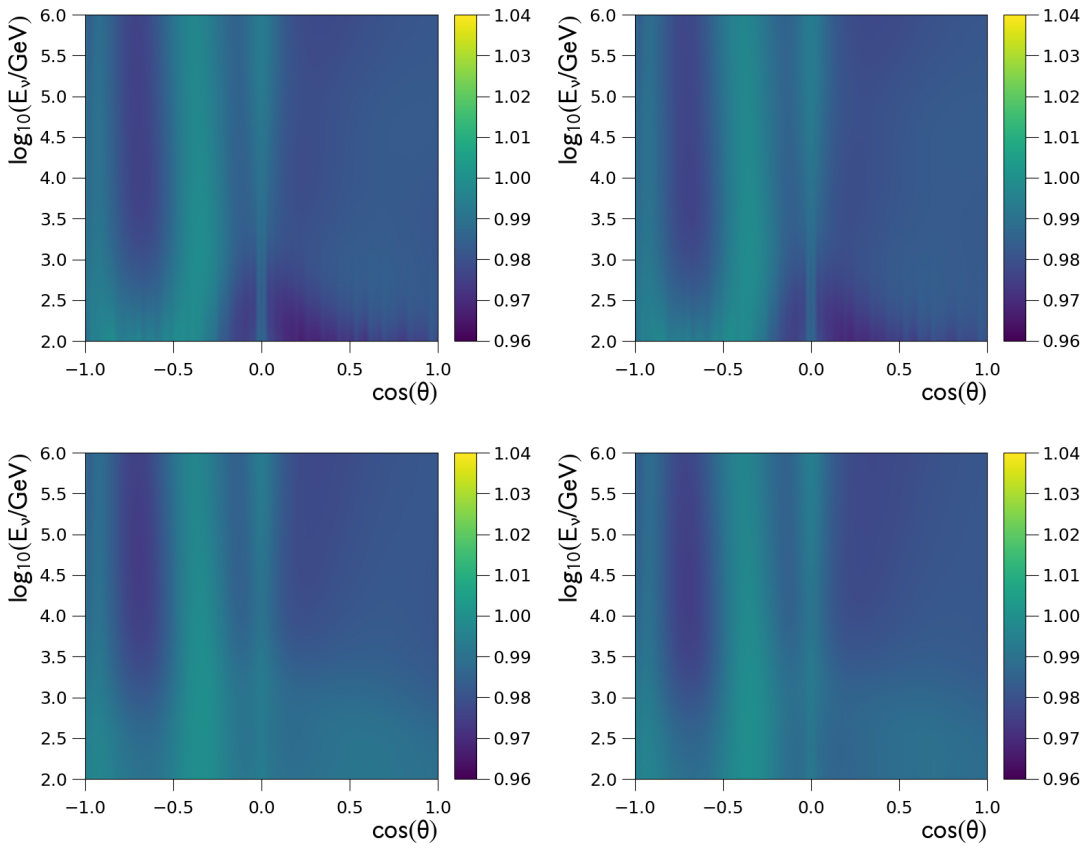

FIGURE 6.14: The ratio of the conventional atmospheric neutrino flux calculated using the NRLMSISE00 model to the one using the U.S. Standard 1976 model in the neutrino energy and zenith bins for ν_e (top left), $\bar{\nu}_e$ (top right), ν_μ (bottom left) and $\bar{\nu}_\mu$ (bottom right). The data used to make these plots are from Ref. [116] and Ref. [115]. The plots are provided by H. M. Niederhausen.

6.3.2 The Self-Veto Effect for Atmospheric Neutrinos

The self-veto effect was originally described in Ref. [109]. The publication mainly focused on the case of the charged pion and kaon two-body decay:

$$\pi^{\pm} \rightarrow \mu^{\pm} + \nu_{\mu}(\bar{\nu}_{\mu}) \tag{6.12}$$

$$K^{\pm} \rightarrow \mu^{\pm} + \nu_{\mu}(\bar{\nu}_{\mu}) \tag{6.13}$$

The filtering system in IceCube and the event selection developed for this analysis are designed to remove muons. When the decay product muon arrives at the detector in the vicinity of the neutrino, the neutrino will be vetoed together with the muon. Ref. [109] reports that in the case of charged pion decay the distances between the muon and the neutrino after a 10 km path is less than 1 m (0.1 m) when the neutrino energy is above 1 TeV (10 TeV). The distance is less than 10 m (1m) in the case of charged kaon decay

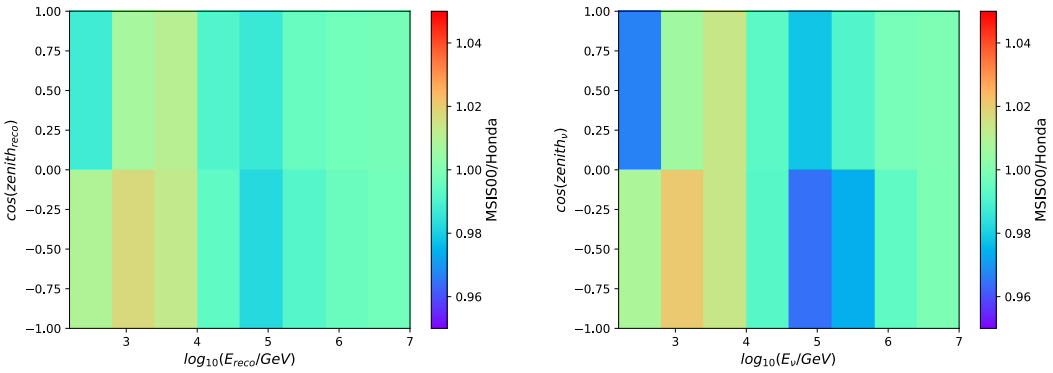

FIGURE 6.15: The comparison between the total event rate calculated with the NRLMSISE00 conventional flux and the U.S. Standard 1976 conventional flux in the reconstructed (left) and true (right) energy and zenith bins for the baseline simulation (H2 30) for neutrinos of all flavors at the final event selection level.

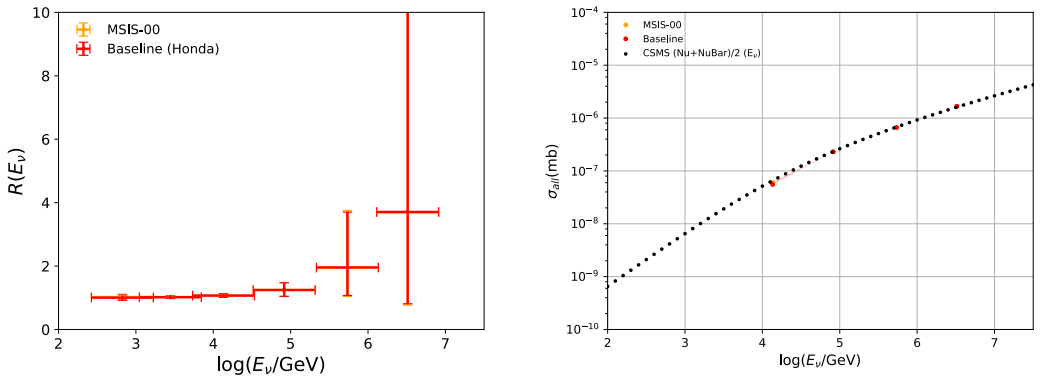

FIGURE 6.16: The systematic uncertainty associated with the atmospheric model on the ratio ($R(E_\nu)$) (left) and the cross section (right) in the neutrino energy bins tested with the Asimov data (H2 30). The data points of different colors represent the result from the unfolding matrices built with the conventional neutrino flux calculated using different atmospheric models. The statistical uncertainties are not shown in the right plot.

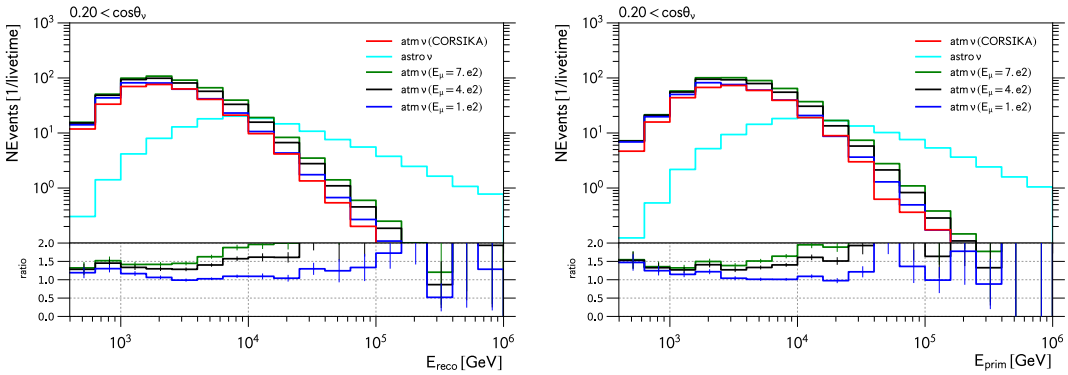

FIGURE 6.17: The comparison between the self-veto effect calculated with different $E_{\mu,\mathrm{min}}$s and the event rate of the atmospheric neutrino with the full CORSIKA simulation in the reconstructed energy bins (left) and in the neutrino energy bins (right). The plots are from Ref. [88].

for the same conditions. This distance is sufficiently small for neutrinos to be vetoed due to the accompanied muons.

The self-veto effect only exists for atmospheric neutrinos originated from the southern hemisphere, since the accompanied muons from the northern hemisphere are all absorbed by the Earth before reaching the detector. This causes a difference in the signal efficiency in the down-going region and the up-going region which is crucial for calculating detector acceptance correction factors (c.f. Sec. 4.3.1) and for building the unfolding matrices (c.f. Chapter 5) in this analysis. It is important to correctly model the veto probability for different neutrino energy and zenith regions for different neutrino flavors. Ref. [93] introduced a method to parameterize the veto probability with one parameter $E_{\mu,\mathrm{min}}$. $E_{\mu,\mathrm{min}}$ is the minimum energy of the muon needed to trigger the veto effect when it reaches the detector.

When we consider the systematic uncertainty associated with the self-veto effect, we are considering the uncertainty of $E_{\mu,\mathrm{min}}$. A study done in Ref. [88] has shown that the choice of $E_{\mu,\mathrm{min}} = 100$ GeV for the event selection of this analysis provides an excellent description of the self-veto effect. The study was conducted using a full CORSIKA [85] simulation which includes the production and the propagation of the neutrinos and muons. The simulation was processed through all the filters and the event selections of this analysis. By simulating the full chain of the atmospheric neutrino production, the event rate expectation from this simulation will reflect the real self-veto effect. By comparing the self-veto effect calculated using different $E_{\mu,\mathrm{min}}$s with the atmospheric neutrino rate expectation from the full CORSIKA simulation, it is concluded that the choice of $E_{\mu,\mathrm{min}} = 100$ GeV provides the best resemblance of the full CORSIKA simulation (Fig. 6.17). Due to the good agreement between the self-veto effect predicated by $E_{\mu,\mathrm{min}} = 100$ GeV and the one from the full CORSIKA simulation, the uncertainty on $E_{\mu,\mathrm{min}}$ should be small. Hence the systematic uncertainty associated with the self-veto effect can be neglected for this analysis.

6.4 The Astrophysical Neutrino Flux

One of the advantages of utilizing the ratio of the down-going events to the up-going events in this analysis is the astrophysical neutrino flux independence. With a general and reasonable assumption of the astrophysical neutrino flux being isotropic, the flux component in both the denominator and the numerator in Eq. 4.4 cancel out.

The astrophysical neutrino flux independence makes this method unique from some of the other cross section measurements conducted with the IceCube data [117], [118], where in both Refs. the assumption about the shape of the astrophysical neutrino flux model was made. The only step in this analysis that involves the shape of the astrophysical neutrino flux is the building of the unfolding matrices. The unfolding matrices reflect the kinematics of the neutrino interaction. They are formed by the probabilities of a neutrino depositing a certain amount of energy into the detector from its primary energy. These probabilities are neutrino flavor dependent. Therefore, the flavor ratio determines the element values for the unfolding matrices. While the neutrino flavor ratio in the astrophysical neutrino predominant energy region and the atmospheric neutrino predominant energy region are fixed, the flavor ratio in the transition region is dependent of the composition of the two. Therefore the shape of the astrophysical neutrino flux could have an impact of the unfolding matrices in this energy region.

The uncertainty of the astrophysical neutrino flux used to estimate its impact on the cross section measurement is chosen as the 68% confidence level contour as shown in the left plot of Fig. 6.18. The contour is formed by the combinations of the astrophysical neutrino flux index and the normalization parameter. The data shown in Fig. 6.18 (left) is from Ref. [88]. The Asimov data is the baseline simulation (H2 30) weighted with the best fit result of the astrophysical neutrino flux. Different unfolding matrices built with the same simulation weighted using different astrophysical neutrino flux parameters from the contour are used to unfold the Asimov data. The cross section measurement results of these tests are shown in the right plot of Fig. 6.18. The red band covers the range of the minimum to the maximum value among all the test results in each neutrino energy bin. The plot shows that the impact of the uncertainty on the astrophysical neutrino flux is mainly in the energy bin of $10^{3.8}$ - $10^{4.6}$ GeV where the transition from the atmospheric neutrino predominant energy region to the astrophysical neutrino predominant energy region happens, and it's relatively small compared to the systematic uncertainty associated with the ice scattering coefficient.

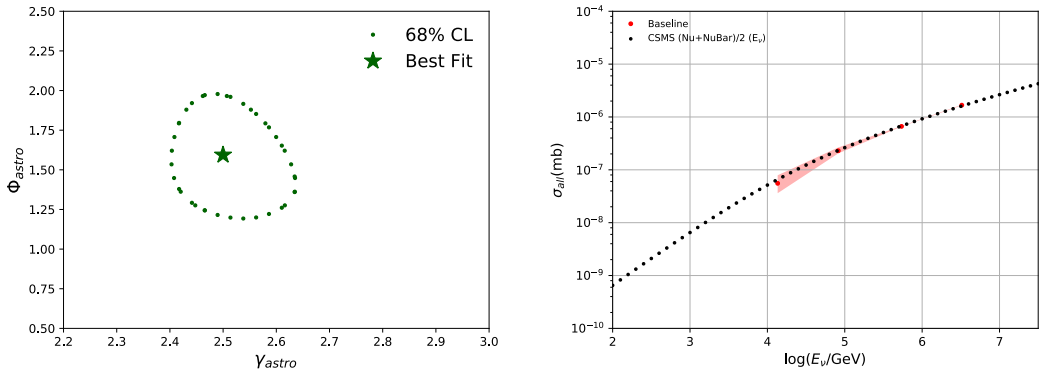

FIGURE 6.18: Left: the 68% confidence level contour of the fit result of the astrophysical neutrino flux (data provided by Ref. [88]) with the best fit value indicated by the star in the center of the contour. Right: the systematic uncertainty associated with the astrophysical neutrino flux (red band) in the cross section measurement result of the Asimov Data. The statistical uncertainties are not shown in the right plot.

Chapter 7

Results

In the previous chapter, we discussed the analysis method and the method to estimate the statistical and systematic uncertainty on the neutrino cross section. The validation of the methods was done with Monte Carlo simulation. The impacts from different systematic parameters were also estimated using Monte Carlos simulation.

In this chapter, we describe the application of the analysis method on the unblinded experimental data. The neutrino interaction cross section measurement result using the five years of IceCube data is presented along with the statistical and systematic uncertainty. The result is compared with two other cross section measurements using different datasets from the IceCube data as well as theoretical predictions. The p-value for the result is calculated and presented.

7.1 Analysis Procedure Summary

The procedure of the analysis can be summarized as below:

- Obtain the distribution of the final level experimental data and the MuonGun background simulation in reconstructed energy and zenith bins. The six reconstructed energy bins are evenly distributed in the logarithmic scale $[\log_{10}(E_{reco}/\text{GeV})]$ from 2.2 to 7. The two reconstructed zenith bins are from 0^o to 90^o (down-going) and from 90^o to 180^o (up-going).
- The Monte Carlo background rates are subtracted from the experimental data rates in each reconstructed energy and zenith bin to obtain the neutrino rate.
- The neutrino rates in the reconstructed energy and zenith bins are used as the input for the unfolding procedure. The unfolding matrices were built with the baseline neutrino Monte Carlo simulation at the final level.
- The unfolded neutrino rates from the experimental data in the neutrino energy and zenith bins are used to form the ratios of down-going events to up-going events. This ratio in each neutrino energy bin is used to find the corresponding cross section.

Energy Range [log(E_ν/GeV)]	2.2 - 3.0	3.0 - 3.8	3.8 - 4.6	4.6 - 5.4	5.4 - 6.2	6.2 - 7.0
Down-going	117^{+14}_{-14}	785^{+35}_{-36}	363^{+25}_{-24}	73^{+11}_{-11}	$4.4^{+2.4}_{-2.3}$	$1.5^{+1.2}_{-1.3}$
Up-going	565^{+30}_{-30}	1918^{+51}_{-52}	554^{+29}_{-29}	50^{+9}_{-9}	$1.5^{+1.2}_{-1.0}$	$0.037^{+0.044}_{-0.026}$

TABLE 7.1: The number of down-going and up-going events in the neutrino energy bins for the unblinded data after unfolding with statistical uncertainties.

- The neutrino rate from the experimental data in the reconstructed energy and zenith bins are unfolded with unfolding matrices built with the systematic neutrino Monte Carlo simulations at the final level to estimate the systematic uncertainty on the measured cross section.

7.2 Unfolding Result

7.2.1 Unfolded Distribution

The number of events for data and Monte Carlo in the reconstructed space are shown in Table 3.14 and 3.15. The corresponding distribution plots are shown in the top row of Fig. 7.1. As discussed in Chapter 6, the Monte Carlo simulation used as the baseline is the H2 holeice model with 30 cm scattering length (H2 30).

The unfolding method described in Sec. 5.1 is applied to the data using the unfolding matrix built with the H2 30 simulation. The unfolded number of events of the unblinded data in neutrino energy bins and in the true down-going and true up-going directions are shown in Table 7.1. The method for the estimation of the statistical uncertainties shown in the table was shown in Sec. 5.2.1. The corresponding distribution of the unfolded data and Monte Carlo in the neutrino space are shown in the bottom row of Fig. 7.1.

7.2.2 Statistical Uncertainty Calculation

The statistical uncertainty was estimated using MCMC (c.f.Sec. 5.2.1). The sampling was done according to the distribution of the unblinded data in the reconstructed space. Each sample is unfolded using the same procedure as used on the experimental data. The posterior distribution of the sampling in the true space is shown in Fig. 7.2. The uncertainty range on the posterior distribution to ensure the 68% coverage in the statistical uncertainty is chosen as: 68% for the first four energy bins, 80 % for the fifth energy bin and 90% for the last energy bin due to the little statistics in the last two energy bins (c.f.Sec. 5.2.2).

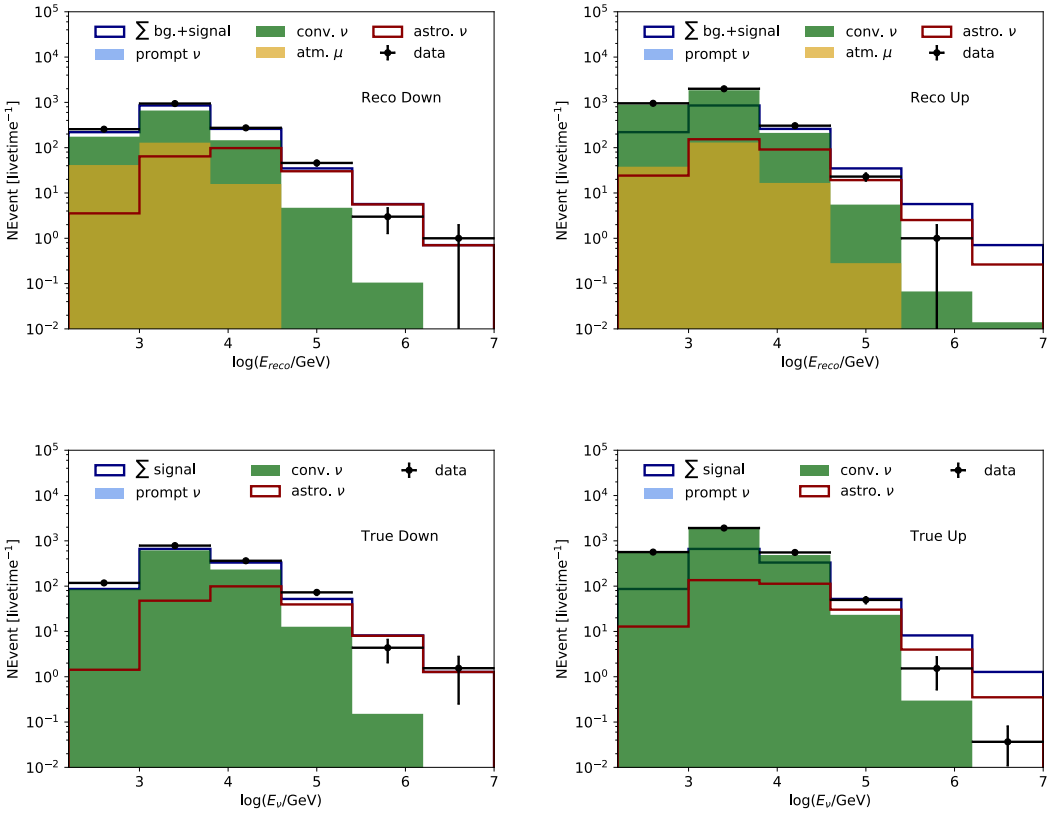

FIGURE 7.1: The reconstructed energy distribution for down-going events (top left) and up-going events (top right). The unfolded distribution in neutrino energy bins for true down-going events (bottom left) and true up-going events (bottom right).

7.3 Cross Section Measurement Result

7.3.1 Statistical Uncertainty

Finally, we calculate the ratio of the unfolded number of down-going to up-going events, corrected for the detector acceptance effect with Eq. 4.9 and Table 4.1. The statistical uncertainty on this ratio was calculated using MCMC. The unfolded ratios of the unblinded data in neutrino energy bins are shown in the left plot of Fig. 7.3 and its posterior distribution of the MCMC sampling is shown in the right plot of Fig. 7.3 with the center value of the ratio indicated with black lines and the 68% confidence level of the statistical uncertainty indicated with colored lines.

We find the cross section value for each ratio in neutrino energy bins utilizing the ratio-cross section correlation as shown in Fig. 4.4. The upper and lower value of the ratio statistical uncertainty was used to find the corresponding statistical uncertainty on the cross section. The result with the statistical uncertainty is shown in Fig. 7.4. As discussed in Sec. 4.4.1, at low neutrinos energies, when the cross section value is low, the Earth

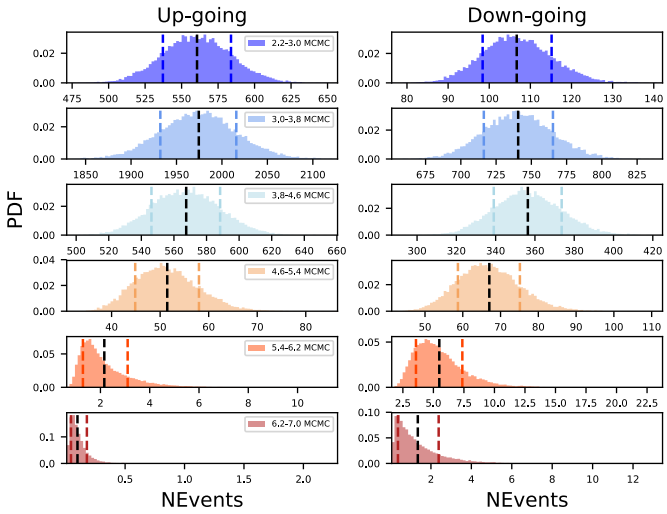

FIGURE 7.2: The unfolded number of events posterior distribution for the unblinded data in all neutrino energy and zenith bins. The vertical black lines indicate the central value and the vertical colored lines indicate the 68% statistical uncertainty range.

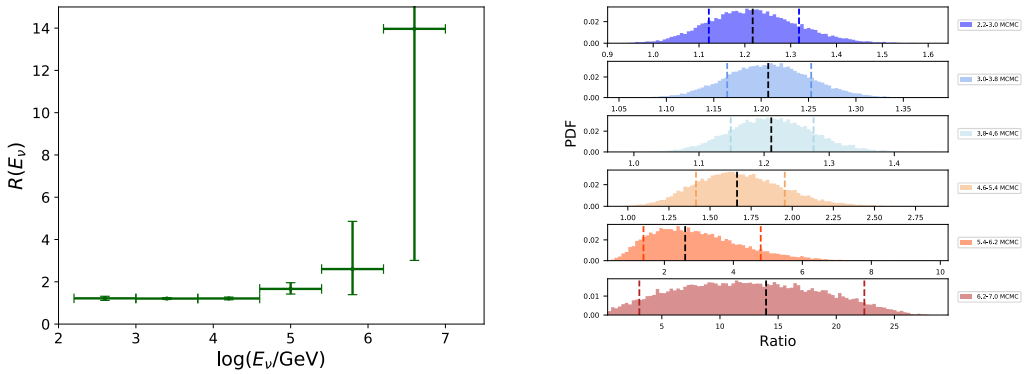

FIGURE 7.3: Left: the unfolded ratio of the unblinded data in neutrino energy bins with statistical uncertainty. Right: the unfolded ratio posterior distribution of the unfolded ratio from the MCMC in neutrino energy bins. The vertical black lines indicate the central value and the vertical colored lines indicate the statistical uncertainty at 68% C. L.

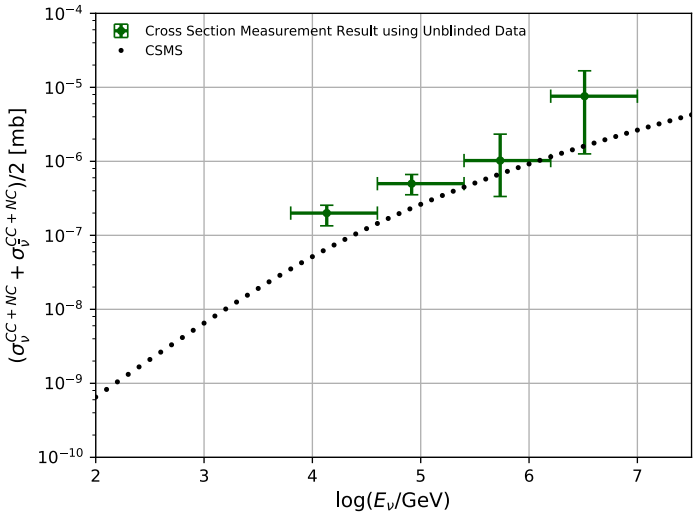

FIGURE 7.4: The cross section measurement result of the unblinded data and its statistical uncertainty (68% C. L.).

Energy Range [log(E_ν/GeV)]	3.8 - 4.6	4.6 - 5.4	5.4 - 6.2	6.2 - 7.0
Bin Center Value	$4.133^{+0.004}_{-0.006}$	$4.916^{+0.011}_{-0.015}$	$5.734^{+0.001}_{-0.017}$	$6.513^{+0.010}_{-0.015}$
Cross Section [mb]	$2.00^{+0.54}_{-0.65} \times 10^{-7}$	$5.0^{+1.6}_{-1.5} \times 10^{-7}$	$1.02^{+1.26}_{-0.68} \times 10^{-6}$	$7.6^{+8.8}_{-6.4} \times 10^{-6}$

TABLE 7.2: The cross section measurement result of the 2011-2015 IceCube cascade sample and its statistical uncertainty (68% C. L.).

absorption effect has little significance and the ratio is inseparable from 1. In Chapter 6, we have shown that the systematic effects are dominant at lower energies. Therefore only the statistically significant results are presented in Fig. 7.4 and Table 7.2

7.3.2 Systematic Uncertainty

The study done in Chapter 6 shows that the most significant systematic uncertainties are associated with the hole ice scattering, the bulk ice scattering, and the astrophysical neutrino flux. Among the three factors, the bulk ice scattering is predominant. In this section, we will calculate the systematic uncertainty associated with these factors using the method discussed in Chapter 6 and present the total value of the systematic uncertainty.

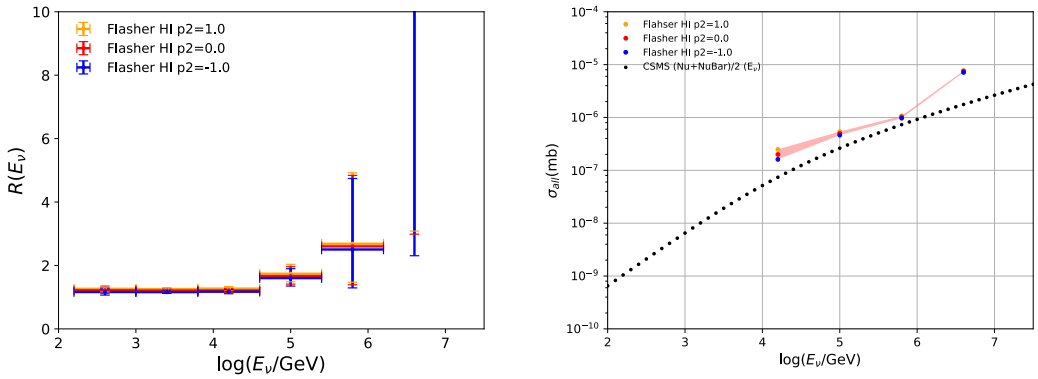

FIGURE 7.5: The ratio (left) and the cross section (right) as a function of neutrino energy for three values of the $p2$ parameter. The data points of different colors represent the result from the unfolding matrices built with the simulation using different p_2 parameters. The statistical uncertainty is not shown in the right plot.

Flasher Hole Ice Model

The effect of changing the p_2 parameter is studied using the H2 50 simulated datasets with variations on the p_2 parameter ($p_2 = -1, 0, 1$). The systematic uncertainty associated with the p_2 parameters is calculated using Eq. 6.2 and 6.3. The uncertainties on the ratio and the cross section measurement result are shown in Fig. 7.5 and their values are shown in Table 7.3.

Bulk Ice Scattering

The largest systematic effect comes from the scattering coefficient in the bulk ice. With the available simulation of H2 50 and H2 50 with a 10% increase in the scattering coefficient, we extrapolate the effect of any change on the scattering coefficient in the H2 50 simulation with Eq. 6.5. To calculate the systematic uncertainty associated with the bulk ice scattering coefficient, Eq. 6.9 is applied. The $\text{Ratio}_{scat,1.0,30}$ is the unfolded ratio of the unblinded data where the unfolding matrix is built with the baseline simulation (H2 30). The uncertainty on the scattering coefficient is estimated as $\pm 10\%$. Therefore the x in $\text{Ratio}_{scat,x,30}$ are 90% and 110%.

The uncertainty on the ratio and the cross section measurement result are shown in Fig. 7.6 and their values are shown in Table 7.3.

Astrophysical Neutrino Flux

To estimate the systematic uncertainty associated with the astrophysical neutrino flux, the unfolding matrices are built with the same baseline simulation but different astrophysical neutrino fluxes (according to the contour in Fig. 6.18) when calculating the total

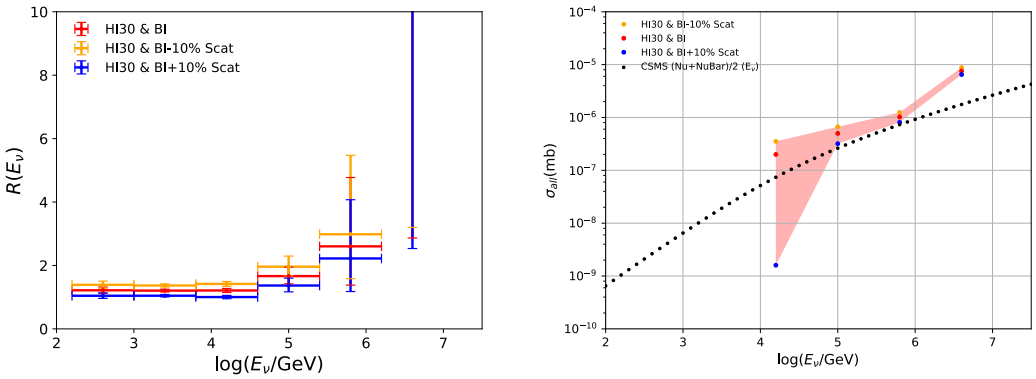

FIGURE 7.6: The ratio (left) and the cross section (right) as a function of neutrino energy for three values of the bulk ice scattering coefficient. The data points of different colors represented the result from the unfolding matrices built with the simulation using different variations on the bulk ice scattering coefficient. The statistical uncertainty is not shown in the right plot.

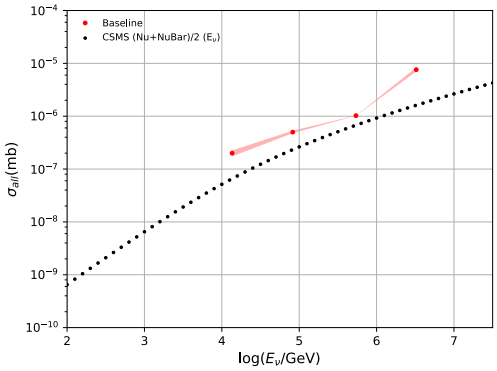

FIGURE 7.7: The systematic uncertainty associated with the change in the astrophysical neutrino flux of the cross section in the neutrino energy bins of the unblinded data. The statistical uncertainty is not shown in the right plot.

neutrino weight [1]. The unblinded data was unfolded with these matrices. The red band in Fig. 7.7 indicates the range of the cross section measurement corresponding to these unfolding results. This range is the systematic uncertainty associated with the change in the parameters of the astrophysical neutrino flux. The values of the uncertainty are shown in Table 7.3.

Table 7.3 summaries all the systematic uncertainties considered in this analysis, and the total systematic uncertainties are all of the above added in quadrature. The lower total systematic uncertainty of the energy range $10^{3.8} - 10^{4.6}$ [$\log_{10}(E_\nu/\text{GeV})$] is equal to the value itself. This indicates that the systematic uncertainty is too large that the ratio of

[1]The simulated neutrinos are generated with a different spectrum from their real flux. The neutrino weight is applied to calculate the real neutrino rate from the simulated spectrum.

Energy Range [log(E_ν/GeV)]	3.8 - 4.6	4.6 - 5.4	5.4 - 6.2	6.2 - 7.0
Hole Ice Scattering [mb]	$2.00^{+0.49}_{-0.39} \times 10^{-7}$	$4.99^{+0.43}_{-0.36} \times 10^{-7}$	$1.02^{+0.05}_{-0.06} \times 10^{-6}$	$7.59^{+0.07}_{-0.47} \times 10^{-6}$
Bulk Ice Scattering [mb]	$2.0^{+1.5}_{-2.0} \times 10^{-7}$	$5.0^{+1.7}_{-1.8} \times 10^{-7}$	$1.02^{+0.22}_{-0.21} \times 10^{-6}$	$7.6^{+1.2}_{-1.1} \times 10^{-6}$
Astro. ν Flux [mb]	$2.00^{+0.25}_{-0.26} \times 10^{-7}$	$4.99^{+0.33}_{-0.22} \times 10^{-7}$	$1.024^{+0.005}_{-0.004} \times 10^{-6}$	$7.59^{+0.79}_{-0.57} \times 10^{-6}$
Total [mb]	$2.0^{+1.6}_{-2.0} \times 10^{-7}$	$5.0^{+1.8}_{-1.8} \times 10^{-7}$	$1.02^{+0.22}_{-0.22} \times 10^{-6}$	$7.6^{+1.5}_{-1.3} \times 10^{-6}$

TABLE 7.3: The cross section measurement result of the 2011-2015 IceCube cascade sample and its systematic uncertainties.

Energy Range [log(E_ν/GeV)]	3.8 - 4.6	4.6 - 5.4	5.4 - 6.2	6.2 - 7.0
Bin Center [log(E_ν/GeV)]	$4.133^{+0.004}_{-0.006}$	$4.916^{+0.011}_{-0.015}$	$5.734^{+0.001}_{-0.017}$	$6.513^{+0.010}_{-0.015}$
Cross Section with σ_{stat} [mb]	$2.00^{+0.54}_{-0.65} \times 10^{-7}$	$5.0^{+1.6}_{-1.5} \times 10^{-7}$	$1.02^{+1.26}_{-0.68} \times 10^{-6}$	$7.6^{+8.8}_{-6.4} \times 10^{-6}$
Cross Section with σ_{sys} [mb]	$2.0^{+1.6}_{-2.0} \times 10^{-7}$	$5.0^{+1.8}_{-1.8} \times 10^{-7}$	$1.02^{+0.22}_{-0.22} \times 10^{-6}$	$7.6^{+1.5}_{-1.3} \times 10^{-6}$
Cross Section with σ_{total} [mb]	$2.0^{+1.7}_{-2.1} \times 10^{-7}$	$5.0^{+2.4}_{-2.4} \times 10^{-7}$	$1.02^{+1.28}_{-0.72} \times 10^{-6}$	$7.6^{+8.9}_{-6.5} \times 10^{-6}$

TABLE 7.4: The cross section measurement result of the 2011-2015 IceCube cascade sample with its statistical uncertainty (68% C. L.), systematic uncertainty, and the combined uncertainty.

the down-going events to the up-going events in that energy range could be lower than 1 within the systematic uncertainty. It was discussed in Sec. 4.4.1 that the method reaches its limit at the point where ratio equals to 1. Hence for this energy bin there is no constraint on the lower end of the measured cross section value.

Table 7.4 shows the statistical uncertainty, the systematic uncertainty, and the combined uncertainty (the statistical uncertainty and the systematic uncertainty added in quadrature) of the measured cross section. We noticed that in the energy range of $10^{3.8} - 10^{5.4}$ [$\log_{10}$(E_ν/GeV)] the dominant uncertainty is the systematic uncertainty while in the energy range of $10^{5.4} - 10^{7.0}$ [$\log_{10}$(E_ν/GeV)] the dominant uncertainty is the statistical uncertainty. To get a better precision in the cross section measurement in the low energy range, a better understanding of the systematic parameters is needed while in the high energy range, more statistics are needed.

7.4 Discussion of the Cross Section Measurement Result

7.4.1 Physical Interpretation of the Measured Cross Section

This analysis utilizes the Earth absorption effect to measure the cross section. The measured cross section reflects all neutrino interactions of which the majority is the deep inelastic scattering (DIS). However, at $E_\nu \sim 6.3$ PeV, the cross section of an electron antineutrino interacting with an electron and producing a W boson becomes significantly large (c.f.Sec. 1.3.2):

$$\bar{\nu}_e + e^- \rightarrow W^- \tag{7.1}$$

This process is called Glashow Resonance (GR). This kind of interaction has only been calculated theoretically without experimental events being detected. Since E_ν of 6.3 PeV is in the energy range of this measurement, this analysis is sensitive to this effect. No other cross section measurements done with IceCube data [117], [118] have such sensitivity.

At high energies where the astrophysical neutrino flux is predominant, the number of up-going events absorbed by the Earth due to DIS is proportional to:

$$\Phi_{\text{astro, total}} \times \sigma_{\text{DIS}} \times N_{\text{p+n, Earth}}, \tag{7.2}$$

where $\Phi_{\text{astro, total}}$ is the total astrophysical neutrino flux for neutrinos and antineutrinos of all flavors, σ_{DIS} is the total cross section of the charged-current interaction and the neutral current interaction averaged over neutrinos and antineutrinos, and $N_{\text{p+n, Earth}}$ is the nucleon target density in the Earth.

In the last energy bin ($10^{6.2} - 10^{7.0}$ [log(E$_\nu$/GeV)]) where the Glashow Resonance is expected to happen, the number of up-going events absorbed by the Earth due to GR is proportional to:

$$\Phi_{\text{astro},\bar{\nu}_e} \times \sigma_{\text{GR}} \times N_{\text{e, Earth}}, \tag{7.3}$$

where $\Phi_{\text{astro},\bar{\nu}_e}$ is the flux of astrophysical electron antineutrinos, σ_{GR} is the cross section of GR and $N_{\text{e, Earth}}$ is the electron target density in the Earth.

The chemical composition of the Earth is shown in Table 7.5 alongside with the number of the electrons and nucleons per atom of the elements. These elements contribute to 99% of the Earth mass. All of these elements except for iron, nickel, and aluminum have isoscalar nucleus which means the number of the electrons of the atom is half of the

Element	Composition	No. of electrons per Atom	No. of nucleons per Atom
Fe	32.1%	26	56
O	30.1%	8	16
Si	15.1%	14	28
Mg	13.9%	12	24
S	2.9%	16	32
Ni	1.8%	28	58
Ca	1.5%	20	40
Al	1.4%	13	27

TABLE 7.5: The chemical composition of the Earth and the number of electrons and nucleons per atom. The numbers are from Ref. [119]

Process	ξ
$pp \rightarrow \pi^{\pm}$ pairs	9/54
$pp \rightarrow \pi^{\pm}$ with damped $\mu^{\pm}$	6/54
$p\gamma \rightarrow \pi^{+}$ only	4/54
$p\gamma \rightarrow \pi^{+}$ only with damped μ^{+}	0

TABLE 7.6: The electron antineutrino fraction in the total astrophysical neutrino flux at Earth for different astrophysical source models. The numbers are from Ref. [30]

number of the nucleons of the atom. For iron, nickel, and aluminum, the ratio of the number of electrons to nucleons is approximately one half. Therefore it is safe to assume the electron target density is one half of the nucleon target density:

$$N_{\text{e, Earth}} \approx \frac{1}{2} N_{\text{p+n, Earth}} \tag{7.4}$$

The flux of astrophysical electron antineutrinos at Earth can be written as:

$$\Phi_{\text{astro},\bar{\nu}_e} = \xi \cdot \Phi_{\text{astro, total}}, \tag{7.5}$$

where, ξ is the fraction of $\Phi_{\text{astro},\bar{\nu}_e}$ in $\Phi_{\text{astro, total}}$, and it depends on the process assumed at the source of the neutrino generation. A list of different processes and their corresponding ξ values are given in Table 7.6.

The total number of the up-going events absorbed in the Earth for any kind of interactions at $E_\nu \sim 6.3$ PeV can be expressed as:

$$\Phi_{\text{astro, total}} \times \sigma_{\text{DIS}} \times N_{\text{p+n, Earth}} + \Phi_{\text{astro},\bar{\nu}_e} \times \sigma_{\text{GR}} \times N_{\text{e, Earth}} \tag{7.6}$$

Utilizing Eq. 7.4 and 7.5, Eq. 7.6 becomes:

$$\Phi_{\text{astro, total}} \times (\sigma_{\text{DIS}} + \xi \cdot \frac{1}{2}\sigma_{\text{GR}}) \times N_{\text{p+n, Earth}} \tag{7.7}$$

The measured cross section includes all neutrino interactions. In the energy range of $E_\nu < 10^{6.2}$ GeV and $E_\nu > 10^7$ GeV, the measured total cross section is the deep inelastic scattering cross section only: $\sigma^*_{total}=(\sigma_\nu^{CC+NC} + \sigma_{\bar{\nu}}^{CC+NC})/2$. In the energy range of $10^{6.2}$ GeV$< E_\nu < 10^7$ GeV, the measured total cross section is the deep inelastic scattering cross section and the Glashow Resonance cross section with the electron antineutrino flux fraction factor: $\sigma^*_{total}=(\sigma_\nu^{CC+NC} + \sigma_{\bar{\nu}}^{CC+NC})/2 + \frac{\xi}{2}\sigma_{\text{GR}}$.

7.4.2 Comparison with Neutrino-Nucleon DIS Cross Section Calculations

The cross section measurement result of this analysis is shown in Fig. 7.8 alongside with several neutrino-nucleon DIS cross section calculations [62], [120], [121], [122], [123] and one previous IceCube cross section measurement result [117]. The black error bars are the statistical uncertainty and the grey error bars are the statistical and systematic uncertainty added in quadrature.

In the energy range of this measurement (6 TeV to 10 PeV), the neutrino-nucleon DIS cross section has not been directly measured in the Earth-based accelerators. However, it can be calculated using the parton distribution functions (PDFs) within the framework of the Standard Model. In Ref. [120] (CTW), the neutrino-nucleon DIS cross section for $E_\nu > 10^4$ GeV region has been calculated using the MSTW 2008 next-to-leading-order (NLO) PDFs [124] using a *leading-order* treatment of the coefficient functions. In Ref. [62] (CSMS) the calculation in the similar energy range was done with the more up-to-date PDFs from HERA [125]. The fit used the next-to-leading-order (NLO) DGLAP formalism [126], [127], [128], [129]. Even though the calculated cross section values of the CTW calculation and the CSMS calculations are consistent, due to the more precise PDFs at very low x, the uncertainty of the calculated cross section at very high energy ($E_\nu > 10^9$ GeV) in the CSMS calculation is much smaller compared to the uncertainty in the CTW calculation. In IceCube simulations, the CSMS cross section is used to estimate the probability of neutrino interactions.

Ref. [121] (BDH) imposes a constraint that the neutrino-nucleon DIS cross section satisfies the saturated Froissart bound [130], [131], [132], [133] at ultra high energies (very low x). Therefore this model is only valid for $E_\nu > 10^6$ GeV.

Ref. [122] (AHW) is another calculation that goes beyond pQCD. It combines the Froissart bound with the dipole model framework [134], [135], [136], [137], [138], [139] of the nucleon in the attempt to account for the potential parton saturation effect [140]. Below 10^8 GeV, the calculated cross section in Ref. [122] is consistent with the pQCD calculated results [62], [120]. Above 10^8 GeV, it is consistent with the results from Ref. [121]. If we

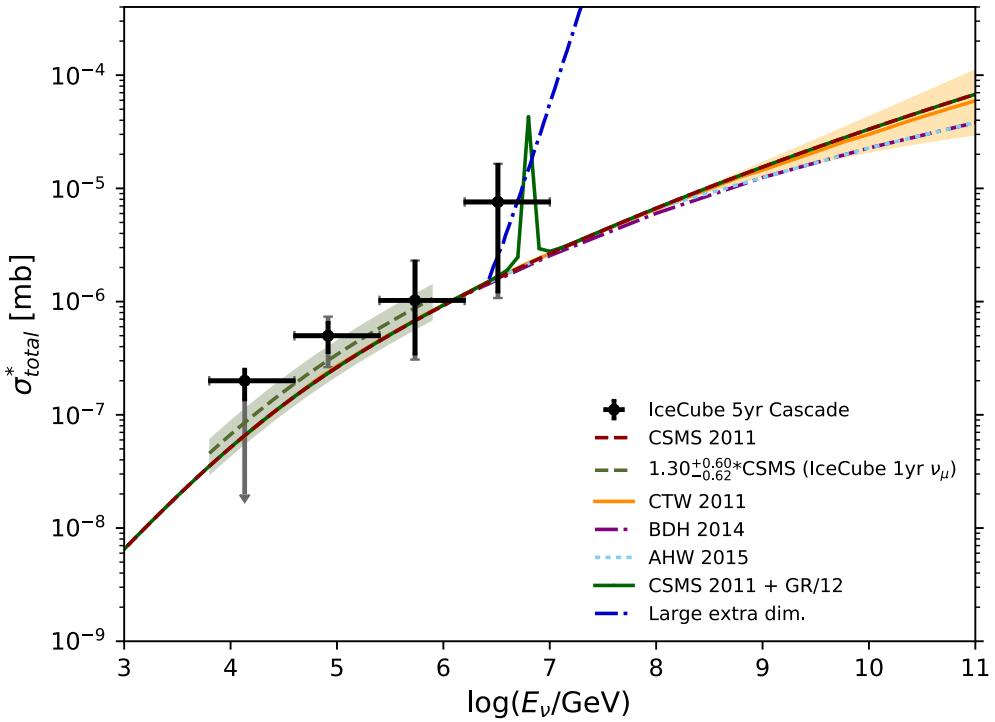

FIGURE 7.8: The cross section measurement result of the unblinded data with its statistical and the systematical uncertainty in comparison with neutrino-nucleon interaction cross section calculations [62], [120], [121], [122], [123] and one previous IceCube cross section measurement result [117]. The measured cross section includes all neutrino interactions. In the energy range of $E_\nu < 10^{6.2}$ GeV and $E_\nu > 10^7$ GeV, the measured total cross section is the deep inelastic scattering cross section only: $\sigma^*_{total}=(\sigma_\nu^{CC+NC} + \sigma_{\bar{\nu}}^{CC+NC})/2$. In the energy range of $10^{6.2}$ GeV$< E_\nu < 10^7$ GeV, the measured total cross section is the deep inelastic scattering cross section and the Glashow Resonance cross section with the electron antineutrino flux fraction factor: $\sigma^*_{total}=(\sigma_\nu^{CC+NC} + \sigma_{\bar{\nu}}^{CC+NC})/2 + \frac{\xi}{2}\sigma_{\mathrm{GR}}$.

were able to collect data that is statistically significant in the energy range of $E_\nu > 10^8$ GeV, the gluon saturation effects could potentially be confirmed or excluded.

Ref. [123] presents a scenario of new physics, where the cross section is enhanced due to the low-scale quantum-gravity effect. This is an effect that can be potentially observed at the energy range of multi-TeV to PeV, which overlaps with the energy range of this measurement. One of the scenarios: large extra dimensions from the ADD scenario [141], [142], [143] is shown in Fig. 7.8. In this scenario the increase of the cross section above 10^6 GeV is much more drastic than the Standard Model cross section.

The green curve in Fig. 7.8 is the combination of the Standard Model DIS cross section calculated in Ref. [62] and the Glashow Resonance cross section [64] assuming the astrophysical neutrinos are produced in the *pp* process.

The first experimental neutrino-nucleon cross section measurement in the multi-TeV neutrino energy range was done in Ref. [117]. It was conducted with one year of the up-going ν_μ sample in the IceCube data. Due to the nature of the sample, it only measured the charged-current neutrino-nucleon DIS interaction cross section. A likelihood fit was performed on the data to find a scaling factor of the CSMS cross section using the Earth absorption effect. The measured scaling factor is for the entire energy range of the sample, therefore it does not have neutrino energy dependence. In Fig. 7.8, the plotted result from Ref. [117] assumes the same scaling factor for the charged-current interaction and the neutral current interaction. The uncertainty is the statistical and systematic uncertainty added in quadrature.

The result from this analysis shows consistency with both the Standard Model cross section calculations and the previously published IceCube result within the uncertainties. At the multi-PeV energy region, the unique nature of this analysis shows the potential for probing the Glashow Resonance by the Earth absorption effect. With more statistics collected in the future, and the assumption that the enhancement of the neutrino interaction cross section in the multi-PeV energy range from the DIS cross section is only due to the Glashow Resonance but not other new physics effects, the fraction of the electron antineutrinos in the total astrophysical neutrino flux could be identified through with this analysis which will indicate the astrophysical neutrino generation process at the source (pp or $p\gamma$).

7.4.3 P-Value

P-value is the probability of observing the data when the given null hypothesis is true. In this analysis, there are two questions are of interest: 1. can we reject the Standard Model with the observed data, 2. can we rule out the existence of the Glashow Resonance with the observed data? In this section, we will show the calculation of the p-value of both cases and the interpretation of the results.

7.4.3.1 The P-Value of the Standard Model DIS Cross Section

In this test, the null hypothesis is that the increase of the DIS interaction cross section with the increase of the neutrino energy follows the CSMS [62] calculation which was done within the Standard Model framework. The simulated neutrino datasets were generated with the CSMS cross section, thus are used for this hypothesis testing. The lifetime used to calculate the expected number of events in the reconstructed down-going and up-going region in each reconstructed energy bin is the same as observed in the experimental data in order to include the statistical uncertainty.

100,000 samples were generated according to the Poisson distribution with means equal to the expected number of events from the Monte Carlo simulation. Each sample is treated with the same procedure as data to get the ratios of the down-going events to the up-going events in the neutrino energy bins. The probability distribution function of the ratios from the 100,000 samples in each neutrino energy bin is shown in Fig. 7.9 (left) with the ratio from the experimental data indicated by the vertical black lines. The

p-value of each neutrino energy bin is calculated as the integral of the probability from the ratio from the experimental data to the closer tail of the distribution:

$$p = \int_{ratio_{data_i}}^{\infty} P(r)dr \tag{7.8}$$

$$\text{p-value}_{bin_i} = \min(p, 1-p) \tag{7.9}$$

We calculate the summed p-value over the four neutrino energy bins as:

$$\text{p-value}_{sum} = \sum_{i=1}^{4} \log_{10}(\text{p-value}_{bin_i}) \tag{7.10}$$

p-value_{sum} is calculated for all the 100,000 samples and the distribution is shown in Fig. 7.9 (right) with the vertical red line indicating the p-value_{sum} for the experimental data. As constructed in Eq. 7.9, the maximum p-value for individual neutrino energy bin is 0.5, therefore the maximum p-value_{sum} is $4\log_{10}(0.5) \approx 1.2$. The greater the p-value_{sum} the more likely to observe the observed data. The overall p-value is calculated as:

$$\text{p-value} = \int_{-\infty}^{\text{p-value}_{sum,data}} P(\text{p-value}_{sum})d\text{p-value}_{sum} \tag{7.11}$$

The overall p-value for measuring the cross section from the observed data given hypothesis of the Standard Model holds with only statistical uncertainty is 0.04. This result only includes statistical uncertainty and is seemingly low. Especially in the first two energy bins, the p-value in the individual energy bin being low affects the overall p-value. The hypothesis shall not be rejected based on the p-value calculated with only statistical uncertainty. The systematic uncertainties also need to be taken into consideration.

To include the systematic uncertainty in the p-value calculation, the systematic uncertainty on the ratio from the experimental data is needed. The probability distribution function of the ratios of the 100,000 samples in each neutrino energy bin alongside with the ratio from the experimental data with the systematic uncertainty is shown in Fig. 7.10 (left). The p-value including the systematic uncertainty in each energy bin is calculated as the maximum p-value among all the p-values calculated using ratios within the systematic uncertainty range. The equations can be expressed as:

$$p(R) = \int_{R}^{\infty} P(r)dr \tag{7.12}$$

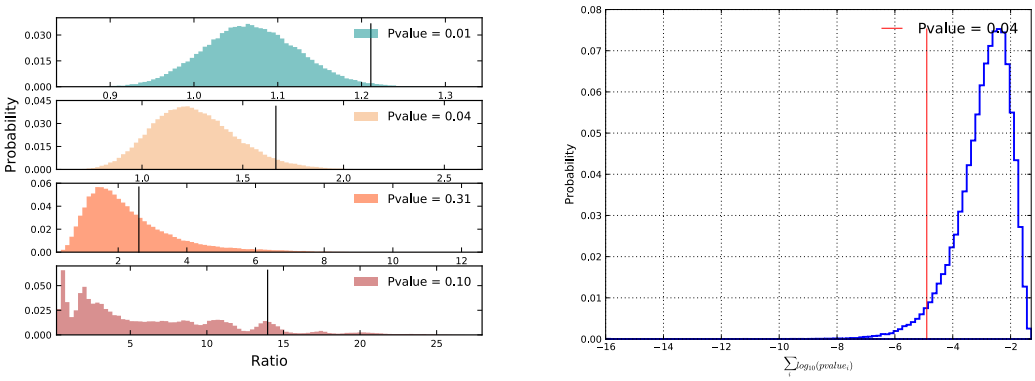

FIGURE 7.9: Left: the distribution of the ratio ($N_{\text{down-going}}/N_{\text{up-going}}$) from the simulation resampling in each neutrino energy bin and the ratio from the experimental data indicated by the vertical black lines. The p-values of individual neutrino energy bins are marked in the plot. Right: the summed p-value distribution from the simulation resample and the summed p-value from the experimental data indicated by the vertical red line.

$$\text{p-value}_{bin_i} = \max_{R\in[ratio_{low,i},ratio_{high,i}]}(\min(p(R), 1-p(R))), \tag{7.13}$$

where $ratio_{low,i}$ and $ratio_{high,i}$ are the lower end and the upper end of the systematic uncertainty range of the ratio from the experimental data in neutrino energy bin_i as indicated by the vertical black dotted lines in Fig. 7.10 (left).

After the calculation of the p-value in individual neutrino energy bins, the summed p-value and the overall p-value can be calculated using Eq. 7.10 and Eq. 7.11 respectively. The overall p-value for measuring the cross section from the observed data given the hypothesis of the Standard Model holds with both statistical and systematic uncertainty is 0.87 (as shown in Fig. 7.10 (right)). This shows the measured result is consistent with the Standard Model DIS cross section.

7.4.3.2 The P-Value of the Glashow Resonance Cross Section

Since the cross section for the Glashow Resonance peaks at 6.3 PeV [64] (c.f.Sec. 1.3.2), the calculation of the p-value only involves the last energy bin. To conduct this calculation, three sets of samples were generated. One set uses the Poisson distribution with the expectation of only neutrino-nucleon DIS interactions. The second set uses the Poisson distribution with the expectation of neutrino-nucleon DIS interactions and electron antineutrino-electron Glashow Resonance. In the second set, the flux of the astrophysical neutrino is assumed to be originated from the *pp* astrophysical sources which means the neutrino flavor ratio is (1:1:1) and the neutrino to antineutrino flux ratio of each flavor at Earth is 1:1 [30]. The third set uses the Poisson distribution with the expectation of neutrino-nucleon DIS interactions and electron antineutrino-electron Glashow Resonance

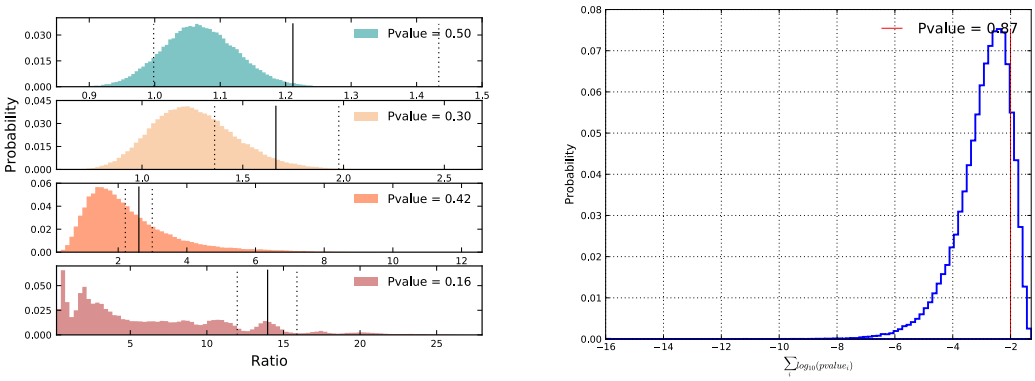

FIGURE 7.10: Left: the distribution of the ratio ($N_{\mathrm{down-going}}/N_{\mathrm{up-going}}$) from the simulation resampling in each energy bin and the ratio from the experimental data indicated by the vertical black solid lines. The systematic uncertainties of the ratio from the experimental data are indicated by the vertical black dotted lines. The p-values of individual neutrino energy bins are marked in the plot. Right: the summed p-value distribution from the simulation resample and the summed p-value from the experimental data indicated by the vertical red line.

as well. In the third set, the flux of the astrophysical neutrino is assumed to be originated from the $p\gamma$ astrophysical sources which means the neutrino flavor ratio at Earth is (1:1:1). The electron neutrino to electron antineutrino flux ratio is 14:4, the muon neutrino to muon antineutrino flux ratio is 11:7 and the tau neutrino to tau antineutrino flux ratio is 11:7 [30].

100,000 samples corresponding to the lifetime of the experimental data were generated for each set. The ratio distributions for the three sets of samples in the last energy bin are shown in Fig. 7.11. The ratio from the experimental data with the systematic uncertainty is shown in the plots as well. Since only one energy bin is involved in the calculation of the p-value, Eq. 7.12 and 7.13 were used. The p-value of the measurement with the assumption that all neutrino interactions are neutrino-nucleon DIS interactions is 0.16. The p-value of the measurement with the assumption of the existence of both DIS interactions and the Glashow Resonance (pp process) is 0.23. The p-value of the measurement with the assumption of the existence of both DIS interactions and the Glashow Resonance ($p\gamma$ process) is 0.20.

It is not unexpected that the three p-values are similar. As shown in Fig. 7.11, in the highest energy bin the systematic uncertainty range is much smaller compared to the spread of the ratio distributions of the samples. This indicates that at this energy range the dominant uncertainty is the statistical uncertainty. Due to the limited statistics, the bin size is rather large. With a falling spectrum, the majority of the events in the bin are concentrated in the energy range below the peak of the Glashow Resonance. Therefore with the current statistics, it is hard to distinguish between the ratio distributions with and without Glashow Resonance, let alone the difference among the astrophysical neutrino generation processes in the case of the existence of the Glashow Resonance.

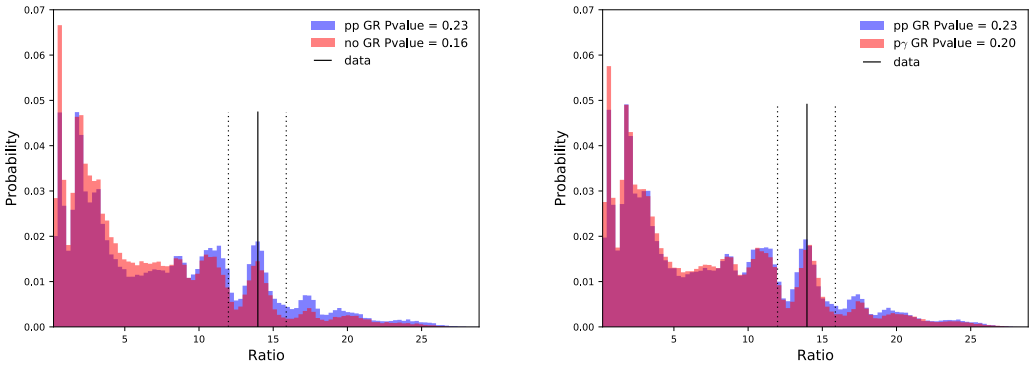

FIGURE 7.11: Left: the distribution of the ratio from the simulation resampling in the [$10^{6.2}$ GeV, 10^7 GeV] energy bin with Glashow Resonance (pp process) and without the Glashow Resonance. Right: the distribution of the ratio from the simulation resampling in the [$10^{6.2}$ GeV, 10^7 GeV] energy bin with the Glashow Resonance from pp process and $p\gamma$ process. The ratio from the experimental data is indicated by the vertical black solid lines, and the systematic uncertainty of the ratio from the experimental data is indicated by the vertical black dotted lines in both plots.

Within the current statistics, the existence of the Glashow Resonance cannot be rejected, and the DIS only assumption cannot be rejected either. In the future, when more data is available, this analysis has the feasibility to test the existence of the Glashow Resonance using the Earth absorption effect. Furthermore, with an increase in the precision of the measurement, one may probe the process of astrophysics neutrino generation.

Chapter 8

Summary and Outlook

In this dissertation, we have presented a novel analysis method to directly measure the neutrino interaction cross section in the energy range of 6.3 TeV to 10 PeV with astrophysical neutrinos. The neutrinos sample used are the cascade events (primarily electron neutrinos and tau neutrinos) from the IceCube data collected from May 2011 to May 2016. A dedicated event selection was developed for the purpose of this analysis and other analyses that are performed with cascade samples. The event selection applies a machine learning (Boosted Decision Tree) classifier for the events with cascade reconstructed energy below 60 TeV (low energy) [88] and applies straight cuts on the events with cascade reconstructed energy above 60 TeV (high energy). The final sample contains 4803 events among which 654 events are in the cascade reconstructed energy range of 6.3 TeV to 10 PeV. This event selection has a 30% higher signal efficiency compared to the last generation cascade events selection [87] and is also background free in the high energy region. In the low energy region, it is a factor of 10 more efficient while keeping the sample purity above 90% [88]. The high energy part of the event selection is also the first one in IceCube cascade selection that does not exclude the dust layer in the detector. It has led to the discovery of one of the most energetic cascade events in IceCube. With a reconstructed energy of 770 TeV, there are only three other cascade events having a higher reconstructed energy. Due to the special optical properties in the dust layer, the conventional reconstruction method yields a significant bias. A regressor based on the Boosted Decision Tree has been developed to reconstruct the deposited energy for these events, and it has been proven to be consistent with another independent computational expensive reconstruction method (DirectFit).

The analysis method for the neutrino interaction cross section measurement utilizes the Earth absorption effect. The final level sample is divided into two groups in each neutrino energy bin: the down-going group and the up-going group. With the increase in the cross section, more up-going neutrinos get absorbed by the Earth while the number of down-going neutrinos remains unchanged. By calculating the ratio of the down-going events to the up-going events in each neutrino energy bin, the corresponding cross section can be calculated. The result is largely independent of the neutrino flux since the flux factor cancels when doing the ratio. The unfolding method was applied to map from the reconstructed energy and zenith distribution to the neutrino energy and true zenith distribution. Markov Chain Monte Carlo was used to estimate the statistical uncertainty.

A true coverage test has proven the chosen uncertainty range corresponds to the 68% confidence interval. Systematic effects associated with the ice optical property, the detector response, the atmosphere, and the astrophysical neutrino flux have been evaluated. The final cross section measurement result is consistent with the Standard Model cross section. It is also consistent with other neutrino cross section measurements using IceCube data. The p-value of observing the result when assuming the Standard Model is 0.87. In the last energy bin (1.6 PeV to 10 PeV), the measured cross section is the combination of the neutrino-nucleon DIS cross section and the electron antineutrino-electron GR cross section with a scaling factor. The scaling factor is correlated to the fraction of the electron antineutrino in the total neutrino flux which is an indicator of the generation process of the astrophysical neutrinos (pp or $p\gamma$). The p-value for assuming pp process and $p\gamma$ process are 0.23 and 0.20 respectively, which means with the current statistics we cannot identify the astrophysical neutrino generation process.

Many different theories have predicted the Beyond Standard Model effects to happen in the neutrino energy range of EeV and above. If enough statistics are obtained in that energy region, this analysis will test the existence of new physics by measuring the neutrino interaction cross section at ultra-high energies. The planned next-generation upgrade of IceCube (IceCube Gen2) [144] will have a target effect volume $\sim$ 100 times more than the IceCube detector at EeV energies. With more statistics in the PeV region, when assuming the Standard Model physics holds, the fraction of the electron antineutrino in the total neutrino flux can also be calculated to a precision so that the astrophysical neutrino generation process can be determined. An exciting future awaits!

Bibliography

[1] C. L. Cowan Jr., F. Reines, F. B. Harrison, H. W. Kruse, and A. D. McGuire. Detection of the Free Neutrino: a Confirmation. *Science*, 124(3212):103–104, 1956.

[2] G. Danby, J-M. Gaillard, K. Goulianos, L. M. Lederman, N. Mistry, M. Schwartz, and J. Steinberger. Observation of High-Energy Neutrino Reactions and the Existence of Two Kinds of Neutrinos. *Physical Review Letters*, 9(1):36–44, 1962.

[3] M. L. Perl et al. Evidence for Anomalous Lepton Production in e+ e Annihilation. *Physical Review Letters*, 35(1489), 1975.

[4] DONUT Collaboration. Observation of tau neutrino interactions. *Physics Letters*, B(504):218–224, 2001.

[5] B. Pontecorvo. Mesonium and Antimesonium. *Journal of Experimental and Theoretical Physics*, 6(2):429, 1958.

[6] Z. Maki, M. Nakagawa, and S. Sakata. Remarks on the Unified Model of Elementary Particles. *Progress of Theoretical Physics*, 28(5):870–880, 1962.

[7] T. K. Gaisser, R. Engel, and E. Resconi. *Cosmic Rays and Particle Physics*. Cambridge University Press, 2016.

[8] R. Davis, D. S. Harmer, and K. C. Hoffman. Search for Neutrinos from the Sun. *Physical Review Letters*, 20(1205), 1968.

[9] C. Patrignani et al. Review of Particle Physics. *Chinese Physics*, C40(100001), 2017.

[10] AMS Collaboration: M. Aguilar et al. Precision Measurement of the Proton Flux in Primary Cosmic Rays from Rigidity 1 GV to 1.8 TV with the Alpha Magnetic Spectrometer on the International Space Station. *Physical Review Letters*, 114(171103), 2015.

[11] AMS Collaboration: M. Aguilar et al. Precision Measurement of the Helium Flux in Primary Cosmic Rays of Rigidities 1.9 GV to 3 TV with the Alpha Magnetic Spectrometer on the International Space Station. *Physical Review Letters*, 115(21101), 2015.

[12] BESS Collaboration: K. Abe et al. Measurements of cosmic-ray proton and helium spectra from the BESS-Polar long-duration balloon flights over Antarctica. *The Astrophysical Journal*, 822(65), 2016.

[13] JACEE Collaboration: K. Asakimori et al. Cosmic-Ray Proton and Helium Spectra: Results from the JACEE Experiment. *The Astrophysical Journal*, 502(278), 1998.

[14] TRACER Collaboration: M. Ave et al. Composition of Primary Cosmic-Ray Nuclei at High Energies. *The Astrophysical Journal*, 678(262), 2008.

[15] KASCADE Collaboration: T. Antoni et al. KASCADE measurements of energy spectra for elemental groups of cosmic rays: Results and open problems. *Astroparticle Physics*, 24, 2005.

[16] IceCube Collaboration: M. G. Aartsen et al. Measurement of the cosmic ray energy spectrum with IceTop-73. *Physical Review*, D88(042004), 2013.

[17] D. Ivanov for the Telescope Array Collaboration. TA Spectrum Summary. *Proceedings of Science*, PoS(ICRC2015)349, 2015.

[18] The Piere Auger Collaboration: J. Abraham et al. Observation of the Suppression of the Flux of Cosmic Rays above 4×10^{19} eV. *Physical Review Letters*, 101(061101), 2008.

[19] J. R. Hoerandel. Cosmic rays from the knee to the second knee: 10^{14} to 10^{18} eV. *Modern Physics Letters A*, 22:1533–1552, 2007.

[20] K. Greisen. End to the Cosmic-Ray Spectrum. *Physical Review Letters*, 17(748), 1966.

[21] G. T. Zatsepin and V. A. Kuzmin. Upper Limit of the Spectrum of Cosmic Rays. *Journal of Experimental and Theoretical Physics Letters*, 4, 1966.

[22] J. R. Jokipii and G. Morfill. Ultra-High-Energy Cosmic Rays in a Galactic Wind and its Termination Shock. *The Astrophysical Journal*, 312:170–177, 1987.

[23] J. R. Jokipii. Rate of Energy Gain and Maximum Energy in Diffusive Shock Acceleration. *The Astrophysical Journal*, 313:842, 1987.

[24] G. Setti, G. Spada, and A. W. Wolfendale, editors. *Origin of Cosmic Rays*. Springer Netherlands, 1981.

[25] G. M. Webb. Hydrodynamical constraints on cosmic-ray acceleration in relativistic shocks. *Astroparticle Physics*, 319:215, 1987.

[26] D. Kazanas and D. Ellison. Origin of ultra-high-energy -rays from Cygnus X-3 and related sources. *Nature*, 319:380–382, 1986.

[27] B. Louis, V. Sanberg, G. Garvey, et al. The Evidence for Oscillations. *Los Alamos Science*, 25:16–27, 1997.

[28] M. Honda, T. Kajita, K. Kasahara, S. Midorikawa, and T. Sanuki. Calculation of atmospheric neutrino flux using the interaction model calibrated with atmospheric muon data. *Physical Review*, D75(4):043006, 2007.

[29] Atri Bhattacharya, Rikard Enberg, Mary Hall Reno, Ina Sarcevic, and Anna Stasto. Perturbative charm production and the prompt atmospheric neutrino flux in light of RHIC and LHC. *Journal of High Energy Physics*, 06(110), 2015.

[30] D. Biehl, A. Fedynitch, A. Palladino, T. Weiler, and W. Winter. Astrophysical neutrino production diagnostics with the Glashow resonance. *Journal of Cosmology and Astroparticle Physics*, 2017.

[31] U. F. Katz and C. Spiering. High-Energy Neutrino Astrophysics: Status and Perspectives. *Progress in Particle and Nuclear Physics*, 67:651–705, 2012.

[32] Fermi-LAT Collaboration. The Second Catalog of Active Galactic Nuclei Detected by the Fermi Large Area Telescope. *The Astrophysical Journal*, 743(171), 2011.

[33] P. Gluesenkamp for the IceCube Collaboration. Analysis of the cumulative neutrino flux from Fermi-LAT blazar populations using 3 years of IceCube data. *EPJ Web of Conferences*, 121(05006), 2016.

[34] IceCube Collaboration, Fermi-LAT Collaboration, MAGIC, AGILE, ASAS-SN, HAWC, H.E.S.S., INTEGRAL, Kanata, Kiso, Kapteyn, Liverpool Telescope, Subaru, Swift/NuSTAR, VERITAS, and VLA/17B-403 teams. Multimessenger observations of a flaring blazar coincident with high-energy neutrino IceCube-170922A. *Science*, 361(eaat1378):146, 2018.

[35] IceCube Collaboration: M. G. Aartsen et al. Neutrino emission from the direction of the blazar TXS 0506+056 prior to the IceCube-170922A alert. *Science*, 361:147–151, 2018.

[36] F. Halzen and D. Hooper. High-energy Neutrino Astronomy: The Cosmic Ray Connection. *Reports on Progress in Physics*, 65:1025–1078, 2002.

[37] C. Kouveliotou et al. Identification of two classes of gamma-ray bursts. *Astrophysical Journal Letters*, 413(2), 1993.

[38] E. Waxman. Cosmological gamma-ray bursts and the highest energy cosmic rays. *Physical Review Letters*, 75:386–389, 1995.

[39] S. R. Kulkarni et al. Radio emission from the unusual supernova 1998bw and its association with the -ray burst of 25 April 1998. *Nature*, 395:663–669, 1998.

[40] D. Eichler, M. Livio, T. Piran, and D. N. Schramm. Nucleosynthesis, neutrino bursts and -rays from coalescing neutron stars. *Nature*, 340:126–128, 1989.

[41] R. Narayan, B. Paczynski, and T. Piran. Gamma-ray bursts as the death throes of massive binary stars Gamma-ray bursts as the death throes of massive binary stars. *Astrophysical Journal*, 395:L83–L86, 1992.

[42] T. Piran. Gamma-Ray Bursts and the Fireball Model. *Physics Reports*, 314:575–667, 1999.

[43] D. Band et al. BATSE observations of gamma-ray burst spectra. I. Spectral diversity. *Astrophysical Journal*, 413(1):281–292, 1993.

[44] E. Waxman and J. Bahcall. High Energy Neutrinos from Cosmological Gamma-Ray Burst Fireballs. *Physical Review Letters*, 78:2292–2295, 1997.

[45] LIGO Collaboration and Virgo Collaboration: B. P. Abbott et al. GW170817: Observation of Gravitational Waves from a Binary Neutron Star Inspiral. *Physical Review Letters*, 119(161101), 2017.

[46] ANTERES Collaboration, IceCube Collaboration, Pierre Auger Collaboration, LIGO Collaboration, and Virgo Collaborations. Search for High-energy Neutrinos from Binary Neutron Star Merger GW170817 with ANTARES, IceCube, and the Pierre Auger Observatory. *Astrophysical Journal Letters*, 850:L35, 2017.

[47] IceCube Collaboration: M. G. Aartsen et al. Extending the search for muon neutrinos coincident with gamma-ray bursts in IceCube data. *Astrophysical Journal*, 843(112), 2017.

[48] K. Hurley et al. The Interplanetary Network Supplement to the Fermi GBM Catalog of Cosmic Gamma-Ray Bursts. *Astrophysical Journal Supplement Series*, 211(13), 2014.

[49] D. Gruber et al. The Fermi GBM Gamma-Ray Burst Spectral Catalog: Four Years Of Data. *Astrophysical Journal Supplement Series*, 211(12), 2014.

[50] E. Waxman. The origin of IceCube's neutrinos: Cosmic ray accelerators embedded in star forming calorimeters. [arXiv:1511.00815], November 2015.

[51] R. C. Jr. Kennicutt. The Global Schmidt Law in Star-forming Galaxies. *The Astrophysical Journal*, 498(2):541–552, 1998.

[52] T. A. Thompson et al. Magnetic Fields in Starburst Galaxies and the Origin of the FIR-Radio Correlation. *The Astrophysical Journal*, 645(186-198), 2006.

[53] E. Waxman and J. Bahcall. High energy neutrinos from astrophysical sources: An upper bound. *Physical Review*, D 59(023002), 1998.

[54] J. Bahcall and E. Waxman. High energy astrophysical neutrinos: The upper bound is robust. *Physical Review*, D 64(023002), 2001.

[55] A. Loeb and E. Waxman. The Cumulative Bakground of High-Energy Neutrinos from Starburst Galaxies. *Journal of Cosmology and Astroparticle Physics*, 0605(003), 2006.

[56] IceCube Collaboration: M. G. Aartsen et al. Evidence for High-Energy Extraterrestrial Neutrinos at the IceCube Detector. *Science*, 342:1242856, 2013.

[57] IceCube Collaboration: M. G. Aartsen et al. Observation of High-Energy Astrophysical Neutrinos in Three Years of IceCube Data. *Physical Review Letters*, 113(10):101101, 2014.

[58] K. Murase, M. Ahlers, and B. C. Lacki. Testing the hadronuclear origin of PeV neutrinos observed with IceCube. *Physical Review*, D 88(121301), 2013.

[59] R. Gandhi, C. Quigg, M. H. Reno, and I. Sarcevic. Ultrahigh-Energy Neutrino Interactions. *Astroparticle Physics*, 5(81-110), 1996.

[60] K. Nakamura. Review of Particle Physics. *Journal of Physics*, G 37(075021), 2010.

[61] J. A. Formaggio and G. P. Zeller. From eV to EeV: Neutrino Cross Sections Across Energy Scales. *Reviews of Modern Physics*, 84(1307), 2012.

[62] A. Cooper-Sarkar, P. Mertsch, and S. Sarkar. The high energy neutrino cross-section in the Standard Model and its uncertainty. *Journal of High Energy Physics*, 42, August 2011.

[63] A. Cooper-Sarkar for the H1 and ZEUS Collaboration. Proton Structure from HERA to LHC. *ISMD 2010*, 2010.

[64] S. L. Glashow. Resonant scattering of antineutrinos. *Physical Review*, 118(1):316, 1960.

[65] Jakob van Santen. *Neutrino Interactions in IceCube above 1 TeV*. PhD thesis, University of Wisconsin-Madison, 2014.

[66] D. Tosi and C. Wendt for the IceCube Collaboration. Calibrating the photon detection efficiency in IceCube. *Proceedings of Science*, PoS (TIPP 2014) 157, 2014.

[67] F. Halzen and S. R. Klein. Invited Review Article: IceCube: An instrument for neutrino astronomy. *Review of Scientific Instruments*, 81(081101), 2010.

[68] IceCube Collaboration: M. G. Aartsen et al. The Design and Performance of IceCube DeepCore. *Astroparticle Physics*, 35(10):615–624, 2012.

[69] IceCube Collaboration: M. G. Aartsen et al. Measurement of South Pole ice transparency with the IceCube LED calibration system. *Nuclear Instruments and Methods in Physics Research Section A*, 711:73–89, 2013.

[70] IceCube Collaboration: M. G. Aartsen et al. Measurement of Atmospheric Tau Neutrino Appearance with IceCube DeepCore. *Physical Review*, D 99(032007), 2019.

[71] IceCube Collaboration: M. G. Aartsen et al. Search for Nonstandard Neutrino Interactions with IceCube DeepCore. *Physical Review*, D 97(072009), 2018.

[72] IceCube Collaboration: M. G. Aartsen et al. Search for Neutrinos from Dark Matter Self-Annihilations in the Center of the Milky Way with 3 years of IceCube/DeepCore. *European Physical Journal*, C 77(627), 2017.

[73] IceCube Collaboration: M. G. Aartsen et al. Search for Transient Astrophysical Neutrino Emission with IceCube-DeepCore. *Astrophysical Journal*, 816(75), 2016.

[74] IceCube Collaboration: M. G. Aartsen et al. IceTop: The surface component of IceCube. *Nuclear Instruments and Methods in Physics Research*, A 700(188-220), 2013.

[75] IceCube Collaboration: R. Abbasi et al. Calibration and characterization of the IceCube photomultiplier tube. *Nuclear Instruments and Methods in Physics Research Section A*, 618:139–152, 2010.

[76] IceCube Collaboration: M. G. Aartsen et al. The IceCube Neutrino Observatory: Instrumentation and Online Systems. *Journal of Instrumentation*, 12(P03012), 2017.

[77] IceCube Collaboration: M. G. Aartsen et al. The IceCube Realtime Alert System. *Astroparticle Physics*, 92(30), 2017.

[78] IceCube Collaboration: M. G. Aartsen et al. Energy Reconstruction Methods in the IceCube Neutrino Telescop. *Journal of Instrumentation*, 9(P03009), 2014.

[79] R. Abbasi et al. Search for neutrino-induced cascades with five years of AMANDA data. *Astroparticle Physics*, 34, 2011.

[80] AMANDA Collaboration. Optical properties of deep glacial ice at the South Pole. *Journal of Geophysical Research (Atmospheres)*, 111(13203), 2006.

[81] J. Lundberg et al. Light tracking through ice and water – Scattering and absorption in heterogeneous media with Photonics. *Nuclear Instruments and Methods in Physics Research A*, 581(3):619–631, 2007.

[82] Askhat Gazizov and M. P. Kowalski. ANIS: High Energy Neutrino Generator for Neutrino Telescopes. *Computer Physics Communications*, 172, 2005.

[83] D. Chirkin and W. Rhode. Propagating leptons through matter with Muon Monte Carlo (MMC). *arXiv*, hep-ph(0407075), 2004.

[84] A. M. Dziewonski and D. L. Anderson. Preliminary reference Earth Model. *Physics of the Earth and Planetary Interiors*, 25(4):297–356, 1981.

[85] D. Heck et al. CORSIKA: A Monte Carlo Code to Simulate Extensive Air Showers. Technical Report FZKA 6019, Forschungszentrum und Universität Karlsruhe, 1998.

[86] S. R. Klein for the IceCube Collaboration. IceCube: A Cubic Kilometer Radiation Detector. *IEEE Transactions on Nuclear Science*, 56(3), JUNE 2009.

[87] H. M. Niederhausen for the IceCube Collaboration. High Energy Astrophysical Neutrino Flux Characteristics for Neutrino-induced Cascades Using IC79 and IC86-String IceCube Configurations. *Proceedings of Science*, PoS(ICRC2015)1109, 2015.

[88] Hans Niederhausen. *Measurement of the High Energy Astrophysical Neutrino Flux Using Electron and Tau Neutrinos Observed in Four Years of IceCube Data*. PhD thesis, Stony Brook University, 2018.

[89] S. Seunarine. 2011 Request for Online Cascade Filter. Technical report, IceCube Collaboration, 2011.

[90] K. Kopper and L. Schulte. Request for the 2012 Online Cascade Filter. Technical report, IceCube Collaboration, 2012.

[91] L. Schulte and M. Lesiak-Bzdak. Request for the Online Cascasdae Filter and Additional Calculations at Level 2 for the IC86 2013 Cascade Filter Stream. Technical report, IceCube Collaboration, 2012.

[92] M. Lesiak-Bzdak and C. H. Ha. Level3 Cuts for IC86 2011 Cascade Channel. Technical report, IceCube Collaboration, 2011.

[93] T. Gaisser, K. Jero, A. Karle, and J. van Santen. Generalized self-veto probability for atmospheric neutrinos. *Physical Review*, D 90(023009), 2014.

[94] R. Enberg, M. H. Reno, and I. Sarcevic. Prompt neutrino fluxes from atmospheric charm. *Physical Review*, D 78(043005), 2008.

[95] Thomas K. Gaisser. Spectrum of cosmic-ray nucleons and the atmospheric muon charge ratio. *Astroparticle Physics*, 35(12):801–806, 2012.

[96] R. J. Lauer. *Extending the search for cosmic point sources of neutrinos with IceCube beyond PeV energies and above the horizon*. PhD thesis, Humboldt University of Berlin, 2010.

[97] J. A. Stoessl. *A search for particle showers at the edge of IceCube's instrumental volume*. PhD thesis, Humboldt University of Berlin, 2016.

[98] D. Chirkin. Evidence of optical anisotropy of the South Pole ice. *Proceedings of the 33rd ICRC*, 2013.

[99] IceCube Collaboration: M. G. Aartsen et al. Observation of Astrophysical Neutrinos in Four Years of IceCube Data. *Proceedings of Science*, PoS(ICRC2015)1081, 2015.

[100] IceCube Collaboration: M. G. Aartsen et al. Observatio of Astrophysical Neutrinos in Six Years of IceCube Data. *Proceedings of Science*, PoS(ICRC2017)981, 2017.

[101] T. Chen and C. Guestrin. XGBoost: A Scalable Tree Boosting System. *Proceedings of the 22nd ACM SIGKDD*, 2016.

[102] T. Hastie, R. Tibshirani, and J. Friedman. *The Elements of Statistical Learning*. Springer, second edition, 2009.

[103] Y. Freund and R. E. Schapire. A Decision-Theorecic Generalization of On-Line Learning and an Application to Boosting. *Journal of Computer and System Science*, 55:119–139, 1997.

[104] J. Friedman. Greedy Function Approximation: A Gradient Boosting Machine. *The Annals of Statistics*, 29(5), 2001.

[105] J. Friedman. Stochastic gradient boosting. *Computational Statistics and Data Analysis*, 38:367–378, 2002.

[106] IceCube Collaboration: M. G. Aartsen et al. Event reconstruction in IceCube based on direct event re-simulation. *Proceedings of Science*, PoS (ICRC2013) 0581, 2013.

[107] D. Chirkin. Likelihood description for comparing data with simulation of limited. arXiv:1304.0735.

[108] D. Hooper. Measuring high energy neutrino-nucleon cross sections with future neutrihno telescopes. *Physical Review*, D65:097303, 2002.

[109] S. Schönert, T. K. Gaisser, E. Resconi, and O. Schulz. Vetoing atmospheric neutrinos in a high energy neutrino telescope. *Physical Review*, D79(4):043009, 2009.

[110] G. Cowan, K. Cranmer, E. Gross, and O. Vitells. Asymptotic formulae for likelihood-based tests of new physics. *European Physical Journal*, C71(1554), 2011.

[111] G.Zech. Iterative unfolding with the Richardson-Lucy algorithm. *Nuclear Instruments and Methods in Physics Research A*, 716:1–9, July 2013.

[112] AMANDA Collaboration:, E. Andres, et al. The amanda neutrino telescope: Principle of operation and first results. *Astroparticle Physics*, 13(1-20), 2000.

[113] D. Chirkin. Ice Model update, hole ice and DOM efficiency. Technical report, University of Wisconsin - Madison, 2015.

[114] J. Pedro. Idea to change the DOM angular acceptance (or hole ice model). Technical report, Michigan State University, 2015.

[115] NASA. U. S. Standard Atmsophere, 1976. Technical Report NASA-TM-X-74335, National Aeronautics and Space Administration, 1976.

[116] J. M. Picone, A. E. Hedin, D. P. Drob, and A. C Aikin. NRLMSISE-00 empirical model of the atmosphere: Statistical comparisons and scientific issues. *Journal of Geophysical Research: Space Physics*, 107(A12), 2001.

[117] IceCube Collaboration: M. G. Aartsen et al. Measurement of the multi-TeV neutrino cross section with IceCube using Earth absorption. *Nature*, 551(596-600), 2017.

[118] M. Bustamante and A. Connolly. Extracting the Energy-Dependent Neutrino-Nucleon Cross Section Above 10 TeV Using IceCube Showers. *Physical Review Letters*, 122(041101), 2019. arXiv:1711.11043.

[119] J. Morgan and E. Anders. Chemical composition of Earth, Venus, and Mercury. *Proceedings of the National Academy of Sciences of the United States of America*, 77(12):6973–6977, 1980.

[120] A. Connolly, R. Thorne, and D. Waters. Calculation of High Energy Neutrino-Nucleon Cross Sections and Uncertainties Using the MSTW Parton Distribution Functions and Implications for Future Experiments. *Physical Review*, D 83(113009), 2011.

[121] M. Block, L. Durand, and P. Ha. Connection of the virtual p cross section of ep deep inelastic scattering to real p scattering, and the implications for N and ep total cross sections. *Physical Review*, D 89(094027), 2014.

[122] C. Arguelles, F. Halzen, L. Wille, M. Kroll, and M. Reno. The High-Energy Behavior of Photon, Neutrino and Proton Cross Sections. *Physical Review*, D 92(074040), 2015.

[123] J. Alvarez-Muniz, F. Halzen, T. Han, and D. Hooper. Phenomenology of High-Energy Neutrinos in Low-Scale Quantum-Gravity Models. *Physical Review Letters*, 88(021301), 2002.

[124] A. D. Martin, W. J. Stirling, R. S. Thorne, and G. Watt. Parton distributions for the LHC. *European Physical Journal*, C(63):189–285, 2009.

[125] H1 Collaboration and ZEUS Collaboration. Combined Measurement and QCD Analysis of the Inclusive ep Scattering Cross Sections at HERA. *Journal of High Energy Physics*, 1001(109), 2010.

[126] Y. L. Dokshitser. Calculation of structure functions of deep-inelastic scattering and e+e- annihilation by perturbation theory in quantum chromodynamics. *Journal of Experimental and Theoretical Physics*, 46(4):641, 1977.

[127] V. N. Gribov and L. N. Lipatov. Deep inelastic e p scattering in perturbation theory. *Soviet Journal of Nuclear Physics*, 15(438), 1972.

[128] L. N. Lipatov. The parton model and perturbation theory. *Soviet Journal of Nuclear Physics*, 20(94-102), 1975.

[129] G. Altarelli and G. Parisi. Asymptotic Freedom in Parton Language. *Nuclear Physics*, B(126):298–318, 1977.

[130] M. Froissart. Asymptotic Behavior and Subtractions in the Mandelstam Representation. *Physical Review*, 123(1053), 1961.

[131] A. Martin. Unitarity and High-Energy Behavior of Scattering Amplitudes. *Physical Review*, 129(1432), 1963.

[132] Y. S. Jin and A. Martin. Number of Subtractions in Fixed-Transfer Dispersion Relations. *Physical Review*, 135(6B):1375, 1964.

[133] A. Martin. Extension of the axiomatic analyticity domain of scattering amplitudes by unitarity-I. *Nuovo Cimento*, 42(930), 1966.

[134] N. N. Nikolaev and B. G. Zakharov. Colour transparency and scaling properties of nuclear shadowing in deep inelastic scattering. *Zeitschrift für Physik C Particles and Fields*, 49(4):607–618, 1991.

[135] N. N. Nikolaev and B. G. Zakharov. The triple-pomeron regime and the structure function of the pomeron in the diffractive deep inelastic scattering at very small x. *Zeitschrift für Physik C Particles and Fields*, C64:631–652, 1994.

[136] A. H. Mueller. Soft gluons in the infinite-momentum wave function and the BFKL pomeron. *Nuclear Physics*, B415(2):373–385, 1994.

[137] A. H. Mueller and B. Patel. Single and Double BFKL Pomeron Exchange and a Dipole Picture of High Energy Hard Processes. *Nuclear Physics*, B425:471–488, 1994.

[138] K. Golec-Biernat and M. Wüsthoff . Saturation effects in deep inelastic scattering at low Q 2 and its implications on diffraction. *Physical Review*, D59(014017), 1998.

[139] E. Iancu, K. Itakura, and S. Munier. Saturation and BFKL dynamics in the HERA data at small x. *Physics Letters*, B590(199), 2004.

[140] L. V. Gribov, E. M. Levin, and M. G. Ryskin. Semihard processes in QCD. *Physics Reports*, 100(1-2):1–150, 1983.

[141] N. Arkani-Hamed, S. Dimopoulos, and G. Dvali. The Hierarchy Problem and New Dimensions at a Millimeter. *Physics Letters*, B(429):263–272, 1998.

[142] N. Arkani-Hamed, S. Dimopoulos, and G. Dvali. Phenomenology, astrophysics, and cosmology of theories with submillimeter dimensions and TeV scale quantum gravity. *Physical Review*, D59(086004), 1999.

[143] I. Antoniadis, N. Arkani-Hamed, S. Dimopoulos, and G. Dvali. New Dimensions at a Millimeter to a Fermi and Superstrings at a TeV. *Physics Letters*, B(436):257–263, 1998.

[144] IceCube-Gen2 Collaboration. IceCube-Gen2: A Vision for the Future of Neutrino Astronomy in Antarctica. *arXiv*, High Energy Astrophysical Phenomena(1412.5106), 2014.